Modeling cancer drug response dynamics in single-cells to predict the emergence of drug-tolerant cells

Marielle Péré

UNIVERSITÉ CÔTE D'AZUR

ÉCOLE DOCTORALE
SCIENCES ET TECHNOLOGIES DE L'INFORMATION ET DE LA COMMUNICATION

THÈSE DE DOCTORAT

Modélisation des dynamiques de réponse de cellules uniques aux anticancéreux pour prédire l'émergence des cellules tolérantes

Marielle Péré

Centre Inria d'Université Côte d'Azur, Institut de Pharmacologie Moléculaire et Cellulaire (IPMC) - CNRS

Présentée en vue de l'obtention du grade de docteur en Automatique et traitement du signal et des images
de l'Université Côte d'Azur

Dirigée par : Madalena CHAVES, Directrice de recherche INRIA, Université Côte d'Azur, équipe Biocore
Co-dirigée par : Jérémie ROUX, Chercheur CNRS, Institut de Pharmacologie Moleculaire et Cellulaire (IPMC), Université Côte d'Azur
Soutenue le : 27 mars 2023

Devant le jury, composé de :
Eugenio CINQUEMANI, Chargé de recherche INRIA, Grenoble
Sébastien BENZEKRY, Chargé de recherche INRIA, Université Côte d'Azur, Marseille
Isabelle MUS-VETEAU, Directrice de recherche CNRS, Institut de Pharmacologie Moléculaire et Cellulaire (IPMC)
Inna LAVRIK, Professor, Otto-von-Guericke-Universität Magdeburg
Jacky CRESSON, Professeur, Université de Pau et des Pays de l'Adour (UPPA)

Inria Inserm

Modélisation des dynamiques de réponse de cellules uniques aux anticancéreux pour prédire l'émergence des cellules tolérantes

Modeling cancer drug response dynamics in single-cells to predict the emergence of drug-tolerant cells

Marielle Péré

Jury :

Présidente du jury

Isabelle MUS-VETEAU, Directrice de Recherche CNRS, Institut de Pharmacologie Moléculaire et Cellulaire (IPMC)

Rapporteurs

Eugenio CINQUEMANI, Chargé de Recherche INRIA, Grenoble

Sébastien BENZEKRY, Chargé de Recherche INRIA Université Côte d'Azur, Marseille

Examinateurs

Inna LAVRIK, Professor Doctor, Otto-von-Guericke-Universität Magdeburg

Jacky CRESSON, Professeur, Université de Pau et des Pays de l'Adour

Directeurs

Madalena Chaves, Senior Researcher, Centre Inria Université Côte d'Azur

Jérémie Roux, Chercheur CNRS, Institut de Pharmacologie Moléculaire et Cellulaire (IPMC) et Centre Inria Université Côte d'Azur

Modélisation des dynamiques de réponse de cellules uniques aux anticancéreux pour prédire l'émergence des cellules tolérantes

Résumé

La **résistance des cellules** aux traitements **anticancéreux** est la première cause d'**échec thérapeutique** en oncologie et sert de **base** pour **évaluer l'efficacité des médicaments**. Malgré des avancées considérables dans l'amélioration des traitements disponibles, et leur personnalisation, l'**émergence de cellules tolérantes** aux médicaments, et plus globalement leur dynamique, sont encore mal comprises.

Cette thèse explore l'**initiation de l'apoptose** déclenchée par les ligands agonistes des récepteurs de mort, dans des **populations tumorales isogéniques**, afin d'étudier l'**émergence de cellules tolérantes** aux médicaments. Dans ce but, nous couplons des **données de fluorescence sur cellule unique**, provenant d'expériences de **microscopie sur cellules vivantes**, avec la **modélisation mathématique de la voie transcriptomique** de l'apoptose extrinsèque et des techniques d'**apprentissage automatique** pour atteindre deux objectifs. Le premier est de **mieux comprendre la dynamique des cellules tolérantes** aux médicaments et les différences par rapport aux cellules sœurs sensibles, qui pourraient expliquer l'apparition d'un phénotype tolérant. Le second objectif est d'**identifier les signes précoces de résistance dans ces cellules clonales** afin de prédire le plus tôt possible le premier événement menant à la tolérance. L'inclusion de cette prédiction dans notre **protocole expérimental FATE-SEQ** contribuera à obtenir les **facteurs moléculaires des états cellulaires transitoires de résistance et de sensibilité**, tout en préservant l'intégrité des cellules de l'impact du médicament. À long terme, ce protocole permettra d'**identifier de nouvelles cibles thérapeutiques** (gènes, protéines, etc.) pour la création de **co-traitements**, dès les **premiers stades pré-cliniques** du développement des médicaments.

Afin de développer un **modèle dynamique pour la voie de l'apoptose**, nous **comparons d'abord le rôle de plusieurs composants** de cette forme de mort cellulaire programmée, afin d'**identifier les contributions dominantes**. Nous utilisons ensuite des données expérimentales de cellules uniques pour **estimer les paramètres de différents modèles mathématiques** d'initiation de l'apoptose extrinsèque par ligands de mort, afin d'**étudier les engagements hétérogènes vers la mort** et de mettre en évidence les d**éterminants cinétiques** (réaction chimique, protéines ou une chronologie spécifique) **de la décision cellulaire**. Enfin, en utilisant ces signes de mort comme seuil prédictif, et en les couplant avec des **classificateurs d'apprentissage automatique**, nous construisons un **prédicteur du destin cellulaire en réponse à un ligand de mort** pour les expériences de microscopie sur cellules uniques vivantes.

Mots-clés : Dynamiques des cellules uniques, Cellules tolérantes, Modèles EDO, Apprentissage automatique, Estimation de paramètres, Prédiction du devenir cellulaire, Anticancéreux, Microscopie sur cellules vivantes.

Modeling cancer drug response dynamics in single-cells to predict the emergence of drug-tolerant cells

Abstract

Cell resistance to cancer treatments is the **first cause of therapeutic failure** in oncology and is used as a **basis to evaluate drug efficacy**. Despite considerable advances in the improvement of available treatments, and their personalization, the **emergence of drug-tolerant cells**, and more globally, their dynamics, are still poorly understood.

This thesis explores the **initiation of apoptosis triggered by death-receptor agonist ligands**, in **isogenic tumoral populations**, to study the **emergence of drug-tolerant cells**. To this end, we couple **single-cell fluorescence data**, from **live-cell microscopy** experiments, with **mathematical modeling** of extrinsic apoptosis **transcriptomic pathway**, and **machine learning** techniques to achieve two aims. The first one is to **better understand the dynamics of drug-tolerant cells**, and the differences with respect to sensitive sister cells, that would explain the appearance of a tolerant phenotype. The second objective is to **identify early signs of resistance** in these clonal cells to **forecast the first event leading to tolerance** as early as possible. The inclusion of this prediction in our experimental **protocol FATE-SEQ** will allow us to obtain the **molecular factors of innate cell states of resistance and sensitivity**, preserving these states from the drug impact. In the long term, this protocol will allow to **identify new therapeutic targets** (genes, proteins, etc.) to create **co-treatments**, from the **early pre-clinical stages** of drug-development.

To develop a **dynamical model for the apoptosis pathway**, we first **compare** the role of several **distinct components** of this form of programmed cell death, to **identify the dominant contributions**. We then use single-cell experimental data to **estimate the parameters** of different mathematical models of extrinsic apoptosis initiation by death ligand to study the **heterogeneous commitments to death**, and **find kinetic determinants** (chemical reaction, proteins, or event specific timing) **of cell decision**. Finally, using these **death signs as a predictive threshold**, and coupling them with **machine learning classifiers**, we build a **predictor of the future single-cell fate in response to death ligands** for live-cell microscopy experiments.

Keywords: Single-cell dynamics, Drug-tolerant cells, ODE models , Machine learning, Parameter estimation, Cell fate prediction, Cancer drugs, Live-cell microscopy

Acknowledgements

In French, there is an expression saying that it takes a whole village to raise a child but I think I needed more than a village to help me achieve my PhD goals! So, without further ado, here are some precious "neighbours" I want to thank.

First, as I wouldn't be here without them, I want to thank my two amazing directors Madalena Chaves and Jérémie Roux for their continuous and enthusiastic support over these three intensive years. Madalena, your constant trust in me and optimism were everything I needed when I didn't believe in myself. You allowed me to take my time and really helped me to grow up as a researcher, always with kindness. Jérémie, you know I like a good challenge and I always need new goals to achieve but I also need someone to guide my ideas and improve them. You were always there when I needed an advice, a review or simply an encouragement so thank you for always following me in all my projects and turn them into a success!

I would like to thank now my reviewers, Eugenio Cinquemani and Sébastien Benzekry, along with my examiners Isabelle Mus-Veteau, Jacky Cresson and Inna Lavrik as I couldn't dream about a better jury. Thank you Eugenio for following my work since the first year by being the head of my "comité de suivi" but also one of the reviewers of this thesis. Your comments and ideas really improved my work all along these years. Sébastien, merci d'avoir pris le temps de lire avec attention mon manuscript et pour tes super retours qui m'ont donné encore plus envie de continuer mes recherches mais aussi ouvert les yeux sur de nouvelles directions! I also want to thanks Pr Dr Inna Lavrik for her relevant comments, especially in Systems Biology. I read her work since day 1 of my PhD and I really hope we can collaborate in the future. Je souhaite ensuite remercier ma présidente du Jury, Isabelle Mus-Veteau: merci pour votre bienveillance et pour avoir su faire de ma soutenance un jour spécial pour moi mais aussi pour ma famille. Enfin, Jacky, je finis par toi car tu es bien la première personne à m'avoir donné envie de faire de la recherche et suggéré que cette voie serait pour moi! J'espère que nos dejeuners/après-midi recherche annuels continueront longtemps et je tiens à te remercier pour tes mails de soutien, ta compréhension mais aussi pour m'avoir montrer qu'on peut faire de la recherche de haut niveau dans la bienveillance.

I can't thanks my research peers without thanking my amazing supervisor during my stay in the biomolecular control group at the University of Edinburgh: Diego Oyarzún. I learnt so much by your side but I also need to thank you for your constant support before and after my research visit.

I'm also so grateful you managed to build such an amazing team. Hence, in the same line, I want to thanks all my "Scottish" friends : the craziest but so brittish greek guy I know Evangelos, the super-sport-woman Hollie, Charlotte, Zuzanna, Arin, Ricardo, Michael, Vanessa, Alexandra, Lilli and Michal for the pub nights and your warm welcome! You really made my stay perfect guys!

Talking about amazing teams, I can't forget the unforgettable and best team ever BIOCORE but also all McCorevid : over these years we did party a lot, worked a bit but most of all shared amazing moments so thanks: Lucie, Colin, Eleni, Walid, Côme, Claudia, Francesca, Juan Carlos, Adel, Frank, Hannah, Good and Bad bunny (David and Ignacio), Joseph, Nicolás and obviously Bruninho. Four special notes about these amazingly crazy people I love so much: Clo, we started together, we finished together, you really were my anchor during these years and I don't know what I'm going to do without our daily discussions and our day trips with Stella! I want also to thanks the guys I shared the best office with: my research sister Odile , my thesis companion Yan, mi guapita Jineth, the bothering Kilian (no I'm kidding!) but also the person that plans on stealing my desk Ali! I have also to mention the incredible McTao Team with the JBs, and the evil duo: Alesia and Lambi! Por fin, no he olvidado los mejores gordos de la planeta: Nicolas y Agustín, merci pour les randos poulet, les plans foireux et toutes nos aventures de beauf!

Je veux également remercier mes super collègues du côté Biologie: Kelly, Marina, Benjamin et bien-sûr Asma pour les meilleures sessions dechiffrage de code! et les deux équipes dans lesquelles nous avons évolué à l'IRCAN, en particulier Victoria et Patrick pour une inoubliable partie de pétanque et l'équipe de Bernard Mari à l'IPMC et leur super accueil!

Je tiens maintenant à remercier mes amis qui me soutiennent depuis si longtemps et qui ont pris le temps de faire les 600 kilomètres qui nous séparent pour venir m'encourager ou m'envoyer regulièrement un petit message de soutien: Laulau, Maïtena, Bichette, Kiki, Baboun mais aussi Romano, Gaoule, Coco et Clem, Merci d'être là depuis si longtemps!

Dans la même lignée, je ne peux pas oublier de remercier mon incroyable famille qui me supporte (dans tous les sens du terme) depuis toujours: Rapha (merci encore pour les cours de stats!), Cycy et Romain, Michou et Aurélie, Thibault, Titi (qui a gentimment relu ce pavé) et Hervé et les petits monstres qui les suivent partout depuis quelques années! Je tiens également à souligner l'incroyable voyage de mes oncles et tantes et de mes parents pour venir m'encourager en personne le jour de ma soutenance et à quel point le geste m'a touché. Enfin, un simple merci n'est pas assez fort pour remercier ma mounette qui depuis 8 ans fait tout pour me soutenir mais aussi venir me voir le plus souvent possible! Merci!

Je tiens à finir ces remerciements par les deux êtres qui ont sûrement le plus compté durant ces trois ans: Momo, le meilleur donneur de calins canin sur terre y por supuesto, Carlito Flaquito, por creer en mí más de lo que yo nunca lo haré y por estar siempre a mi lado.

Good Reading!

Table of content

Appendices

Acronyms

DTP: Drug-Tolerant Persisters
MRD: Minimal Residual Disease
C8: Caspase 8 (initiator)
FACS: Fluorescence-activated cell sorting
FISH: Fluorescence in situ hybridization
C10: Caspase 10 (initiator)
C3/C7: Caspase 3-7 (effector)
pC8: pro-Caspase 8
FADD: Fas-Associated protein with Death Domain
MOMP: Mitochondrial Outer Membrane Permeabilization
DISC: Death Inducing Signaling Complex
RNA: Ribonucleic acid
mRNA: messenger RiboNucleic Acid
DNA: DeoxyriboNucleic Acid
p53: cellular tumor antigen p53 - onco-protein
TRAIL: Tumor necrosis factor related apoptosis inducing ligand
Bax: Bcl-2-associated X protein
Bcl-2:B-cell lymphoma 2
FRET: Förster resonance energy transfer
CFP: Cyan Fluorescent Protein
YFP: Yellow Fluorescent Protein
IC-RP: Initiator-Caspase Reporter Protein
c-FLIP: cellular FLICE-Like Inhibitory Protein
NF-κB: Nuclear Factor-kappa B (transcription factor)
CD95: Cluster of Differentiation 95 protein
CD95L: CD95 Ligand
TNF: Tumor Necrosis Factor
NK: Natural Killers
PD-1: Programmed cell death protein 1, immune checkpoint
CTLA-4: Cytotoxic T-lymphocyte-associated protein 4, or CD152, protein receptor and immune checkpoint
IAP: Inhibitors of Apoptosis Protein

XIAP: X-linked inhibitor of apoptosis protein
HeLa cells: Cervix cancer cell line
APO-1: APO-1 antigen
DED: death-effector domain
STAT1: Signal transducer and activator of transcription 1
STAT3: Signal transducer and activator of transcription 3
KRAS: Kirsten rat sarcoma virus, gene
SMAD4: Mothers against decapentaplegic homolog 4, transcription factor
CDKN2A: cyclin-dependent kinase inhibitor 2A, gene
JAK2: Janus kinase 2, non-receptor tyrosine kinase
STAT5: Signal transducer and activator of transcription
AMPK: Adenosine Monophosphate-Activated Protein Kinase
OXPHOS: Oxidative phosphorylation, metabolic pathway
ATP: Adenosine triphosphate
ADP: Adenosine diphosphate
mTOR: mechanistic target of rapamycin, protein kinase
ERK: Extracellular signal-regulated kinases
C:N: Cytoplasm: Nucleus ratio
ODE: Ordinary Differential Equations
SDE: Stochastic Differential Equations
EAICM: Extrinsic Apoptosis Initiation Core Model
EAICRM: Extrinsic Apoptosis Initiation Core Reaction Model
ARIMA: AutoRegressive Integration Moving Average model
ETS: Error, Trend and Seasonal model
Nelder-Mead: Downhill simplex method, optimization method based on simplexes deformation
LFGB: Broyden-Fletcher-Goldfarb-Shanno algorithm, iterative method for solving unconstrained nonlinear optimization problem
PINN: Protein-Protein Interaction Network
ACC: Accuracy
T: Tolerant
S: Sensitive
ML: Machine Learning
DL: Deep-Learning
DT: Decision-Tree
RF: Random Forest
GB: Gradient Boosting
AB: AdaBoost
SVC: Support Vector machine Classifier

MLP: Multi-Layer Perceptron
K-NN: K-Nearest Neighbors
PCA: Principal Component Analysis
MCC: Matthews correlation coefficient
MK: Markedness
TPR: True Positive Rate
TNP: True Negative Rate
PPV: Positive Predicted Value
NPV: Negative Predicted Value
FNR: False Negative Rate
FPR: True Positive Rate
FOR: False Omission Rate
FDR: False Discovery Rate
TP: True Positive
TN: True Negative
FP: False Positive
FN: False Negative
TSC: Time-series Classification
RISE: Random Interval Spectral Ensemble
TSF: Time series Forest Classifier
ROCKET: RandOm Convolutional KErnel Transform
DrCIF: Diverse Representation Canonical Interval Forest Classifier
CIF: Canonical Interval Forest Classifier
HIVE-COTE: Hierarchical Vote Collective of Transformation-based Ensembles
BOSS: Bag Of Symbolic Fourier approximation Symbols

List of figures

List of tables

PART I

Introduction

CHAPTER 1

Motivations

The US National Cancer Institute defines cancer as a disease in which certain cells in the body grow uncontrollably and spread to other parts of the body (metastasis). These cancer cells have the ability to proliferate, grow and invade other parts of the body, without any signal (over **growth and proliferation**). On the other hand, they can also ignore signals to divide or die (escape **apoptosis**), or hide from the immune system's surveillance. In summary, a cancer cell has a **different way of processing external signals**, and **making a fate decision** accordingly. Understanding these processes is key to discover efficient and sustainable treatments in the future.

The most common strategy to fight cancer after surgical resection, is **combination therapy** [Chatterjee and Bivona, 2019, Mokhtari et al., 2017, Pomeroy et al., 2022]. The principle is to combine different therapeutic agents (surgery, radiotherapy [Ansari et al., 2022, Najafi et al., 2022, Tagliaferri et al., 2022], immuno-oncology [Carlsen et al., 2022], chemotherapy [Pomeroy et al., 2022], etc), to increase the global efficacy of the treatment, by targeting different mechanisms responsible for cancer. For instance, a first drug targets cancer cells or oncogenes, meanwhile, an additional agent aims to reduce side-effects, or tackle the causes of the first drug-resistance [Hasanovic et al., 2020], whether in a direct way, or indirectly, through the immune system. In immuno-oncology, 80% of the trials are combination therapies [Hatron, 2021, Ciccolini et al., 2020]. Nowadays, the majority of the treatment routines for a patient with cancer include a combination from 3 to 9 different drugs over the course of the disease management.

However, despite extensive efforts in pre-clinical and clinical research, to elaborate personalized, more efficient and less invasive treatments, the available drugs are expensive, and lack efficacy. Oncology has the lowest rate of success, all areas confounded [Wong et al., 2019], for an average cost per approved molecule of $3 billions. As for the next-generation of treatments, the attrition rate of immuno-oncology therapeutic agents are one of the highest, only 3% of the molecules in pre-clinical trials are approved. Eventually, only one molecule out of 10,000 gets on the market , after more than 15 years of research and development [Hatron, 2021, Wouters et al., 2020].

There is an urgent need to improve the drug design process, starting with the early stages of drug development [Honkala et al., 2022]. Better drug screening combined with more accurate ways

of finding new therapeutic targets will be mandatory to cope with the increasing number of cancers in the upcoming decades worldwide. Specifically, for the design of combination therapies, we need to :

I - implement rational and systematic methods to identify bio-markers of drug resistance

II - design drug combination from the first steps of pre-clinical research [Ciccolini et al., 2020],

to lower down the attrition, the costs and accelerate drug discovery. This improvements requires also to improve the evaluation of drug efficacy in cell-based assays to better evaluate drug-candidate therapeutic potential.

The current way to evaluate drug efficacy in cell-based assays is based on fractional killing, yet, paradoxically, it also defines the main cause of therapeutic failure in cancer treatments. **Fractional killing** [Inde et al., 2020, Pomeroy et al., 2022, Roux et al., 2015] defines a striking reality: isogenic cancer cells, in the same environmental conditions, [Purvis et al., 2012, Spencer et al., 2009], can all respond to cytotoxic drugs, with different timing and magnitude though, with only a fraction of them commit to apoptosis [Inde and Dixon, 2018, Roux et al., 2015]. These tolerant cells are called **drug-tolerant persisters**. The most drug-tolerant persisters observed, the less efficacious the drug is, with higher chances of therapeutic failure and relapses. Indeed, these cells will form the minimal residual disease (MRD) [De Conti et al., 2021, Mikubo et al., 2021], a reservoir of emergent drug-resistant cells, with sustainable genetic mutations, leading to acquired drug-resistance, that could recreate a tumor later. Eventually, it leads to drug evasion, incomplete tumor clone eradication, and at the end, treatment failure [Strasser and Vaux, 2020].

1.1 Studying drug-tolerant persisters

Among all the types of drug-resistance in cancer, non-genetic resistance, or **drug-tolerant persisters (DTP)**, remains one of the less understood nowadays [Cabanos and Hata, 2021, De Conti et al., 2021, Kochanowski et al., 2018, Mikubo et al., 2021], with a complete characterization of these cells still lacking [De Conti et al., 2021, Vallette et al., 2019]. However, DTP are key to understand drug-resistance, as they are its first manifestation. In this work, we will focus on the **first emergence of these drug-tolerant persisters in a clonal population.**

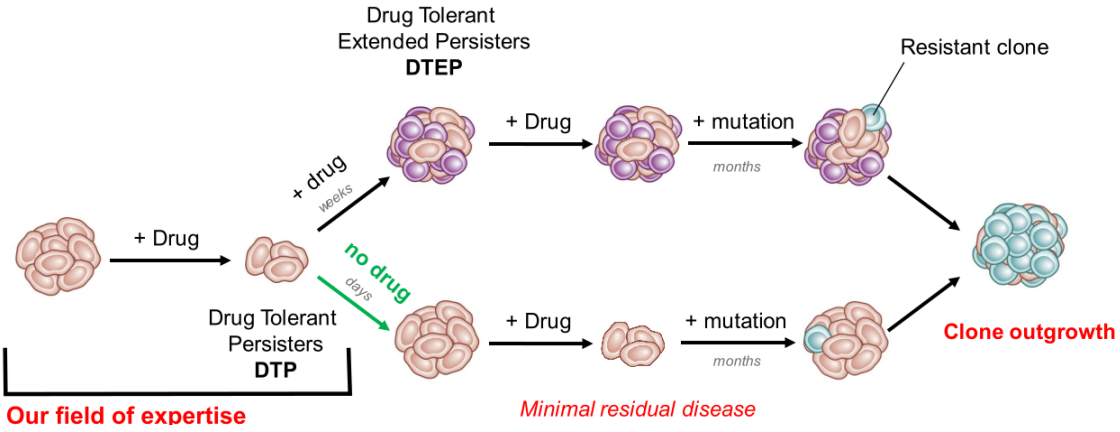

Figure 1.1: **Drug-tolerant persisters, the first step toward drug-resistance**: How the first emergence of drug-tolerant cells leads to sustainable genetic resistant. Figure from Jérémie Roux's presentation at ECMTB 2022 conference and at the EMBO workshop 2022: Persistent cancer cell 2022 - adapted from [Oxnard, 2016]

1.1.1 Characteristics, regulations and origins

Drug-tolerant persisters are a common characteristic of all the possible clones in a tumor, as shown by Rehman et al. [Rehman et al., 2021]. But how cancer cells become and remain DTPs, even though they never see the drug before, and what characterize them is still largely unknown.

Different reviews describe the key features of drug-tolerant persisters [Cabanos and Hata, 2021, De Conti et al., 2021, Mikubo et al., 2021] among which: slow cell cycle [Vallette et al., 2019], quiescent cells like features, remodeled metabolism with more dependency to mitochondrial oxidative phosphorylation [Kalkavan et al., 2022, Kosaisawe et al., 2021], the use of other sources of nutrients, like fatty acid oxydation [De Conti et al., 2021, Mikubo et al., 2021, Shen et al., 2020], up-regulation of epithelial-mesenchymal transition markers [Mikubo et al., 2021, Peyre et al., 2021], disruption of apoptosis signal transduction [Meyer et al., 2020, Roux et al., 2015], escape from immune system effectors [Roux et al., 2015], or a boosted cellular plasticity. Hopefully, drug-tolerant persisters states are also known for their reversibility. Indeed, several studies have shown that drug-sensitivity is a transient cell state [De Conti et al., 2021, Echeverria et al., 2019, Fallahi-Sichani et al., 2013, Flusberg et al., 2013, Forcina et al., 2017, Shen et al., 2019], but little is known about how cells can switch from one state to another.

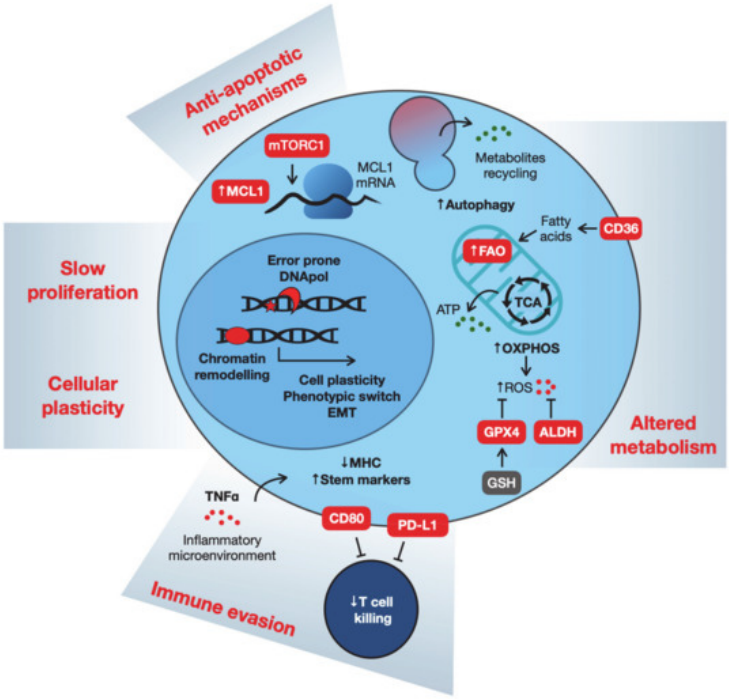

(a) From [De Conti et al., 2021]: **Features and vulnerabilities of drug-tolerant cells**

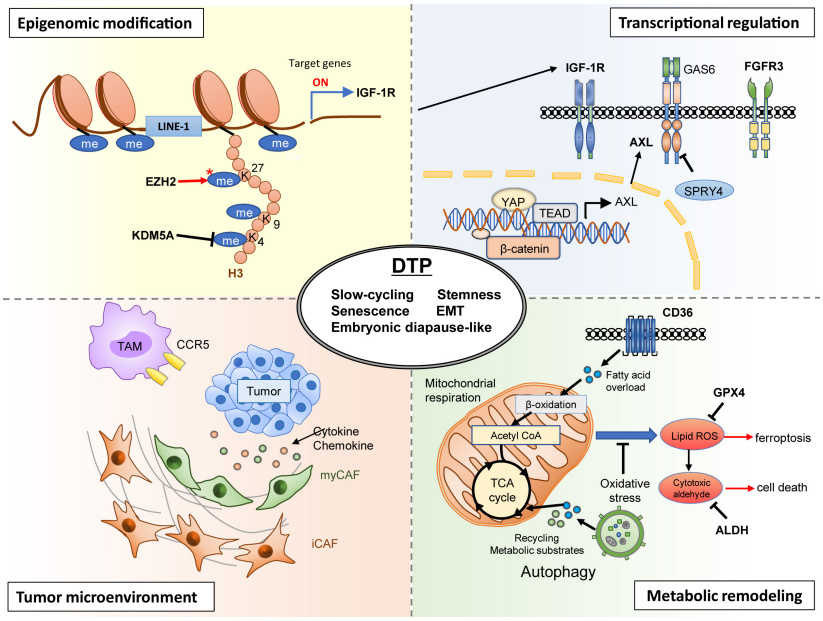

(b) From [Mikubo et al., 2021]: **Biological features and regulating mechanisms of DTPs**

Figure 1.2: **Overview of drug-tolerant persisters: characteristics, regulations and potential targets**

Nevertheless, several mechanisms has been shown to regulate, or induce, drug-tolerant states [Kochanowski et al., 2018]: activation of stress responses pathways [Kalkavan et al., 2022, Terai et al., 2018, Zhang et al., 2022b], adaptation of the signaling pathways [Guilbaud and Galluzzi, 2022, Kalkavan et al., 2022], regulation by transcriptional processes [Kalkavan et al., 2022, Roux et al., 2015, Meyer et al., 2020], along with the impact of tumor-microenvironment [Echeverria et al., 2019, Mikubo et al., 2021, Swayden et al., 2020], are potential regulators or/and inducers of drug-tolerant persisters states that will require further studies.

Finally, the question of innate or acquired is central in drug-tolerant persisters, as there is no consensus on their definition yet: whether the DTP state is a pre-existing cell state, already present before the drug input, that is only revealed by the drug, whether it is a state induced by the drug after the treatment. In both cases, for now, those tolerant cells are drug-tolerant persisters, whether tolerance is acquired or innate. **In this work, we will follow the first hypothesis and study the state of DTPs revealed by the addition of a cytotoxic drug, in a clonal cancer cell population, but before drug could have an impact on this cell state.**

1.1.2 Therapeutic target

Although much remains to be elucidated to understand the mechanisms behind drug-tolerant persisters, therapeutic strategies have been proposed to eliminate DTPs: [Cabanos and Hata, 2021, Kochanowski et al., 2018, Mikubo et al., 2021]: maintaining the cells in a persistent state, such that cells remain in a slowly proliferating state, before they turn into fully resistant cells [Mikubo et al., 2021], resensitising persister cells to cancer drug, as in persistent bacteria [Kochanowski et al., 2018], or targeting the origins or necessary factors that keep persistent cells tolerant to drugs, so cells can never enter a resistant state, or force them to switch into a susceptible one [Cabanos and Hata, 2021, Meyer et al., 2020].

In summary, lot of efforts have been done to establish a common characterization of the DTP, find biomarkers to identify them, and create potential combination therapies to target the DTP [Cabanos and Hata, 2021, Zhang et al., 2022b], but none of them made it to the clinical step yet.

1.1.3 Toward rational identification of biomarkers of drug-tolerance for combination therapy

Pre-clinical research on drug combinations remains experimentally divrese. There is no unified method, with clearly defined steps to follow, to create effective drug combinations in cell-based assays [Ciccolini et al., 2020], or even to identify potential therapeutic targets (see [Ali et al., 2021, Ward et al., 2020] for general examples of different methods to find therapeutic targets).

Therefore, for several years, many efforts have been made to find rational and systematic methods to create drug combinations, through drug re-purposing [El Zarif et al., 2022, Schipper et al., 2022, Sun et al., 2016, Wuerth et al., 2016], drug-combination prediction (with machine learning [Ballester et al., 2021, Kong et al., 2022, Torkamannia et al., 2022a] combined with drug-screening cell based assays [Jaaks et al., 2022, Xia et al., 2022]), or upstream identification of therapeutic targets responsible for drug-resistance [Liao et al., 2022, Rees et al., 2022].

Identifying the origins of drug resistance [Salgia and Kulkarni, 2018], along with potential biomarkers, is a long-term challenge [Chatterjee and Bivona, 2019, Gottesman et al., 2002, Kyrochristos et al., 2019, Wang et al., 2019, Ward et al., 2020]. Whether one is interested in genetic resistance ([Hu and Zhang, 2016, Kyrochristos et al., 2019, Rueff and Rodrigues, 2016, Long et al., 2020], acquired resistance [Sun et al., 2022, Shi et al., 2021], or non-genetic tolerance [Bell and Gilan, 2020, Inde and Dixon, 2018, Kalkavan et al., 2022, Labrie et al., 2022, Leonce et al., 2022, Meyer et al., 2020, Nam et al., 2021], deciphering a cell's negative response to one drug (or more [Long et al., 2020]), in the sense that the cell is not dead at the end of a cytotoxic treatment, is a delicate task [Cabanos and Hata, 2021]. This process requires the ability to compare sensitive and resistant cells, before the sensitive cells die (and so to be able to identify them before death), to determine molecules with "significant" differences between drug-tolerant and sensitive populations. Distinguishing the causes from the factors necessary in the implementation of the cellular decision, from the effects of the cross-talk with the tumor environment [Weiss et al., 2022], seems even more difficult, as cell systems are complex and deeply intertwined, and still largely unknown. Finally, the validation of new targets requires the existence of a second drug capable of targeting the drug tolerance factor, which represents an additional challenge to assess the druggability of the target [Liao et al., 2022].

1.2 Single-cell analysis to decipher the mechanisms leading to cell decision

To tackle these challenges, and have a better understanding of intra-tumor heterogeneity and cell response variability, from the earliest pre-clinical stage, single-cells studies are key [Tellez-Gabriel et al., 2016]. Single-cell analysis is the study of all potential omics levels (from genomic [Bowes et al., 2022] and epigenomic [Nam et al., 2021] to proteomic [Vistain and Tay, 2021]), for **each cell** of a population, from one specific analysis to multi-omics studies [Casado-Pelaez et al., 2022, Kashima et al., 2020, Ma et al., 2022].

Compare to their cousins, the bulk analyses, that hide cell difference in a mean behaviour, **single-cell experiments** are designed to **study heterogeneity** between cell types, or in our case, within a cell type by comparing cells sates of isogenic cells. The idea is that each cell has its own specificity [Coskun et al., 2016], and this specificity might be an actual clue to understand the general behaviour observed at the population level. Studying each cell separately is crucial to get a complete picture of the adaptability of the system under study, and to decipher by which regulatory process **two identical cells**, responding to the **same signal** in the apparent **same conditions**, with a **similar evolution over time**, are able to **take different decisions** leading to **opposite phenotypes**. The perfect example is the case of drug-tolerant persisters, that appear after drug treatment in a clonal cancer cell population, as a non-genetic decision of the cells to evade apoptosis.

1.2.1 Cell states, signaling pathways and cell decision

At every second, cells make **fate decisions**, in response (or not) to their environment, and the signals they process, but also by taking into account their current inner state. Cell differentiation [Brand and Morrissey, 2020, Sagar and Grün, 2020], proliferation or senescence [Jones et al., 2022], pathway activation [Kosaisawe et al., 2021], division or quiescence [Matson and Cook, 2017], production or not [Cinquemani et al., 2019, De Jong et al., 2017], survival or death [Roux et al., 2015], resistance or sensitivity [Simsir and Mus-Veteau, 2020], so many crucial decisions that ultimately lead a cancer cell to become drug-tolerant, while its clonal neighbor sister decides to commit to apoptosis, or to switch from a tolerant state to a sensitive one, at a different time scale [Flusberg et al., 2013, Saint-Antoine et al., 2022].

To make these decisions, but also reverse the process if needed, cells use **signaling pathways**. signaling pathways are complex interwoven networks of multiple layers (DNA, RNA, proteins, etc) of molecules, that interact together in a specific order, with different time scales [Spiller et al., 2010], and shape the cell-state, allowing them to fine-tune their response to a stimulus, in our case a cancer drug [Kramer et al., 2022, Schneider et al., 2012].

These states are, most of the time, **transient**. This is the case for drug-induced apoptosis [Flusberg et al., 2013, Kosaisawe et al., 2021], or cell differentiation [Olsson et al., 2016], for instance. The reversibility of these states, and the resulting cellular decisions, are strong motivations to understand cell decision making process, especially the state-switching [Saint-Antoine et al., 2022], as it would open the way for controlling these states, and force cells to remains drug-sensitive.

Timing is key to observe state-switching, and have a glimpse of the dynamics at play in cell decision making. In fact, multiple studies have shown that cell decision is strongly time-depending [Inde et al., 2020, Paek et al., 2016, Roux et al., 2015, Schneider et al., 2012, Yurkovsky and Nach-

man, 2013]. Therefore, time-lapses imaging are preferred than static snapshot data. These methods allow to follow cells changing over-time without destroying them, whether with fluorescent activity reporter proteins [Albeck et al., 2008b, Paek et al., 2016, Szalai et al., 2021], or by measuring features describing cells, like shape and size evolution [Jones et al., 2022].

Connecting single-cell time-trajectories with the phenotype observed, along with the potential signaling pathways leading the decision-making process, creates a picture of the cell state, from the signal reception to the final implementation of the cell decision, that can help identifying the causes of the specific phenotype. Indeed, time-trajectories make the connection between the phenotype, and the signaling pathways evolution. The assumption behind this last statement is the following: a specific dynamic (in time, in amount of molecules and in topology of the network) in the signaling pathway corresponds to a distinct decision in the future, but also leads to a specific evolution for the time-trajectory (shape, activation speed, etc), that we can observe **before** the decision is implemented. By comparing the different time-trajectories observed (and the corresponding phenotype) between cells, we can predict the corresponding signaling pathways dynamics, identify the causes of a specific cell decision, but also discover key features in the time-trajectory, that can be predictive of the cell decision, and therefore being used to forecast the future phenotype. The ultimate goal is to be able to control this future phenotype by targeting its causes upstream.

1.2.2 Data challenges: sparsity and observability

As simple as it seems, linking time-trajectories, cell decision and signaling pathways is a complex exercise. Time-trajectories are often **noisy**, the **few measurements available are sparse**, and there is a lot of **overlapping**, even between cells with different phenotypes, in the long term. When it comes to forecasting a phenotype from the signal, to have an early prediction, an additional problem is raised when the data available are not informative enough, because too early in the process, or simply hidden by other signals. These complications bring us back to the key question: **what information lies in the signal and especially when and how could it be extracted to forecast cell drug-response?**

In other words, the question is about the **observability** of our phenomenon of interest [Bijman et al., 2021], in terms of timing but also of tools and meanings to observe the implementation of cell decision. Taking the example of a fluorescent signal, it is impossible to know definitively which exact pathway led to the activation of the fluorescent reporter protein, or even if the observed signal is a combination of several **cell signaling mingled into one**, as several pathways can lead to the same time-trajectory observed (the same way that different sets of parameters leads to the same output in a mathematical model). What is actually observed is the fluorescence intensity per time, reproducing in some way (depending on the probe used), the dynamics of the signaling pathway of

interest. In addition, between cell decision and its implementation, a **delay** is often observed, in particular in the reporter protein activation, and so the first measurements may not be informative at all. One last challenge is also the comparison between cells, when we do not have the same amount of data for each of them (especially when they are dead), and that each cell has its own timing.

1.2.3 Single-cell multi-omics: the current approach to understand cellular decision-making

To tackle the challenges above, and create a detailed picture of the cell state, single-cell multi-omics studies are key [Zhu et al., 2020], yet as we will see, only a few take the cell responses (i.e the time-depending function) into account.

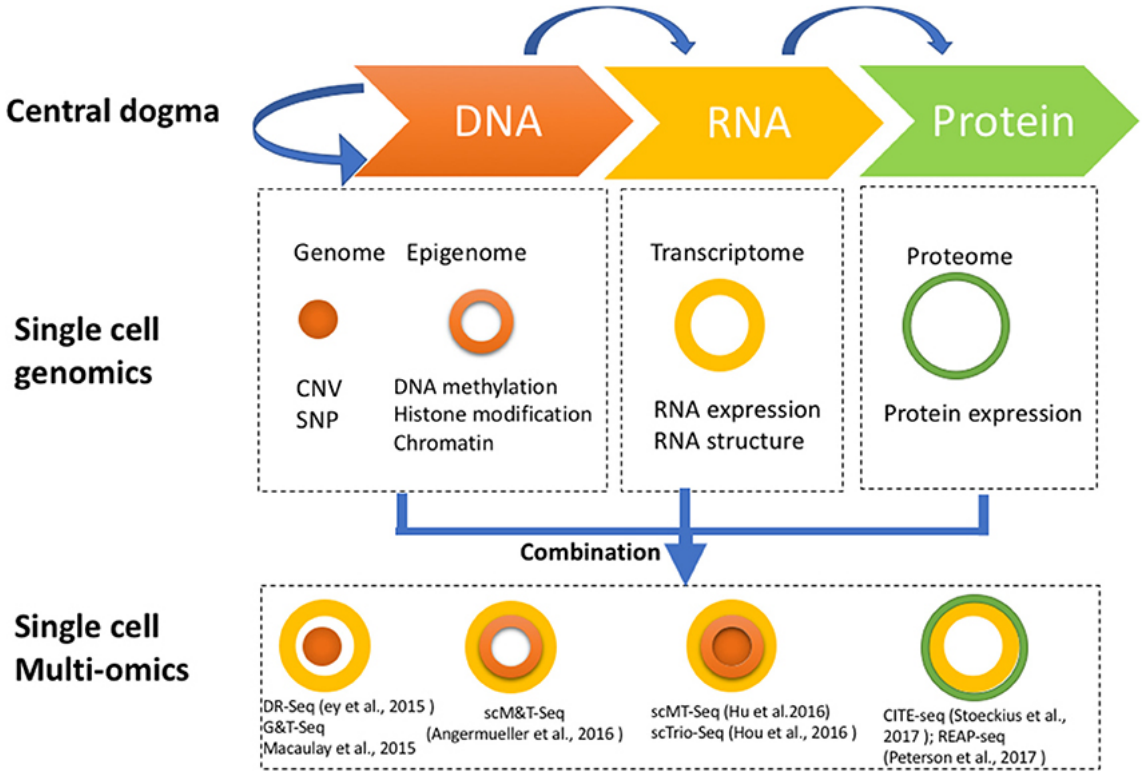

Figure 1.3: **Strategies for multi-omics profiling of single cells:** Three major types of molecules relating to biological central dogma (Top). Single cell genomics methods profiling the genome, epigenome, transcriptome, and proteome are shown by different shapes with variable colors (Middle). Single cell multi-omics methods are built by combining different single cell sequencing methods to simultaneously profile multiple types of molecules of a single cell genome wide (Bottom). For example, G&T-seq was built by combining genome (orange) and transcriptome (yellow) to simultaneously detect DNA and RNA of the same cell genome wide - Figure 2 and legend from [Hu et al., 2018]

These multimodal analyses combine different single-cell approaches to gain new information [Ma et al., 2020, Nam et al., 2021, Peng et al., 2020, Gabor et al., 2021, Zhu et al., 2020, Hu et al., 2018, Bai et al., 2021, Watson et al., 2021] on several layers of regulation in the same cell (genomic

and transcriptomic (smart-seq, quart-seq, etc), proteomic and genomic [Demaree et al., 2021], epigenome with transcriptome, etc [Hu et al., 2018, Macaulay et al., 2017]). Yet, they do not link the actual cell's function at the single-cell level.

Indeed, each layer is important to understand cell heterogeneity. sc-DNAseq methods, like single cell whole genome amplification (scWGA), identify structure modification and genome mutation. scRNA-seq techniques [Chen et al., 2019, Nath and Bild, 2021] reveal major transcriptomic changes, that help deciphering the molecular profile of drug efficacy in a single-cell [Meyer et al., 2020], or the extent of intra-tumour heterogeneity [Rodriguez-Meira et al., 2019, Yang et al., 2020a, Nath and Bild, 2021]. Finally, proteomic help quantifying protein amounts for each cell [Kelly, 2020, Pham et al., 2021], and even their spatial location with spatially resolved transcriptome technologies (ex: FISH [Wen and Tang, 2022], etc), event though the proteomic protocols still needs some major improvements to facilitate reproducibility [Kelly, 2020] and produce large-scale studies. We refer to [Zhu et al., 2020, Jiao et al., 2022, Hu et al., 2018, Lee et al., 2020, Leonavicius et al., 2019] for the technical protocols to combine the sequencing methods as it is beyond the scope of this work, but in summary, 2 steps are needed to carry the study: the selection and the capture of the cells, before a destructive sequencing deteriorate the cell samples to have new insights of their inner state.

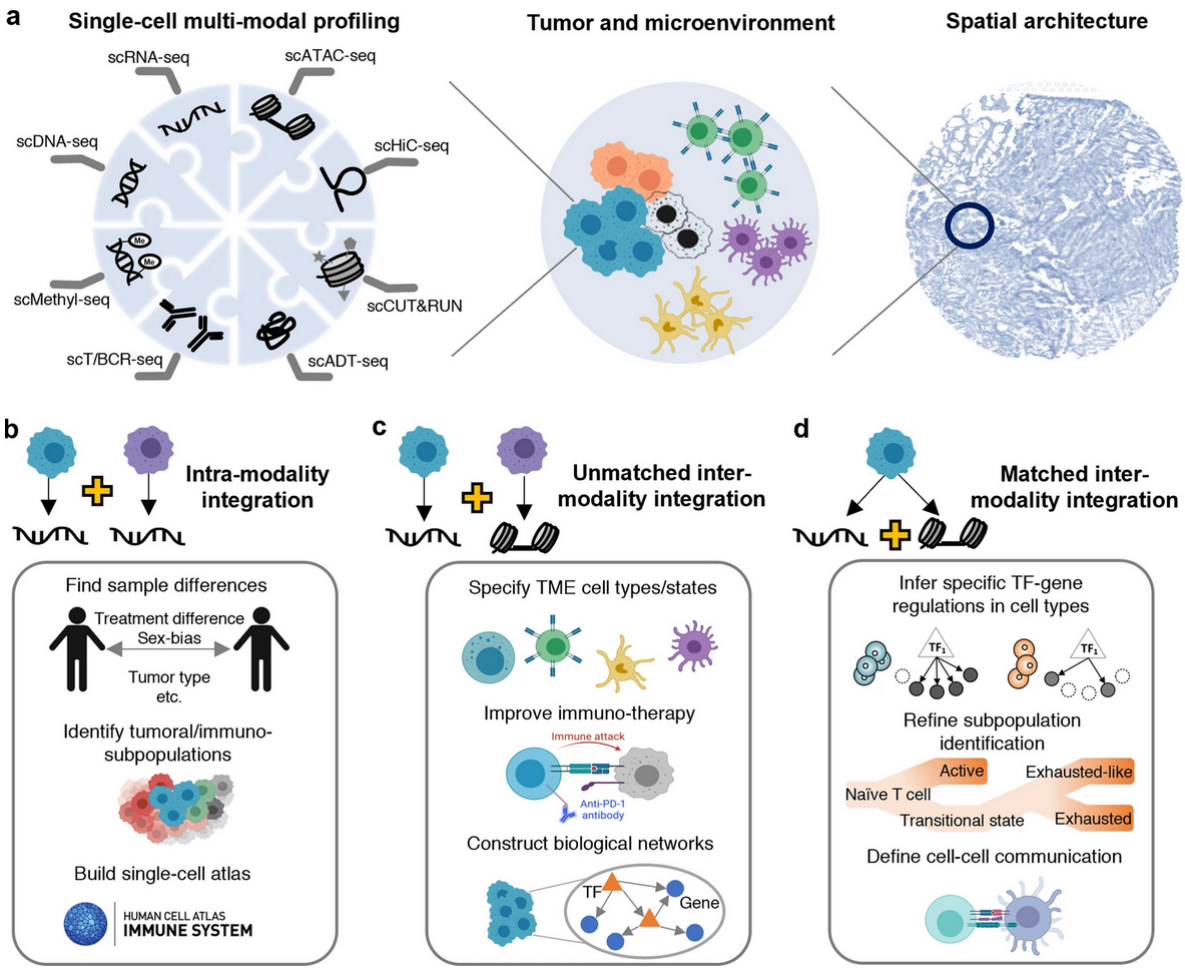

Figure 1.4: **scMulti-omics profiling and application examples in immuno-oncology:** a - An overview of various scMulti-omics data types. Sequencing techniques including single-cell DNA sequencing (scDNA-seq) for DNA sequence profiling, single-cell RNA sequencing (scRNA-seq) for gene expression profiling, Single-cell sequencing assay for transposase-accessible chromatin sequencing (scATAC-seq) for chromatin accessibility profiling, single-cell high-throughput chromosome conformation sequencing (scHiC-seq) for chromatin architecture organization, single-cell cleavage under targets and release using nuclease (scCUN&RUN) for histone modification profiling, single-cell antibody-derived tag sequencing (scADT-seq) for protein abundance profiling, single-cell T cell or B cell receptor sequencing (scT/BCR-seq) for receptor repertoire (the recombination of the variable (V), diversity (D), and joining (J) genes of T/B cell receptors) diversity and clonality profiling, and single-cell methylation sequencing (scMethyl-seq) for DNA methylation status profiling. b–d - scMulti-omics enabled immuno-oncology research. - Figure 1 and legend from [Ma et al., 2022] with the corresponding legend

Selection and capture can be in both order: first **isolation** and capture of the cells, and then selection according to a pre-defined criteria checked before ([Pham et al., 2021, Camp and Lukonin, 2022]) or after sequencing, for instance by barcoding cells. Vice versa, the other possibility is to, first, select cells, and then isolate them according to the selection, like we do in the lab [MP1, Meyer et al., 2020]. We can cite for instance selection technologies at the proteomic level: mass spectrometry, electro-mechanical methods [Jiao et al., 2022], or a fluorescent probe [Jiao et al., 2022] (at a fixed time, like FACS [Hu et al., 2018] (Fluorescence-activated cell sorting), or

using the signal evolution over time [MP1, Meyer et al., 2020, Kosaisawe et al., 2021]), coupled with a laser micro-dissection to isolate cells, or any isolation technique. In both cases, experiments could be performed in population (with 96-cell plate, frame slide [MP1, Meyer et al., 2020], micro-fluidic platforms [Liu et al., 2022, Jiao et al., 2022], etc), or cells can be already isolated, one per compartment. Obviously, population studies are preferred, as they are closer to reality where cells constantly interact with each other. Once isolated and put in a tube, **destructive sequencing techniques** could be applied [Jiao et al., 2022].

However, as every technology used to study cells, data obtained are noisy and sparse, drop out or confounded factors are frequent [Zhu et al., 2020]. In addition, these studies are sources of very large datasets, or on the contrary small ones, with only a dozens of cells, necessitating the adaptation of the statistic techniques used accordingly, but also to be able to cross data from different sources. See [Adossa et al., 2021, Hu et al., 2018, Ma et al., 2020, Leonavicius et al., 2019, Ma et al., 2022] for reviews of the clustering, graph-based and statistical methods used for single-cell multi-omics integration. See also [Chen et al., 2019] for methods dedicated to RNA-seq data, the current method we use in our lab. All together, this makes reproducibility, and comparing datasets between different labs, difficult [Hu et al., 2022], each lab creating its own pipeline for images and data analysis [Watson et al., 2021, Mund et al., 2022, Hu et al., 2022], even though the sequencing techniques are the same.

In summary, new technologies with high throughput and precision are available, and new biomarkers have emerged [Nath and Bild, 2021], but there is still no comprehensive understanding that unifies the observed tumor cell type-specific behaviors, in particular the differential responses to cancer drugs, and the apparition of drug-tolerant persisters. The collective realization is that no single gene or protein expression measurements is predictive or therapeutic outcome.

In this work, we will focus on the molecular mechanisms that allow the emergence of drug-tolerant persisters. In Chapter 2, we will present in detail, the different steps of our Systems pharmacodynamic approach for the pro-apoptotic death ligand TRAIL, and how mathematical modeling helped deciphering some of the mechanisms involved. Based on these insights, we will also introduce a workflow developed in the lab: **FATE-SEQ**. This single-cell pipeline aims to bring answers to the problematics we just have mentioned in cancer pharmacology for drug-tolerant persisters: the need for a better drug efficacy evaluation, a systematic and reproducible way to identify the causes of drug-tolerance that leads to a rational method to discover new biomarkers and therapeutic targets for combination therapy.

As we will be studying TRAIL-induced apoptosis in cancer cells in the following, we will refer to the cell's lethal decision between apoptosis (death) and drug tolerance (survival) as **cell fate decision**.

CHAPTER 2

Deciphering the molecular origins of TRAIL-tolerant persisters to design better combination therapies

The previous chapter highlighted the necessity to link time trajectories, signaling pathways and cell decision to find the causes of drug-tolerance, and better control single-cell drug-response. This chapter describes the recent efforts and advances to understand the non-genetic causes of the first drug-persistence event observed in isogenic cancer cells during a treatment by TRAIL (tumor-necrosis-factor related apoptosis inducing ligand).

Cancer and Apoptosis

Apoptosis is a critical cellular decision in **cancer emergence**, but also in **tissue homeostasis** in general. This form of **programmed cell death** exhibits a wide range of variability in cell populations, where even identical sister cells can exhibit a considerable degree of heterogeneity in apoptosis commitment in response to drug treatment [Roux et al., 2015]. This **non-genetic heterogeneity** has impaired single-cell technologies to identify **predictive biomarkers of tumor sensitivity to anti-cancer therapies** [Meyer et al., 2020].

Immunotherapies

To **induce cell death in tumor cells**, many treatments have already been designed and tested so far. Among them, **immunotherapies** [Tang et al., 2018] are a promising way to treat cancer [Carlsen et al., 2022, Sancho-Araiz et al., 2021]. The principle of immunotherapy is to **reactivate the immune system** of the patient, to allow his immune cells to better target and kill the tumoral population, while sparing healthy cells. To do so, we can use drugs that stimulate the immune system or mimic it (like the **cytokines** [Berraondo et al., 2019]), or block cancer cells to send inhibitory signals to the immune cells (like **checkpoint inhibitors** that target co-inhibitory immune checkpoints like PD-1 and CTLA-4) [Esfahani et al., 2020, Shin, 2021, Jenkins et al., 2018, de Miguel and Calvo, 2020]).

Inside the cytokine family, the tumor necrosis factors (TNF) family members (or death ligands [Sancho-Araiz et al., 2021, Holland, 2014]) are proteins, naturally produced by immune-cells, like T-cells or Natural Killers (NK), that trigger cell death by binding to their respective receptor at the cell membrane [Wu et al., 2020]. Among death-receptors ligands, we can cite the TNF itself, CD95L or TNF-related apoptosis-inducing ligand (TRAIL) [Falschlehner et al., 2009].

Today, immunotherapies are available in clinics, but for only a few cancers, and for patients with highly specific biomarkers. Hence scientific research aims at widening the application spectrum of these treatments [Ciccolini et al., 2020]. However, studying the immune-system/ tumor cross-talk is challenging experimentally, as two distinct entities (tumor and immune-system), with strong influence on each other, has to be study simultaneously. The available protocols go from the patient level, with the analysis of biopsies, to the cell scale, with organ-on-chips and co-culture studies, or simply the use of molecules, released by immune cells, as drug in *in vitro* experiments [Roux et al., 2015].

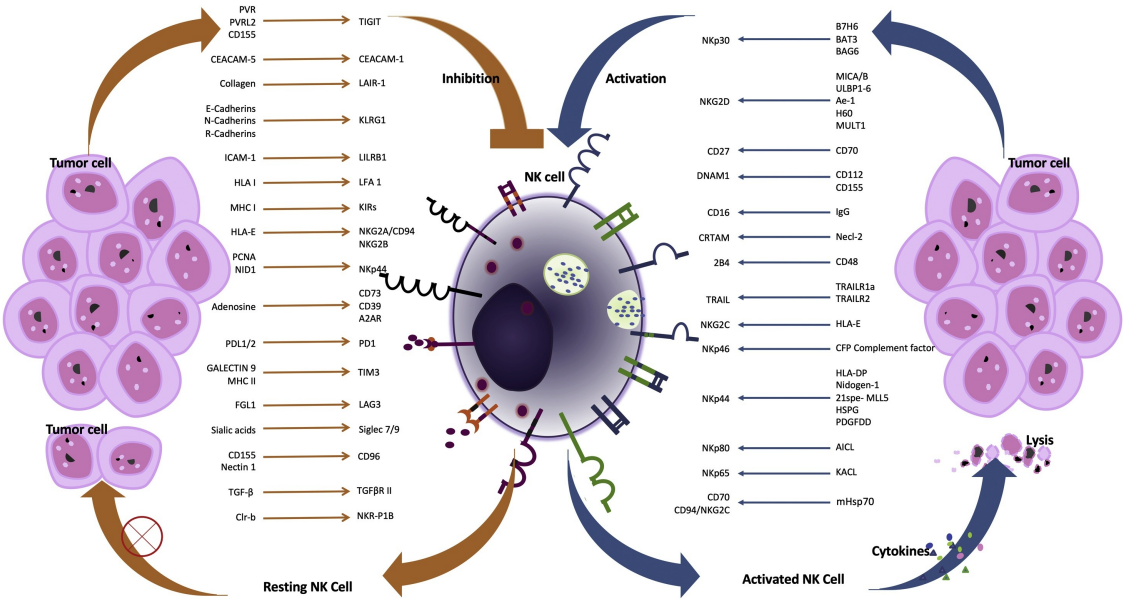

Figure 2.1: **Natural Killers (NK) cell opposing functions:** On the right side, NK cells activation relies on stimulation of activating receptors on the surface of NK cells such as NKG2D, DNAMQ, CD16, etc, which finally trigger the expression of inflammatory cytokine including IFN-γ, TNF-α, IL2 and IL18 and then, mediates the killing ability of NK cells. On the other hand, inhibiting receptors on NK cell surface functioned as negative regulator of NK cell-mediated cytotoxicity (on the left side), which decreases cytokines production of NK cells. Thus, suppression of these kinds of receptors such as PD-1 and KIRs alter NK cells status in tumor microenvironment. The corresponding ligands of NK cell surface receptors was also stated. Figure and legend from [Wu et al., 2020].

Why TRAIL?

Among all the molecules released by immune cells to target tumours, the tumor-necrosis-factor related apoptosis inducing ligand (or TRAIL) has been pointed out for the last decade.

Although **TRAIL** seemed to be a very promising drug [Yuan et al., 2018], thanks to its ability to target specifically cancer cells, it **showed only limited success in the clinic** due to a **lack of efficacy**, with a **large fraction of resistant cells**, even at saturating doses [Fallahi-Sichani et al., 2013, Flusberg et al., 2013, Holland, 2014, Micheau et al., 2013].
Hence, we will focus in this case also on this death-ligand [Montinaro and Walczak, 2022, Soto-Gamez et al., 2022, Suo et al., 2022], as it is a good example to understand drug-tolerant persisters.

2.1 TRAIL inducing apoptosis

Death ligands, like TRAIL [Holland, 2014], trigger cell death, mainly via the extrinsic apoptosis pathway [Elmore, 2007, Lawen, 2003]. Binding on the death receptors DR4/DR5 [Shlyakhtina et al., 2017] on the cell membrane, they form the Death-Inducing Signaling Complex (DISC) by recruiting Fas-Associated proteins with Death Domain (FADD) [Dickens et al., 2012] and next, pro-caspases

8 (pC8) [Chang et al., 2003, Fox et al., 2021, Neumann et al., 2010]. Then, this complex activates the initiator caspases 8 (C8 hereafter). Recognized as the key of extrinsic apoptosis [Roux et al., 2015], C8 mediates Bid cleavage that governs the mitochondrial permeabilization (MOMP) [Eskes et al., 2000, Kalkavan et al., 2022], and causes the activation of the effector caspases 3 and 7 [Boice and Bouchier-Hayes, 2020]. Finally, DNA fragmentation drives the cell to death [Albeck et al., 2008b, Rehm et al., 2006].

During drug-triggering apoptosis, TRAIL can also activate other metabolic pathways. Through caspase 8, the intrinsic apoptosis pathway [Gaudet et al., 2012, Ooi and Ma, 2013] includes several proteins from the BCL-2 family, with both pro- and anti- apoptosis roles, and involved the mitochondria, leading to MOMP. On the other hand, TRAIL can directly trigger the surviving pathway [Buchbinder et al., 2018, Fulda et al., 2010, Li et al., 2021, Neumann et al., 2010, Portt et al., 2011], creating a **complex signaling network that enables cells to take heterogeneous decisions from a same stimulus**, in our case from TRAIL binding.

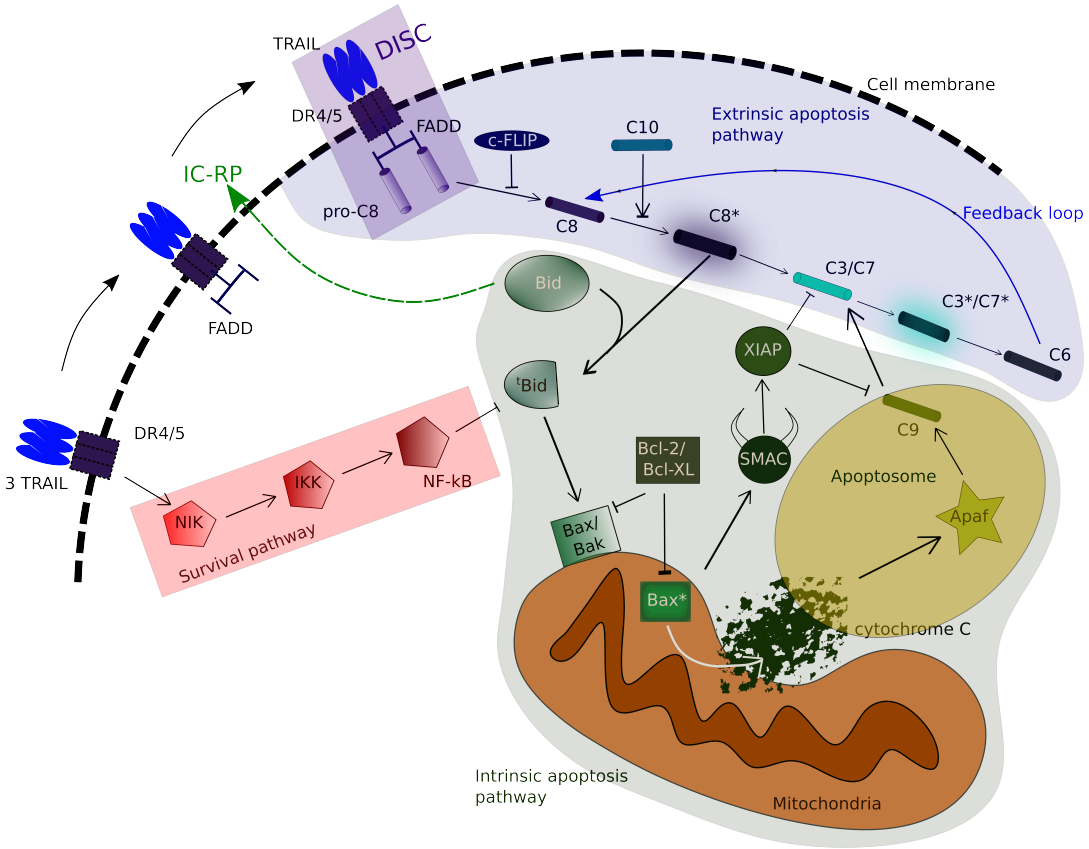

Figure 2.2: **Apoptosis transcriptional pathways triggered by TRAIL** inspired by Albeck et al. [Albeck et al., 2008b]: blue: extrinsic pathway, red: survival pathway, green: MOMP

2.2 Modeling TRAIL-triggering apoptosis to determine the topology and the timeline of the signaling pathways involved

To have a better understanding on the functional mechanisms of TRAIL, a lot of mathematical models of TRAIL inducing apoptosis, in different cell types and combined with other drugs, have been proposed, following the surge of experimental protocols available to study death receptors agonists. The following section presents the different types of modeling used, how they have been calibrated (which type of data, etc), and what they taught us.

2.2.1 A long history of mathematical modeling of apoptosis

The majority of mathematical models for drug-inducing apoptosis [Lavrik et al., 2009], for the past two decades, are mainly deterministic systems, using ordinary differential equations, and applying mass action kinetic. Nevertheless, four Boolean networks [Calzone et al., 2010, Chaves et al., 2009, Plaugher and Murrugarra, 2021, Schlatter et al., 2009] have been proposed, as they offer more flexibility in the modeling. Three other papers use stochastic equations to reproduce the natural noise in all biological systems [Bertaux et al., 2014, Buchbinder et al., 2018, Matveeva et al., 2019] and two discrete systems [Amstein et al., 2022, Plaugher and Murrugarra, 2021] exist too.

Most of the models focus on transcriptional pathways, but three articles use multi-scale modeling: Bertaux et al.[Bertaux et al., 2014] includes the mRNA level, Kallenberger et al.[Kallenberger et al., 2014], Liu et al.[Liu et al., 2021] and Waldherr et al. [Waldherr et al., 2009] model also the population level. Following and completing the literature work of L. Pereira in his thesis [Pereira, 2019], five summary tables of the mathematical models proposed to study drug-inducing apoptosis, and its mechanisms, at the transcriptional level, are available in Appendix A.3, p.194. See the articles of Schleich et al., and Srinivasan et al. for recent reviews [Schleich et al., 2016, Srinivasan et al., 2022], and the connections with other types of death (necroptosis, ferroptosis, pyroptosis), Lavrik et al. article for a review of ODE models for apoptosis before 2009 [Lavrik et al., 2009], and Loos et al. for a global review of the computational systems proposed to model single-cell heterogeneity in general [Loos and Hasenauer, 2019]. Finally, Eydgahi et al. gives also a comparison of the different ways to calibrate a model, using Bayesian optimization, and a detailed presentation of the use of ODE systems to model apoptosis and the challenges in parameter estimations (identifiability, data accessibility, etc)[Eydgahi et al., 2013].

Focusing on the deterministic systems describing extrinsic apoptosis process [Albeck et al., 2008b, Pereira, 2019], these models involve tens of chemical reactions and proteins, trying to be as exhaustive as possible. But the number of variables and parameters is often too large to understand

the role of each component, or even to estimate these parameters from the data available. Therefore, we can also cite several attempts to reduce the models' size [Chaves et al., 2021, Neumann et al., 2010, Ortega et al., 2022], or use smaller models (less than 10 equations) [Chen et al., 2007a, Cui et al., 2008, Eissing et al., 2004, Lee et al., 2021b, Liu et al., 2021, Stucki and Simon, 2005, Roux et al., 2015, Voropaeva et al., 2017, Xie et al., 2022, Yin et al., 2017], focusing on a special event in the signaling pathways.

Specifically, for TRAIL-inducing apoptosis, Albeck, Aldridge, Gaudet, Spencer, Ortega and their teams [Albeck et al., 2008b, Aldridge et al., 2011, Gaudet et al., 2012, Spencer et al., 2009, Ortega et al., 2022] study extrinsic apoptosis and calibrate their models on FRET time-trajectories of HeLa cells treated with TRAIL and cycloheximide, Roux, Chaves, Marquez and Matveeva use the same protocol but without cycloheximide, to obtain tolerant cells too, and analyse TRAIL effect alone [Roux et al., 2015, Chaves et al., 2021, Márquez-Jurado et al., 2018, Matveeva et al., 2019]. Bertaux, Lederman and Stoma study TRAIL on other cell lines [Bertaux et al., 2014, Lederman et al., 2018, Stoma et al., 2013]. Considering a larger scope, other models of receptor-mediated apoptosis have been proposed on other death-ligands such as CD95-L or FAS-L [Aldridge et al., 2011, Bentele et al., 2004, Bertaux et al., 2014, Buchbinder et al., 2018, Fricker et al., 2010, Hillert et al., 2020a, Hua et al., 2005, Ivanisenko and Lavrik, 2020, Kallenberger et al., 2014, Neumann et al., 2010].

Finally, there has been a growing number of papers using fluorescent proteins for live-cell microscopy experiments, a trend that is still going on today, in many biology-related fields [Kosaisawe et al., 2021], not only for studying apoptosis [Albeck et al., 2008a, Aldridge et al., 2011, Bertaux et al., 2014, Chaves et al., 2021, Gaudet et al., 2012, Lederman et al., 2018, Márquez-Jurado et al., 2018, Pereira, 2019, Ortega et al., 2022, Spencer et al., 2009, Stoma et al., 2013]. Even though the models remain simplified, the progresses in single-cell experiments allow a better validation and calibration of the models, with more quantitative and qualitative data for each cell, that we will take advantage of in this work to study TRAIL-induced apoptosis.

2.2.2 Understanding cell response heterogeneity during TRAIL treatment

To have an insight of how cells process TRAIL and make their decision, we have already shown that many studies and mathematical modeling efforts have evaluated the origins and mechanisms involved in drug response heterogeneity in apoptosis triggered by TRAIL, at several cell levels.

These models study **drug-tolerance inheritance and general cell response heterogeneity** [Flusberg et al., 2013, Spencer et al., 2009], and highlight special mechanisms such as the **random binding of the death ligand** on the DR4/5 [Matveeva et al., 2019, Shlyakhtina et al., 2017] and the

presence of **decoy receptors** (which impair the formation of a functional DISC after ligand binding [Bouralexis et al., 2005, Jong et al., 2022]).

Gene roles in TRAIL efficiency have also been extensively studied, to explain cell response heterogeneity [Seidel and von Karstedt, 2022, Strasser and Vaux, 2020], with especially two genes that stand out. **p53**, an oncogene, whose mutation could be found in many cancers, plays a determinant role in apoptosis [Ballweg et al., 2017, Baslan et al., 2022, Chong et al., 2019, Friedel and Loewer, 2022, Xie et al., 2022, Yang et al., 2020b], but we can also mention the impacts of **gene CD-95** as a regulator of FADD, an essential protein for the pC8 binding to the DISC [Bentele et al., 2004, Buchbinder et al., 2018, Fricker et al., 2010, Neumann et al., 2010].

At the metabolic level, the role of key-proteins in apoptosis and their activation time is also determinant. **c-FLIP antagonist role** has been revealed, and gives a better understanding of how it "competes" with pC8 at DISC level to trigger (or not) apoptosis [Fricker et al., 2010, Han et al., 2008, Hillert et al., 2020b, Tsuchiya et al., 2015, Fox et al., 2021, Seyrek et al., 2020], (even if C8 and FLIP seem to bind the DISC on different sites, pC8 favors c-FLIP recruitment [Hughes et al., 2016]).

However some of the proteins known to be involved in apoptosis have less well identified roles, with opposite function sometimes. As an example, the initiator caspase 10 (C10) may be an anti-apoptotic factor in some cases [Horn et al., 2017], as some members of Bcl-2 family that compete to activate MOMP downstream [Albeck et al., 2008b, Eskes et al., 2000, Rehm et al., 2006], but can also have a pro-death role [Wachmann et al., 2010, Wang et al., 2001]. Indeed, C10 can trigger apoptosis in absence of C8 [Kischkel et al., 2001, Raulf et al., 2014], and favors anti-tumorigenesis [Kumari et al., 2019] too.

Finally, **C8 activation has been defined as a determining factor in cell death decision** [Dickens et al., 2012], by showing a **threshold in rate and timing for C8 activation that distinguishes resistant and sensitive cells** [Chaves et al., 2021, Roux et al., 2015]. These studies lead to the conclusion that **cell decision happens before MOMP and the effector caspase cascade**.

In the following, we will describe thoroughly the key articles on which this thesis is based, in order to gain a better understanding of the link between signaling pathway - cell dynamic - cell death decision for TRAIL-induced apoptosis in clonal HeLa cells, to identify the causes of TRAIL-tolerant persisters. This section is summarized by Figure 2.3.

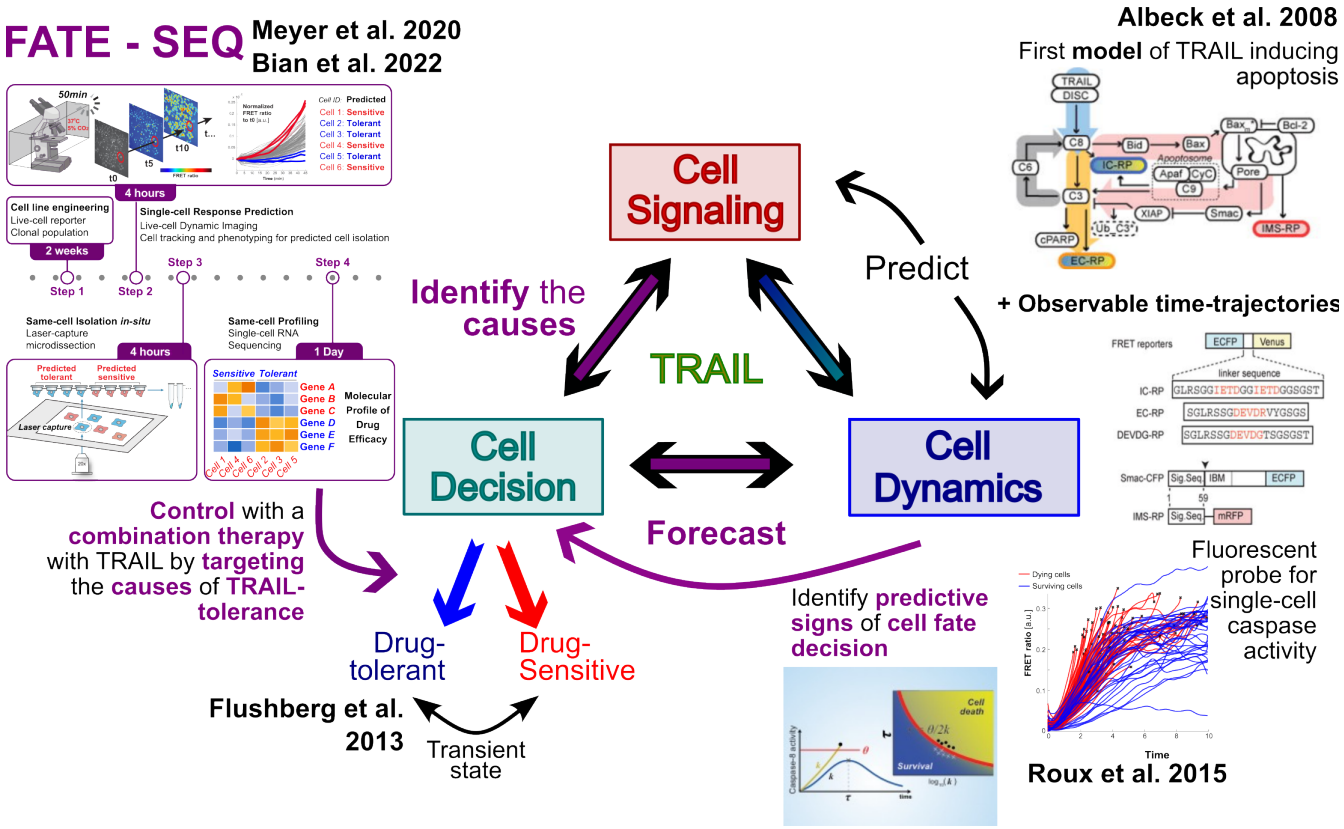

Figure 2.3: **Our Systems Pharmacology approach for TRAIL inducing apoptosis**: a brief summary of the following section Our Systems Pharmacology approach: Deciphering the links between Cell Signaling, Cell Dynamics and Cell Decision for TRAIL-inducing apoptosis

2.3 Our Systems Pharmacology approach: Deciphering the links between Cell Signaling, Cell Dynamics and Cell Decision for TRAIL-inducing apoptosis

2.3.1 Observing non-genetic reactions to TRAIL over time

2.3.1.1 Reporter protein and FRET

To study TRAIL, Albeck et al. [Albeck et al., 2008a] designed an Initiator Caspase-Reporter Protein (IC-RP), a FRET (Foster Resonance Energy Transfert) [Szalai et al., 2021] pair of fluorescent proteins (CFP and FRET), that are linked by the peptide sequence of Bid, cleaved by caspase 8 (C8). FRET therefore decreases once IC-RP molecules are cleaved by C8. In the same time, Bid is cleaved in tBid, which regulates MOMP in extrinsic apoptosis. As there is no degradation of IC-RP, contrary to tBid, it accumulates leading to the FRET stabilization at the end of the experiment, for tolerant cells, that corresponds to the tBid degradation, and give the particular shape to FRET time-trajectories (see Figure 2.3 p.49, Roux et al. 2015). In this work, we will refer to **FRET signal,**

the actual ratio CFP/FRET.

In his study [Albeck et al., 2008b], Albeck improved one of the first ordinary differential equation (ODE) models of apoptosis [Fussenegger et al., 2000], modeling both extrinsic (type 1) and intrinsic (or mitochondrial/type 2) apoptosis. By combining his model with live-cell reporters, flow cytometry, and immuno-blotting, he showed the crucial role of initiator and effector caspases to generate cell heterogeneity leading to fractional killing, during death-ligand inducing apoptosis. This model is the basis of a dozen of papers [Aldridge et al., 2011, Bertaux et al., 2014, Chaves et al., 2021, Gaudet et al., 2012, Lederman et al., 2018, Márquez-Jurado et al., 2018, Pereira, 2019, Ortega et al., 2022, Spencer et al., 2009, Stoma et al., 2013], where they complete or reduce the model, with mathematical tools or simply by focusing on a special part of the model. They also make the parameters variate to reproduce single-cell heterogeneity. Using Albeck et al. fluorescent probe, the most recent models were able to fit each cell of the experiments [Chaves et al., 2021, Roux et al., 2015].

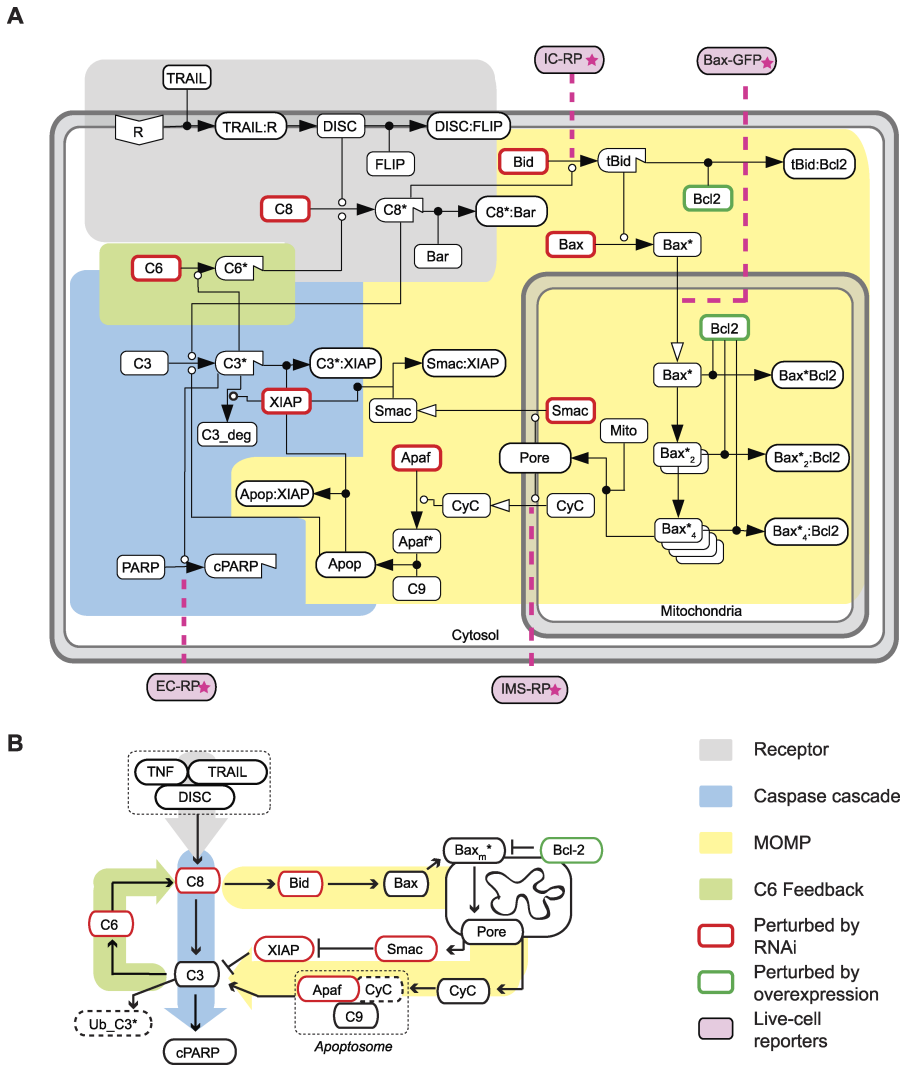

Figure 2.4: **Extrinsic apoptosis reaction model (EARM):** A - The major features of the network are highlighted by color: gray, receptor module; blue, direct caspase cascade; green, positive feedback loop; yellow, mitochondrial feed-forward loop. B - A condensed alternate representation of the network. Figure and legend from [Albeck et al., 2008b]

2.3.1.2 Transient cell state of TRAIL-sensitivity

In 2013, Flusberg *et al* [Flusberg et al., 2013] studied the hereditary aspect of TRAIL-tolerance on several generations of cancer cells.

Interestingly, treating TRAIL-tolerant persisters a second time with the same amount of drug, in the same conditions, leads to the same proportion of sensitive and tolerant cells observed in the first experiment [Fallahi-Sichani et al., 2013, Flusberg et al., 2013], and fractional killing is once again observed. This repetition, and its particular outcomes, shows evidence that **drug-sensitivity is a transient cell state**, rather than a permanent disposition. Cancer drug only reveals the cell

sensitivity state at the moment the drug is given, and cells could actually switch from one state to another, opening the door of a potential control of the switching by co-treatments.

But to be able to actually control the cell state, we need to find the origins of the tolerant state to influence cell drug-response.

2.3.2 Understanding non-genetic drug-resistance origins

In 2015, Roux et al. [Roux et al., 2015] studied the **non-genetic resistance origins**, in particular the **first emergence of tolerance** in drug-tolerant cells.

Data presented in this article are **single-cell fluorescent time-trajectories**. These time-lapses data measure C8 activity before MOMP happens for **clonal HeLa cell** treated with **different amounts of TRAIL** (and not with cycloheximide contrary to [Albeck et al., 2008b, Rehm et al., 2006]), for 10 hours, thanks to the Initiator Caspase-Reporter Probe (IC-RP) designed by Albeck *et al*. The experiment set-up is described in Figure A.11.1. The time-trajectories from this study will be used all along this work to validate our studies.

This study shows the existence of a **biological threshold in Caspase 8 dynamic** (represented both by the derivative of the fluorescent signal, and two parameters of a small phenomenological model of TRAIL triggering apoptosis (B, C and D subplots in Figure 2.5 p.53)), that cells have to **overcome to be sensitive** to the death ligand. It was the **first study** showing a **clear relationship between a response phenotype and a set of protein dynamics (C8, FLIP, Bcl-L an -XL) over time**.

This **biological threshold** was then adapted into a **predictive threshold** to be used as a proxy of cell fate phenotype (sensitive/tolerant), to forecast cell drug-response in our experiment workflow **FATE-SEQ**.

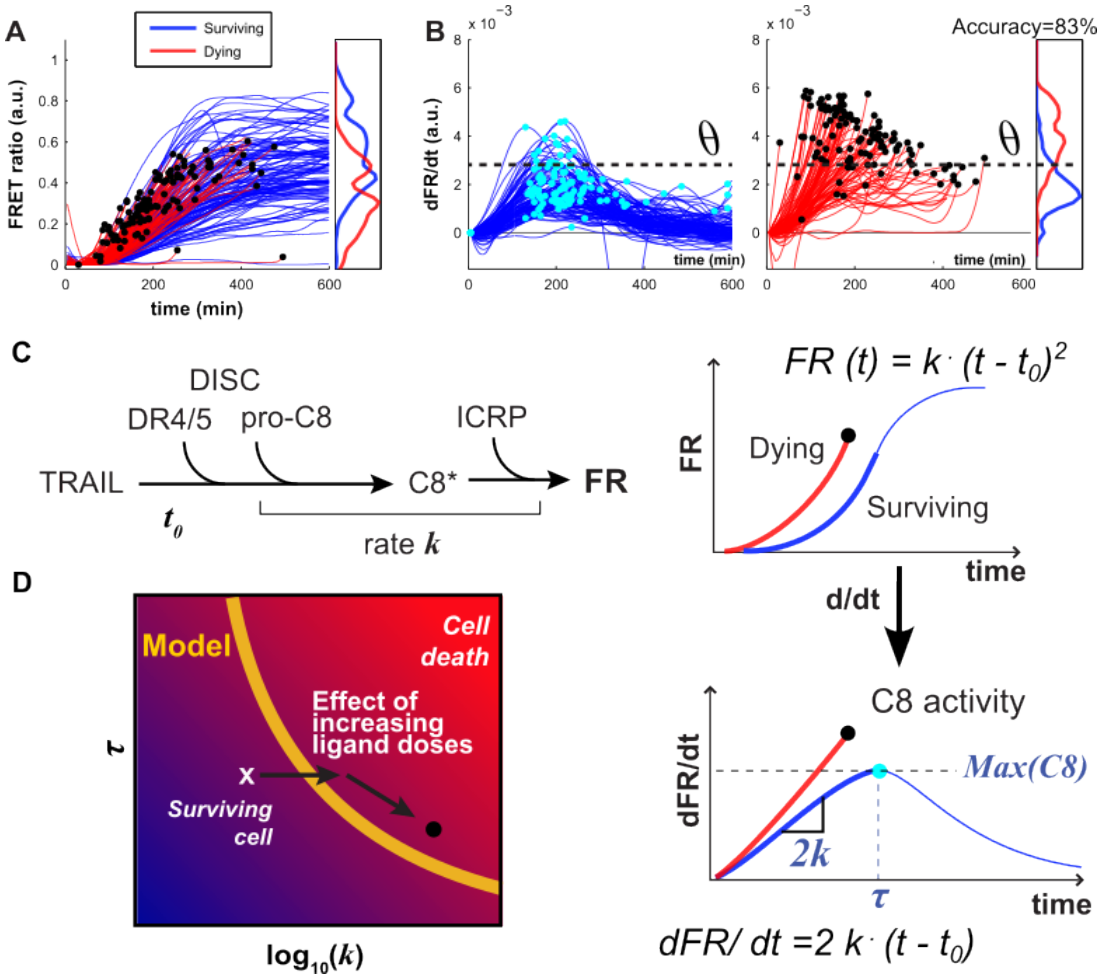

Figure 2.5: **Fractional killing arises from cell to cell variability in overcoming a caspase activity threshold**: A - FRET ratio trajectories for ICRP−expressing and surviving HeLa cells (blue) or cells that died (yellow) following treatment with 25 ngml of TRAIL (ICRP cleavage reports on initiator caspase (C8) activity). Black dots denote cell death, at which point trajectories were truncated. All cells exhibited some C8 activation, and the right panel shows the distribution of maximal FRET ratio levels for ≈ 300 dying and living cells. B - Derivative of the FRET ratio for surviving cells (blue, left panel) and cells committing to apoptosis (red, middle panel) for the same experiment as in (A). Cyan and black dots show the maximal value of the derivative (note that black dots also denote the time of cell death). The right panel shows the distribution of maximal values of the derivative for both populations. The red line indicates the optimal value $\theta\, T25 = 2.61 \times 10^{-3}$ that separates the two populations with 83% accuracy. C - Phenomenological model of caspase 8 activation and ICRP probe cleavage. FR stands for FRET ratio. D - Caspase 8 activity landscape defined by the rate of C8 activation (k) and the duration of C8 activation phase (τ) for the same experiment as in (A). The yellow line is the fate boundary. The background color is based on the fate of cells (blue for surviving and redfor dying). Figure and legend from [Roux et al., 2015]

2.3.3 FATE-SEQ identifies molecular factors of transient cell states of drug-sensitivity

A systematic and logical approach to identify therapeutic targets in drug-tolerant persisters for combination therapy, is the following. First, select a potential drug, then find the molecular causes and biomarkers of cell tolerance to that drug, and finally, use the molecular factors as a target for

a second therapeutic agent. The second drug will increase the sensitivity of the cell to the first treatment. Therefore, the first treatment will be more effective than alone [Chung et al., 0] and the global efficacy will increase consequently.

Indeed, targeting the causes of the drug-tolerant persisters is a potential way to avoid the emergence of resistant mutants leading to relapses and therapeutic failure [Cabanos and Hata, 2021, Sharma et al., 2010]. These sensitivity states being transient [Flusberg et al., 2013, Sharma et al., 2010], controlling the switching state of resistant cells seems pertinent and feasible, but in fact, numerous challenges underlie the process.

FATE-SEQ [Meyer et al., 2020] pipeline aims at providing a better evaluation of the therapeutic efficacy of a drug by identifying the molecular factors of drug-efficacy, and at determining corresponding biomarkers and therapeutic targets for a combination therapy, with the drug studied. The second drug will target one factor causing the DTP to make cells more sensitive to the first drug studied, increasing the global efficacy of the treatment. The main benefit of the method lies in the rational design of combination therapies from the early stages of drug-design process, to reduce the attrition cost of new anti-cancer molecules.

Specifically, FATE-SEQ output consists in one molecular signature, describing a chosen omic (here transcriptomic (RNA)), for **both drug-tolerant and drug-sensitive states**, observed in an **isogenic tumoral population**. To do so, FATE-SEQ couples three single-cell techniques (Figure 2.6):

A) A **predictive measure of single-cell response** by **live-cell microscopy** associated to the **cell fate predictor**. Live-cell microscopy uses a fluorescent signal (CFP/YFP not CFP/FRET). The fate prediction is done after 50 min of experiment, based on outliers in [Roux et al., 2015] parameters values, to select early responders. An early prediction of the cell drug-response preserves the integrity of the genome from the drug action, and enables to sequence the genes corresponding only to the initial tolerant/sensitive states of the cell, not a drug-induced dynamic. Indeed, after two hours of experiment, Meyer et al demonstrated a significant difference in the RNA state of the cells treated with TRAIL compared to the state at the beginning of the experiment and the states from control experiments, identifying 2h as the time-point when TRAIL has already an impact on the cell state.

B) A **laser-capture microdissection** to **isolate predicted tolerant cells from predicted sensitive** ones.

C) And a **single-cell RNA sequencing** to profile each cell, that could be replaced by any omic method. To obtain between 6 and 10 biomarkers, genes are then ranked with the algorithm GeNetRank [Sales de Queiroz et al., 2022], that uses a Protein-Protein Interaction Networks,

with random walks, to determine which genes highlighted by the RNA sequencing, impact the most cell drug-response.

The complete protocol is described in [MP1] and the microscope set-up in Figure A.11.1 p.191.

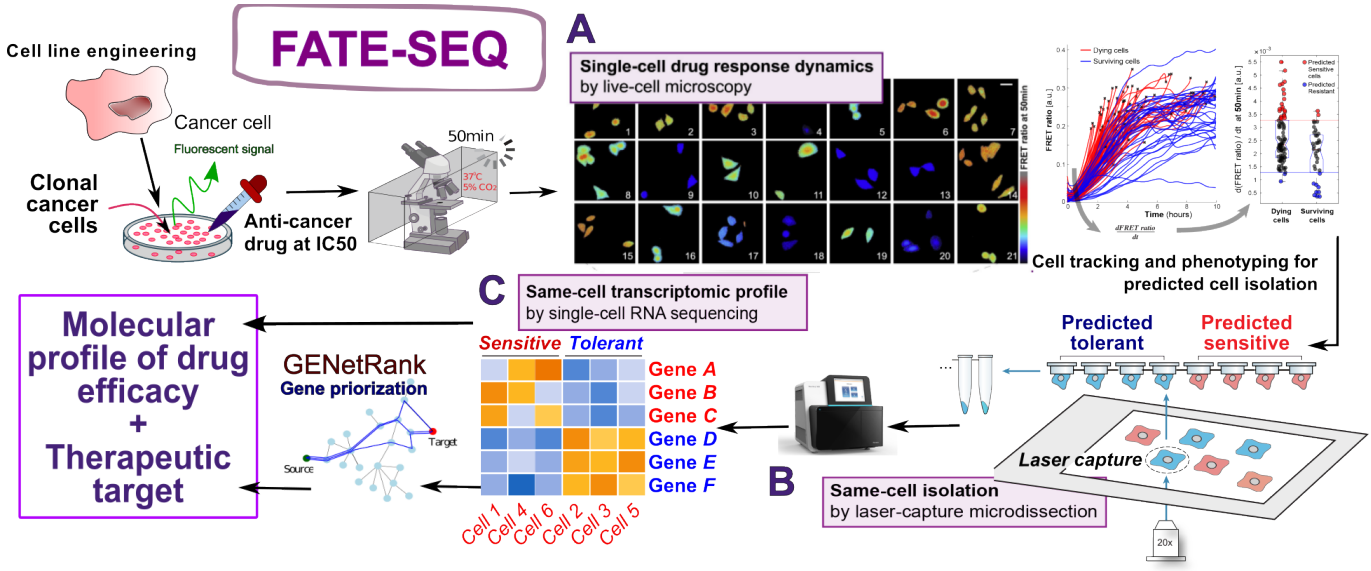

Figure 2.6: **FATE-SEQ:** A - Live-cell microscopy on clonal HeLa cells treated with TRAIL at the IC50 and predictive measure of single-cell drug-response based of the FRET time-trajectory's slope. B - Isolation by laser-microdissection. C - RNA Sequencing. Adapted from [Meyer et al., 2020]

A proof of concept, using TRAIL at its IC50 on clonal HeLa cells, is given in the article [Meyer et al., 2020]. From the 20 cells analyzed, 7 genes over- or under-expressed for the drug-tolerant persisters, were discovered. All those genes were validated experimentally in clonal HeLa cells, either genetically (over-expression of the gene) or pharmacologically (for the genes over-expressed in tolerant cells). All the cells were sensitive in those experiments. These genetically modified cells were compared to parental ones, and observed using the fluorescent ratio CFP/YFP. In Chapter 6, we will be using the un-modified HeLa cells dataset.

Nevertheless, **only a few cells could be sequenced because of the prediction accuracy**. The cell fate predictor is based on the results of [Roux et al., 2015], and uses the value of the FRET slope (the maximum of the time derivative of the FRET trajectory for each cell), before 50 min of experiment. This method is based on outliers identification as explained in Chapter 6 p.115. To be predicted sensitive, a cell must have its FRET slope value (obtained by taking the maximum of the signal derivative), at 50 min of experiment, greater than the red threshold in Figure 2.7 p.56. Conversely, the blue line, in the same figure, represents the tolerant threshold. Cells for which the maximum of their FRET derivative is lower than the blue threshold would be predicted tolerant. A

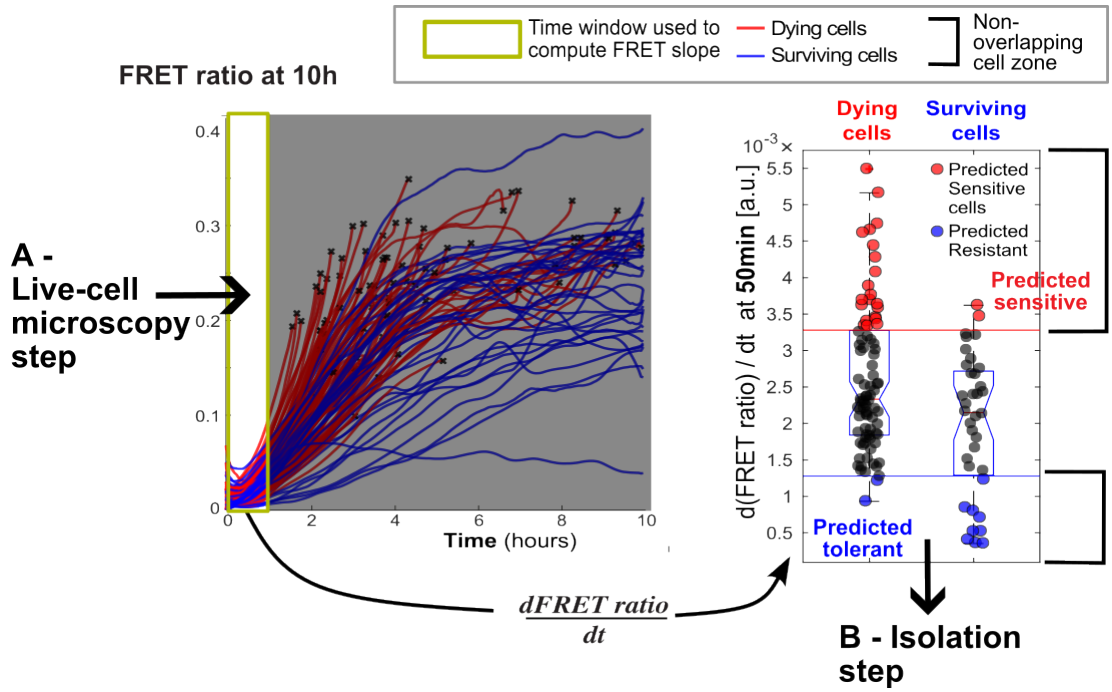

Figure 2.7: **A predictive measure of single-cell drug-response based on the FRET time-trajectory's slope at 50 min of experiment and the principle of non-overlapping cells: the link between the two first steps (A and B) of the FATE-SEQ pipeline**

detailed explanation of the identification protocol used is given in Part III introduction.

Although the FRET slope is a good predictor of cell fate after 6 hours of experimentation [Roux et al., 2015], the fewer data points used, the less accurate the prediction, mainly due to cell trajectory overlapping. Finally, cells are also eliminated during live-cell microscopy before the prediction step, and once again during isolation. At the end, less than 4% of cells were sequenced.

Therefore, one of the main **objectives** in this thesis is to **improve the early prediction of single-cell fate** from the **short fluorescent time-trajectories** obtained by live-cell microscopy, to predict and sequence more cells.

2.4 Forecasting cell decision to control it

2.4.1 Prediction or forecasting?

Despite the absence of a full understanding of the mechanisms behind cell decision, the **need to accurately predict or forecast a certain phenotype** [Li and You, 2013], from experimental measurements (static or time-trajectories data), is a priority in oncology [Benzekry, 2020], and

medicine in general [Partin et al., 2022, Singh and Kaushik, 2022]. Among the numerous reasons advanced to implement effective algorithms for the prediction and forecasting in medicine, we can cite: develop a precision medicine with drug-response or relapse forecasting for each patient [Fröhlich et al., 2018, Ciccolini et al., 2020, Benzekry et al., 2021, Nicolò et al., 2020], more accurate diagnosis [Benzekry, 2020] or a better stratification using new biomarkers [Meyer et al., 2020, Ebert et al., 2022], time and resources gain, especially in drug design [Partin et al., 2022], improvement of the treatments and workflows available, or simply have a better understanding of the dynamics at play [Loos and Hasenauer, 2019, Roux et al., 2015]. In Oncology, the desired phenotypes to forecast or predict, at the cell level, could be cell death/alive, proliferation/senescence, drug-tolerance/sensitivity, healthy/tumoral among many others.

In the lab, one of our objective is to create a pipeline to accurately forecast drug-response for a large number of clonal cancer cells in less than an hour, from only the FRET time-trajectories. Achieving this goal is key to upgrade FATE-SEQ workflow and have a large-scale (and confident) study of the molecular factors of the sensitive/tolerant states, while preserving initial cell states. Moreover, we already showed that **classifying** cell response between tolerant and sensitive phenotype was possible for a few cells [Meyer et al., 2020].

Here, we emphasize the importance to make the ***difference between prediction of a phenotype, and its forecasting****. In the next sections and chapters,* ***prediction defines the identification of a phenotype a posteriori****, whereas* ***forecasting is the ability to determine the future phenotype in advance****, before cells commit to this phenotype. Finally, forecasting time-series also refers to signal/time-series extension in the literature, hence we will also make the difference, and prefer the term* ***time-series extension****.*

2.4.2 Classification task

Classification problems (opposed to regression tasks) are now a regular challenge in oncology [Cai et al., 2022b, Sammut et al., 2022, Torkamannia et al., 2022b], and in medicine in general [Shehab et al., 2022], where the needs to personalize the treatments and to predict patients' responses keeps increasing. Classification simply consists in determining to which class, among several classes (for us tolerant or sensitive), an observation (here clonal cancer cells) belongs. The classification could be a priori (forecasting) or during/a posteriori of the event (prediction).

To tackle these challenges, **machine learning** [Greener et al., 2022, Partin et al., 2022, Singh and Kaushik, 2022] have brought a large panel of models (decision-tree based, deep-learning, support vector machines, K-nearest-neighbours, etc [Hastie et al., 2009]), with the promise of

amazing results [Dempster et al., 2020]. In cancer research in general, and for several decades now, these machine-learning models have demonstrated their powerful ability to improve cancer diagnosis from images [Bera et al., 2022], find new therapeutic targets [Gabor et al., 2021], or identify potential drug designs [Gottipati et al., 2020, Singh and Kaushik, 2022].

However, models performances are strongly related to the amount and the quality of data used to calibrate them. Therefore, nowadays several huge databases [Singh and Kaushik, 2022] and atlas are available to train and compare models. However these databases were built without the experimental constraints we can face in our lab (noise in data acquisition, sparse measurements, human and material resources limited, time, etc). Yet, datasets are crucial in machine-learning, and applying these very promising algorithms, without adapting them, leads often to poor accuracy and efficiency (see Chapter 7).

Here, we will use **machine learning models dedicated to time-trajectories classification,** our case in FATE-SEQ pipeline. These models are inspired from the classic machine learning models for classification that combine a transformer step to extract quantitative features (mean, power spectrum, etc), about the different type of time-trajectories measured experimentally (for instance in image processing, size of cell evolution, fluorescence dynamic, etc), and then use these time-related features in a classic machine learning model. See Chapter 7 fore more detailed references. In the following, **identifying relevant features**, and patterns, in time-trajectories will be **one of our biggest challenge**.

An other way to classify time-trajectories is to use **mathematical modeling** [Ildefonso et al., 2022, Roux et al., 2015, Schneider et al., 2012, Fröhlich et al., 2018]. The parameters of a mathematical modeling, with an observable variable corresponding to the time-trajectories observed during experiments, is fitted on the data (and/or the model is completed with data-driven methods with machine-learning [Fröhlich et al., 2018, Cai et al., 2022a, Stapor et al., 2022, Ciccolini et al., 2020]) and then, some characteristics of the models (parameters values, activation time, certain type of dynamics, etc), are used to classify observations over time into several phenotypes - the classification step can be a machine learning classifier, or simply some manual thresholds [Meyer et al., 2020, Paek et al., 2016]. The mathematical modeling allows to look for more precise features describing our signal, in non-observable variable sometimes, by adding mechanistic prior knowledge about the processes underlying the system studied. In summary, the mathematical model replaces the transformer algorithm in the classification pipeline.

2.4.3 Challenges of single-cell time-trajectories classification for forecasting

These time-trajectories classification methods have one drawback, they need to use long-time trajectories, with a certain amount of points, to be really efficient. However, FATE-SEQ has one particular time-constraint: the classification of the future cell phenotypes must be done before the first hour of experiment to preserve the cell state from the impact of the drug.

In the case of our previous experiments, only 10 data-points over the first hour of experiment are available for each cell in [Roux et al., 2015], and 15 for [Meyer et al., 2020]. In addition, the first half-hour, the photoactivation of the FRET modifies the dynamic of the time-trajectory but does not depend on the apoptosis initiation, which reduces the relevant time window. The classic observation noise in all biological experiments, the noise from cells themselves [Gaudet et al., 2012], but also maybe their indecision, lead also to a lot of overlaps between the trajectories, even after 6 hours of experiments (cf Figure 2.5.A and Figure 2.6.A). See Part III introduction for more details about FATE-SEQ protocol constraints.

In addition to our data specificities, we can also mention the classic challenges in machine learning, highlighted by Singh and Kaushick, in their review on the machine-learning and deep learning models for the prediction of anticancer drug response [Singh and Kaushik, 2022]: too small training set, over-fitting, complexity and non-interpretability of the models (black box, etc), drop-out in the data (not the same amount of data per cell for instance) [Berthoumieux et al., 2011], class imbalanced or curse of dimensionality (too many features per observation).

In summary, our time-trajectories available are sparse, noisy and short, with a lot of overlaps, which make them difficult to classify. On the other hand, we have already proven that this forecasting was possible for a few cells [Meyer et al., 2020], and the study of Schneider et al. [Schneider et al., 2012] also provides evidence of its feasibility for proliferation and differentiation.

CHAPTER 3

Thesis presentation

In Chapter 1, I highlighted the need for a better comprehension of drug-tolerant persisters to be able to identify them, and their biomarkers, to design effective combination therapies from the beginning of the process.
Using the state-of-the-art of TRAIL-inducing apoptosis presented in Chapter 2, this chapter will present the goals and challenges of this thesis, and its outline, to gain a better understanding of TRAIL-tolerant persisters, and increase the throughput and the accuracy of FATE-SEQ.

3.1 A better modeling of apoptosis signaling pathways: trade-off between precision and simplicity

Mathematical modeling has become an essential tool in cancer research [Benzekry et al., 2014, Anderson and Maini, 2018, Cristini et al., 2017, Kazerouni et al., 2020, Rockne and Scott, 2019, Sancho-Araiz et al., 2021]. Whether it is to assess drug efficacy on a special system (with quantitative systems pharmacology (QSP) [Bradshaw et al., 2019, Ferreira et al., 2020, Fleisher et al., 2017, Ramanujan et al., 2016, Sorger et al., 2011, Zhang et al., 2022a] from the cell to the patient scale), to study specific mechanisms or topologies in signaling pathways, or to combine the two in a pharmacodynamic-pharmacokinetics model (PKPD) [Dudal et al., 2022, Lam et al., 2022, Ren et al., 2022, Schneider et al., 2019] to predict future outcomes [Kazerouni et al., 2020, Fröhlich et al., 2018], mathematical modeling is a key element to test hypotheses and control techniques *in silico* [Ferreira et al., 2020, Sontag, 2020], to compare different types of data [Okada et al., 2022, Ramanujan et al., 2016], or to get access to un-observable molecules [Loos and Hasenauer, 2019].

In single-cell experiments, taking advantage of the recent improvements of time-lapse imaging, combining and crossing experimental data with *in silico* results is getting more accessible [Loos and Hasenauer, 2019]. Moreover, deciphering the links between time-trajectories (or data observed) with cell decision and signaling pathways leads naturally to the use of mathematical modeling, as the processes involved are strongly dynamic and time-dependent [Albeck et al., 2008b, Ildefonso et al., 2022, Kosaisawe et al., 2021, Jones et al., 2022, Paek et al., 2016, Xie et al., 2022, Llamosi et al., 2016].

Applying mathematical modeling requires a good knowledge about the mechanisms underlying the biological system under study [Vittadello and Stumpf, 2022] to obtain the **"right model"**. The experimental results, but also the questions raised, will determine the **type of dynamic of the system** (deterministic, stochastic, boolean, data-driven models, discrete like agent-based models, etc) [Kazerouni et al., 2020], the **network topology**, and the **scale** of the model (only transcriptomic pathways, multi-scale modeling, from cell to tumour, etc). Moreover, the amount and the type of data available will be key to define the **trade-off between accuracy, reality and simplicity**, and will eventually determine the size of the model (number of equations) too. The available data are also important for the choice of the method for parameter estimation and validation of the model, which can involve high computational cost, especially in the presence of large datasets [Kazerouni et al., 2020].

Indeed, once a model is designed, parameters estimation is a decisive step to get a reliable model [Fröhlich et al., 2018, Villaverde et al., 2019, Raue et al., 2015]. Therefore, inferring parameters experimentally, taking them from the literature, or estimating them with optimisation

techniques using qualitative [Schmiester et al., 2020, Villaverde et al., 2019] or quantitative data [Waldherr et al., 2009, Stefan et al., 2015, Stapor et al., 2018], is mandatory during the modeling. In addition, assessing their identifiability [Berthoumieux et al., 2013, Llamosi et al., 2016] and the uncertainties surrounding them [Ildefonso et al., 2022, Schmiester et al., 2021] can be complicated, especially when some variables are not observable at once.

In this work, we will investigate the functional role of TRAIL at the transcriptional level, by using small ODE models of extrinsic apoptosis induced by death-ligands binding. These models will be calibrated on each single-cell FRET time trajectory of Roux et al. live-cell microscopy experiments on TRAIL in a clonal population of HeLa cells [Roux et al., 2015]. We infer parameters for each cell, as opposed to a population behaviour, or simply a stochastic variation of parameters from literature, because, in our team, we believe these methods will not reflect all the heterogeneity of dynamics observed at the single-cell level in isogenic population, in response to a drug [Llamosi et al., 2016].

The impact of cellular communication and the population scale [Kallenberger et al., 2014, Waldherr et al., 2009] are beyond the scope of this work. The assertion of parameter uncertainty and model reduction bias, or the comparison of parameter [Götz et al., 2022] and topology network inference techniques [Gonzalez et al., 2013] will not be addressed either to focus on the construction of a minimal model, satisfying our single-cell data constraints and able to reproduce all the heterogeneity observed at the single-cell level.

3.2 Upgrading FATE-SEQ

3.2.1 Increasing FATE-SEQ throughput by overcoming experimental limitations

To increase the throughput of the workflow, **FATE-SEQ** protocol will be slightly **modified** in the future. A new setup allowing live-cell microscopy and single-cell isolation in the same platform will be used to isolate a hundred cells at once. The setup is described in Figure A.11.B, p.191, resulting in the **absence of untreated cells** to be compared with the treated ones, like in [Meyer et al., 2020] and [Roux et al., 2015]. In the following, this change will be taken into account to adapt the current pipeline for cell selection to the new setup.

3.2.2 Automatic cell lineage tracking for better pharmacological indicators

In cell-based assays, only the final amount of drug-tolerant persisters per drug dose is used to create the pharmacological profile of a drug, with its Emax and half maximal inhibitory concentration (IC50) [Stewart and Watson, 1983, Trilla-Fuertes et al., 2020]. The drug-impact on cell division,

death time, and cell cycle in general, even the variability in sensitive cells death time, is not taken into account in the traditional pharmacological indicators (see Figure 3.1). Including cell lineage information, and a better characterization of the heterogeneous commitments to apoptosis, is crucial to better understand drug-response, make drug-design process more efficient (faster and cheaper), or characterize drug-tolerant persisters, from their origins to their definition [Eyler et al., 2020]. Several articles already addressed the challenge by using probabilities [Comandante-Lou et al., 2020] and time-lapse live cell microscopy, or partial differential equations combined with RNAseq data [Fischer et al., 2019].

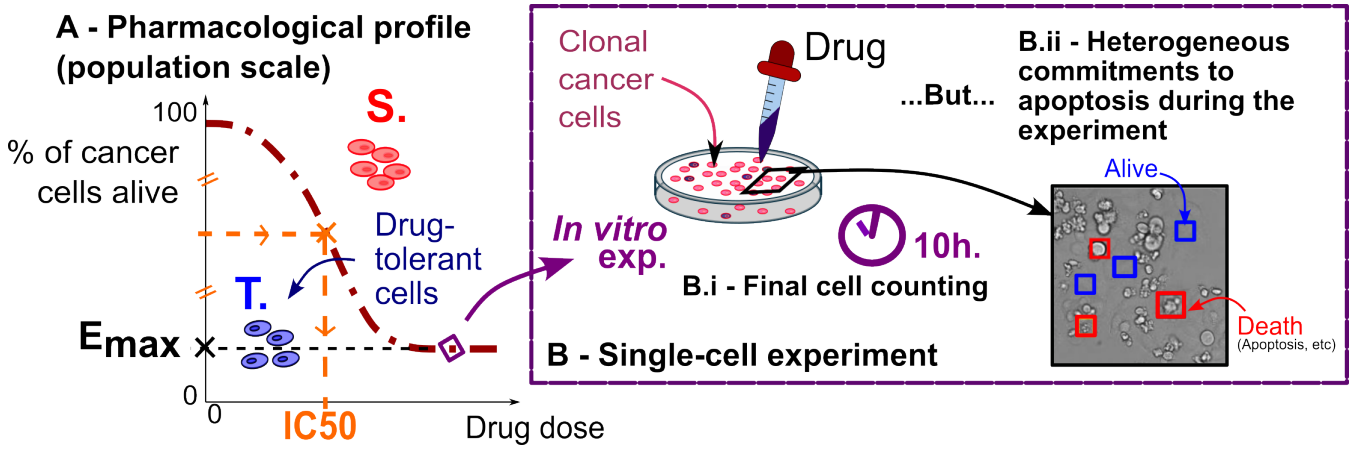

Figure 3.1: **Drug-tolerant cells: the basis of drug-efficacy evaluation in cell-based assays but a partial evaluation of heterogeneous commitments to apoptosis by drug efficacy metrics:** A - The pharmacological profile of a drug is obtained by repeating the same live-cell experiment in an isogenic population varying the drug dose. B - One point on the pharmacological profile corresponds to a single-cell experiment with the drug dose specified in x axis. B.i - The y axis corresponds to the amount of tolerant-cells that are alive at the end of the experiment. B.ii - The heterogeneous commitments to apoptosis, and more globally any cell event happening between the drug input and the final cell counting (cell division, different types of death, quiescence, etc) are not taken into account in the final counting.

To explore the methods already available and adapt them to our own constraints and type of data obtained from FATE-SEQ (short time-trajectories, fluorescent signal, etc), in parallel to this thesis project, an other PhD subject focuses on **automatizing the live-cell microscopy** part with image-processing techniques. The objective is to develop an automatic pipeline to follow cells and record their fluorescence during the experiment. This workflow will also integrate the detection of cell lineage event, like death or division from the entire time-trajectories of important features describing quantitatively the behaviour of the cells. Finally, the fluorescent time-trajectory for each cell will also be an output of the program (cf Figure G.22 p.233).

A part of the project is already fulfilled by using a U-Net model (deep-learning) to track cells overtime and extract fluorescent signals. Then, correlation filters are used to detect cell lineage

events, like death, division, etc. The final aim is, once again, to create better metrics to evaluate drug-efficacy in cell-based assays. It will also save time and allow a better reproducibility, which is a difficult task to perform manually for each cell during the live-cell microscopy step.

3.2.3 Augmenting the number of cells predicted to obtain large-scale study

In addition to automatizing the live-cell microscopy step, the forecasting step needs also an upgrade to forecast drug-response for more cells, while conserving the same degree of accuracy in the drug-response forecasting (more than 90% for the cells isolated). The authors from [Anchang et al., 2018, Niepel et al., 2013, Loo et al., 2017, Schneider et al., 2012] showed strong evidence that studying cell signaling dynamic, shortly after drug-input, could allow the forecasting of a longer-term response. Therefore , a entire part of this thesis is dedicated to this goal (Part III). As stated in Chapter 2, this task will be one of our greatest challenges during this thesis.

3.3 Scientific questions

This thesis extends the work of my team to have a better comprehension of how drug-tolerant cells emerge and identify the regulatory dynamics of cell death decision triggered by death ligands. Hence, the main objectives of this work are to **have a better understanding of single-cell decision during cancer drug treatments**, and to **forecast cell response early after treatment for a maximum number of cells**, in order to isolate cells before they commit to their fate and to improve the current FATE-SEQ pipeline. In other words, this thesis aim at bringing new elements to answer the following questions:

1. Which **mechanisms** in extrinsic apoptosis **generate all the response heterogeneity** observed in single-cell experiments?
2. **How** and **when** do cells make their **commitment to cell death** after TRAIL treatment?
3. What are the **early signs** of this cell fate decision? Can we use those signs to forecast cell decision?

More generally, we are also addressing the following problems:

1. Which information could be extracted from single-cell trajectories when data are sparse and noisy and most of the cell state is non-observable?
2. Can we **predict single-cell drug-response for all the cells**? If yes, **when** could we make the prediction and with **which accuracy**?

3. How can we **improve the FATE-SEQ** pipeline and **adapt** it to other **cell lines, drugs and diseases**?

To answer these questions, Part II compares several ordinary differential equation (EDO) models of extrinsic apoptosis to identifies dynamic determinants of cell death with a minimal model. Part III combines the conclusions of Part II and the current FATE-SEQ approach to improve the cell selection step before isolation in the FATE-SEQ pipeline. Finally, Part IV summarizes my contributions in this thesis and presents the perspectives opened with this work.

To estimate the parameters of our models and validate them, we will use different datasets from previous experiments carried by my team and already used in different lab publications. These datasets are described by chapter in Appendix A, p.191.

In a nutshell, this thesis aims at better **identifying future drug-tolerant cells** for the FATE-SEQ workflow. To this purpose, we will be using **mathematical modeling** to understand the **links between cell decision, cell signaling and cell dynamic** leading to the **emergence of drug-persisters** during a treatment with TRAIL on isogenic cancer cells.

Thesis-related publications

My publications

[MP1] Benjamin Bian, Agnès Paquet, Marie-Jeanne Arguel, Mickael Meyer, Ludovic Peyre, Asma Chalabi, Marielle Péré, Kevin Lebrigand, Rainer Waldmann, Pascal Barbry, et al. Coupling live-cell imaging and in situ isolation of the same single cell to profile the transient states of predicted drug-tolerant cells. *STAR Protocols*, 3(3):101600, 2022.

[MP2] Marielle Péré, Madalena Chaves, and Jérémie Roux. Core models of receptor reactions to evaluate basic pathway designs enabling heterogeneous commitments to apoptosis. In *International Conference on Computational Methods in Systems Biology*, pages 298–320. Springer, 2020.

[MP3] Marielle Péré, Madalena Chaves, and Jérémie Roux. Trail-induced apoptosis signaling modeling identifies dynamic signs of efficient cell death initiation, enabling an early prediction of the cell response. In *19th International Conference on Computational Methods in Systems Biology (CMSB 2021)*, 2021.

[MP4] Marielle Péré, Diego Oyarzun, Jérémie Roux, and Madalena Chaves. Modeling isogenic cancer cell response upon varying trail stimulations to decipher the kinetic determinants of cell fate decision. *IFAC-PapersOnLine*, 55(23):46–51, 2022. 9th IFAC Conference on Foundations of Systems Biology in Engineering FOSBE 2022.

Lab publications

[LabChaves et al., 2021] Chaves, M., Gomes-Pereira, L. C., and Roux, J. (2021). Two-level modeling approach to identify the regulatory dynamics capturing drug response heterogeneity in single-cells. *Scientific reports*, 11(1):1–15.

[LabMeyer et al., 2020] Meyer, M., Paquet, A., Arguel, M.-J., Peyre, L., Gomes-Pereira, L. C., Lebrigand, K., Mograbi, B., Brest, P., Waldmann, R., Barbry, P., et al. (2020). Profiling the non-genetic origins of cancer drug resistance with a single-cell functional genomics approach using predictive cell dynamics. *Cell systems*, 11(4):367–374.

[LabPereira, 2019] Pereira, L. C. G. (2019). *Modeling cell response heterogeneity to pro-apoptotic ligands*. PhD thesis, COMUE Université Côte d'Azur (2015-2019).

[LabPeyre et al., 2021] Peyre, L., Meyer, M., Hofman, P., and Roux, J. (2021). Trail receptor-induced features of epithelial-to-mesenchymal transition increase tumour phenotypic heterogeneity: Potential cell survival mechanisms. *British Journal of Cancer*, 124(1):91–101.

[LabRoux et al., 2015] Roux, J., Hafner, M., Bandara, S., Sims, J. J., Hudson, H., Chai, D., and Sorger, P. K. (2015). Fractional killing arises from cell-to-cell variability in overcoming a caspase activity threshold. *Molecular systems biology*, 11(5):803.

[LabSales de Queiroz et al., 2022] Sales de Queiroz, A., Sales Santa Cruz, G., Jean-Marie, A., Mazauric, D., Roux, J., and Cazals, F. (2022). Gene prioritization based on random walks with restarts and absorbing states, to define gene sets regulating drug pharmacodynamics from single-cell analyses. *Plos one*, 17(11):e0268956.

PART II

Modeling Apoptosis to predict cell drug response

Systems biology, and more specifically mathematical modeling has become essential in medicine and pharmacology nowadays. To show a few examples of successful applications, we can cite: understanding a functional model of a molecule [Roux et al., 2015], studying the dynamic between a host and a pathogen, identify the causes of the emergence of resistance (in cancer, but also against antibiotic for instance), or the control of bio-processes to produce a molecule of interest [Martinez et al., 2022]. In pharmacology, mathematical models of drug-response are used to assess the future patient response and control it with PKPD models [Schneider et al., 2019], deciphering the mode of action of anti-cancer molecules from the transcriptional level [Kovachka et al., 2021] to the *in vivo* scale [Benguigui et al., 2018] or study their combination *in silico* [Kovachka et al., 2021, Schneider et al., 2019]. In all the cases above, mathematical modeling has shown its effectiveness to make accurate predictions and leads to a better understanding of the observed response heterogeneity [Loos and Hasenauer, 2019].

Here, we will study the functional mode of action of TRAIL in a clonal population of tumoral cells (HeLa), to understand how drug-tolerant persisters can emerge from an isogenic population, by modeling the single-cell transcriptional level. The goal is to identify dynamic signs of efficient cell death initiation, while conserving a reasonable level of simplicity in our model, to better understand the important cell mechanisms at stake.

Part II relies on **new mathematical models** to determine the **core reactions of extrinsic apoptosis triggered by TRAIL**, that leads to all the **cell-to-cell heterogeneity** observed in Roux *et al.* experiments. The goal is multiple: (i) highlight the **key-mechanisms** (timeline, chemical reactions, kinetics, etc) involved in cell decision, (ii) study how they are affected by **TRAIL variation**, and (iii) assess which **information** in the Roux data is **essential to predict and forecast cell fate** or the manifestation of a lethal change in these protagonists reaction dynamic. With these methods, we aim at refining our Systems Pharmacology approach in the lab. More specifically, we want to fine-tune the links between cell signaling, cell dynamics and cell decision for TRAIL-induced apoptosis. Indeed, we believe that the processes underlying cell fate decision are strongly deterministic [Baslan et al., 2022, Roux et al., 2015], and with a good knowledge about the network topology, we can predict cell death initiation for a majority of cells, and even forecasting it (see Section 2.4.1 p.56 for the difference between prediction and forecasting). Here, we will try to find the trade-off between incorporating all the key-mechanisms that generate cell heterogeneity (after identifying them) into a model while keeping its complexity at a reduced level [Bijman et al., 2021] as we will then use sparse FRET time-trajectories to calibrate and validate our models, with less than 10 data points for some sensitive cells. To increase parameter identifiability, our models will be of reduced dimensions and involved between 8 and 11 parameters.

Experimental data

FRET time-trajectories obtained by [Roux et al., 2015], will be used to estimate the parameters of several **ODE models of TRAIL inducing extrinsic apoptosis**. The time-trajectories were pre-processed in the same way as [Roux et al., 2015] (see Table A.3 p.193), with the subtraction of the mean non-treated cell, a re-scale step by the minimum value on the 10^{th} first frames, so every cell starts at 0 and can be compared to others (similarly to [Albeck et al., 2008a, Roux et al., 2015, Chaves et al., 2021]), and a smoothing step at the end.

In Chapter 4, we chose the same dataset, and the same re-scale step as in [Pereira, 2019, Chaves et al., 2021]. This dataset contains the FRET time-trajectories of clonal HeLa cells treated with 50ng/ml of TRAIL only (as done in [Albeck et al., 2008b]). The re-scale consists in multiplying the FRET amount by the initial quantity of uncleaved fluorescent protein FP(0) and divide it by 1+FRET, as presented in Section 2.3 of Pereira thesis [Pereira, 2019], and inspired by [Birtwistle et al., 2011]. This technique allows to obtain the number of molecules of IC-RP (initiator caspase reporter-probe) and keeps the model units consistent. In the models presented in Chapter 5, the re-scale by FP(0) is no longer used as the FRET is now modeled by a specific equation (with arbitrary units). In reality, FRET is expressed in a ratio of pixel unity, but this ratio depends on numerous external factors such as the degree of wear of the lamp used, the exposition time or simply the amount of day light cells are exposed to. Therefore, to simplify and as FRET is just an observable variable, we consider arbitrary units. The other proteins included in our model will be expressed in number of molecules. When the initial amount of protein is not explicitly given, the same initial conditions as in [Pereira, 2019, Albeck et al., 2008a] will be used.

Goals and outline of Part II

To decipher **TRAIL-induced cell death decision**, while keeping a good balance between biological and computational constraints, this part will therefore address the following questions:

- What are the key mechanisms in the apoptosis pathway that lead to the observed cell response heterogeneity? (Chapter 4, Chapter 5)
- What is the minimal model that can still reproduce the main extrinsic apoptosis dynamics? (Chapter 4, Chapter 5)
- What information can be extracted from the FRET signal to predict cell drug-response? Does it encode for a biological threshold, or has it a predictive power to forecast cell decisions? (Chapter 4, Chapter 5, Chapter 7)

- Is there a time interval associated to cell decision? How do cells implement their decision (identification of well defined mechanisms or biological thresholds, characterization of the step-by-step time dynamics)? (Chapter 5)

- How does TRAIL variation affect time dynamics and the key mechanisms of the apoptosis pathway?(Chapter 5)

In details, Chapter 4 compares basic pathways of extrinsic apoptosis triggered by TRAIL and shows that initiator caspase clustering, caspase 8 degradation and the feedback-loop from the effective caspase on caspase 8 are key-mechanisms of cell decision.

Chapter 5 integrates the conclusion of chapter 4 in a bigger model of extrinsic apoptosis initiation core reaction (EAICR). By estimating the parameters of this new model for all cells of [Roux et al., 2015], treated with different amounts of TRAIL, we reconstruct the apoptosis timeline and locate a first cell decision just after TRAIL binding. We also show that TRAIL variation affects mainly the early beginning of apoptosis by affecting differently resistant and sensitive cells to increase the gap between resistant and sensitive states. Finally, we could also reduce the EAICR model to get an approximated explicit solution. The parameters of this solution can be used to create a new predictor of the cell fate.

CHAPTER 4

Core models of receptor reactions evaluate basic pathway designs enabling heterogeneous commitments to apoptosis

Here, considering caspase-8 (C8) level as the main determinant of cell fate, like shown in Chapter 2, I aim at identifying basic extrinsic pathway designs that capture both cell response heterogeneity to TRAIL, and C8 signaling properties. For this family of basic circuits, I will characterize and compare the regulatory events in each circuit, to understand the effect of different proteins on C8 signaling dynamics and on cell-to-cell variability.
For that purpose, I especially focus on three points: (i) FADD role and its capacity for regulating C8 , (ii) the relevance of caspase clusters composed of C8 and C10, and (iii) the regulatory effect of the effector caspases on C8 which depends on a positive feedback loop (see Section 2.1 p. 44 for the description of the extrinsic apoptosis pathway).
To investigate the effect of these interactions and their relative timing on apoptosis, I propose four alternative minimal ODE models. Based on the results of [Roux et al., 2015], these models are calibrated from single-cell data and the distributions of the different parameters are analysed to find links between the models, C8 dynamics, and cell fates. Finally, I study the feedback loop action, quantify the influence of FADD and C10, and validate our models, explaining the special distribution of C8 degradation.

This chapter was presented at the 18th International Conference on Computational Methods in Systems Biology (CMSB 2020) [MP2].

4.1 Modeling the main processes of extrinsic apoptosis initiation

In this chapter, the first goal is to establish the **mechanisms responsible for the main pathway dynamics**, and their **impact on the C8 activation threshold**, **distinguishing** between **TRAIL tolerant and sensitive cells**. The second goal is to **understand how** these mechanistic **models can reproduce cell response heterogeneity**.

Therefore, this study focuses on three different regulation points : the FADD protein and its capacity for regulating of C8, the importance of C8/C10 cluster in C8 activation [Horn et al., 2017] and the possible presence of a downstream regulatory effect of C8 [Albeck et al., 2008b, Rehm et al., 2006], symbolized here by a positive feedback loop from the effector caspase cascade on C8. In each case, our analyses aim to understand **the effect of a given mechanism on the C8 dynamic's main features** and in which measure this **process is a source of heterogeneity** or, at least, source of extrinsic noise.

4.1.1 Models' assumptions

To capture the extrinsic apoptosis core reactions, our **models are thus constructed with a minimal number of components and steps** : the **TRAIL binding on the death-receptor** DR4/5, the **recruitment of the FADD protein and the initiator** to form the DISC, the pC8 dimerization, and finally the activation of C8. (c-FLIP is considered to be in very small quantities and so has a lower impact on C8 recruitment.)

TRAIL is denoted by **T**, the **DR4/5 receptors** become a single component named **R** (for Receptor), the **pC8 and C8 are grouped** to form a unique protein **C8**. Instead of the recruitment of a single pC8, our models assume two molecules simultaneously bind to DISC, since only dimerization or trimerization of pC8 can trigger apoptosis. $\mathbf{F}_D$ denotes the **FADD** protein and Z_0 **the complex TRAIL-receptors**. The **downstream caspase cascade, the MOMP and cell death** are grouped into the component **D** (for death), with a intermediary complex Z_1.

4.1.2 Extrinsic apoptosis initiation core models (EAICM)

Four extrinsic apoptosis initiation core models (EAICM) are proposed, corresponding to the four possible combinations of **presence or not of a feedback loop on C8** conjugated with either the **adaptor protein or C8/C10 binding**.

The **feedback loop** is represented by the **red links** on Figure 4.1 p. 80. Two models focus on **C10/C8 coupling**, where the C8 dimerization happens before the C10 binding (models **-cf** and **-c**) to understand how C10 interacts with C8, and finally two others, where only the **FADD reaction**

and the C8 dimerization are taken into account (models **-af** and **-a**) to examine the importance of the adaptor protein FADD, especially its regulatory capacity of pC8 recruitment. In models without feedback loop, $\widetilde{C8}$ is a constant parameter representing available pC8.

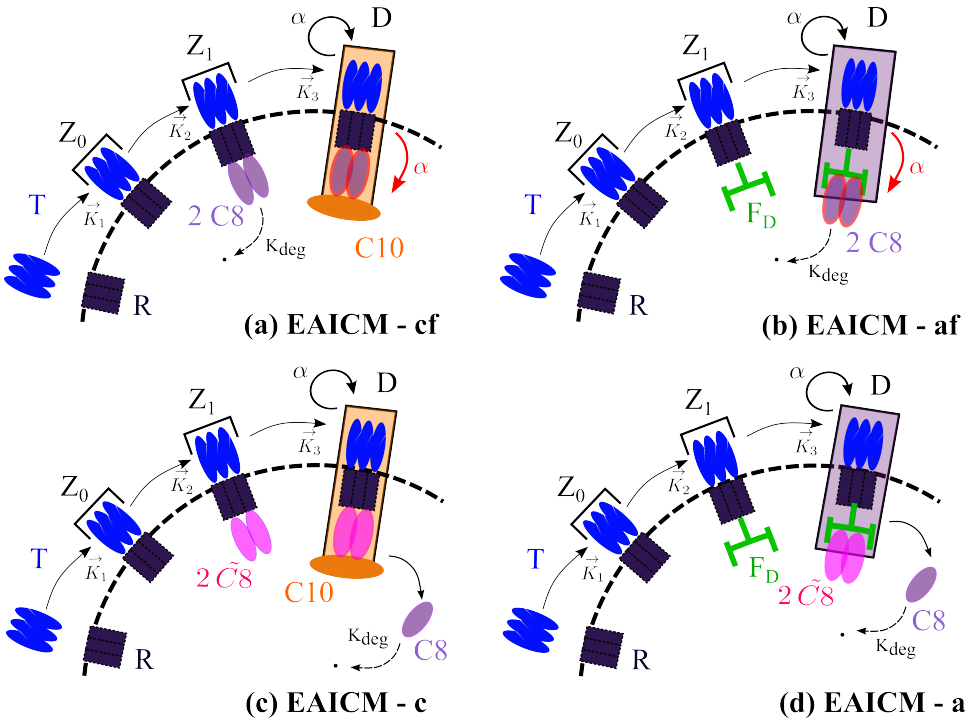

Figure 4.1: **Extrinsic apoptosis initiation core models (EAICM)**

To model the different reactions, we apply **mass-action kinetics** and obtain four models of the form $dX/dt = f_{P_r}(X)$, with $f : \mathbb{R}^7 \to \mathbb{R}^7$ depending on the time-independent reaction rate vector $P_r = (\vec{K_1}, \overleftarrow{K_1}, ..., \alpha)$, and the initial conditions:

$$\begin{cases} X_0^c &= (T_0,\ R_0,\ C8_0, C10_0,\ Z_{0,0},\ Z_{1,0},\ D_0) \\ X_0^a &= (T_0,\ R_0,\ C8_0, F_{D,0},\ Z_{0,0},\ Z_{1,0},\ D_0) \end{cases}$$

EAICM-cf:

$$\begin{cases} \frac{dT}{dt} &= -\overrightarrow{K_1}\,TR + \overleftarrow{K_1}\,Z_0, \\ \frac{dR}{dt} &= -\overrightarrow{K_1}\,TR + \overleftarrow{K_1}\,Z_0, \\ \frac{dZ_0}{dt} &= \overrightarrow{K_1}\,TR - \overleftarrow{K_1}\,Z_0 - \overrightarrow{K_2}\,Z_0C8^2 + \overleftarrow{K_2}\,Z_1, \\ \frac{dC8}{dt} &= -2\overrightarrow{K_2}\,Z_0C8^2 + 2\overleftarrow{K_2}\,Z_1 + \alpha\,D - K_{deg}\,C8, \\ \frac{dZ_1}{dt} &= \overrightarrow{K_2}\,Z_0C8^2 - \overleftarrow{K_2}\,Z_1 - \overrightarrow{K_3}\,Z_1C10 + \overleftarrow{K_3}\,D, \\ \frac{dC10}{dt} &= -\overrightarrow{K_3}\,C10Z_1 + \overleftarrow{K_3}\,D, \\ \frac{dD}{dt} &= \overrightarrow{K_3}\,Z_1C10 - \overleftarrow{K_3}\,D. \end{cases} \tag{4.1}$$

EAICM-af:

$$\begin{cases} \frac{dT}{dt} &= -\overrightarrow{K_1}\,TR + \overleftarrow{K_1}\,Z_0, \\ \frac{dR}{dt} &= -\overrightarrow{K_1}\,TR + \overleftarrow{K_1}\,Z_0, \\ \frac{dZ_0}{dt} &= \overrightarrow{K_1}\,TR - \overleftarrow{K_1}\,Z_0 - \overrightarrow{K_2}\,Z_0F_D + \overleftarrow{K_2}\,Z_1, \\ \frac{dF_D}{dt} &= -\overrightarrow{K_2}\,F_DZ_0 + \overleftarrow{K_2}\,Z_1, \\ \frac{dZ_1}{dt} &= \overrightarrow{K_2}\,Z_0F_D - \overleftarrow{K_2}\,Z_1 - \overrightarrow{K_3}\,Z_1C8^2 + \overleftarrow{K_3}\,D, \\ \frac{dC8}{dt} &= -2\overrightarrow{K_3}\,Z_1C8^2 + 2\overleftarrow{K_3}\,D + \alpha\,D - K_{deg}\,C8, \\ \frac{dD}{dt} &= \overrightarrow{K_3}\,Z_1C8^2 - \overleftarrow{K_3}\,D. \end{cases} \tag{4.2}$$

EAICM-c:

$$\begin{cases} \frac{dT}{dt} &= -\overrightarrow{K_1}\,TR + \overleftarrow{K_1}\,Z_0, \\ \frac{dR}{dt} &= -\overrightarrow{K_1}\,TR + \overleftarrow{K_1}\,Z_0, \\ \frac{dZ_0}{dt} &= \overrightarrow{K_1}\,TR - \overleftarrow{K_1}\,Z_0 - \overrightarrow{K_2}\,Z_0\widetilde{C8}^2 + \overleftarrow{K_2}\,Z_1, \\ \frac{dC8}{dt} &= \alpha\,D - K_{deg}\,C8, \\ \frac{dZ_1}{dt} &= \overrightarrow{K_2}\,Z_0\widetilde{C8}^2 - \overleftarrow{K_2}\,Z_1 - \overrightarrow{K_3}\,Z_1C10 + \overleftarrow{K_3}\,D, \\ \frac{dC10}{dt} &= -\overrightarrow{K_3}\,C10Z_1 + \overleftarrow{K_3}\,D, \\ \frac{dD}{dt} &= \overrightarrow{K_3}\,Z_1C10 - \overleftarrow{K_3}\,D. \end{cases} \tag{4.3}$$

EAICM-a:

$$\begin{cases} \frac{dT}{dt} &= -\overrightarrow{K_1}\,TR + \overleftarrow{K_1}\,Z_0, \\ \frac{dR}{dt} &= -\overrightarrow{K_1}\,TR + \overleftarrow{K_1}\,Z_0, \\ \frac{dZ_0}{dt} &= \overrightarrow{K_1}\,TR - \overleftarrow{K_1}\,Z_0 - \overrightarrow{K_2}\,Z_0C10 + \overleftarrow{K_2}\,Z_1, \\ \frac{dF_D}{dt} &= -\overrightarrow{K_2}\,F_DZ_0 + \overleftarrow{K_2}\,Z_1, \\ \frac{dZ_1}{dt} &= \overrightarrow{K_2}\,F_DZ_0 - \overleftarrow{K_2}\,Z_1 - \overrightarrow{K_3}\,Z_1\widetilde{C8}^2 + \overleftarrow{K_3}\,D, \\ \frac{dC8}{dt} &= \alpha\,D - K_{deg}\,C8, \\ \frac{dD}{dt} &= \overrightarrow{K_3}\,Z_1\widetilde{C8}^2 - \overleftarrow{K_3}\,D. \end{cases} \tag{4.4}$$

Comparing these four alternatives to experimental measurements is then necessary to investigate which of the mechanisms more faithfully reproduces the data and is capable of better generating the single-cell dynamic properties.

4.2 Single cell model calibration

Our models are calibrated using the dataset of from Roux and al. [Roux et al., 2015] including **FRET signals for 414 single cells** (**114 tolerant and 300 sensitive**) treated **only with 50ng/mL of TRAIL** and **observed for 10 hours**.

The four **EAIC models are fitted to each single cell time-trajectory separately**, as opposed to a parameter estimation using only one averaged time-series [Llamosi et al., 2016, Pereira, 2019]. This approach is meant to study each single cell's heterogeneous features and it allows to obtain the parameter distribution without any assumption.

The **same model topology** is used for both tolerant and sensitive cells, since the clonal cells are genetically homogeneous. (The main differences between the two populations are attributed to the protein expression levels.)

Since our data consists on the evolution of FRET ratio in time, and because the models do not represent directly FRET activation, we assume that the **FRET creation corresponds to a re-scale of C8**, *ie* that the FRET dynamic is obtained from the C8 dynamic by changing the amplitude of the C8 curve and the activation time with an additional delay. Thus, our calibration method directly compares the modeled C8 concentration to the real cleaved C8, where the FRET activation slope becomes a major indicator of the C8 activation speed.

4.2.1 From qualitative criteria to quantitative reference values

To evaluate and compare the four models, it is essential to define a **set of criteria to determine how closely each model approaches the real data**. This involves **translating the main qualitative properties of the C8 curves into quantitative values** that can be calculated from the model's solutions. Three fundamental properties are relevant in C8 dynamic and can be evaluated as reference values, as follows (see Figure 4.2): (i) the **time delay before activation of C8** is triggered; (ii) the **mean slope during the C8 activation phase**; and (iii) the **stable value of C8 concentration**, over the last 300 minutes (especially for tolerant cells). These properties can be turned into reference values by defining:

- T_{100000} evaluates the initial delay by setting C8$(T_{100000}) = 100000$ molecules;
- S is the C8 activation slope, as the maximum of the derivative of C8(t) between 25 and 275 minutes, computed using the Matlab function *sgolayfilt*;
- V_{final} gives the final stabilization value, *ie* C8(600), or the value of C8 at death time, for sensitive cells.

It must be noticed that the initial decreasing phase during the first half an hour is not taken into account. It is due to the photoactivation of the FRET and doesn't depend on the apoptosis initiation and as a result, of our models.

4.2.2 Distinguishing the effects of initial conditions and rate parameters on the dynamics

Here, we use a **nonlinear least-squares method to determine the parameters** $P = (P_r, P_i^j,\ j \in \{c, a\})$ of our models $dX/dt = f_{P_r}(X),\ P_i^j \in X_0$, where $P_r = (\overleftarrow{K_1}, \overrightarrow{K_1}, ..., K_{deg}, \alpha)$ represents the reaction rates and $P_i^c = (R_0, C8_0, C10_0)$ and $P_i^a = (R_0, C8_0, F_{D,0})$ represent the initial conditions to be evaluated during the model fit, of models EAICM-cf or EAICM-af, respectively.

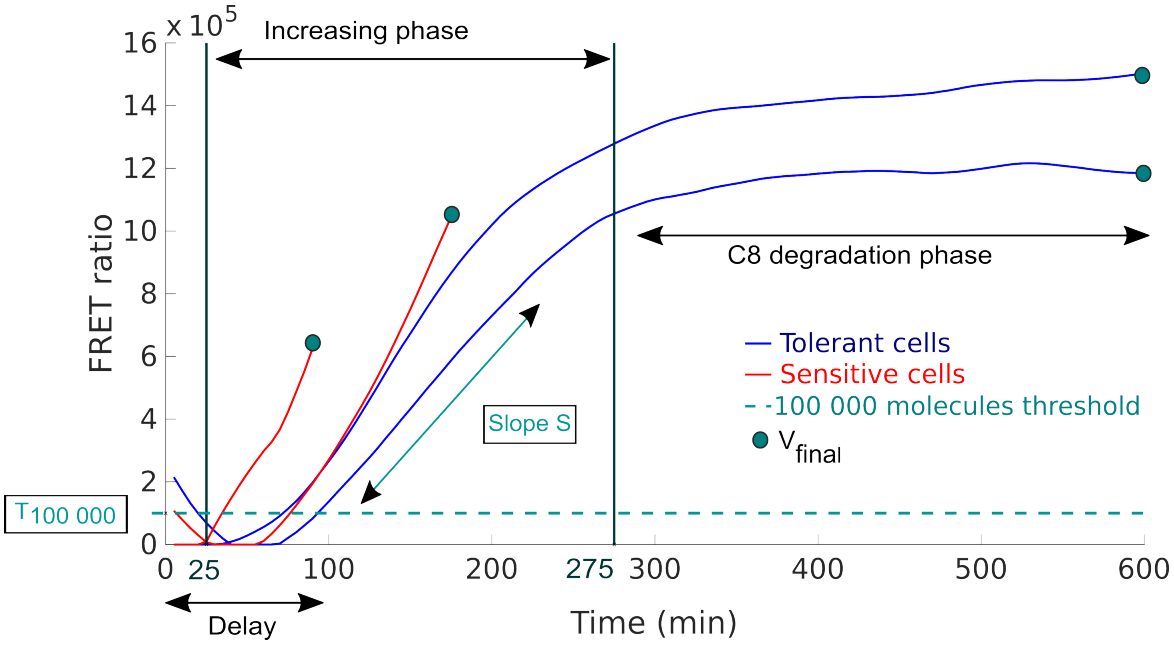

Figure 4.2: **Reference values and C8 features scheme - FRET signal essential features to describe C8 heterogeneous dynamic:**FRET time-trajectory obtained after 10h of experiments for two sensitive and two tolerant cells treated with 50 ng/mL of TRAIL and the three references values computed in this chapter: the initial delay computed thank to the $T_{100\,000}$ threshold, the Slope calculated between 25 and 275 time points,, during the increasing phase, and the C8 value during the degradation phase.

The other initial conditions are fixed with values from literature [Albeck et al., 2008b].

An **euclidean norm** is used to compute the cost, given by the differences between the measurements, denoted by C8_{t_i}, $t_i \in \mathbb{T} = \{5, 10, ..., 600\}$, and the computed solution C8^c of the model, taken every 5 minutes.

To take into account the slope and the final C8 concentration relevance, the **cost is weighted from the 25^{th} minute time-point** (approximately the beginning time of the increasing phase) until the end with heavier weight ω between the 25^{th} and the 275^{th} (for the slope calculated during the increasing phase). For instance, $\omega = 1000$ between min 25 and min 275. After 280 min, $\omega = 500$. Finally, denoting T_d, the cell death time, the cost $\mathcal{C}$ is given by:

$$\mathcal{C}^2 = \sum_{t_i \in \{5,\dots,\min(20,T_d)\}} \left(C8_{t_i} - C8^c_{t_i}\right)^2 + \sum_{t_i \in \{25,\dots,\min(275,T_d)\}} \omega \times \left(C8_{t_i} - C8^c_{t_i}\right)^2 + \sum_{t_i \in \{280,\dots,\min(600,T_d)\}} \frac{\omega}{2} \times \left(C8_{t_i} - C8^c_{t_i}\right)^2. \tag{4.5}$$

Alternatively, for the tolerant population, adding the squared slope difference between the data and the computed solution, improves the fit. For the sensitive population, we remove the last parts of the cost when the death time T_d is smaller than the first boundary of the time interval for each one of the three terms of the sum. To minimize $\mathcal{C}$, we used *Matlab* and its function *fminsearchbnb*, to

solve an optimization problem with a physiologically significant initial guess based on the literature.

To **access both the individual and joint effects** of reaction rate parameters and initial conditions on the dynamics, the **algorithm solves three different optimization problems**,

F1. Minimize the cost C with respect to both P_i and P_r;

F2. Fix initial conditions P_i and minimize cost C with respect to P_r;

F3. Fix reaction constants P_r and minimize cost C with respect to P_i.

Fitting only initial conditions, assumes that the model's topology is well-known, and that the response heterogeneity comes from environmental conditions and extrinsic noise only. Conversely, fitting reaction rates only, admits model's variability, and possibly unknown or not considered reactions or proteins the could impact the behaviour of C8.

The heterogeneity factors are expected to be a mix of the two explanations and so the fit obtained on both initial conditions and reaction rates is the best but, in this case, the results are less straightforward to interpret.

4.3 Analysing mechanisms for generating heterogeneity

To simulate the models, we set the initial conditions for TRAIL at $T_0 = 1500$ (from [Albeck et al., 2008b]), and the intermediary complexes $Z_{0,0}$, $Z_{1,0}$ and D_0 equal to 0.

Simulations are performed with *ode23* for 600 minutes with a weight $\omega = 1000$ for $\mathcal{C}$. For the parameter set and the other initial conditions, when they aren't estimated by the algorithm, values obtained during a first manual fit on a median real cell are used.

4.3.1 Comparison of the four core apoptosis models

The first point is to elucidate **which of the reactions**, binding of the receptor complex to F_D or to C10, **best reproduces the behaviour heterogeneity of C8**.

To determine which of the models of type 1 or 2 best captures the extrinsic apoptosis dynamics, the norm $\mathcal{C}$ and the reference values are computed for 114 tolerant cells and 300 sensitive ones. Then, for each type of fit F1 to F3, we confront the four models by computing, for each cell and each model, the absolute value of the difference between the data slope and the $C8^c$ slope (that is to say $|S_{EAICM,i} - S_{data,i}|$, $i \in \{1, ..., 414\}$).

Finally, comparing the four results for each cell, the number of cells for which each model gives the lowest result is counted. The model with the highest score (*i.d.* the largest number of cell for which the given model gives the lowest result comparing the four models) is considered to have the best performance, as summarized in Table 4.1.

In Appendix B.1 p.199, tables for the cost $\mathcal{C}$, the C8 final value and the delay are given.

Fit \ Model	Fate	EAICM-cf	EAICM-c	EAICM-af	EAICM-a	Best model
F1	Sens. cells	120	78	57	45	EAICM-cf
	Tol. cells	59	11	32	12	EAICM-cf
F2	Sens. cells	108	79	71	42	EAICM-cf
	Tol. cells	75	12	26	1	EAICM-cf
F3	Sens. cells	269	8	20	3	EAICM-cf
	Tol. cells	51	23	31	9	EAICM-cf

Table 4.1: Number of cell best approached per EAICM model (columns), type of fits (F1,F2,F3) and drug-response (rows) according to the slope

Table 4.1 shows clearly that **EAICM-cf outperforms the other models**, suggesting that the **caspase cluster** and the **feedback loop** are the main mechanisms **necessary to reproduce the variability in C8 slope** and the general cell response heterogeneity observed *in vitro*. The same results are obtained for the delay criteria.

Moreover, the **feedback loop seems essential to capture cell C8 dynamics**, because none of the models without feedback loop accurately reproduces the three C8 properties. This result agrees with the findings of Schwarzer and al. [Schwarzer et al., 2020] in which they demonstrate *in vivo*, the downstream inducing apoptosis effectors' effects on caspase 8.

These outcomes also reveal that the **clusterization of C8/C10**, and so the recruitment and the activation of C8, **is more important to C8 dynamics than the presence of $\mathbf{F}_D$** in pC8 fixation on DISC. Tummers and al. showed that caspase-8 mediates inflammasome activation independently of FADD in epithelial cells [Tummers et al., 2020], further evidence that FADD is not mandatory for caspase 8 activity.

Future work would expand the study of this cluster reaction, perhaps adding more variables to take into account the effects of other proteins since the reactions around pC8 recruitment (especially

its interactions with pC10 and c-FLIP) are still unclear. Another hypothesis could also be made, assuming that in EAICM-cf, the F_D action is not present in the equations but indeed taken into account since C8 is still recruited at the DISC level.

4.3.2 The feedback loop mechanism

The second question addressed in this section concerns **the effects of the positive feedback loop on C8** to understand its importance on C8 dynamics.

To **evaluate the feedback loop impacts on the C8 dynamic**, we use the **parameters** obtained from fit F1, **on both initial conditions and reaction rates**. Figure 4.3 and Figure 4.4 (a) and (c) compare the FRET ratio and the $C8^c$ curve corresponding to the models 1, with and without feedback, for selected tolerant and sensitive cells from the cell populations in [Roux et al., 2015]. It seems clear that the model without feedback fails to reproduce the initial delay before C8 activation.

In a second plot, Figure 4.3 and Figure 4.4 (b) and (d) compare the relative weights of the different terms that contribute to C8 activation. This method, called **Principal Process Analysis (PPA)**, and developed by Casagranda and al. in [Casagranda et al., 2018], consists in representing the absolute values curve of each term that composes the C8 equation, divided by the sum of all absolute values, to normalize. For instance, if we consider the following C8 equation of EAICM-cf:

$$\frac{dC8}{dt} = -2\vec{K_2}\, Z_0 C8^2 + 2\overleftarrow{K_2}\, Z_1 + \alpha\, D - K_{deg}\, C8, \tag{4.6}$$

then the plotted curves are:

$$\begin{cases} \dfrac{|K_{deg}\, C8|}{|K_{deg}\, C8| + |\alpha\, D| + |2\overleftarrow{K_2}\, Z_1| + |2\vec{K_2}\, Z_0 C8^2|}, \\ \dfrac{|\alpha\, D|}{|K_{deg}\, C8| + |\alpha\, D| + |2\overleftarrow{K_2}\, Z_1| + |2\vec{K_2}\, Z_0 C8^2|}, \\ \dfrac{|2\overleftarrow{K_2}\, Z_1|}{|K_{deg}\, C8| + |\alpha\, D| + |2\overleftarrow{K_2}\, Z_1| + |2\vec{K_2}\, Z_0 C8^2|}, \\ \dfrac{|2\vec{K_2}\, Z_0 C8^2|}{|K_{deg}\, C8| + |\alpha\, D| + |2\overleftarrow{K_2}\, Z_1| + |2\vec{K_2}\, Z_0 C8^2|}. \end{cases} \tag{4.7}$$

Similar plots for the EAICM-af and EAICM-a models can be found in Appendix B.2 p.200. First, comparing Figure 4.3 and Figure 4.4, notice that there are **essentially no differences between tolerant and non tolerant cells in the component-wise analysis**. However, there is no activation delay in C8 curve for the models without a feedback loop.

Then, focusing on the $|\alpha D|$ variation (corresponding to the feedback loop effect), one can observe that $|\alpha D|$ reaches its maximum and $|K_{deg} C8|$ its minimum at approximately the same moment, which also coincides with the moment when C8 starts increasing. Recall that αD drives

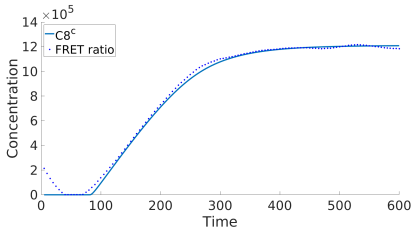

(a) Real FRET ratio and $C8^c$ for EAICM-cf

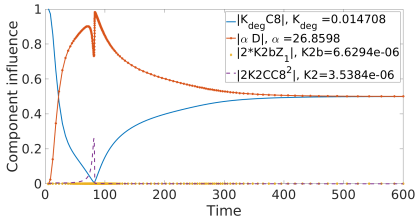

(b) C8 equation component dynamics for EAICM-cf

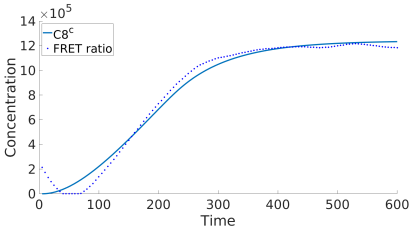

(c) Real FRET ratio and $C8^c$ for EAICM-c

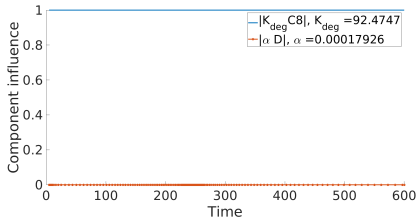

(d) C8 equation component dynamics for EAICM-c

Figure 4.3: **Comparison of C8 dynamics and main properties** for models EAICM-cf (a),(b) and EAICM-c (c),(d), for the tolerant cell n. 10 curve legends are given in each subplot

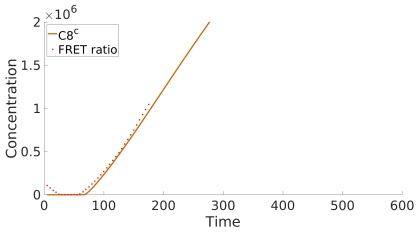

(a) Real FRET ratio and $C8^c$ for EAICM-c

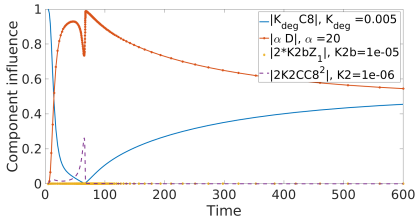

(b) C8 equation component dynamics for EAICM-cf

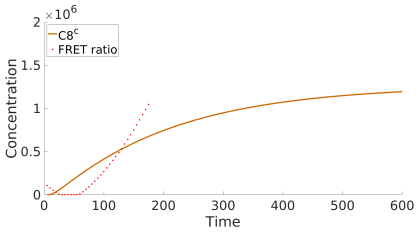

(c) Real FRET ratio and $C8^c$ for EAICM-c

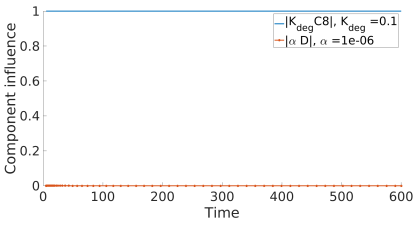

(d) C8 equation component dynamics for EAICM-c

Figure 4.4: **Comparison of C8 dynamics and main properties** for models EAICM-cf (a),(b) and EAICM-c (c),(d) for the sensitive cell n. 121 *simulations were performed for 600 min for comparison needs - curve legends are given in each subplot*

all the effective caspase cascade and the feedback loop, so the coincidence between maximum of αD and beginning of C8 activation suggests that the **feedback loop markedly increases the**

production of C8. Finally, observe that, **in the absence of feedback loop**, the term $|K_{deg}\mathbf{C8}|$ **is responsible for all the dynamics of C8**, inducing similar activation slopes for the two phenotypes.

Overall, the **feedback loop helps to refine cell decision, by improving modulation of the activation slope**, as illustrated by the term αD: for the sensitive cell, in the first 50 minutes αD increases in a much steeper manner. The feedback represents a additional set of regulatory mechanisms that is surely independent from the complex TRAIL/receptors and possibly downstream, yet with a decisive impact on C8 activation.

The next step is evaluating the **effect of variability in initial conditions on both C8 and cell fate**.

4.3.3 Initial conditions impacts on slope values

This section analyses the initial conditions distributions and compares them with our reference values, to **identify mathematical patterns that can help predicting cell fate**. The goal is to find those distributions for which the tolerant and sensitive phenotypes present a significant difference, or a link between the initial conditions and C8 dynamics.

To represent the data obtained after model's fitting, the bar chart of the cell density after model fitting, according to their parameter distribution, along with the scatter plot of the initial condition distribution in logscale as a function of reference values (for example, the slope), are used. For each type of graph, tolerant and sensitive cells are differenciated to find specific behaviours.The parameters used for comparison are those obtained from fit F3 (only on the initial conditions), to evaluate the environmental impacts.

A clear difference is observed between tolerant and sensitive cells for $C10_0$, as seen in the logscale scatter plots in Figure 4.6 p.89, with a **linear correlation between the slope and the initial protein** value with highly clustered points for the two types of cells. This is also the case for the F_D distribution that can be found in Figure 4.5 p.89.

To **understand how these two initial conditions**, as well as R_0 variation, **affect C8 dynamics**, we next carry a **one-parameter-at-the-time variation analysis**. Figure 4.7 shows the evolution of the $C8^c$ curves for each model, as two of the initial conditions are fixed and the third is given by the median value obtained with the fit on all the parameters for tolerant cells (given in Appendix B.3 p.201, in black dash dots on Figure 4.7) multiplied by $m \in \{0, 0.2, 0.4, 0.6, 0.8, 1.2, 1.4, 1.6, 1.8, 2, 4, 10\}$.

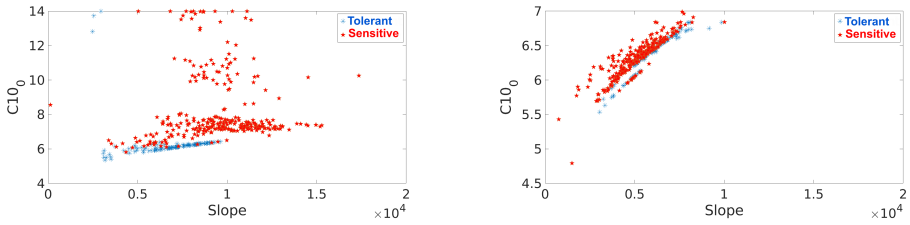

(a) EAICM-cf (b) EAICM-c

Figure 4.5: **Scatter plot of $C10_0$ values according to the slope**, depending on cell fate, for the EAICM-cf and EAICM-c

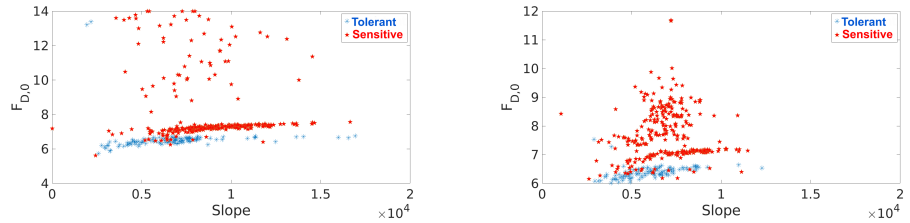

(a) EAICM-af (b) EAICM-a

Figure 4.6: **Scatter plot of $F_{D,0}$ values according to the slope**, depending on the cell fate for EAICM-af and EAICM-a

First of all, observe that **an increase in the receptor number enhances the slope of C8**, it **speeds up C8 production and delays C8 degradation**, since the stabilization happens later, but it **doesn't influence the total C8 production** (C8 stabilization at the same value). Hence, R_0 is likely to contribute to determination of the C8 activation threshold.

A **saturation effect is observed in every model**, for the recruited C8, that can't exceed a certain threshold in the total C8 production. This is in agreement with single cell traces since, independently of the TRAIL dose, even at saturated concentration with all the receptors occupied, not every cell commits to apoptosis. An improvement in our models may be necessary to take into account the necessary receptors trimerization that leads to DISC formation [Dickens et al., 2012].

Another observation is that **larger $C10_0$ induce larger values for C8 stabilization**. An increase in $C10_0$ enhances the C8 production speed but doesn't impact the degradation beginning time. Observe that **$C10_0$ also plays a significant role in feedback loop-free models**. This effect of $C10_0$ on C8 behaviour confirms the essential role of caspase cluster to trigger cell-death, as shown in Dickens and al. [Dickens et al., 2012].

Finally, **increasing $F_{D,0}$ delays C8 degradation and improves C8 production** or recruitment, but **doesn't speed up the C8 production** since the activation slope doesn't show much variation.

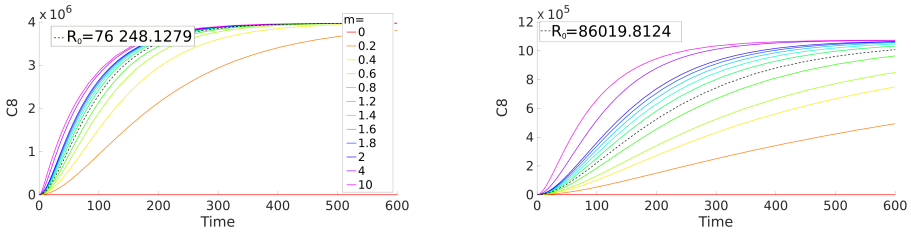

(a) EAICM-cf - R_0

(b) EAICM-c - R_0

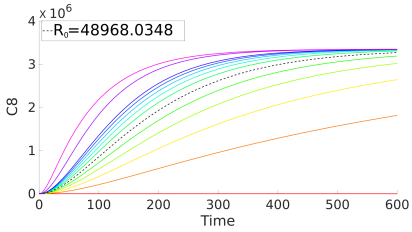

(c) EAICM-af - R_0

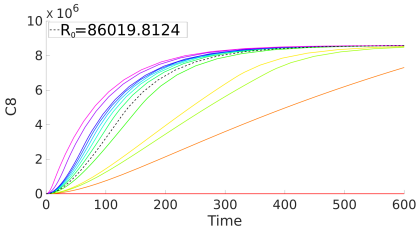

(d) EAICM-a - R_0

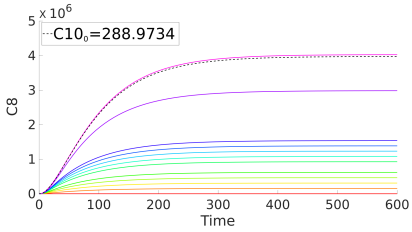

(e) EAICM-cf - $C10_0$

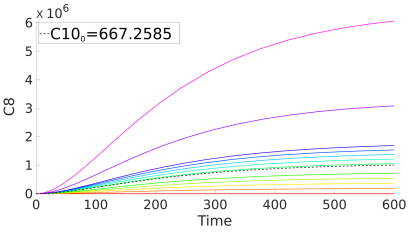

(f) EAICM-c - $C10_0$

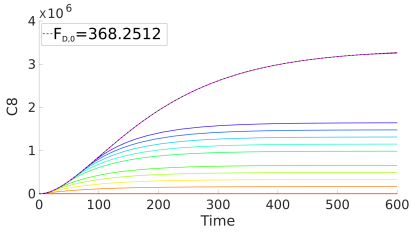

(g) EAICM-af - $F_{D,0}$

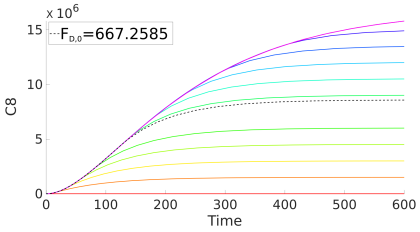

(h) EAICM-a - $F_{D,0}$

Figure 4.7: **Initial condition variation effects on C8 dynamic**. The estimated parameters P_i are indicated at the top left corners and used as reference values to vary the initial condition, in the range $[0, 10X_0]$, where $X_0 = \mathrm{R}_0$ in (a)-(d); $X_0 = \mathrm{C10}_0$ in (e)-(f); and $X_0 = \mathrm{F}_{D,0}$ in (g)-(h).

Furthermore, **increasing $F_{D,0}$ leads to an increase in C8**, thus making it possible to exceed the C8 threshold responsible for cell death and confirming that FADD is necessary to trigger the extrinsic cell death as demonstrated by Kuang and al. in [Kuang et al., 2000]. Similarly to $C10_0$, **$\mathbf{F}_D$ also has more influence on the model without feedback loop**, suggesting that the **feedback loop has a saturation effect on C8 dynamic**.

4.3.4 Model validation and degradation specificity

Comparison of the reaction rates distributions, **singles out C8 degradation rate which exhibits a large discrepancy between tolerant and sensitive populations**, with values related by a factor $K^r_{deg} \approx 10K^s_{deg}$.

As seen in Section 4.3.2, **degradation is the process that counteracts C8 activation** and, when the term $K_{deg}C8$ becomes sufficiently high, the stabilization phase sets in. Decreasing the degradation rate constant should lead to higher activation slopes and effectively "switch" cells from the tolerant to the sensitive populations.

Data from [Roux et al., 2015] includes a **second group of 563 cells treated with 50ng/mL of TRAIL and 100ng/mL of Bortezomib**, a proteasome inhibitor drug that **blocks C8 degradation** and drives cells to commit apoptosis.

To validate our models, our hypothesis is that, **setting K_{deg} to zero** in model EAICM-cf (while keeping other parameters as estimated for each tolerant cell), **will elicit the same response as Bortezomib**, thus transforming the tolerant population into sensitive.

Figure 4.8(a) shows the FRET ratio of the two groups of cells: the tolerant population of 114 cells treated only with TRAIL and the second group of 563 cells treated with TRAIL and Bortezomib. These experimental results are to be compared with Figure 4.8(b), that represents the C8^c EAICM-cf model curves for our original tolerant population, with all the corresponding estimated parameters except for K_{deg}, which is set to 0.

The model predictions in Figure 4.8 (b) and (c) are quite similar to the experimental data. Figure 4.8 shows that, **imposing a null degradation for our model, allows to reproduce a large heterogeneity range and the main features (delay and bigger slope) of C8 dynamic of the population treated with Bortezomib**, thus validating our hypothesis.

Why does the sensitive population of the first group of cells show a markedly lower K_{deg} constant? Perhaps a (negative) feedback or similar mechanism is also acting on the degradation process, canceling its effect in the case of a steep C8 activation.

However, it might be the case that the estimation of K_{deg} among the sensitive population is not fully reliable: indeed, recall that the degradation term is linear, K_{deg}C8, and that active caspase 8 is absent at the beginning (C8$(0) = 0$), implying a very low degradation when compared to terms of the form K_2Z_1 or αD which are proportional to T_0R_0. In addition, sensitive cells die relatively

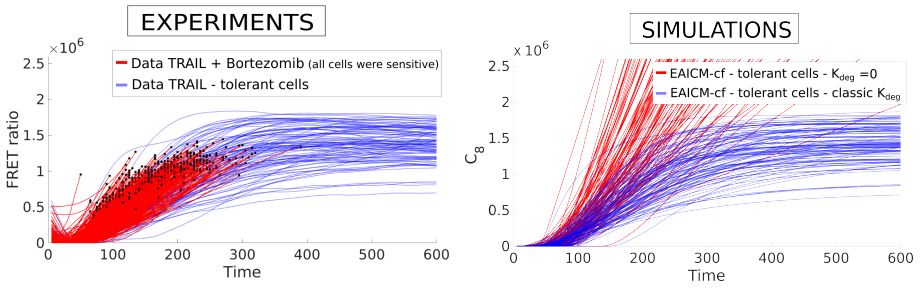

(a) Comparison of FRET ratio between tolerant cells treated with TRAIL only and cells treated with TRAIL and Bortezomib.

(b) Comparison of $C8^c$ from EAICM-cf for tolerant cells treated with TRAIL only, with $K_{deg} = 0$ and with classic degradation.

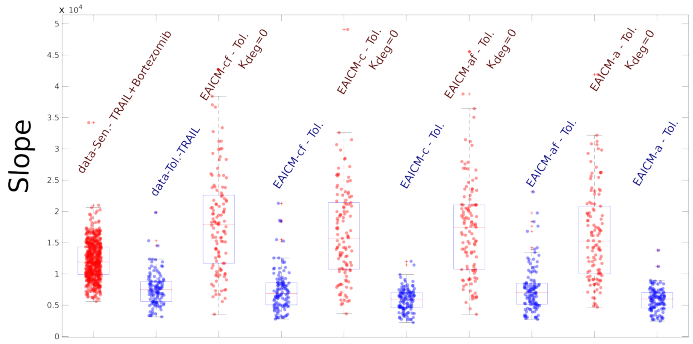

(c) Slope distribution according to the model used and the C8 degradation rate.

Figure 4.8: **Degradation study**.

early during the first 150 minutes, so that there are much fewer measurement points available than for tolerant cells. New modeling steps are needed to further study the C8 degradation process.

4.4 Discussion and Conclusion

This chapter studies the **role and the relevance of several components of the extrinsic apoptosis initiation pathway in cell response heterogeneity**.

Four minimal ODE models are proposed, taking into account the major steps of the extrinsic pathway: the **TRAIL/receptors association**, the **DISC formation** with the recruitment of procaspase 8 and, either a focus on the **FADD action**, or a particular attention to the **cluster formation of C8 and C10**. These models also represent **C8 activation**, **with (or without) a positive feedback loop on C8**, to integrate a supplementary regulation of C8 downstream. Finally, as cell decision to commit apoptosis seems to happen before effective caspase activation and MOMP, all the

downstream apoptosis steps were combined in a single variable.

The models were calibrated to single cell data from a cloned population treated with death ligand TRAIL. The corresponding initial conditions and/or parameters were analysed to **search for correlations between molecular factors and/or network interactions, and the resulting cell fates**.

Our analysis **selects two mechanisms that significantly contribute to cell response heterogeneity**: the **clusterization of the caspases C8/C10** and subsequent C8 activation and, to a larger extent, the **positive feedback loop**. The formation of C8/C10 clusters accelerates C8 activation by increasing C8 production as well as the slope of the curve (see the effect of $C10_0$), while the F_D reaction does not greatly affect the slope but delays the stabilization time. Therefore, caspase clusterization has a greater capacity to generate variability in cell response.

The **positive feedback is important in the timing of C8 dynamics, particularly in reproducing the initial delay observed in C8 activation**. Studying the components of the C8 equation shows that activation of C8 is triggered when the feedback loop has a maximum effect on C8 and degradation is still negligible. Conversely, when the degradation and the feedback loop terms reach similar levels C8 leaves the high slope phase, revealing that the **balance between feedback loop and C8 degradation plays a major role in cell fate**. Another role of the **feedback loop is to introduce a saturation on the maximum level of C8** induced by variability in initial conditions: indeed, for our two models with positive feedback, increasing the initial numbers of molecules leads to an increase in the maximum C8 levels, but this maximum value has an upper-bound independent of the initial numbers. This reveals a large robustness of the feedback models with respect to variations in initial amounts of molecules.

Finally, our **models faithfully reproduce the experiments involving Bortezomib**, a drug that blocks C8 degradation by setting $K_{deg} = 0$. The corresponding effect is to increase all activation slopes into the range observed for the sensitive population.

Based on the mechanisms and interactions selected by our methods, the next chapter includes the development of a more detailed model to answer further questions such as the need for trimerization of the death receptor, understanding the process of caspase degradation during the first hours of C8 activation, or adding new variables to investigate the impact of the closest proteins to C8 like pro-caspase 8.

CHAPTER 5

Modeling isogenic cancer cell response upon varying TRAIL stimulations deciphers the kinetic determinants of cell fate decision

In this chapter, I investigate the effects of TRAIL dose on cell fate decision. I present a new ODE model of the extrinsic apoptosis initiation by death-ligands, constructed from the analysis and conclusions in Chapter 4. This model is calibrated on FRET time-trajectories from [Roux et al., 2015] of hundreds of clonal HeLa cells treated with different amounts of TRAIL.
Highlighting the different steps in the regulation of apoptosis, and the associated timeline, the improved model detects an initial cell fate decision just after TRAIL binding and the presence of additional regulation at the receptor that benefits only the drug-sensitive population.
This study also shows that increasing the dose of TRAIL actually has small effects within each population (resistant or sensitive), but rather accentuates the differences between the two, affecting the population dynamics in two different ways depending on their response to the drug.
Finally, the distribution of 3 parameters of the mechanistic model, according to the cell drug response, suggests the existence of a determinant threshold in C8 dynamics, independent of the drug dose, that distinguishes cells drug-resistant or sensitive, that could be used to control or predict cell drug-response in the future.

A part of this chapter was presented at the 19th International Conference on Computational Methods in Systems Biology (CMSB 2021) [MP3] as a poster, and the entire chapter was also published at the 9th International Conference on the Foundations of Systems Biology in Engineering (FOSBE 2022) [MP4].

5.1 Modeling TRAIL-inducing extrinsic apoptosis

Based on the results of Chapter 4, the Extrinsic Apoptosis Initiation Core Reactions model (EAICRm), obtained by applying mass action kinetic law (Figure 5.1), only integrates the receptor (R) trimerisation when TRAIL (T) binds to the cell, while it does not represent FADD and c-FLIP actions.

The major novelty of this system is incorporating all the steps leading to $C8$ activation, whether with the dimerisation of $pC8$ (p for pro, C for caspase), or with the recruitment of an already active $C8$. Hence, the dimerisation of pC8, which is required to activate C8, is modelled, as well as the C8/C10 clustering and the downstream feedback loop on C8 (in red on Figure 5.1). As in [MP2], the effector caspases are grouped under the variable C^{eff}, and the intermediary complexes are denoted by Zi, $i \in \{0, 1, 2\}$. Finally, the model also accounts for the FRET activation by $C8$. A

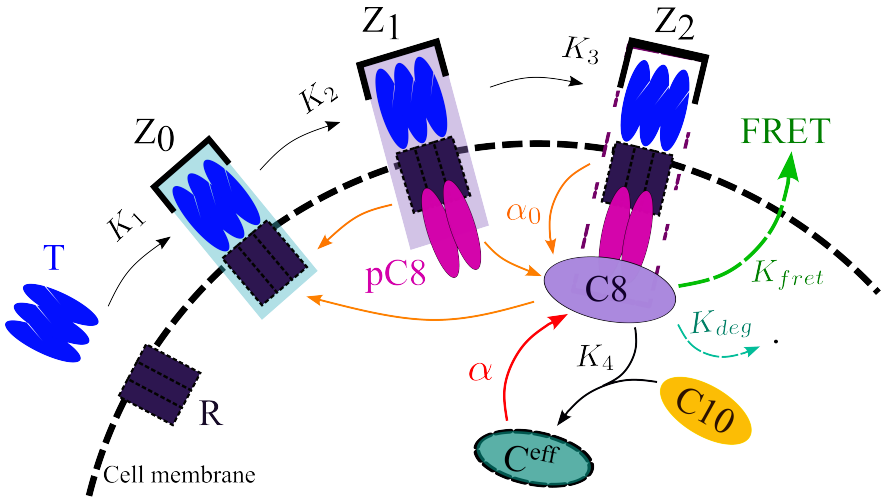

Figure 5.1: **Extrinsic Apoptosis Initiation Core Reactions model (EAICRm)**

classic mathematical study of the existence, uniqueness and stability of the solution of the EAICR system is available in Appendix C.4 p.203.

5.2 Dynamic Analysis of chemical reaction timeline with a principal process analysis

As explained in Chapter 4, a PPA [Casagranda et al., 2018] evaluates the impact of each chemical reaction (represented by each equation term) on each protein (variable) all along the system

simulation.

The EAICR parameters were estimated for each cell of the dataset from [Roux et al., 2015], treated with 50ng/mL of TRAIL. The calibration method is the same than in Chapter 4. Then, each cell system were analysed with the PPA method.

5.2.1 Dynamic description of Apoptosis timeline

To run a PPA, we first split the simulation into **characteristic time checkpoints**. We decided to base their definition on dynamic events (rather than using same-size steps) and divide our 10 hours of simulations into time-slots corresponding to important protein dynamic turnovers (in italic the mean value in minutes for cells treated with 50ng/ml of TRAIL (see Appendix C.3 p.202 for computation):

1. $\boldsymbol{\tau_{T.trigger}}$ (*1e-5*) : $Z0$ reaches its first local maximum - it corresponds to the moment when TRAIL is in sufficient quantity to trigger a cellular reaction;
2. $\boldsymbol{\tau_{DISC.ass}}$ (*1.15*): at this time, the DISC assembly expands, R decreasing speed strongly draws down and $pC8$ becomes linear;
3. $\boldsymbol{\tau_{drug.0}}$ (*5.20*): T falls down to the equilibrium $T = 0$, R stabilizes to $-3T_0 + R_0$ while $Z1$ reaches its local maximum $Z1 = T_0$;
4. $\boldsymbol{\tau_{DISC.end}}$(*400*) : $Z1$ collapses to almost 0 and $Z0$ becomes bigger than $pC8$;
5. $\boldsymbol{\tau_{C8.final}}$ (*412*) : $C8$ reaches its maximum before decreasing (or remaining constant for the major part of sensitive cells)

Hence, we obtain 6 models summarised in Table 5.1 p.99.

5.2.2 An early cell decision

The PPA shows that the first changes between sensitive and tolerant population happen after $\tau_{T.trigger}$ and continue until cell death (before $\tau_{DISC.end}$ for the sensitive), which locates the main events leading to fractional killing between these two times. Comparing tolerant and sensitive cell dynamic during this timelapse reveals that the term $\overline{K_2}Z1$ comes into action sooner in the sensitive population and potentially adds a regulatory effect on the DISC in the form of a positive feedback, driving the cell to death.

Table 5.1 also highlights the significant impact of $Z0$ (T:R) and $Z1$ (DISC - T:R:2pC8) on every step of the cell fate. These complexes appear to be decision-triggers whereas C8 is simply the

var.	All experience	[0 $\tau_{\text{T.trigger}}$]	]$\tau_{\text{T.trigger}}$ $\tau_{\text{DISC.ass}}$]	]$\tau_{\text{DISC.ass}}$ $\tau_{\text{drug.0}}$]
$\dot{T}$	$-K_1 TR^3$			
$\dot{R}$	$-3K_1 TR^3$			
$\dot{Z}0$		$K_1 TR^3$ $-K_2 Z0pC8^2$	$K_1 TR^3 + \alpha_0 Z1$ $-K_2 Z0pC8^2$ $+\overline{K_2} Z1$	$K_1 TR^3 + \alpha_0 Z1$ $-K_2 Z0pC8^2$ $+\overline{K_2} Z1$
$\dot{pC8}$	$-K_2 Z0pC8^2$			$2\overline{K_2} Z1$
$\dot{Z}1$	$K_2 Z0pC8^2$		$-\alpha_0 Z1 - \overline{K_2} Z1$	$-\alpha_0 Z1 - \overline{K_2} Z1$
$\dot{Z}2$	$K_3 Z1C8$			
$\dot{C^{eff}}$	$K_4 C10Z2$			
$\dot{C10}$	$-K_4 C10Z2$			
$\dot{C8}$	$\alpha_0 Z1$	$-K_{deg} C8$		
$\dot{FRET}$	$K_{fret} C8$			

var.	]$\tau_{\text{drug.0}}$ $\tau_{\text{DISC.end}}$]	]$\tau_{\text{DISC.end}}$ $\tau_{\text{C8.final}}$]	]$\tau_{\text{C8.final}}$ $\tau_{\text{cell.death}}$]	
$\dot{T}$	$+\overline{K_1} Z0$	$+\overline{K_1} Z0$	$+\overline{K_1} Z0$	
$\dot{R}$	$+3\overline{K_1} Z0$	$+3\overline{K_1} Z0$	$+3\overline{K_1} Z0$	
$\dot{Z}0$	$K_1 TR^3 + \alpha_0 Z1$ $-K_2 Z0pC8^2$ $+\overline{K_2} Z1$	$K_1 TR^3 + \alpha_0 Z1$ $-K_2 Z0pC8^2$ $-\overline{K_1} Z0 + \overline{K_2} Z1$	$K_1 TR^3 + \alpha_0 Z1$ $-K_2 Z0pC8^2$ $-\overline{K_1} Z0$	
$\dot{pC8}$	$+2\overline{K_2} Z1$	$+2\overline{K_2} Z1$	$+2\overline{K_2} Z1$	
$\dot{Z}1$	$-\alpha_0 Z1 - \overline{K_2} Z1$	$-\alpha_0 Z1 - \overline{K_2} Z1$	$-\alpha_0 Z1 - \overline{K_2} Z1$	
$\dot{Z}2$	$-\overline{K_3} Z2 - \alpha_0 Z2$	$-\overline{K_3} Z2 - \alpha_0 Z2$	$-\overline{K_3} Z2 - \alpha_0 Z2$	
$\dot{C^{eff}}$	$-\alpha C^{eff}$	$-\alpha C^{eff}$	$-\alpha C^{eff}$	
$\dot{C10}$	$+\alpha C^{eff}$	$+\alpha C^{eff}$	$+\alpha C^{eff}$	
$\dot{C8}$	$-K_{deg} C8$	$-K_{deg} C8$	$-K_{deg} C8$	
$\dot{FRET}$				

Table 5.1: **Principal Process Analysis Results for the EAICR model** - Only the reactions above 0.05 and the one above 0.0005 for more than half of the cells (more than 57 cells for tolerant and 150 for the sensitive population) are kept. The reactions available only for the sensitive population, and between 0.0005 and 0.05, are in olive and the sensitive reaction above 0.05 in red. For only the tolerant cells, the reactions above 0.005 are in blue.

result of their actions.

Finally, $\tau_{drug.0}$ marks the moment when the effective caspase downstream feedback is activated but, at least in this model, this feedback seems not to have enough impact to influence the cell's decision in most cases. We also notice that C8 degradation disappears just after TRAIL binding,

during the DISC formation phase, before regaining importance between $\tau_{drug.0}$ and $\tau_{C8.final}$.

In summary, it seems clear that cells undergo a first decision stage before $\tau_{drug.0}$. However, the mechanisms responsible for cell fate implementation and regulation are really acting between $\tau_{DISC.ass}$ and $\tau_{DISC.end}$.

5.2.3 Reducing Extrinsic Apoptosis Initiation Core Reaction model

The PPA method was originally designed as a model reduction technique. Removing the group of proteins that appear only in their own rows in Table 5.1 all along the experiment ($C10$, C^{eff} and $Z2$), we obtain a reduced EAICR model **(rEAICR)**:

$$\begin{cases} \dot{T} &= -K_1\,TR^3 + \overline{K_1}\,Z0, \\ \dot{R} &= -3K_1\,TR^3 + 3\overline{K_1}\,Z0, \\ \dot{Z0} &= K_1\,TR^3 - \overline{K_1}\,Z0 - K_2 Z0 pC8^2 \\ & \quad +\overline{K_2}Z1 + \alpha_0 Z1, \\ p\dot{C}8 &= -2K_2 Z0 pC8^2 + 2\overline{K_2}Z1, \\ \dot{Z1} &= K_2 Z0 pC8^2 - \overline{K_2}Z1 - \alpha_0 Z1, \\ \dot{C}8 &= \alpha_0 Z1 - (K_{deg} + K_{fret})C8, \\ F\dot{R}ET &= K_{fret}C8. \end{cases} \tag{5.1}$$

A mathematical analysis of the model is done in appendix.
To further simplify this model and analyse its variables, we proceed as follows. Using mass conservation:

$$\dot{T} + \dot{Z1} + \dot{Z0} = 0. \tag{5.2}$$

As $Z0$ and $Z1$ are intermediary complexes, they are assumed to be absent at the beginning of the experiment and we get the following relation:

$$T + Z1 + Z0 = T_0. \tag{5.3}$$

Model simulation (data not shown but simulation parameters available), with different cell sets of parameters, show that between $\tau_{drug.0}$ and $\tau_{DISC.end}$,

$$Z1 \approx T_0, \tag{5.4}$$

that leads to:

$$p\dot{C}8 = -2\alpha_0 T_0, \tag{5.5}$$

which gives us the slope of pC8 when this variable becomes linear .
Hence, we approximate $Z1$ and $Z0$ by step functions, setting $Z1 = T_0$ between 0 and $\tau_{DISC.end}$ (as $\tau_{drug.0} < 6$ min), and assuming $Z1 = 0$ after $\tau_{DISC.end}$ in $C8$ and $FRET$. Therefore, before $\tau_{DISC.end}$,

$$\dot{C8} = \alpha_0 T_0 - (K_{deg} + K_{fret})C8, \tag{5.6}$$

so an approximated explicit solution for C8 is given by :

$$\begin{aligned} C8_{0,\tau_{DISC.end}}(t) &= C8_0 e^{-t(K_{deg}+K_{fret})} \\ &\quad + \frac{\alpha_0 T_0 \left(1 - e^{-t(K_{deg}+K_{fret})}\right)}{(K_{deg} + K_{fret})}. \end{aligned} \tag{5.7}$$

Integrating this solution in FRET equation:

$$\begin{aligned} FRET(t) &= \frac{K_{fret}}{K_{deg} + K_{fret}} \times \Bigg(\alpha_0 T_0 t \\ &\quad + \left(C8_0 - \frac{\alpha_0 T_0}{K_{deg} + K_{fret}}\right)\left(1 - e^{-(K_{deg}+K_{fret})t}\right)\Bigg) \end{aligned} \tag{5.8}$$

Defining:

$$\begin{cases} \beta_0 = & K_{deg} + K_{fret}, \\ \beta_1 = & \dfrac{K_{fret}\alpha_0 T_0}{\beta_0}, \\ \beta_2 = & \dfrac{K_{fret}C8_0 - \beta_1}{\beta_0}, \end{cases} \tag{5.9}$$

we find a sigmoid formula for FRET :

$$FRET(t) = \beta_1 t + \beta_2 \left(1 - e^{-\beta_0 t}\right). \tag{5.10}$$

Keeping the same notation, between $\tau_{DISC.end}$ and $\tau_{C8.final}$:

$$\begin{cases} Z1 = & 0, \\ \dot{C8} = & -\beta_0 C8. \end{cases} \tag{5.11}$$

Hence,

$$\begin{cases} C8(t) = & C8_{\tau_{DISC.end}} e^{-\beta_0(t-\tau_{DISC.end})}, \\ FRET(t) = & \dfrac{K_{fret}C8_{\tau_{DISC.end}}}{\beta_0}\left(1 - e^{-\beta_0(t-\tau_{DISC.end})}\right) \\ & + FRET(\tau_{DISC.end}). \end{cases} \tag{5.12}$$

Equation (5.10) and Equation (5.12) provides an approximated explicit solution, denoted by **FRET-exp**, for the time interval $[0, \tau_{DISC.end}[$, and between $\tau_{DISC.end}$ and the cell death, respectively.

From this analysis, we improved our fitting method for the next steps by using the parameters of the FRETexp explicit solution to have a better initial guess (see Appendix C.2 p.202), dividing our fitting computation time by 4 in the process. Decreasing our parameter estimation computing time is crucial when large-scale studies with hundreds of time-trajectories are involved [Stapor et al., 2022]. Moreover, this analysis provide the primary elements - and only identifiable parameters [Berthoumieux et al., 2013] - of the extrinsic apoptosis pathway - $C8_0$, $pC8_0$, K_{deg} and α_0 - and confirming that the number of receptors at the cell membrane in our cell lines in not limiting (data of Roux et al. unpublished).

Lastly, taking the power series of this explicit solution recovers the empiric model from [Roux et al., 2015], thus confirming the straightforward model suggested in that paper, as a simplification of a mechanistic and more detailed signaling pathway.

5.3 Impact of TRAIL concentration

To understand how TRAIL dose variations affect cell decision, the rEAICR model parameters (and the corresponding characteristic times) were estimated for each cell of 4 datasets from [Roux et al., 2015], treated with 4 different doses of TRAIL (5,10,25 and 50 ng/mL), using our new fitting method (see Appendix C.2 p.202), and imposing the same T_0 for all the cells treated with the same amount of TRAIL (see Appendix C.1 p.202). Figure 5.2 p.103 summarizes the analysis.

5.3.1 Measuring TRAIL effects on timeline

To characterize TRAIL variation effects on the cell timeline, the 5 characteristic time checkpoints - $\tau_{T.trigger}$, $\tau_{DISC.ass}$, $\tau_{drug.0}$, $\tau_{DISC.end}$, $\tau_{C8.final}$ - are computed for all the cells, along with 4 associated time-lapses:

1. **DISC formation phase** (**DISC-fp** - $[0, \tau_{drug.0.}]$): during this time-interval, $Z0$ reaches a maximum before decreasing to 0. It seems that this time correspond to the reception of the apoptotic message sent by TRAIL binding on the cell. Then, when $Z0$ reaches 0, the DISC complex starts to form : T decreases toward 0 (all cells go toward the same model equilibrium space $T = 0$), marking the end of signal reception, R decreases until $\tau_{DISC.ass}$ toward the value $-3T_0 + R_0$ (with mass conservation). $pC8$ lowers too.

2. **DISC action phase** (**DISC-ap** - $]\tau_{DISC.ass}, \tau_{DISC.end}]$): $Z1$ represents the DISC in the system. From $\tau_{DISC.ass}$, and until $\tau_{DISC.end}$, $Z1$ reaches its maximum level and remains constant so we consider this time-lapse as the DISC action. In addition, $\tau_{DISC.ass}$ marks a turn-over in $pC8$ dynamics as $pC8$ becomes linear. During this time, $Z0$ starts to increase but very slowly, leading to the subsequent decrease of $Z1$, initiating the end of the phase and the major dynamic turn-over.

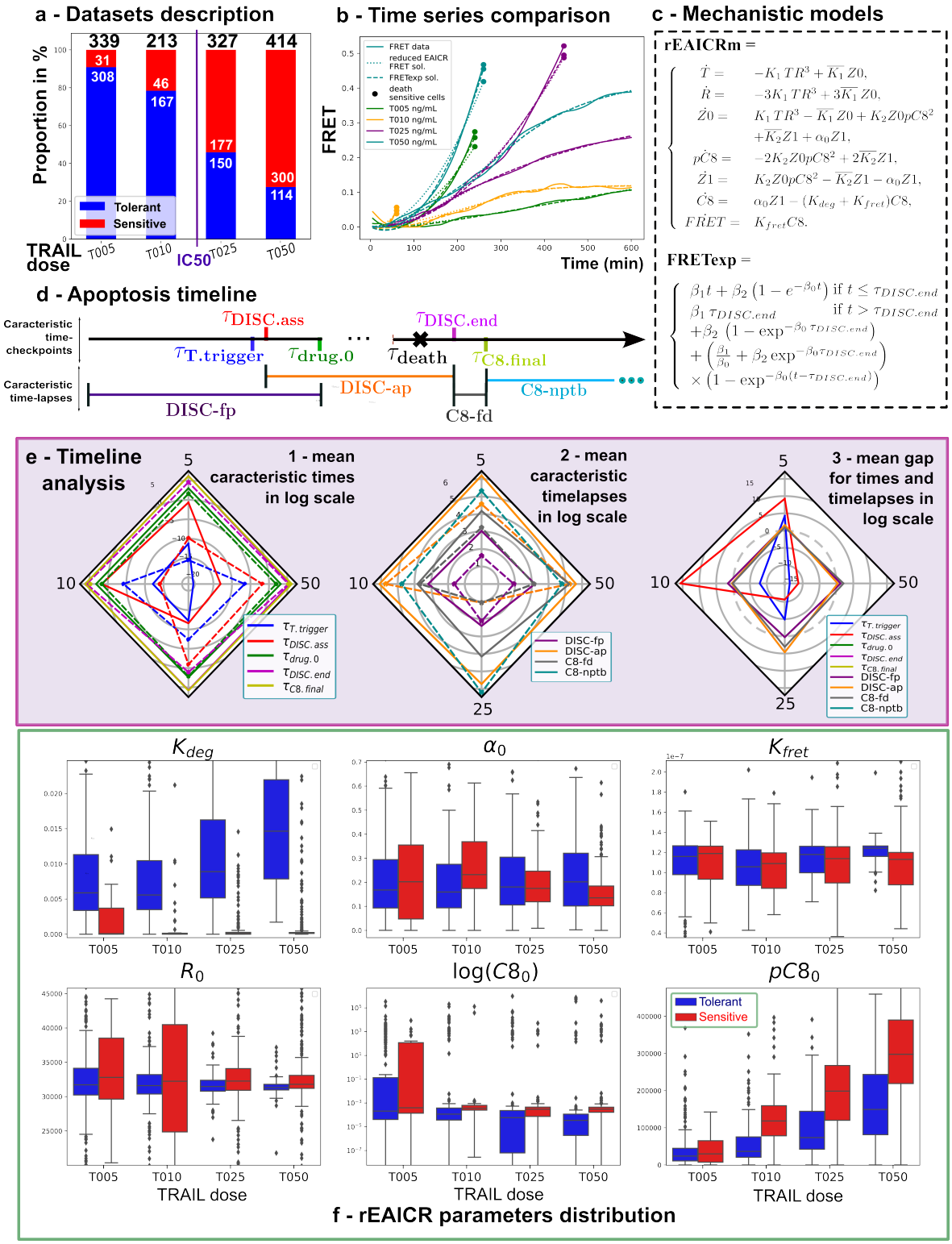

Figure 5.2: **Summary of the rEAICR model analysis for four drug doses:** a - Datasets description. b - Comparison of the time-series obtained with rEAICR model, the FRETexp solution and the real FRET measurements for a sensitive and a tolerant cell of each dataset. c - Mechanistic models. d - Apoptosis timeline. e - Radar plots analysis according to the TRAIL dose in ngmL (1 dose=1 vertex) of the mean timeline analysis according to the drug response (sensitive in dashed line, tolerant in plain): 1-time-checkpoints, 2-time-lapses, 3-ratio mean tolerant mean Sensitive (gap=$\frac{\text{mean R}}{\text{mean S}}$). f - Parameters distribution boxplots according to the drug response of the identifiable parameters of the reduced EAICR model.

3. **C8 final decision** (**C8-fd** - $]\tau_{DISC.end}, \tau_{C8.final}]$): DISC activity ends, only $C8$ keeps evolving. Most of sensitive cells are already dead at that time but we believe that a perturbation in C8 concentration toward higher level during this interval may lead a tolerant cell to become sensitive.

4. **C8 no possible turning back** (**C8-nptb** - after $\tau_{C8.final}$ until death)

Between $\tau_{\text{DISC.ass}}$ and $\tau_{\text{drug.0}}$, the two DISC involved phases **DISC-fp** and **DISC-ap** overlap.

5.3.2 TRAIL dose influences the early stages of apoptosis

Comparing the distribution of the characteristic times, and the associated time-lapses (only the mean value is represented in Figure 5.2.e-1 and 2 p.103), shows that an increase in TRAIL affects mostly the beginning of apoptosis initiation (before $\tau_{drug.0}$) in two different ways according to the drug response.

For tolerant cells, more TRAIL means an earlier death signal trigger ($\tau_{T.trigger}$ is decreasing meaning that Z0 (T:R) reaches a first maximum earlier), smaller $\tau_{DISC.ass}$ and smaller DISC action phase too, but a longer C8-final decision phase. On the opposite side, the sensitive cells benefit from larger $\tau_{T.trigger}$ and $\tau_{DISC.ass}$ with a longer DISC formation phase too. However, the other time-lapses do not seem linked to the TRAIL dose since they are only notably changing at the IC50 (Figure 5.2.e-2).

The fraction between the mean time values for tolerant and sensitive cells confirms that the main differences between them are located before $\tau_{drug.0}$ for all doses of drug, with strong variations for $\tau_{T.trigger}$ and $\tau_{DISC.ass}$ between the two populations, when TRAIL increases (Figure 5.2.e-3). However, these variations do not affect the gap between tolerant and sensitive in time-lapses. Indeed, for the time intervals, the biggest gaps, between tolerant and sensitive cells, are observed for the DISC action phase and the C8-final decision interval, but at the IC50 (25 ng/mL), whereas it remains constant for the others TRAIL doses.

Finally, focusing on the difference of the mean timeline between tolerant and sensitive cells for the IC50 drug concentration (25ng/mL), Figure 5.2 (e -1) shows that sensitive cells have a slower activation of the extrinsic apoptosis pathway - with larger $\tau_{T.trigger}$ and $\tau_{DISC.ass}$ and a longer DISC-formation phase. However, after $\tau_{DISC.ass}$, they speed up and benefit from a longer DISC-action phase, reach similar mean values for the three last characteristic times than the tolerant cells.

5.3.3 TRAIL variation differently impacts cells according to their drug sensitivity

Figure 5.2.f compares the distribution of the 3 identifiable reaction rates (K_{deg}, α_0 and K_{fret}) and the 3 initial conditions to be estimated (R_0, $C8_0$ and $pC8_0$) for the rEAICR model, according to the drug response and TRAIL dose received. This subplot shows that TRAIL variation affects differently the tolerant and sensitive cells.

For tolerant cells, an increase in TRAIL leads to a huge increase of C8 degradation rate (K_{deg}) and a moderate augmentation in α_0. For sensitive cells, varying TRAIL slightly affects K_{deg} values (translated by a small increase) but α_0 is increasing until the IC50 is reached, before decreasing again after. Finally, K_{fret} keeps the same behaviour, whether cells are tolerant or sensitive, and increases until reaching IC50 and decreases afterwards, like the sensitive cells for α_0 and the time-lapses.

For the initial conditions, increasing TRAIL dose leads to a diminution of $C8_0$ for the tolerant cells whereas the initial amount of C8 recruited by the sensitive cells remains almost constant. In the meantime, $pC8_0$ increases with TRAIL dose for all cells, but in a more pronounced way for sensitive cells. Finally, as expected, R_0 is not observable, like demonstrated by the Section 5.2.3, and is not affected by TRAIL variations in our model.

5.4 Predicting cell drug response

5.4.1 A clear distinction between survival and death at 10h

Figure 5.3 reveals two distinct distributions for the FRETexp parameters, whether cells are drug tolerant or sensitive, regardless of the initial amount of TRAIL. As the FRETexp β depend on the initial amount of C8, but also on the degradation (K_{deg}) and the activation rate (α_0) of the initiator caspase (Equation (5.9)), their dual distribution is a sign of a complex biological threshold, with predictive value, around C8 activity, that distinguishes cells in a sensitive or tolerant state, but also confirms the central role of C8 in apoptosis [Roux et al., 2015].

Indeed, Figure 5.3 reveals the conditions (reaction rate and initial amount of protein) that cells must meet to be in a susceptible state, thus paving the way for controlling the cellular response to drugs. This clear difference between the two phenotypes also offers a possible way to predict cell drug response. Using only these 3 mechanistic parameters and our location of the cell death decision time, we may have the opportunity to create a new predictor of the apoptotic decision.

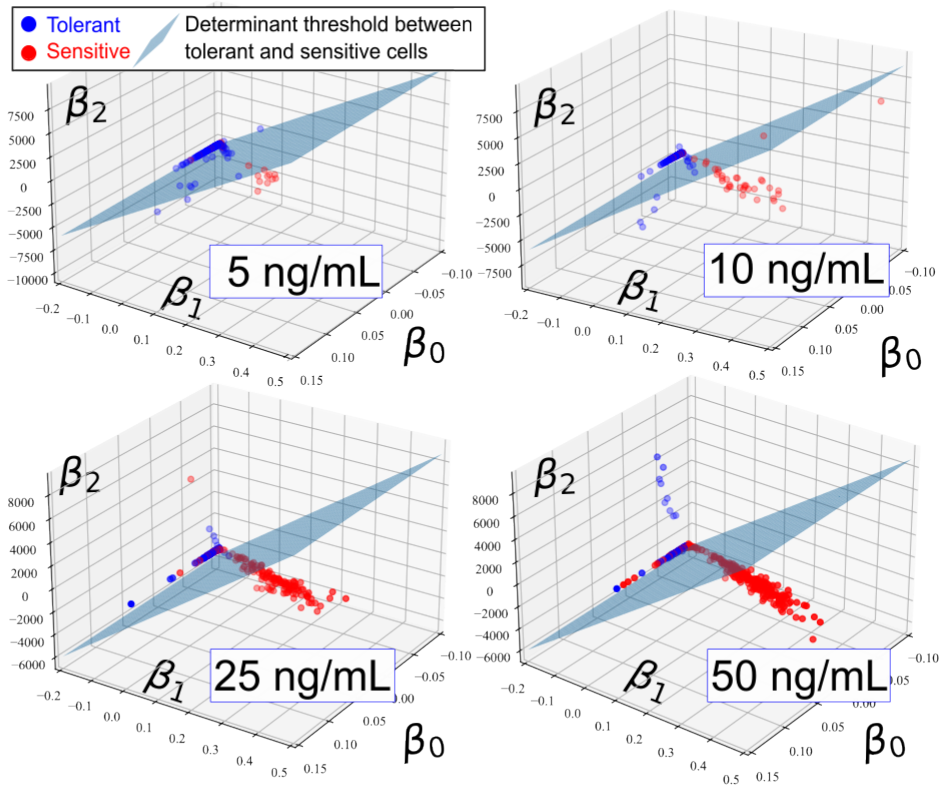

Figure 5.3: **FRETexp β parameters distribution** according to the drug response and **common cell decision threshold** between life and death: the decision threshold is obtained with a linear support vector classifier ($>$ 85% of accuracy). FRETexp parameters were estimated on time-trajectories from 10h long experiments.

5.4.2 A high accuracy in the forecasting of single-cell drug-response comes with longer experiments

In order to assess feasibility of forecasting cell drug-response with the β parameters, before a majority of sensitive cells die from the treatment, but also compare our method with [Roux et al., 2015], we estimated the FRETexp parameters after 1, 3 and 6 hours of experiment for 25ng/mL of TRAIL, using the same time-trajectories than [Roux et al., 2015].

As in the previous subsection, we applied a SVC (support vector classifier) to forecast cell drug response, but preceded by a scaling step with the function *QuantileTransformer* of sklearn library this time. The scaling step prevent the appearance of outliers (contrary to FATE-SEQ current method for forecasting cell drug response - see Figure 2.7 p.56 and Section 6.2 p.118). Hence, it will in-

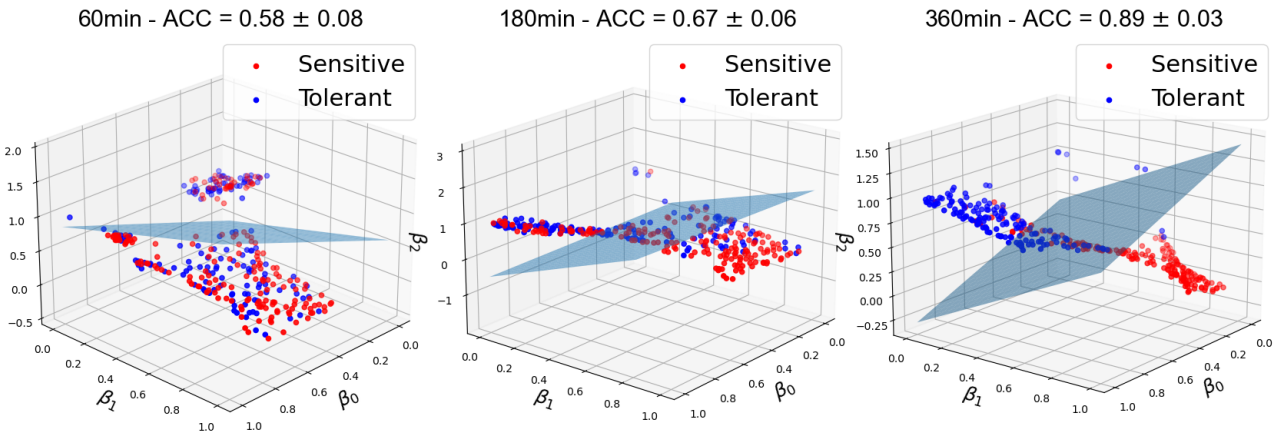

Figure 5.4: **Forecasting single-cell drug-response from FRETexp β parameter** according to the time when the time-trajectories were cut: Once again the threshold between tolerant and sensitive cells is obtained with an linear support vector classifier

crease the global accuracy of the SVC but, on the other side, it will not be possible to use this method to identify non-overlapping cells for which the drug response is obvious, as Roux et al. do with their methods. We then compute the mean accuracy after 5-fold cross-validation to asses the ability of our algorithm to forecast drug-response (see Appendix E.1 p.218 for a definition of the accuracy).

In [Roux et al., 2015], the authors obtained an accuracy of 0.83 ± 0.03 for the predictor using the FRET derivative value, and $0.72\% \pm 0.04$ using the two-dimensional landscape of τ and k, obtained with its 2-equations model of apoptosis, fitted on each FRET time-trajectory of single-cell treated with 25 ng/mL of TRAIL (see Equation (E.39) p. 225). Finally, as a comparison, a classic support vector classifier using directly each time point as feature, up to 6h of experiment, obtained a mean accuracy of 0.86 during a 5-fold cross validation and only predict cells that are not dead before 6H, as the others have NaN ((not-a-number) values in their time-trajectories that the model cannot handle.

At 6 hours, our algorithm performs better than both Roux's prediction methods, with an increase of 0.06 in the mean accuracy. It also outperforms the SVC classifier that uses directly the time-points as input features. A second positive point of the method is the handling of not-a-number (NaN) values for sensitive cells, that could be problematic for a machine learning model. With our method, we could successfully estimate all the features for all the cells.

On the other hand, before 6 hours, our method shows poor results. The accuracy at 1 hour is barely one point above the no-result line fixed at 0.57, corresponding to the proportion of tolerant

cells in the 25ng/mL of TRAIL dataset. At 3 hours, the accuracy is slightly improving, but not as fast as expected. Moreover, at 3 hours, 40% of the sensitive cells are already dead. Finally, at 1h, no non-overlapping zone exists yet, meaning that we cannot identify outliers cells for which the drug response is clear (see Chapter 6 p. 115). On the other hand, featurizing the signal with mechanistic parameters and use them as a proxy to cell decision, is en efficient method to include biological prior knowledge, but also to deal with the challenge of the different amount of data for each cell.

5.5 Discussion and parallel with Chapter 4

In this study, we presented a new ODE model of TRAIL-triggered extrinsic apoptosis initiation (EAICR) and used it to analyze the timeline of cell fate decision.
By studying the dynamic balance between the proteins involved in extrinsic apoptosis initiation, and the associated timeline for each cell, we **located an initial cell fate decision** just after TRAIL binding. In addition, this study leads to several approximations to obtain a **reduction of our model (rEAICR)** which can be solved explicitly for the caspase 8 and FRET early dynamics.

Due to this explicit solutions, the rEAICR model was next much more accurately fitted for all the isogenic cells in 4 datasets from the same study [Roux et al., 2015], varying TRAIL doses from 5 ng/mL to 50 ng/mL. The characteristic time distributions obtained from these data demonstrated that an **increase in TRAIL** has a more profound impact on the onset of cell commitment to apoptosis, but with **two different ways of changing the cell fate timeline depending on the sensitivity state of the cell**. The different ways in which tolerant and sensitive cells evolve, when the dose of TRAIL varies, are caused by distinct model parameter distribution changes: tolerant cells are characterized by an increase in their degradation rate and $C8_0$, while the sensitive population is more affected in terms of the initial amount of $pC8$. Overall, we show that **increasing TRAIL dose amplifies the gap between tolerant and sensitive cells** as reflected in the boxplots of Figure 5.2.

Like in Chapter 4, the crucial roles of the DISC complex and the caspase 8 degradation and activation rates are once again observed. Refining our model allowed a deeper study of the role of feedback loops in cell decision. The parameter distribution of the EAICR model clearly shows that the feedback loop from the DISC on the complex TRAIL:Receptor is determinant in sensitive cells, a point missed by the previous EAIC models. On the other hand, the EAICR model did not identify the feedback loop from the effector caspase to caspase 8 as important, contrary to the EAIC and Albeck et al models [Albeck et al., 2008a]. Further investigation will be needed to better understand the role of this special feedback loop with a more detailed model of the extrinsic

apoptosis signaling pathway downstream.

Finally, distribution of the parameters associated to the approximated solution of the reduced EAICR model helps deciphering the effects of C8 dynamic on cell decision, and suggests a **potential procedure for predicting (and potentially controlling) drug response for any drug dose**. By integrating these parameters estimated at 6 hours in a support vector classifier pipeline, we show that our method outperforms the thresholds used by Roux et al. in [Roux et al., 2015]. In contrast, the accuracy of our forecaster is very low before 6 hours and does not allow identification of outlier cells for which the drug-response is obvious, contrary to the method in [MP1, Meyer et al., 2020] (see Chapter 6).

The following parts first describes in detail the method used in [MP1, Meyer et al., 2020] and evaluates its performances on Roux et al. datasets before comparing their approach with the one proposed in this Chapter 5 and others classification methods.

PART III

Hybrid models to forecast cell drug response

In this part, I propose the first comparison study of diverse classification methods to forecast, in a short time, the cellular response to a specific drug (here TRAIL), from a unique signal (FRET or CFP/YFP), that reflects a specific signaling pathway (extrinsic apoptosis), obtained by live-cell microscopy. This classification will allow to sort cells according to their predicted drug-response to perform a profiling study, comparing the two cell decisions, while preserving the cell state from any drug effect. The goal is to upscale the FATE-SEQ pipeline and give an answer to:

How to forecast apoptosis triggered by TRAIL, for a maximum of cells of an isogenic tumoral population, before cell state changes in response to the drug, in a live cell microscopy assay ?

Therefore, Part III combines the conclusions of Part II and Part I with machine learning techniques to create a **forecasting pipeline of cell drug-response**. This workflow must be able to **accurately forecast single-cell fate decision before one hour of experiment from fluorescent time-trajectories** obtained during live-cell microscopy assays. This forecaster will be integrated in the FATE-SEQ pipeline of the team presented in Chapter 2. Finally, parameters estimations and how we can deduce useful information from sparse and noisy data will be at the center of the Part III. This part is composed of three chapters.

Chapter 6 evaluates the performance of the current method used to select cells for isolation in the FATE-SEQ pipeline, when the method is applied to the datasets of Roux et al. to create a comparison basis, but also describes the challenges tackled in the two following chapters.

Chapter 7 presents my first attempts to forecast cell decision for all the cells before 1 hour of experiment, to preserve cell state from the impact of TRAIL, using the state-of-the-art of machine learning models for time-series classification. Hence, this chapter is dedicated to the comparison of classic machine-learning classifiers, in combination, or not, with our new forecaster from the Chapter 5. This benchmark chapter is a first step toward the early forecasting of single-cell drug-response in live-cell microscopy and it evaluates the challenges of forecasting cell response in one hour. The conclusions of this chapter are rather pessimist, and forecasting cell-decision for all cells before one hour of experiment is not possible with the high accuracy required for the FATE-SEQ pipeline.

Facing the low accuracy problem, in Chapter 8, I propose different methods to remove unpredictable cells, and increase the accuracy of the forecasting. This chapter also presents the final pipeline that will be integrated in FATE-SEQ.

CHAPTER 6

Cell selection for isolation in FATE-SEQ

As an introduction to this part dedicated to the forecasting of single-cell drug response, I dedicate a small chapter to the challenges raised by the drug-response forecasting step in the FATE-SEQ pipeline, and the current method we are using in the lab.

6.1 FATE-SEQ constraints

In Chapter 3, we have seen that to increase the throughput of FATE-SEQ, we need to overcome experimental limitations. With our new custom setup (combining a live-cell microscope to a laser-capture micro-dissection device), we will be able to isolate 100 cells at the same time, **only if** we can **accurately forecast** their response to drugs.

With this new setup, fluorescent signal is obtained using the ratio CFP over YFP, and not the ratio CFP / FRET anymore. We will also have access to other types of time-trajectories such as the position of the cells over time, the entropy of the phase contrast signal, or the evolution of their size. At the moment, we do not have these time trajectories to be obtained with the new setup. Although we have access to the fluorescence time trajectories of HeLa cells obtained with the CFP/YFP ratio from Meyer's study [Meyer et al., 2020], the dataset is very small (less than 200 cells in total for only two doses of TRAIL, both above the IC50, the 4 replicates combined). A part of this dataset is presented in Appendix A, p.191.

Due to these current limitations, we will start by using the two datasets from [Roux et al., 2015] to conduct our experiments *in silico* - the preprocessed time-trajectories like in Part II (Table A.3) and the initial ratio 1/FRET time-trajectories dataset (see Table A.3 p.193 for the preprocessing techniques applied. These datasets contain the single-cell IC50-dose responses for several replicates, for more than 200 cells per replicate. Other features like the cell size changes over time, their migration, or the entropy of the wide field image will not be used.

In addition to these temporary obstacles, FATE-SEQ protocol has its own **constraints to obtain the innate molecular profile of drug efficacy, not a drug-induced state**. As a reminder, FATE-SEQ aims at studying the innate drug-tolerant state of the cells (which leads to the first emergence of drug-tolerant persisters in a clonal population), not an acquired tolerance. To preserve this initial cell state from the drug impact, we need to forecast cell drug-response, **before 2 hours** of treatment. At 2 hours, the authors of [Meyer et al., 2020] showed that TRAIL begins to impact on genes and their transcriptional levels. Finally, as we will compare the profiles between the forecast sensitive and the forecast tolerant cells, and because this **comparison** is crucial to identify biomarkers and therapeutic targets, we need to reach a very high accuracy (over 90%) for the forecasting. In our case, **a high accuracy is more important than the number of cells isolated**.

Finally, as the final algorithm will be integrated in a bigger pipeline of image processing for live-cell microscopy implemented in **Python**, we have chosen Python as programming language too, for consistency. The previous methods performed on Matlab ([Roux et al., 2015]), are also translated into Python and the actual algorithms used in FATE-SEQ are already available on github.

Nevertheless, this translation into Python brought small modifications of the algorithm and the functions used (see once again Table A.3 p.193).

6.2 Measuring the performances of the current selection method in FATE-SEQ

6.2.1 Selecting outliers cells for isolation and the principle of non-overlapping

To forecast cell-drug response in FATE-SEQ assays, Meyer et al. used the forecasting method presented in [Roux et al., 2015]. This method is based on the **identification of outliers cells**. We define outliers as cells for which the value of a certain feature is significantly different from the values of the rest of the cells. To identify these cells, we use the **principle of non-overlap**: sensitive outliers have values that none of the tolerant cells can reach (and vice-versa). In FATE-SEQ, this feature is the slope of FRET time-trajectory.

In [Meyer et al., 2020], the authors first pre-processed the data (see Table A.3 p.193), then computed the FRET time-trajectory derivative for each cell on Matlab, between 35 and 50 min of experiment. Finally, the **FRET slope** is obtained by taking the mean derivative value:

$$\mathcal{S}_{\text{cell}} = \underset{\tau \in [35,50\text{min}]}{\text{mean}} \left(\frac{dFRET_{\text{cell}}}{dt}(\tau) \right) \tag{6.1}$$

The 50 min time point was selected because it is the first time when sustainable outliers in slope values, for both tolerant and sensitive cells, were found in several replicates.More precisely, they chose this specific time slot to have more than 4 outlier cells for each phenotype in each replicate, to be larger than the isolation capacity, while preserving the inner cell state from the drug effects. Then, the slope values are ranked, and the first four cells with the highest values (corresponding to sensitive outliers) are isolated. The same way, the first four cells with the lowest values, corresponding to early non-responding cells, were also selected for isolation.

Before isolating these cells, a double checking of the time-trajectories is done by the engineer, looking at the FRET signal, to confirm that the dynamic observed corresponds to an outlier cell. The other cells rest unpredicted. This method ensured that the 8 isolated cells (corresponding to the **maximum number of cells** that could be isolated with the microscope during Meyer et al. experiment), were predicted with a high precision and accuracy, but a lot of cells remained unpredicted, and could not be sequenced.

6.2.2 On the evaluation of the forecasting method performances

Comparing the performances of this technique with the classic machine learning classification approach is challenging, as a classification model will forecast every cell, so the performance metrics will be computed on the entire dataset. In addition, this comparison is also irrelevant: our new setup (Chapter 3) is still constraining us to isolate only 100 hundred cells at the time. Hence there is no need to forecast every cell on the frame slide.

Hence, in Chapter 7, we will use classic performance metrics that will be presented in the method section, to evaluate if we can forecast cell drug-response for all cells simultaneously, and if yes, with which accuracy. On the other hand, we will present in Chapter 8 several methods to increase the number of cells predicted for isolation, but **conserving the same performances as the method currently used** in our pipeline. One of the main challenges will be to assess the maximum number of cells we could select for isolation, while keeping a high accuracy. The challenge here is to find finer features, with a stable number of outliers cells across replicates, larger than the derivative criteria, and to determine the number of outliers we can isolate with confidence, for each phenotype in future experiments.

Therefore, we still need to evaluate the current method, and compare it with the ones we will present in Chapter 8, but in the same experimental conditions. To do so, but also to be as close as possible to the new FATE-SEQ pipeline, we used the datasets from [Roux et al., 2015], combining the three replicates of clonal HeLa cells treated with 25ng/mL of TRAIL (TRAIL IC50), observed for 10 hours, with the ratio CFP/FRET recorded every 5 min. We compute the derivative of each cell time-trajectory in the interval between 0 and 50 min of experiment, by using the *gradient* function of the package numpy in python and take its mean value over the last 15 min, for each cell. Then, we evaluate different methods to select cells for isolation as we are not constrained to 8 cells anymore. We will repeat the same process on the initial data from [Roux et al., 2015], but also on two replicates of [Meyer et al., 2020], that use the ratio CFP/YFP not CFP/FRET, measured every 3 min, but contains time-trajectories for only 120 cells in the two replicates combined. The idea here is to evaluate the impact of the fluorescent techniques and the methods to preprocess these time-trajectories on the forecasting step but also to analyse how the heterogeneity across replicates could be helpful to forecast drug-response in a new experiment.

6.2.3 Method description

In [Meyer et al., 2020], the authors identified a recurring number of four cells for both sensitive and tolerant classes, across 2 replicates, by using a two-step method combining the determination of

two thresholds (one for each class), and the identification of a recurring number of cells overcoming this threshold.

1 - Determining the thresholds In detail, for each replicate i, Meyer et al define sensitive and tolerant thresholds ($\mathcal{T}_S^i$ and $\mathcal{T}_T^i$) on the FRET data slope, to identify cells for isolation as follows. Since for 6-hour long experiment, the maximum of the FRET derivative over time (called slope), for each cell, tended to be greater for sensitive cells, like demonstrated in [Roux et al., 2015], Meyer and al. defined the two thresholds this way:

$$\mathcal{T}_S^i = \max_{\text{cell in true tol. cells in rep. i}} \underbrace{\left(\underset{\tau \in [35,50\text{min}]}{\text{mean}} \left(\frac{dFRET_{\text{tol. cells}}}{dt}(\tau) \right) \right)}_{\text{Slope value for each tolerant cell}} \tag{6.2}$$

$$\mathcal{T}_T^i = \min_{\text{cell in true sen. cells in replicate i}} \left(\underset{\tau \in [35,50\text{min}]}{\text{mean}} \left(\frac{dFRET_{\text{cell}}}{dt}(\tau) \right) \right) \tag{6.3}$$

Hence, to be identified as non-overlapping sensitive, a cell in the replicate i has to verify:

$$\underset{\tau \in [35,50\text{min}]}{\text{mean}} \left(\frac{dFRET}{dt}(\tau) \right) \geq \mathcal{T}_S^i \tag{6.4}$$

and respectively, forecast non-overlapping tolerant cells satisfy:

$$\underset{\tau \in [35,50\text{min}]}{\text{mean}} \left(\frac{dFRET}{dt}(\tau) \right) \leq \mathcal{T}_T^i \tag{6.5}$$

2 - Identify a stable number of non-overlapping cells for isolation across multiple replicates To identify a recurring number of non-overlapping cells for each phenotype, for which their slope value does not overlap with any slope value obtained in the opposite phenotype population, Meyer et al. created 3 replicates (rep.) of the same experiment for 10 hours, to identify true tolerant (positives in machine learning terminology), and sensitive cells (resp. negatives). They then computed $\mathcal{T}_S^i$ and $\mathcal{T}_T^i$ for each replicate i, cutting the time-trajectories at 50 min, and counting the number of true tolerant cells verifying Equation (6.5): $\mathcal{N}_T^i$ (also called true positives - respectively $\mathcal{N}_S^i$ for the true sensitive cells (true negatives) and the Equation (6.4)). Finally, the recurring numbers of non-overlapping sensitive ($\mathcal{N}_S$), and tolerant ($\mathcal{N}_T$) cells are given by:

$$\mathcal{N}_S = \min_{i \in \text{rep.}} \mathcal{N}_S^i \tag{6.6}$$

$$\mathcal{N}_T = \min_{i \in \text{rep.}} \mathcal{N}_T^i \tag{6.7}$$

Once $\mathcal{N}_T$ and $\mathcal{N}_S$ are identified, during the 50 min-experiments cells are ranked according to their slope value. The $\mathcal{N}_S$ cells with the highest slope values are selected as sensitive for isolation, and the $\mathcal{N}_T$ cells with the lowest slope values are isolated as tolerant cells. The threshold is only used to determine $\mathcal{N}_T$ and $\mathcal{N}_S$, and not to identify cells for isolation. This way, the forecasting is adapted to each replicate, despite the high variability between them, illustrated in Figure 6.1 p.122, but also in Appendix D p.211, by the different ranges for the slope values across the replicates (between -0.05 and 0.15 in TRAIL_Roux_25_1, but only between 0.06 and -0.05 for the two others).

Figure 6.1 p.122 illustrates the method on Meyer et al. applied to 1/FRET dataset from Roux et al. article [Roux et al., 2015] with the three replicates, using the preprocessing techniques described below.

Preprocessing FRET signal choices The results presented here used time-trajectories filtered with a Savitsky-Golay (SG) filter of order 3 and a window of 9 frames, re-scaled by the FRET value in the first frame for each cell. This is the algorithm described in the STAR PROTOCOL [MP1], with a filter window larger though (5 frames in the STAR PROTOCOL). Meyer et al used the Matlab function *smooth*, or, in other terms, a moving average filter, with a window of 13, as they have 16 frames before 50 min (1 frame every 3 min) [Meyer et al., 2020]. The smooth function was also applied in [Roux et al., 2015] *. The choice of 9 frames was therefore a mid-term between the STAR PROTOCOL and Meyer et al. algorithms [Meyer et al., 2020, MP1]. Nevertheless, one must notice that a window of 5 does not allow to find a recurring number of non-overlapping cells for both drug-responses when a SG filter is used before the computation of the FRET slopes and the non-overlapping thresholds (see Appendix D.2 p.212). Here, we only present the results with a SG filter but the results obtained with the Moving Average filter are similar.

In Chapter 7, we will compare the Moving Average filter (the function *smooth* from MATLAB), with the SG filter and the two re-scaling methods, to see if the re-scaling or the smoothing have an impact on the accuracy of the drug-response forecasting when we use the initial 1/FRET time-trajectories. In the meantime, the boxplots of Figure D.15 compare the FRET slope value obtained with the two re-scaling methods on the 2 un-preprocessed datasets (initial 1/FRET from Roux et al. and CFP/YFP ratio from Meyer et al.), with a SG filter is applied with different windows lengths (5 frames and 13 frames), to see the effects of the re-scaling and filters on the FRET slope feature. Nevertheless, for the FRET slope feature only, the re-scaling has no effects as the derivative of a constant is always 0.

*only when the time-trajectories were shorter than 27 time-points for filter-window reasons. When the time-trajectories were longer, a 0-phase digital filter was applied with the MATLAB function *filtfilt*

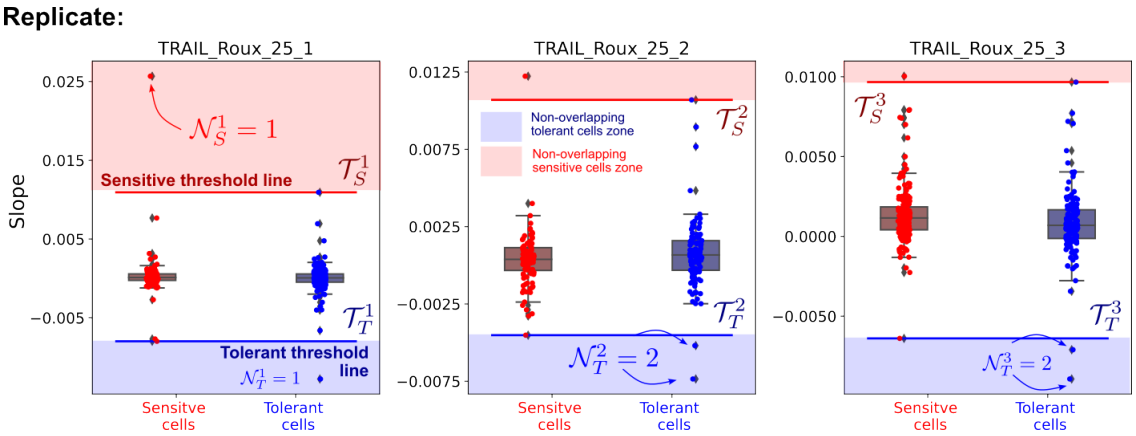

Figure 6.1: **Determine predictive thresholds for both sensitive ($\mathcal{T}_S^i$) and tolerant cells ($\mathcal{T}_T^i$) in each replicate i, to identify a recurring number of non-overlapping cells ($\mathcal{N}_S = 1$ and $\mathcal{N}_T = 2$) across the experiment replicates:** illustrated with the initial 1/FRET dataset from [Roux et al., 2015]. Each subplot represents the study carried for one replicate of the dataset. Each subplot represent the distribution boxplots of the slope value for each cell of the replicate according the real drug-response (Sensitive/Tolerant), the two non-overlapping cell zone (red for sensitive, blue for tolerant), the corresponding thresholds ($\mathcal{T}_S^i$ and ($\mathcal{T}_T^i$)) and the corresponding number of non-overlapping cells for each drug-response ($\mathcal{N}_S^i$ and $\mathcal{N}_T^i$)

In the example shown in Figure 6.1, for [Roux et al., 2015] initial 1/FRET dataset combining the 3 replicates, this method gives a 100% accuracy, but only identifies two tolerant and one sensitive cells for isolation, representing less than 1% of the replicate, in the best case.

6.2.4 Evaluate the performances

In Chapter 7 and Chapter 8, we will use only the datasets from [Roux et al., 2015]), which contains sufficient data for the application of machine learning models. So we will apply the forecasting method on these datasets from to allow a fair comparison.

Therefore, we will evaluate the performances of the method on our 3 different datasets: [Roux et al., 2015] - **initial FRET** (3 replicates), [Roux et al., 2015] - **FRET ratio** (3 replicates) and [Meyer et al., 2020] - **CFP/YFP ratio** (2 replicates), as the method was created using these two replicates. See Appendix A p.191 for the details of the datasets. Nevertheless, as the FRET ratio datasets were already preprocessed, we will just compute the derivative step for these cells. For each dataset, we determine $\mathcal{T}_T$, $\mathcal{T}_S$, $\mathcal{N}_T$ and $\mathcal{N}_S$.

To measure the method's performances, we carry a 3-fold cross validation (resp. 2), by using two replicates (resp. 1) as training set, and the last one for the testing part, each replicate being once the testing set. This way, we could reproduce the actual experimental setup where the final drug response is unknown at 50 minutes for the testing replicate, and $\mathcal{T}$ and $\mathcal{N}$ are computed on the 2 (resp. 1) 10-hours experiment replicates, using the time-trajectories cut at 50 min but knowing each

cell drug-response. Similarly, we carry a 5-fold cross-validation on the 3 replicates concatenated (resp. 2), and divided in 5 subsets training/testing, keeping the same balance tolerant/sensitive in each set. The results of the 3 and 5-fold cross validation for FRET ratio from Roux et al. and the CFP/YFP from Meyer et al. datasets can be found in Appendix D.3, p.213, along with the 5-fold cross-validation for initial FRET.

Eventually, we will compare three different methods to isolate cells:

i) **Overcoming threshold:** $\mathcal{T}_S$ and $\mathcal{T}_T$ are determined from the training set (on the two replicates combined), and then cells verifying Equation (6.4) (resp. Equation (6.5)) are selected in the testing set. This method assesses the necessity of using the ranking step.

ii) **Ranking method with 4 cells for each class (T/S) isolated:** as done in [Meyer et al., 2020], this method consists in selecting the seven cells with the greatest slope values and identifies them as potentially sensitive (resp. lowest values for potentially tolerant), then plotting all the single-cell trajectories of these 7 cells in red (for potentially sensitive, resp. blue for tolerant), and the biologist selects himself 4 forecast sensitive cells among the 7 cells, for isolation (idem for tolerant). Ideally we want to automate the process as much as possible, so we will select the 4th first and last cells directly, without user input. This method reproduces the complete protocol (un-adapted) of [Meyer et al., 2020]. As $\mathcal{N}_S$ and $\mathcal{N}_T$ are always lower than 4, it also evaluates whether more cells can be isolated and the accuracy lost by doing so.

iii) **Ranking method with the isolation of the same number of cells predicted during training with threshold:** In this case, we only use the training replicates to determine $\mathcal{N}_T^{\text{train}}$ and $\mathcal{N}_S^{\text{test}}$. This method reproduces the actual experimental conditions when the testing set is unknown and $\mathcal{N}$ is not calculated on the testing set (similar to a K-fold cross validation in machine learning terminology).

For the 3 methods, we will compute the accuracy, the proportion of cells predicted, precising the number of tolerant and sensitive cells isolated. See also Appendix E.1 p. 218 for a definition of accuracy. When none of cells is predicted, we choose to exclude the testing set of the K-fold cross-validation and attribute a NaN for accuracy.

The following table summarizes the results obtained for the initial 1/FRET ratio from [Roux et al., 2015]:

Testing set	TRAIL_Roux_25_1	TRAIL_Roux_25_2	TRAIL_Roux_25_3	mean	std
Dataset description					
N cells in testing	344	221	327	297.333	54.42
% tol. cell. in test	72.674	51.131	45.872	56.559	11.596
% tol. cell. in train	47.993	59.613	64.248	57.284	6.837
Method application					
$\mathcal{N}_T$	1	1	1	1.0	0.0
$\mathcal{N}_S$	1	1	1	1.0	0.0
% of cell represented by $\mathcal{N}_T$ and $\mathcal{N}_S$ in test	0.581	0.905	0.612	0.699	0.146
$\mathcal{N}_T^{\text{train}}$	2	1	1	1.333	0.471
$\mathcal{N}_S^{\text{train}}$	1	1	1	1.0	0.0
$\mathcal{T}_T^{\text{train}}$	-0.006	-0.008	-0.008	-0.007	0.001
$\mathcal{T}_S^{\text{train}}$	0.011	0.011	0.011	0.011	0.0
$\mathcal{N}_T^{\text{test}}$	1	2	2	1.667	0.471
$\mathcal{N}_S^{\text{test}}$	1	1	1	1.0	0.0
i) Overcoming threshold method					
i - ACC on test	0.5	0.0	1.0	0.5	0.408
i - % of cell pred. for iso. in test	1.744	0.452	0.306	0.834	0.646
i - # cell pred. tol. for iso. in test	4	0	1	1.667	1.7
i - # cell pred. sen. for iso. in test	2	1	0	1.0	0.816
ii) Ranking method with 4 cells for each class					
ii - ACC on test	0.5	0.375	0.75	0.542	0.156
ii - % of cell pred. for iso. in test	2.326	3.62	2.446	2.797	0.584
iii) Ranking with $\mathcal{N}_T^{\text{train}}$ and $\mathcal{N}_S^{\text{train}}$					
iii - ACC on test	0.667	1.0	1.0	0.889	0.157
iii - % of cell pred. for iso. in test	0.872	0.905	0.612	0.796	0.131

Table 6.1: Dataset description and performances of the current FATE-SEQ drug-response forecasting method used to select non-overlapping cells for isolation during 3-fold cross-validation on initial 1/ FRET dataset (Roux et al.) - tol. : tolerant, sen.: sensitive, pred. predicted, iso.: isolation, std: standard deviation

6.2.5 Results

Table 6.1 shows that the 2-step method used by Meyer et al. clearly outperforms its two other variations, with an accuracy of 1 for the two last replicates. The poor results of the threshold method could be explained by the heterogeneity across the replicates that impacts the FRET slope values and prevents the use of the same threshold in all the replicates. One solution to use this technique would be to rescale the FRET values by the maximum of the FRET values of all cells for each replicate to have similar values in all replicates. Finally, selecting more cells than $\mathcal{N}_T^{\text{train}}$ and $\mathcal{N}_S^{\text{train}}$, in order to increase the number of cells profiled, did not improve the method.

Figure D.17 p.212 - representing the slope values of the initial 1/FRET for each replicate from [Roux et al., 2015], filtered with a SG filter with a window of 5 frames - but also the results on the twice smoothed CFP/FRET dataset (Table D.15 p.214), demonstrates how important the filter window is, and how it impacts the slope values and *in fine* the accuracy of the forecasting. This importance is also observable in the results for the CFP/YFP datasets from [Meyer et al., 2020], where the method is not able to identify a single cell. The tables of the results for the 2 replicates from Meyer et al (Table D.14 p.213), along with the figures representing the associating 2-fold cross-validation (Figure D.16 p.212 for different size of filter windows and Figure D.17 p.212) confirm the need to better choose the preprocessing of the initial time-trajectories before slope computation.

Finally, the results for the 5-fold cross-validation (Table D.17 p.216, Table D.16 p.215, Table D.18 p.217) are similar for the three datasets, $\mathcal{N}_T$ and $\mathcal{N}_S$ are equal to 0. However, in this case selecting 4 cells or using the threshold alone yields to a better performance than during the 3-fold cross validation, even though their mean accuracy is still below 0.7 in the best cases.

One alternative that could increase the numbers of cells isolated without lowering too much the accuracy will be to fix $\mathcal{N}_T$ (resp. $\mathcal{N}_S$) as the mean of $\mathcal{N}_T^{\text{train}_i}$, rounded up to the superior whole number, i being the number of the replicates in training. In our case, not using the minimum would have lead to $\mathcal{N}_T = 2$, instead of 1, while keeping the same mean accuracy of 0.889 (see iii in the table).

Finally, using slope value leads to $\mathcal{N}_S^{\text{train}} = 1$ in all cases, suggesting that it could be interesting to have a larger pool of outliers from which to select sensitive cells for isolation, perhaps using another feature for the selection of sensitive cells.

6.2.6 On the importance of the balance tolerant/sensitive cells in experimental replicates

Figure 6.1 p. 122 shows a large difference between the FRET slopes values obtained for cells from the replicate TRAIL_Roux_25_1 and the values for cells from the two other replicates. Interestingly, TRAIL_Roux_25_1 is also the replicate with the biggest proportion of tolerant cells (73% for only 51% and 46% in the two other replicates). These differences result in a lower accuracy obtained with iii) ranking method, and even poorer results for the two other selection techniques.

These disparities between the replicates are indicative of a **significant difference in the overall population dynamics** of the TRAIL_Roux_25_1 replicate, compared to the two others. TRAIL_Roux_25_1's singularity is reflected by different dynamics observed at the single-cell

level, imperceptible by simply looking at the curves, but reflected by the wider range of slope values.

Lot of parameters could explain these differences: a small variation in the drug dose, a delay in the drug input or an accidental exposure to ambient light during image acquisition for instance. Deciphering if these disparities led to a different balance between tolerant and sensitive cells in this replicate or whether they were an actual consequence of this unbalance is a question out of the scope of this work but it has serious consequences on the experimental results, especially when the objective of the experiment is to determine the IC50 of the drug and more generally to evaluate the cytotoxic effects of the drug, measured by the amount of tolerant cells at the end of the experiment. In our case, it also results in a less accurate forecasting of the cell's drug response.

In Chapter 7, which is a benchmarking chapter to evaluate the ability of machine-learning models to forecast drug-response, we will combine our three replicates and use training and testing sets with the same balance drug-tolerant/drug-sensitive to evaluates our methods. In Chapter 8, we will reproduce the actual experimental conditions and therefore, we will not merge our replicates into one dataset but train our models on a replicate and carry the testing on another, conserving their original balance. Nevertheless, TRAIL_Roux_25_1 is significantly different from the two other replicates and hence will not be included in our study.

6.3 Conclusions

In this chapter, we evaluate the performances of the FATE-SEQ method to select cells for isolation, put in place in Meyer et al. article [Meyer et al., 2020], on all the datasets we will be using in the following chapters. This method is based on the identification of a recurring number of outliers cells, regarding their value for the FRET slope before 50 min of experiment, thanks to specific thresholds for each drug-response (sensitive/tolerant).

Two main adaptations of the method were necessary to take into account our current constraints in the lab. The first one is due to the translation of the codes from MATLAB to Python, for compatibility needs between algorithms developed in the lab. The second lies in the fact that the ratios CFP/FRET, 1/FRET and CFP/YFP have their own subtle specificities. However, we still applied the same method to compute the slope for all the datasets, without a preliminary selection of the most suitable method to compute the slope or preprocess the datasets before.

Regarding the larger number of cells isolated by Meyer et al. but also our results using different filters and filter windows, the decisive parameter in the preprocessing step is the time window selected, and not the type of filter, even though in the case of Meyer et al, the performances scores

on an unknown testing set were not given.

Applying the adapted method on our three datasets showed really poor results both in terms of accuracy, or regarding the number of cells isolated. These dramatic performances strongly motivate the need to improve the method to select cells for isolation by considering finer features than the slope but maybe also to reconsider the choice to identify only non-overlapping cells. Nevertheless, this study was just a first evaluation of the method performances and some limitations must be considered.

Limitations A part of this study was done on FRET signals preprocessed by Roux et al on Matlab. The first step of the preprocessing of these time-trajectories consisted in removing the mean untreated cell to the FRET ratio for each cell. In our new experimental setup, such control experiments carried at the same time than the drug experiment will not be possible on a slide frame. Similarly, in the following, we will use the same preprocessed FRET signals from [Roux et al., 2015], that have been filtered twice with the MATLAB function *filtfilt*. However, some methods (Fourier transform, statistic models,etc) tested in the following performed better on noisy data and take advantage of the noise. To overcome this limitation, we will also use the second type of time-trajectory data of [Roux et al., 2015], obtained from the same experiments, containing only the initial ratio 1/FRET (not CFP/FRET), but not smoothed and not re-scaled by the mean untreated cells. Moreover, in the future setup, we will be using the ratio CFP/YFP instead of CFP/FRET anymore. The only datasets using CFP/YFP are from [Meyer et al., 2020], with only 121 cells tracked, not enough to use machine learning approaches. Hence, these datasets will not be used in the following chapter. Finally, our pipeline will be on Python, to be included in the complete image processing software, so we will not use the same function *smooth* for noise removing, instead a Savitsky-Golay filter of order 3 with a window of 5 will be preferred.

In summary, the conclusions of our tests presented in this part will be valuable for a 96-well plate experiment, using smoothed CFP/FRET ratio, or directly the initial 1/FRET ratio, but the methods implemented will still be useful for us to benchmark the techniques, and speed-up the isolation for selection step in the future. Eventually, the tests carried in Chapter 7 and Chapter 8 will be further improved as new and more complete data becomes available.

Goals and outline of part III

This evaluation of the method used to select cells for isolation in the FATE-SEQ pipeline raised a lot of questions and highlighted several limitations of the process. Hence, in the two following chapters, we will tackle the following questions:

- Can we forecast cell drug response as early as 50 minutes after drug addition for all cells? (Chapter 7)
- How do pre-processing techniques affect cell fate prediction accuracy? (Chapters 7 and 8)
- How and when can we extract pertinent information about cell decision from the fluorescent signal? (Chapter 7)
- How can we forecast fluorescent time-trajectories? and how many hours of experimental data do we need to have a good forecasting ? (Chapter 7)
- Is forecasting the fluorescent signal pertinent to improve the accuracy of the cell fate prediction? (Chapter 7)
- How can we know if a cell is unpredictable or not? (Chapter 8)
- How can we integrate a cell fate prediction step in FATE-SEQ pipeline? (Chapter 8)
- What is the maximum number of cells we can accurately forecast recurrently in all replicates, and how can we determine this number? (Chapter 8)

CHAPTER 7

Coupling a mechanistic transformer with machine learning classifiers predicts cancer drug responses but does not forecast them accurately

*In the last decades, machine-learning models showed strong abilities to accurately forecast time-series on highly heterogeneous types of data. This chapter will present the performances of the **classic machine-learning approaches** (classic models [Greener et al., 2022] and algorithms specifically dedicated to time-series classification [Dempster et al., 2020, Middlehurst et al., 2021]) on forecasting drug-response from short FRET time-trajectories, but also their combination with new ways to featurize the FRET signal or forecast it. In contrast to the methods presented in the previous chapter **that only forecast drug-responses for a couple of cells** (Chapter 6 p.115), the methods evaluated in the following will forecast drug-response for every cell of the experiment. One of the goals here is to measure how much accuracy we are losing when the number of cells isolated increases drastically (from less than 1% to 100%) and to asses if this loss is reasonably small such that we could use the method in the FATE-SEQ pipeline. This chapter will allow us to create a library of tools to forecast cell drug-responses, using machine-learning models, but also bring new insights on the FRET signal.*

Therefore, we will benchmark a large part of the methods available to determine if all cell's drug-response can be forecast within one hour of experiment. During this comparison study, we will determine which signal is more informative (CFP/FRET or 1/FRET), how the choice of the pre-processing impacts the forecasting, which period of time is the most useful to identify the future drug-response, and what type of features captures the best all the information contained in the signal to forecast cell drug response.

To study the models' performances, we will use the datasets from [Roux et al., 2015] composed of the three replicates of HeLa cells treated with 25ng/mL of TRAIL. Roux et al. used Föster-Resonance-Energy-Transfert (FRET) and preprocessed the time-trajectories (Appendix A) but the initial 1/FRET time-trajectories are available too. Therefore I will use both types of time-trajectories to evaluate our models.

A part of the following work has be done during a research visit at the school of Informatics of the University of Edinburgh, in the bio-molecular control group of Diego Oyarzun.

7.1 Methods

7.1.1 Performance metrics

Our aim is to forecast cell drug-response from the FRET time-trajectories before 1h of experiment. In other words, using short time series data from fluorescent live-cell microscopy experiments, we aim at classifying cells into two different classes defining their future phenotype: emergent drug-tolerant persisters and sensitive cells. Drug dose used is the IC50 so the datasets obtained will be unbalanced with more tolerant cells. However, both tolerant and sensitive classes have the same importance for us, and therefore should be predicted with the same precision (see Appendix E.1 p.218 for performance metric descriptions). Hence, we will compute the classic performance metrics: accuracy, balanced accuracy, recall, precision and F1 but also the Markedness (MK) and the Matthews correlation coefficient (MCC). Moreover, we will use MCC to select the best machine learning model (ML model in the following). All the scores will be between 0 and 1, except for the MCC (between 1 and -1), with 1 as the best score.

MCC is defined as:

$$MCC = \sqrt{TPR \times TNR \times PPV \times NPV} - \sqrt{FNR \times FPR \times FOR \times FDR} \tag{7.1}$$

with TPR: true positive rate (or recall), TNR: true negative rate, PPV positive predicted value (precision), NPV: negative predicted value, FNR: false negative rate, FPR: false positive rate, FOR: False omission rate, FDR: False discovery rate.

Markedness is defined as the sum of the precision obtained for the tolerant class (or Positive predictive value PPV) and the precision obtained for the sensitive class (Negative predictive value NPV) minus 1 so the score will be between 0 and 1:

$$MK = \frac{TP}{PP} + \frac{TN}{PN} - 1. \tag{7.2}$$

Both coefficients, MK and MCC, provide a good measure of the precision for both tolerant and sensitive classes. However, previous works have shown that MCC is a better score for model selection, especially for almost balanced datasets and classification tasks [Chicco et al., 2021, Powers, 2020]. In our case, 57% of cells are tolerant and 43% are sensisitive, thus we use MCC.

7.1.2 Datasets

We use both datasets from [Roux et al., 2015]. The CFP/FRET preprocessed as in the article, and the initial 1/FRET signal with different filters from [Meyer et al., 2020, MP1].

7.1.3 Programming

Python is the programming language here for compatibility reasons with the others algorithms developed in our lab. ClassicML classifiers were coded using **scikit-learn** library [Pedregosa et al., 2011]. ML models for time-series classification (TSC) were implemented with **sktime** [Löning and Király, 2020]. Parameter estimation for time-series statistic models [Hyndman and Athanasopoulos, 2018] were done with **statsmodels** library [Seabold and Perktold, 2010]. Feature computation, time-series forecasting andML model training steps were parallelized using **joblib** [Team, 2020]. Explicit solution of deterministic models were fitted using **lmfit** package with a weight of 10 on the last 5 frames and a Nelder-Mead algorithm as minimisation method for short time-trajectories (less than an hour), and with the weights described in Section 4.2.2 p.82 for longer signals.

We compare different types of machine-learning models for classification tasks: a Constant Classifier (CC) for comparison basis (that classifies every cell as tolerant), tree-based models (Decision Tree (DT), Random Forest (RF), Gradient Boosting (GB), AdaBoost (AB)), Support Vector machine Classifier (SVC) with a Radial Basis Function (RBF) kernel, Deep-learning (Multi-Layers Perceptron (MLP)), a Ridge Classifier (RC) and Nearest-Neighbors (NN) type (1-NN and 5-NN). See [Hastie et al., 2009] for the description of the models'algorithms. In the following, when we use these models without specifying the features used as input, we will use each FRET time-point is an input feature in the classifier.

Several models have been designed to take into account the temporal link between measurements and are specially dedicated to time-series classification (TSC) [Löning and Király, 2020, Faouzi, 2022], with some of them promising amazing results, like the ROCKET model [Dempster et al., 2020]. Hence, we also evaluate 8 of them, all consisting in combining features extracted from the time-trajectories with a ML classifier. The following list summarizes the features used in each of the TSC models (in bold) to compare with our features from Chapter 5 and the features of Roux et al. (see Figure 2.5 p.53 and Equation (E.39) p.225):

- **Shapelet Transform Classifier (Shapelet)** [Hills et al., 2014] combines a Shapelet transformer that finds similarities in time-series sub-sequences, with a rotation forest classifier. See sktime website to have a graphic explanation of the shapelet principle.
- **KNN** is, in this case, a one-nearest neighbour (1-NN) classifier coupled with with Dynamic Time Warping (DTW). A DTW model aims to align time-trajectories by stretching, shifting or contracting them.

- **RISE** (Random Interval Spectral Ensemble) [Flynn et al., 2019] is a tree-based time-series classifier. Each tree uses a different set of features based on power spectrum (Fourier), autocorrelation and partial autocorrelation, and auto-regressive (AR) model coefficients.

- **ShapeDTW** [Zhao and Itti, 2018], transforms an univariate time-series in a multivariate one, then applies a DTW (dynamic time wrapping) algorithm.

- **TSF** (Time series Forest Classifier) [Deng et al., 2013], is a tree-based method, exactly like the classic Random Forest, but uses a combination of an entropy gain and a distance measure to evaluate the splitting (the classic random forest uses the entropy or the gini criteria). The features are the mean, standard deviation and slope computed on random interval in the time-series in the *sktime* implementation.

- **Arsenal** is an ensemble of ROCKET classifiers. A **ROCKET classifier**[Dempster et al., 2020] couples a ROCKET (RandOm Convolutional KErnel Transform) transformer to extract new features, combined with a Ridge Classifier (aML model that makes a regression to determine the the binary targets).

- **DrCIF** (Diverse Representation Canonical Interval Forest Classifier) is an extension of the Canonical Interval Forest (CIF) that uses the multiple representations methods presented in the HIVE-COTE article [Middlehurst et al., 2021] (contrary to CIF that use only one representation). Regarding the CIF [Middlehurst et al., 2020], it combines a TSF and the featurization method **catch22** (22 CAnonical Time-series CHaracteristics) that extracts 22 features from the time-series) [Lubba et al., 2019], these 22 features were obtained applying a feature selection pipeline on the 4791 features from the *hctsa* "bank" of features [Fulcher et al., 2013],

- **HIVE-COTE-2** (Hierarchical Vote Collective of Transformation-based Ensembles) that is an ensemble of classifiers (BOSS, Shapelet, DrCIF, Arsenal, etc) (H.V.-C. V2) [Middlehurst et al., 2021], a BOSS classifier(Bag-Of- Symbolic Fourier approximation-Symbols [Schäfer, 2015], is a dictionary-based method, which uses a representation of the frequency of the patterns repetition in time series.

All these time-series classification (TSC) models were previously evaluated on the same datasets, the UEA and UCR Time Series Classification Repository [Bagnall et al., 2017, Chen et al., 2015], a database that includes ECG, images or sensors data but not FRET signals.

Some ML models can be very sensitive to distance in the feature space. Therefore, for each classifier, we have tested 14 different rescaling methods from the **sklearn library**: no preprocessing, Principal Component Analysis (PCA), Standard (Stand.), MaxAbs, MinMax,Robust (Rob.), Quantile Uniform (Quant. Unif.), Power Gaussian (Pow. Gaus.) and the combination of the PCA

with each of the other scaling methods (see sklearn documentation for more details). For each model, we will give the best preprocessing scaler found according to the score of interest, along with the best ML model. These pre-processing techniques are applied transversely, on each feature across all cells, whereas our filters and re-scaling are applied longitudinally (along the time axis for each cell). For the time-series dedicated classifiers (TSC in the following), no PCA or re-scaling techniques from the sklearn library will be used to keep the correlations and temporal links between the time-points.

For each machine-learning and dataset tested, we carry a stratified 5-fold cross validation, meaning that testing and training have the same balance 57% of tolerant - 43% of sensitive cells, but no hyperparametrization or feature selection are performed. To evaluate the performance of the classifiers during the cross-validation, we use the following scores: MK, MCC, accuracy, F1, Precision, Recall and balanced accuracy but we select the couple model/ scaling technique with the highest MCC as discussed in Section 7.1.1 p.131.

7.2 Signal featurization

In this section, we compare two types of ML classifiers (classic or TSC), along using different types of methods to preprocess the FRET signal. This will provide a comparison basis, as Roux et al. never tried to forecast the fate of each cell at 50 min due to the small isolation capacity constraint (see Chapter 6 for more details about FATE-SEQ constraints).

7.2.1 Signal preprocessing

The three articles of Roux lab applied different filters to remove noise in time-trajectories: **0-phase digital filter** for 10h-long time-trajectories, or **Moving Average** filter for shorter ones for Roux et al. [Roux et al., 2015], Moving Average for Meyer et al. [Meyer et al., 2020], or **Savitzky-Golay filter** for Bian et al. [MP1]). Here, we use only the datasets from [Roux et al., 2015] and apply the different rescaling techniques and filters on the initial 1/FRET dataset, to assess information contained in the noise recorded in the time-trajectories, and how re-scaling and filtering affects the forecasting of cell drug-response. We will compare these results with the performances obtained on the CFP/FRET already preprocessed from the same experiment. The following list summarizes the pre-processing techniques and Figure 7.1 p.136 reproduces the time-trajectories obtained after filtering for a sensitive and a tolerant cell:

1. Initial 1/FRET time-trajectories: **1/FRET**

2. Initial 1/FRET filtered once with a Savitzky-Golay filter with a 5-frames window + normalized by the FRET value on the first frame as in [MP1]): **1/FRET - 5 fw - SG**

3. Initial 1/FRET filtered with a Savitzky-Golay filter with a 9-frames window + normalized by minimum of FRET values during the first 50 min of experiment, a trade-off between [Roux et al., 2015] and [Meyer et al., 2020]), using a filter and not a smoothing algorithm: **1/FRET - 9 fw - SG**

4. Initial 1/ FRET, smoothed with a moving average filter with a 9-frames window and normalized by minimum of FRET values during the first 50 min of experiment, an adaptation of [Roux et al., 2015] without removing the mean untreated cell as it will not be available in the new set-up: **1/FRET - MA**

5. CFP/FRET ratios preprocessed with Matlab (FRET ratio) from [Roux et al., 2015] (mean untreated cell subtracted, filtered twice with a window of 11 with the MATLAB function *filtfilt* (zero-phase digital filtering), re-scaled by the minimum of FRET during the first 50 min of experiment [*]) : **CFP/FRET ratio**

   In addition, as the drug-response forecasting has a time constraint (before two hours such that the drug does not impact the initial cell state), we carry the same study at 2h to see if this additional hour - when TRAIL starts impacting the innate state - is informative or not, and at 6h to compare with the results obtained in Chapter 5. The results, when accuracy is chosen as the selection score, are available in Appendix E.2 p.219. Finally, one must notices that at 30 min, the **1/FRET - 9 fw - SG** is actually a **1/FRET - 5 fw - SG**, because the time-trajectories are too short (only 6 frames), but we still apply a re-scale by the minimum value of FRET.

7.2.2 Observing the impact of the filters on the initial time-trajectories

Figure 7.1 p.136 shows the time-trajectories of a sensitive and a tolerant cells from the third replicate of the experiment of Roux et al. dataset (TRAIL_Roux_25_3), when the different filters and re-scaling are applied on the ratio 1/FRET.

The red time-trajectories, obtained for the same sensitive cell, show that the 1/FRET initial signal continues long after the cell death, contrary to the ratio CFP/FRET. These longer time-trajectories are not due to the signal CFP but were not cut manually at the cell death time, contrary to the CFP/FRET dataset.

[*]We do not have access to the initial CFP/YFP time-trajectories without the mean untreated cell time-trajectory removed

Figure 7.1 shows that the Moving Average filter gives the smoothest trajectory for both drug-responses. Then, applying the Moving Average filter once or twice leads to almost overlapping trajectories so we decided to keep the same protocol than Meyer et al [Meyer et al., 2020] and apply the Moving Average filter twice. Finally, if there is no noticeable difference between the two re-scaling method (a re-scaling by the minimum of FRET before 50 min or a re-scaling by the FRET value at the first frame) for the sensitive cell, the different re-scalings have a bigger impact on the dynamic of the tolerant cells.

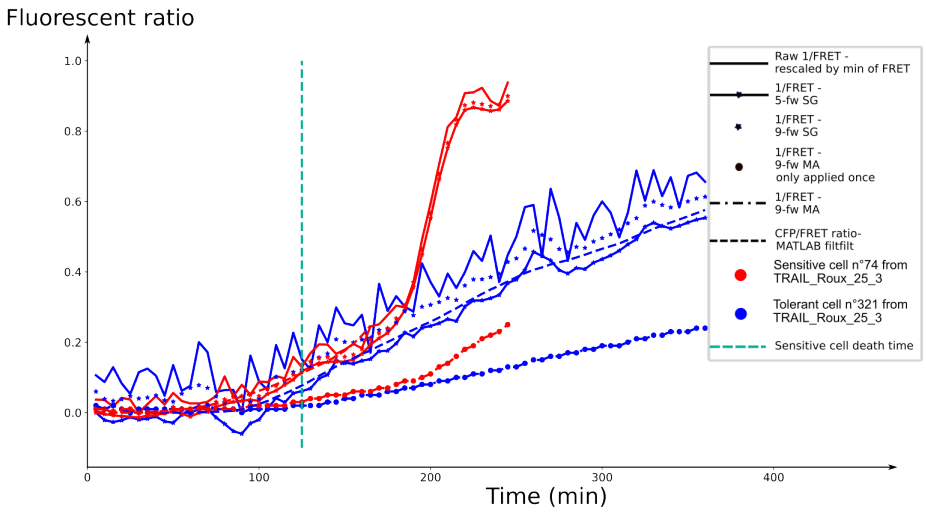

Figure 7.1: **Filtration impact on FRET time-trajectories:** 1/FRET time-trajectory for the sensitive cell n°74 and the tolerant cell 321 from TRAIL_Roux_25_3 when the Moving Average, Savitzky-Golay or 0-phase digital filtering(filtfilt) is applied with different windows size for the SG filter. The 0-phase digital filter is applied on the signal CFP/FRET and directly extracted from Roux et al. available datasets

7.2.3 Results for classic machine learning models using time-points as features

Type of classifier - Time frames used	Best model/ Scores	**1/FRET**	**1/FRET - 5 fw - SG**	**1/FRET - 9 fw - SG**	**1/FRET - MA**	**CFP/FRET ratio**
ML - 30 min	Model	5NN+ Pow. Gauss.	1NN + Quant. Unif.	DT+ Rob.	constant+ no p.	Ridge + Quant. Unif.
	MCC	0.128 ± 0.058	0.048 ± 0.051	0.020 ± 0.100	0.000 ± 0.000	0.251 ± 0.039
	ACC	0.577 ± 0.031	0.536 ± 0.029	0.521 ± 0.053	0.575 ± 0.002	0.638 ± 0.012
	F1	0.640 ± 0.040	0.598 ± 0.038	0.584 ± 0.060	0.730 ± 0.002	0.750 ± 0.008
	BACC	0.563 ± 0.028	0.524 ± 0.025	0.509 ± 0.050	0.500 ± 0.000	0.583 ± 0.016
	MK	0.131 ± 0.059	0.049 ± 0.051	0.021 ± 0.100	-0.425 ± 0.002	0.381 ± 0.066
	Prec.	0.626 ± 0.022	0.594 ± 0.020	0.581 ± 0.043	0.575 ± 0.002	0.622 ± 0.008
	Rec.	0.659 ± 0.068	0.604 ± 0.062	0.589 ± 0.082	1.000 ± 0.000	0.945 ± 0.025
ML - 50 min	Model	5NN+ Pow. Gauss.	SVC + Quant. Unif.	DT MaxAbs	constant+ no p.	AB+ Pow. Gauss.
	MCC	0.128 ± 0.058	0.071 ± 0.120	0.101 ± 0.072	0.000 ± 0.000	0.284 ± 0.063
	ACC	0.577 ± 0.031	0.566 ± 0.061	0.563 ± 0.040	0.575 ± 0.002	0.659 ± 0.028
	F1	0.640 ± 0.040	0.689 ± 0.087	0.624 ± 0.056	0.730 ± 0.002	0.733 ± 0.021
	BACC	0.563 ± 0.028	0.512 ± 0.042	0.549 ± 0.034	0.500 ± 0.000	0.631 ± 0.030
	MK	0.131 ± 0.059	0.180 ± 0.215	0.106 ± 0.077	-0.425 ± 0.002	0.307 ± 0.067
	Prec.	0.626 ± 0.022	0.577 ± 0.030	0.614 ± 0.027	0.575 ± 0.002	0.669 ± 0.022
	Rec.	0.659 ± 0.06	0.871 ± 0.182	0.641 ± 0.097	1.000 ± 0.000	0.813 ± 0.031
ML - 30 to 50 min	Model	MLP+ Rob.	SVC + Quant. Unif.	Ridge + Quant. Unif.	1NN+ PCA + Pow. Gauss.	Ridge + PCA +MaxAbs
	MCC	0.051 ± 0.103	0.112 ± 0.063	0.081 ± 0.091	0.038 ± 0.071	0.313 ± 0.072
	ACC	0.546 ± 0.055	0.584 ± 0.035	0.569 ± 0.050	0.536 ± 0.027	0.666 ± 0.024
	F1	0.641 ± 0.079	0.703 ± 0.061	0.680 ± 0.085	0.599 ± 0.102	0.757 ± 0.023
	BACC	0.513 ± 0.040	0.531 ± 0.018	0.523 ± 0.033	0.516 ± 0.031	0.622 ± 0.024
	MK	0.100 ± 0.156	0.204 ± 0.112	0.156 ± 0.171	0.044 ± 0.083	0.407 ± 0.128
	Prec.	0.581 ± 0.027	0.592 ± 0.011	0.586 ± 0.022	0.602 ± 0.048	0.653 ± 0.018
	Rec.	0.732 ± 0.180	0.881 ± 0.146	0.832 ± 0.180	0.647 ± 0.188	0.904 ± 0.066
ML - 2h	Model	MLP+ no p.	Ridge+ Pow. Gauss.	MLP+ Pow. Gauss.	constant+ no p.	MLP+ Rob.
	MCC	0.290 ± 0.023	0.347 ± 0.022	0.340 ± 0.070	0.000 ± 0.000	0.367 ± 0.106
	ACC	0.650 ± 0.014	0.681 ± 0.013	0.679 ± 0.035	0.575 ± 0.002	0.695 ± 0.058
	F1	0.749 ± 0.017	0.766 ± 0.007	0.742 ± 0.044	0.730 ± 0.002	0.758 ± 0.073
	BACC	0.604 ± 0.027	0.640 ± 0.022	0.656 ± 0.029	0.500 ± 0.000	0.661 ± 0.045
	MK	0.430 ± 0.107	0.438 ± 0.047	0.373 ± 0.095	-0.425 ± 0.002	0.425 ± 0.145
	Prec.	0.640 ± 0.025	0.663 ± 0.020	0.687 ± 0.019	0.575 ± 0.002	0.712 ± 0.028
	Rec.	0.912 ± 0.086	0.912 ± 0.049	0.813 ± 0.095	1.000 ± 0.000	0.826 ± 0.147
ML - 6h	Model	SVC+ no p.	SVC + PCA	RF + PCA +MaxAbs	constant+ no p.	Ridge + PCA +Quant. Unif.
	MCC	0.719 ± 0.052	0.712 ± 0.049	0.721 ± 0.061	0.000 ± 0.000	0.340 ± 0.068
	ACC	0.862 ± 0.027	0.858 ± 0.026	0.861 ± 0.036	0.575 ± 0.002	0.908 ± 0.013
	F1	0.890 ± 0.020	0.887 ± 0.021	0.881 ± 0.038	0.730 ± 0.002	0.951 ± 0.008
	BACC	0.844 ± 0.035	0.841 ± 0.031	0.855 ± 0.029	0.500 ± 0.000	0.600 ± 0.017
	MK	0.752 ± 0.047	0.745 ± 0.053	0.733 ± 0.071	-0.425 ± 0.002	0.616 ± 0.258
	Prec.	0.848 ± 0.042	0.844 ± 0.035	0.882 ± 0.033	0.575 ± 0.002	0.921 ± 0.003
	Rec.	0.939 ± 0.042	0.937 ± 0.048	0.887 ± 0.088	1.000 ± 0.000	0.982 ± 0.018

Table 7.1: Performances of the best ML models (according to Matthew coefficient - MCC) to forecast drug-response from FRET time-trajectories during 5-fold cross-validation after benchmarking of the state-of-the-art models available - using FRET time points as features: red: best accuracy obtained before an hour of experiment, blue: difference in accuracy according to the length of the window for SG filter; pink: the loss of information when a Moving Average is applied led to the poorest results and the selection of the Constant Classifier, green: highlights the gain in accuracy using CFP/FRET compared to using 1/FRET, yellow: Using CFP/FRET gives a better accuracy at 6h but using 1/FRET allows a better classification of the sensitive cells reflected in higher balanced accuracy, MK and MCC.

Table 7.1 p.137 shows the performance scores of the "best ML models" - the model that gives the highest MCC score - with respect to the number of time points used as input, along with the type of filters and fluorescent signal ratio employed. Similarly to the test carried out in Section 5.4.2 p.106 when using a SVC combined with our FRETexp β parameters to forecast drug-response, 6h of experiment are needed to reach an accuracy higher than 90% using the ratio CFP/FRET (in yellow in the table). However, even though the accuracy is lower, using the ratio 1/FRET with a Savitzky-Golay filter with a 9-frames window gives much higher MCC and MK, which reflects a better precision for the sensitive class (a higher true negative rate). A much higher balanced accuracy score for **1/FRET - 9fw - SG** confirms this better ability at classifying sensitive cells at 6h. Before 1h of experiment, the best MCC score is obtained by the Ridge Classifier prepreceded by a PCA and a scaling step with MaxAbs scaler, with a corresponding accuracy of 0.666 (red).

The column **1/FRET - MA** shows how much information we are losing with the Moving Average filter. Indeed, with this filter, the best scores are obtained with a Constant Classifier (in pink in the table), even for 6h-long data. Hence in the future, only a Savitzky-Golay filter will be used for our short time-trajectories. Regarding the window size to use with a SG filter, it seems that the 5-frames window give slightly better results than the 9-frames window, except for 6-hour long data. Using no filter at all gives a higher accuracy for 30 min, 50 min and 6h hour long data (in blue in the table), highlighting the presence of information in the noise removed by the filters.

Using the accuracy obtained during the 5-fold cross-validation as an indicator of the usefulness and informativeness of the time-trajectories for forecasting drug-response and locating the first signs of cell decision, it is clear that the ratio 1/FRET ratio strictly before 2h is barely predictive of the cell future (the best accuracy possible obtained is smaller than the no prediction accuracy fixed at 0.575 by the Constant classifier). On the other hand, using the ratio CFP/FRET forecasts cell decision already at 30 min (in green in the table), when there is still the saturation noise from the microscope and moves forward the first signs of cell decision. Indeed, the accuracy obtained at 50 min with the ratio CFP/FRET is similar to the one obtained using 1/FRET at 2h and only 0.012 separates the accuracy obtained at 30 min for CFP/FRET from the best accuracy obtained at 2h for the 1/FRET ratio. This last result must be qualified by the fact that using accuracy as a selection criterion, repeatedly identifies the Constant Classifier as the best at 30 min and that results are obtained using the time-trajectories taken between 30 and 50 min, instead of the all the time-points before 50 min for all the preprocessed time-trajectories (see Table E.19 p.220). Nevertheless, we believe that the signal CFP increases the gap between sensitive and resistant and therefore leads to this better forecasting of drug-response.

The differences between the best models according to the selection score chosen, also highlight the importance of choosing bi-classes (MCC, MK, BACC) instead of uni-classes (Precision, Recall,

F1) scores for our classification problem. Regarding the choice between MCC and MK as selection score, their results are aligned and most of the time both scores select the same model.

Waiting 2h, letting TRAIL impact the cell state, allows a better prediction of the sensitive class (showed by an increase in MCC score of more than 0.150) and therefore leads to a significant increase in accuracy, especially for the 1/FRET ratio. Several hypotheses could explain this difference. Figure 5.2 p.103, and especially the analysis of the mean timeline according to the drug-response in Section 5.3.2 p.104, showed that sensitive cells have a slower initiation to apoptosis (with the two first mean characteristic times much bigger than the tolerant ones) before speeding up just before death (with their three last mean characteristic times close to tolerant values). This phenomenon could explain this improvement in predicting sensitive cells only, but an increase in the differences between tolerant and sensitive dynamics, thanks to the impact of TRAIL on the cell state, could also be a valid explanation.

Finally, using the accuracy score, or the MCC score for long time-trajectories (2h or more) to select the best models (see appendix Appendix E.2 p.219) identifies the same best models. For shorter signals, using accuracy as a selection model score favors the models with a high recall. Using accuracy as criteria for model selection identified the MLP (and in a smaller extend the Ridge Classifier) as the best models, especially for 2-h long and between 30 and 50 min time-trajectories. With MCC, it is once again the Ridge classifier that gives the best MCC score for 6 hours and before 50 min. A Ridge classifier attributes at each class a number, typically 1 or -1, and turns the classification into a regression problem. These improved results, with more balanced abilities to predict any of the classes suggest that transforming the classification problem into a regression problem (forecast death time, use our FRETexp β parameters as a proxy of cell drug-response, etc) could be better way to forecast cell drug-response. On the other hand, regarding the results obtained with the MCC as selection criteria, none of the others models seem to stand out. More precisely, the tree-based models (RF, AB, GB, DT) all showed poor performances. The other results obtained with the accuracy as selection score confirm the conclusions above.

7.2.4 Performances for ML for time-series classification models

Table 7.2 p.140 gives the performance scores obtained during the 5-fold cross-validation for the time-series dedicated models.

First, the column **CFP/FRET ratio** confirms that this signal is more informative than 1/FRET, except at 6h (yellow), and allows to forecast cell drug-response sooner (in green) but with a similar accuracy than using 1/FRET at 2h. An hypothesis to explain this better accuracy at 50 min would be that CFP amplifies the differences between sensitive and tolerant. To verify this hypothesis, we

Type of classifier - Time frames used	Best model/ Scores	**1/FRET**	**1/FRET - 5 fw - SG**	**1/FRET - 9 fw - SG**	**1/FRET - MA**	**CFP/FRET ratio**
TSC - 30 min	Model	ShapeDTW	KNN	ShapeDTW	KNN	Arsenal
	MCC	0.127 ± 0.062	0.086 ± 0.070	0.076 ± 0.091	0.039 ± 0.086	0.194 ± 0.035
	ACC	0.574 ± 0.030	0.554 ± 0.031	0.548 ± 0.041	0.538 ± 0.044	0.621 ± 0.014
	F1	0.632 ± 0.028	0.613 ± 0.019	0.606 ± 0.031	0.617 ± 0.046	0.722 ± 0.014
	BACC	0.563 ± 0.031	0.543 ± 0.035	0.538 ± 0.046	0.518 ± 0.042	0.580 ± 0.013
	MK	0.127 ± 0.062	0.085 ± 0.070	0.076 ± 0.092	0.041 ± 0.088	0.237 ± 0.050
	Prec.	0.629 ± 0.026	0.613 ± 0.031	0.610 ± 0.039	0.588 ± 0.031	0.624 ± 0.008
	Rec.	0.636 ± 0.040	0.614 ± 0.017	0.604 ± 0.043	0.649 ± 0.066	0.856 ± 0.030
TSC - 50 min	Model	DrCIF	Shapelet	Arsenal	RISE	Arsenal
	MCC	0.142 ± 0.068	0.065 ± 0.094	0.075 ± 0.078	0.010 ± 0.096	0.266 ± 0.057
	ACC	0.592 ± 0.033	0.551 ± 0.047	0.563 ± 0.039	0.541 ± 0.046	0.651 ± 0.024
	F1	0.673 ± 0.030	0.629 ± 0.045	0.654 ± 0.040	0.656 ± 0.044	0.741 ± 0.022
	BACC	0.567 ± 0.031	0.531 ± 0.045	0.534 ± 0.036	0.502 ± 0.041	0.612 ± 0.022
	MK	0.151 ± 0.074	0.068 ± 0.097	0.083 ± 0.085	0.019 ± 0.114	0.317 ± 0.075
	Prec.	0.623 ± 0.021	0.598 ± 0.035	0.598 ± 0.026	0.575 ± 0.026	0.648 ± 0.013
	Rec.	0.733 ± 0.043	0.664 ± 0.057	0.723 ± 0.060	0.764 ± 0.075	0.868 ± 0.039
TSC - 30 to 50 min	Model	ShapeDTW	TSF	Shapelet	Shapelet	Shapelet
	MCC	0.033 ± 0.058	0.09 ± 0.061	0.078 ± 0.027	0.076 ± 0.085	0.201 ± 0.044
	ACC	0.529 ± 0.029	0.552 ± 0.032	0.554 ± 0.016	0.572 ± 0.037	0.621 ± 0.027
	F1	0.594 ± 0.030	0.600 ± 0.034	0.621 ± 0.026	0.680 ± 0.03	0.703 ± 0.026
	BACC	0.517 ± 0.029	0.545 ± 0.031	0.539 ± 0.013	0.532 ± 0.037	0.592 ± 0.02
	MK	0.034 ± 0.058	0.09 ± 0.061	0.08 ± 0.027	0.091 ± 0.099	0.22 ± 0.055
	Prec.	0.589 ± 0.024	0.615 ± 0.026	0.606 ± 0.012	0.596 ± 0.026	0.641 ± 0.012
	Rec.	0.600 ± 0.041	0.587 ± 0.044	0.639 ± 0.048	0.793 ± 0.05	0.78 ± 0.057
TSC - 2h	Model	Shapelet	DrCIF	DrCIF	Shapelet	Shapelet
	MCC	0.321 ± 0.069	0.301 ± 0.056	0.306 ± 0.024	0.220 ± 0.041	0.358 ± 0.048
	ACC	0.675 ± 0.03	0.666 ± 0.024	0.667 ± 0.010	0.624 ± 0.019	0.702 ± 0.021
	F1	$0.740 \pm 0.$	0.733 ± 0.012	0.733 ± 0.009	0.688 ± 0.014	0.774 ± 0.015
	BACC	0.652 ± 0.03	0.643 ± 0.032	0.644 ± 0.016	0.608 ± 0.021	0.664 ± 0.023
	MK	0.338 ± 0.06	0.318 ± 0.049	0.325 ± 0.023	0.225 ± 0.041	0.391 ± 0.051
	Prec.	0.686 ± 0.029	0.681 ± 0.029	0.681 ± 0.019	0.659 ± 0.018	0.710 ± 0.016
	Rec.	0.805 ± 0.023	0.795 ± 0.025	0.797 ± 0.040	0.719 ± 0.021	0.852 ± 0.016
TSC - 6h	Model	DrCIF	DrCIF	DrCIF	Arsenal	KNN
	MCC	0.731 ± 0.034	0.728 ± 0.035	0.751 ± 0.041	0.696 ± 0.040	0.202 ± 0.137
	ACC	0.870 ± 0.017	0.869 ± 0.017	0.879 ± 0.020	0.854 ± 0.019	0.863 ± 0.030
	F1	0.895 ± 0.011	0.894 ± 0.013	0.902 ± 0.016	0.881 ± 0.014	0.924 ± 0.017
	BACC	0.854 ± 0.023	0.855 ± 0.021	0.865 ± 0.021	0.839 ± 0.022	0.591 ± 0.067
	MK	0.755 ± 0.021	0.748 ± 0.032	0.772 ± 0.045	0.713 ± 0.036	0.247 ± 0.204
	Prec.	0.856 ± 0.028	0.859 ± 0.025	0.866 ± 0.023	0.848 ± 0.023	0.921 ± 0.013
	Rec.	0.940 ± 0.011	0.932 ± 0.020	0.941 ± 0.030	0.918 ± 0.013	0.928 ± 0.032

Table 7.2: Performances of the best ML models (according to Matthew coefficient - MCC) to forecast drug-response from FRET time-trajectories during 5-fold cross-validation after benchmarking of the state-of-the-art models available - for models dedicated to Time-series classification (TSC): red: best accuracy obtained before an hour of experiment, blue: difference in accuracy according to the length of the window for SG filter; purple and orange: CrCIF and Shapelet stand out, green: highlights the gain in accuracy using CFP/FRET compared to using 1/FRET before 2h, yellow: Using 1/FRET gives a better accuracy at 6h but contrary to the results obtained using FRET time-points only

should carry the same experiment using only the CFP signal. On the other hand, the results at 30 min, 50 min, or between 30 and 50 min, are similar to those obtained using simply the time-points

as features, and below the constant threshold, with the Arsenal model giving the best MCC score with an accuracy of 0.651 (in red).

Next, the accuracies obtained for all types of signal and filters before 2h between the time-series dedicated classifiers and the models simply using the time-points as features, demonstrates that there is no need to use the time-series dedicated models.The scores of these models after 5-fold cross-validation are lower than the classic models. One potential cause is the length of the time-trajectories that are too short to compute relevant features with the time-series classifiers. This hypothesis is also supported by the fact that, contrary to the classifier using only the time points as features, the time-series dedicated models perform better using the full time-trajectories until 50 min, when the approach without feature extraction gave better results using only time-points after 30 min (in blue).

Similarly to classic ML using time-points as input features, the initial 1/FRET signal gives a higher accuracy until 50 min than the same signal filtered (also in blue), and once again the moving average filter obtains the poorest results. The difference between 5 and 9-frames window for the SG filter is barely noticeable before 50 min.

During this experiment using the MCC score as selection criterion, two models stand-out: the DrCIF for long time-trajectories (in purple) and the Shapelet for the shorter ones (orange). Results using the accuracy to select the models, also identify Arsenal as a potential good model for short experiments but its lower MCC and Markedness prevent it to be used for our case, as it performs poorly for sensitive classification.

The comparison between 2h and 50 min confirms the conclusions of the previous subsection but waiting 2h is still not enough to forecast drug-response with more than 90% of accuracy.

To simplify the tests, in the following, we will use only the dataset: **CFP/FRET** as we believe subtracting the mean untreated cells mostly affect the FRET signal at the end of the experiment. Considering CFP/FRET ratio is more important than using un-preprocessed data, thus keeping a continuity with the previous chapters and other articles [Chaves et al., 2021, Roux et al., 2015, Matveeva et al., 2019], that were also using this dataset.

7.3 Developping our own features

In the previous sections, we have shown that we can increase the accuracy of drug-response forecasting by extracting some features (e.g. Fourier-like, autocorrelation, or statistic) from our temporal signal. These algorithms that extract a set of features from time-trajectories are called

transformers. Unfortunately, using transformers results in an increase of accuracy in the forecasting only after two hours of experiment. Here, we take advantage of our knowledge on the biology underlying the FRET signals, to extract mechanistic features from the time-trajectories, and see if these features perform better than the ones proposed in the literature.

7.3.1 Mechanistic transformers

We compute features based on Roux et al. [Roux et al., 2015] findings and the conclusions of the Chapter 5, and use them in combination with the time-measurements, to augment the dimensions of the input feature space. We then compare the performances of the classic machine-learning models for classification obtained with them as an input.

7.3.1.1 Differentiate the fluorescent signal

In [Roux et al., 2015], using a phenomenological model of caspase-8 activation and ICRP probe cleavage, the authors demonstrated that the slope of the FRET signal (maximum of the time-derivative of the FRET-trajectory) is the most important descriptive feature of the signal to determine whether a cell is drug-tolerant or drug-sensitive. Here, we compute the derivative with the function *gradient* of the package *numpy*, using the initial 1/FRET time-trajectories filtered with Savitzky-Golay filter with a window of 9 frames. The slope is computed with three different methods: taking the mean value over the last 5 frames [MP1], taking the value on the last time point [Meyer et al., 2020], or taking the maximum of the derivative [Roux et al., 2015] on the last 5 frames.

7.3.1.2 Features inspired by mathematical modeling

In Chapter 5, we developed new features of the FRET signal with predictive values. These features are fitted parameters of FRETexp, the explicit solution of a reduced model of extrinsic apoptosis initiation core reactions (see Chapter 5). These parameters represent new features to describe the fluorescent signal with prior knowledge on the dynamic observed.

Keeping the idea that mathematical modeling is a pertinent way to extract feature from our FRET signal, we will also test the parameters of Roux et al. model (k, t_0 and τ - see Equation (E.39) p.225), and combine our features with the FRET measurements.

The three 3D scatter plots in Figure 7.2 p.143, representing the distribution of our mechanistic parameters, according to the cell drug-response, do not allow the identification of a consistent number of outliers for any of the features presented and shows how difficult it is to forecast cell drug-response using only data before 50 min of experiments and thresholds criteria.

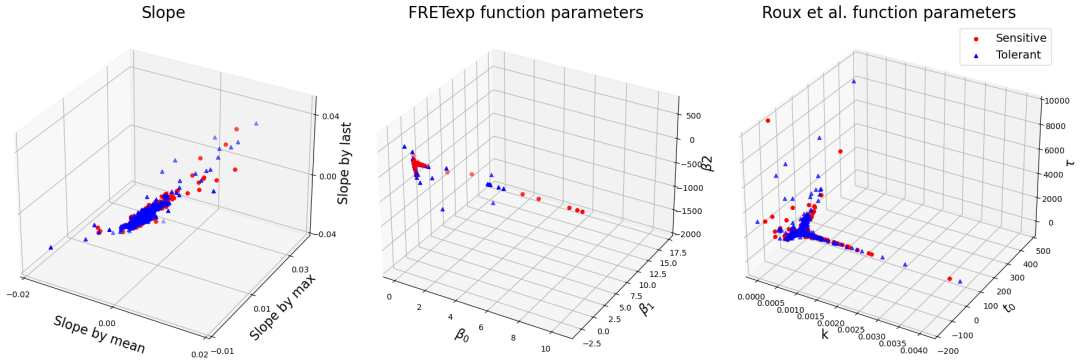

Figure 7.2: **3D Scatter plots of the mechanistic parameters distribution for the Slope features (subplot 1), the FRETexp β parameters (subplot 2) and Roux et al.'s model parameters (subplot 3)**

7.3.2 Performances

Table 7.3 p.144 summarizes the mean scores, and the corresponding standard deviations, obtained during a 5-fold cross validation, using our mechanistic features as input of classic ML classifiers with the CFP/FRET dataset from Roux et al when we use the MCC score to select our best models. Similar tables for the case when the accuracy is the selection score, and when using the 1/FRET datasets with a SG filter with a 5-frames window are available in Appendix E.3 p.222.

Type of model-Time	Best / Scores	Slopes	FRETexp model	Roux et al model	FRET + Slope	FRET + FRET-exp	FRET + Roux et al. param.
50 min	Model	MLP + PCA+ Quant. Unif.	Ridge+ Quant. Unif.	MLP + PCA + Rob.	RF + Rob.	SVC + PCA+ MinMax	SVC+ Quant. Unif.
	MCC	0.260 ± 0.106	0.161 ± 0.062	0.247 ± 0.053	0.280 ± 0.091	0.276 ± 0.044	0.261 ± 0.087
	ACC	0.646 ± 0.051	0.600 ± 0.032	0.640 ± 0.025	0.652 ± 0.047	0.646 ± 0.015	0.640 ± 0.044
	F1	0.720 ± 0.052	0.681 ± 0.044	0.724 ± 0.033	0.718 ± 0.056	0.758 ± 0.008	0.729 ± 0.066
	BACC	0.618 ± 0.048	0.573 ± 0.025	0.607 ± 0.018	0.629 ± 0.038	0.588 ± 0.019	0.598 ± 0.030
	MK	0.287 ± 0.119	0.179 ± 0.079	0.288 ± 0.082	0.304 ± 0.111	0.439 ± 0.073	0.353 ± 0.133
	Prec.	0.659 ± 0.036	0.626 ± 0.015	0.646 ± 0.011	0.670 ± 0.026	0.626 ± 0.010	0.639 ± 0.016
	Rec.	0.797 ± 0.091	0.750 ± 0.093	0.826 ± 0.078	0.777 ± 0.103	0.963 ± 0.017	0.865 ± 0.149
30 to 50 min †	Model	MLP+ Quant. Unif.	Ridge+ Quant. Unif.	SVC + PCA+ Quant. Unif.	Ridge + Rob.	Ridge + PCA+ MinMax	Ridge + PCA + Rob.
	MCC	0.257 ± 0.088	0.161 ± 0.062	0.245 ± 0.050	0.289 ± 0.067	0.302 ± 0.067	0.310 ± 0.067
	ACC	0.642 ± 0.047	0.600 ± 0.032	0.639 ± 0.025	0.658 ± 0.024	0.663 ± 0.023	0.666 ± 0.023
	F1	0.709 ± 0.059	0.681 ± 0.044	0.717 ± 0.034	0.747 ± 0.025	0.756 ± 0.020	0.751 ± 0.026
	BACC	0.619 ± 0.041	0.573 ± 0.025	0.610 ± 0.020	0.618 ± 0.025	0.618 ± 0.026	0.627 ± 0.021
	MK	0.280 ± 0.099	0.179 ± 0.079	0.275 ± 0.069	0.362 ± 0.114	0.394 ± 0.114	0.385 ± 0.123
	Prec.	0.664 ± 0.030	0.626 ± 0.015	0.651 ± 0.014	0.652 ± 0.019	0.649 ± 0.019	0.659 ± 0.015
	Rec.	0.770 ± 0.112	0.750 ± 0.093	0.803 ± 0.080	0.879 ± 0.068	0.906 ± 0.057	0.877 ± 0.076
2h	Model	Ridge+ Quant. Unif.	Ridge+ Quant. Unif.	MLP + Rob.	SVC+ Quant. Unif.	SVC+ Quant. Unif.	SVC+ Quant. Unif.
	MCC	0.371 ± 0.123	0.327 ± 0.102	0.372 ± 0.064	0.380 ± 0.074	0.366 ± 0.084	0.358 ± 0.079
	ACC	0.689 ± 0.068	0.669 ± 0.052	0.693 ± 0.033	0.703 ± 0.040	0.697 ± 0.044	0.694 ± 0.044
	F1	0.740 ± 0.088	0.725 ± 0.063	0.747 ± 0.042	0.769 ± 0.052	0.768 ± 0.052	0.763 ± 0.055
	BACC	0.666 ± 0.048	0.650 ± 0.046	0.674 ± 0.032	0.668 ± 0.031	0.658 ± 0.040	0.656 ± 0.037
	MK	0.420 ± 0.172	0.361 ± 0.126	0.401 ± 0.082	0.436 ± 0.118	0.433 ± 0.124	0.417 ± 0.114
	Prec.	0.726 ± 0.035	0.690 ± 0.037	0.709 ± 0.034	0.716 ± 0.023	0.707 ± 0.029	0.706 ± 0.026
	Rec.	0.775 ± 0.175	0.777 ± 0.134	0.799 ± 0.102	0.842 ± 0.118	0.851 ± 0.118	0.842 ± 0.122
6h	Model	5NN + Pow. Gaus.	MLP + Rob.	MLP + PCA + Quant. Unif.	MLP + PCA + Standard	MLP + PCA + Standard	Ridge + PCA+ Quant. Unif.
	MCC	0.388 ± 0.079	0.654 ± 0.045	0.720 ± 0.063	0.339 ± 0.125	0.302 ± 0.066	0.315 ± 0.085
	ACC	0.901 ± 0.028	0.827 ± 0.023	0.860 ± 0.034	0.914 ± 0.012	0.903 ± 0.016	0.896 ± 0.026
	F1	0.946 ± 0.017	0.864 ± 0.016	0.883 ± 0.028	0.954 ± 0.006	0.948 ± 0.010	0.943 ± 0.016
	BACC	0.637 ± 0.029	0.806 ± 0.027	0.849 ± 0.039	0.587 ± 0.041	0.589 ± 0.043	0.610 ± 0.022
	MK	0.617 ± 0.290	0.699 ± 0.034	0.746 ± 0.062	0.705 ± 0.277	0.622 ± 0.272	0.496 ± 0.262
	Prec.	0.929 ± 0.006	0.793 ± 0.027	0.852 ± 0.048	0.919 ± 0.008	0.920 ± 0.008	0.924 ± 0.004
	Rec.	0.965 ± 0.040	0.949 ± 0.011	0.922 ± 0.062	0.992 ± 0.010	0.978 ± 0.026	0.965 ± 0.034

Table 7.3: Forecasting single-cell drug-response using mechanistic features in a ML classifier - Performances according to MCC score - for CFP/FRET datasets of Roux et al.: olive and pink: Ridge Classifier and MLP stand out, yellow: best score at 6h with only 3 features, red: best accuracy before 1 hour of experiment using only mechanistic features or combining them with FRET time-points, blue: using mechanistic features improves the classification of sensitives cells after 2h, as shown by higher MMC and MK scores.

This study clearly highlights the fact that combining our features with the time-points is unnecessary and leads to poorer accuracy by comparison with the results obtained using only the time-points as features. Nevertheless, for the features from Roux et al. model, but also the slope features, at 6h, we can have a better MCC using only three features instead of the 72 time-points (in blue). Coupling these features with the 24 time points available at 2h increases the MK score too, showing a better ability to predict sensitive cells. However, it is not the case at 50 min and before.

Comparing these results with the classifiers integrating a feature extraction step, coupling ML classifiers with mechanistic feature transformer, or augmenting the feature space composed of the time-points with the mechanistic features, perform better than using these time-series dedicated classifiers but, as stated before, it does not outperform the methods using only the time points. Similarly to the approach using classifier on time-point directly, the Ridge classifier (in purple) gave the best MCC scores before 2h and is replaced by the MLP after (in olive).

Nevertheless, one can notice that for 6-hours, the slopes features capture in only three parameters all the information of the FRET signal and allow the prediction of drug-response with the same performances than using the time-points (yellow). These features are also useful as they can deal with NaN value and time-series with different lengths.

7.4 Extending time-trajectories to forecast cell drug-responses

The previous sections, but also the Section 5.4.2 p.106 demonstrated that we could predict drug-response for all cells from the FRET time-trajectories with more than 89% of accuracy, if using 6h of experiments. To prevent time-dependent change in cell-state induced by the drug, we need to stop the reaction at 50 min. Indeed, Meyer et al. demonstrated that up to this time, the cell state is unchanged, but not at two hours anymore (differently expressed genes can be detected at 2 hours after drug addition). In the previous section, we showed that using only 50-min data as input for any ML classifier always gives poor performances. Hence, we propose to extend these time-trajectories up to 6h, using mathematical functions. In this way, instead of using 6h data, we use a combination of real data (50 min) with simulated data (from 50 min to 6h) to predict drug response and evaluate if it improves the forecasting performances.

We test 4 different models: Roux et al. phenomenological model of caspase 8 activation, our FRETexp model described in Equation (5.10) p.101, and two time-series models: ARIMA and ETS. A description of the models is given in Appendix E.5 p.225, the parameter estimation process is described in Section 7.1.3 p.132.

7.4.1 Fitting time-series

We first evaluate the ability of the methods to reproduce the 6h-signal, for each cell according to the number of frames used for the fitting. To do so, we compute a cost per frame for each cell (so we can compare tolerant cells with more measurements with sensitive cells with fewer frames). We then compute the mean cost, across all cells, for each dataset. The cost is simply the euclidian norm of the difference between the data and the model's solution divided by the numbers of measurements available for each cell. We did not use the classic regression scores in regression problems (Root Mean

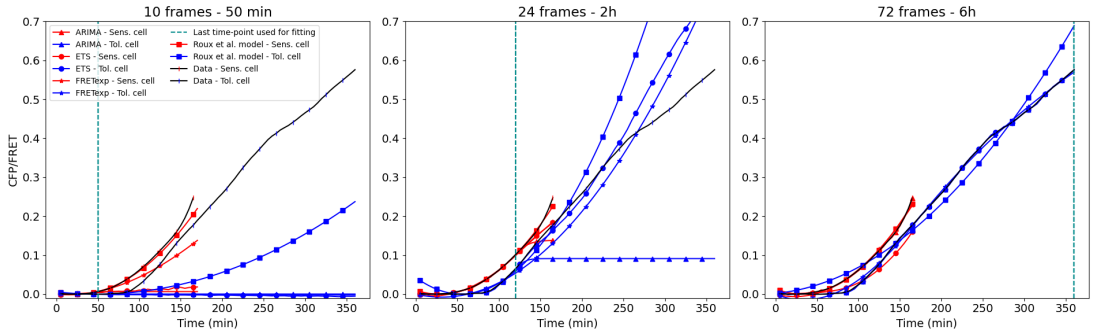

Figure 7.3: **Extended time-trajectories for the n°74 sensitive cells and the n°321 tolerant one from TRAIL_Roux_25_3.** blue lines: extended time-trajectories for the tolerant cell, red line: extended time-trajectories for the sensitive cell - sensitive trajectories have been cut at the time of death in this plot but during the experiments, all time-trajectories were simulated until 6 hours, dot-line: last time-point used for fitting

Square Error (RMSE), Mean Square Error (MSE), etc) because sensitive cells have different lengths.

We selected three different lengths of time-trajectories defined by their last time-point: 50 min corresponds to the last time point used in the current FATE-SEQ pipeline, 2h was highlighted by Meyer et al. [Meyer et al., 2020] as the time-point when drug has already an impact on the initial cell state (see Section 2.3.3 p.53), and 6-hours after the experiment beginning was the necessary time-lapse needed to reach more than 90 % of accuracy in the drug-response forecasting using the β parameters - see Section 5.4.2 p.106. We will not evaluate the execution time needed to obtain the estimated parameters for each cell and each method as the algorithms run fast, using 3 CPU at the time, and in real lab conditions cells are cooled down to 4°C before the cell selection for isolation step. The initial guess for parameters and parameters of the time-series models are given in Appendix E.5 p.225. Figure 7.3 shows the extended time-series according to the number of frames used for parameters estimation, for a sensitive and a tolerant cells.

Number of frames used in the fit	10 frames (50 min)	24 frames (2h)	72 frames (6h)
ARIMA	$3.093e-02 \pm 4.072e-02$	$1.599e-02 \pm 2.263e-02$	$1.655e-05 \pm 1.435e-04$
ETS	$4.718e-02 \pm 1.429e-01$	$9.097e-03 \pm 5.241e-02$	$4.840e-04 \pm 1.087e-03$
FRETexp	$2.458e-02 \pm 3.838e-02$	$7.857e-03 \pm 2.704e-02$	$9.104e-05 \pm 4.122e-04$
Roux et al. model	$4.604e+00 \pm 7.491e+01$	$2.324e-02 \pm 6.939e-02$	$5.736e-04 \pm 1.569e-03$

Table 7.4: Mean fitting cost for the four types of models (columns) used to extend the time-trajectories of the CFP/FRET datasets according to the last time-point used (row) to estimate the models' parameters: best cost in yellow

Table 7.4 shows that the lowest mean costs for 10 and 24 frames are associated with the FRETexp model. This shows that a more detailed model, more accurate with respect to the elements modeled, captures better the dynamics observed in real conditions when short time-trajectories are

used for fitting. Nevertheless, the time-series models (ARIMA or ETS) have similar costs with FRETexp.

Surprisingly, Roux et al. model, despite being the model with the biggest costs, is the one with the best accuracy when using its parameters as features to forecast cell drug-response. Similarly, the RISE TSC model uses features extracted with autoregressive modelS (AR) and this model obtained poor scores during the 5-fold cross validation for any of the time-lapses compared, despite ARIMA being the second closest model to data.

The remaining question is: **Does the time-trajectory extension method, with the lowest cost at 6h, give the best performances, using the extended time-trajectories, to forecast drug-response for all cells?** To answer this question, we will use the best time-series model to forecast drug-response at 50 min identified in Section 7.2, with our extended time-trajectories as input, for each time-trajectory extension method presented above.

7.4.2 Performances in forecasting drug-response

Here, we once again compare the classifiers after 5-fold cross-validation but only the models dedicated to time-series classification following the same protocol defining in the programming Section 7.1.3 p.132. For each classifier, we use the extended time-trajectories obtained with one model at the time only, the last test uses the extended time-trajectories from the 4 models combined. We compare the performances of the 5 best models according to the MCC score with the best ML classifier until now: the Ridge classifier coupled with a PCA and MaxAbs scaling, using data points from 30 to 50 min of experiment as input, that obtained a mean accuracy of 0.666.

TT model	ARIMA	ETS	FRETexp	Roux et al. model	All models
TSC model	Arsenal	DrCIF	DrCIF	DrCIF	DrCIF
MCC	0.279 ± 0.092	0.215 ± 0.075	0.219 ± 0.067	0.216 ± 0.03	0.273 ± 0.1
ACC	0.656 ± 0.037	0.629 ± 0.032	0.629 ± 0.029	0.629 ± 0.014	0.655 ± 0.043
F1	0.746 ± 0.028	0.718 ± 0.029	0.707 ± 0.02	0.716 ± 0.012	0.737 ± 0.034
BACC	0.617 ± 0.038	0.594 ± 0.029	0.602 ± 0.032	0.596 ± 0.015	0.621 ± 0.043
MK	0.334 ± 0.113	0.246 ± 0.096	0.234 ± 0.07	0.241 ± 0.032	0.307 ± 0.117
Prec.	0.649 ± 0.024	0.638 ± 0.017	0.648 ± 0.023	0.64 ± 0.013	0.657 ± 0.027
Rec.	0.877 ± 0.044	0.821 ± 0.05	0.78 ± 0.03	0.813 ± 0.027	0.838 ± 0.047

Table 7.5: Performance after 5-fold cross-validation of the best ML classifiers dedicated to time-series (according to the MCC score), obtained using the 6h-extended CFP/FRET time-trajectories from Roux et al after 50 min of experiment, according to the type of model used to extend the time-trajectories. red: best accuracy obtained at 50 min. The results obtained with the accuracy as selection score are identical.

Once again the new models give lower performances than the model using only the time-points between 30 and 50 min. But we notice that using the ARIMA model to extend the time-trajectories

allows an accuracy of 0.656, only 0.01 less than the Rigde Classifier. On the other hand, combining all the time-trajectories does not lead to an improvement of the accuracy.

Finally, similarly to the results in Table 7.3 p.144, out study confirms that the DrCIF, which uses catch22 features set as input, is the most accurate model to forecast cell drug-response and therefore captures the most pertinent information about the future cell drug-response in the CFP/FRET signal.

7.5 Discussion

This benchmarking demonstrated how difficult forecasting cell drug response before 50 min is. With so short time-trajectories, even the most performing models, like the ROCKET algorithm, shows poor results. Eventually, the more accurate model was a simple Ridge Classifier that uses directly the time-points between 30 and 50 min as feature input and reached an accuracy of 0.667, 0.1 bigger than the Constant Classifier. Even though this increase in accuracy (and in the other scores) shows actually a big improvement, it not enough for the FATE-SEQ pipeline for which the minimal accuracy is 0.9 (Chapter 6).

Nevertheless, this study allowed us to identify the key points and techniques to consider in the selection of the best drug-response forecasting method. A special attention should be given to the choice of the signals used to forecast the drug-response, as demonstrated by a significant difference of performances between CFP/FRET and 1/FRET. On the other hand, the re-scaling step (first frame of lowest value), the type of filter or the size of the window for the filters seem to be less important, even though the Moving Average filter should be avoided.

The models using a transformer to extract features showed poor performances, probably due to the short time-trajectories. In the future, we will record more time-points (one frame each 3 minute). On the other hand, more data point could not have a great impact on the performances, as having more hours of data seem to be decisive to reach more than 90% of accuracy.

One strategic point in the future will be to better locate the best time period to forecast drug-response, according to the type of method we want to use (features-based, classic machine-learning, coupling mechanistic features with time-points, etc) as our study highlights the difference of performances between using the full 50 min data or just the time-point between 30 and 50 min.

Finally, many of our features seems to be redundant (with the example of the slope, or the linear relation between τ and t_0, two parameters from Roux et al. model), and have a low variance across cells, preventing the model to separate cells in two classes due to overlapping values. In summary, a detailed work on the observability (when (locate a time-period) and how (which feature), etc)

will be key to improve the forecasting step for the new set-up.

By lack of time and data, we did not create our own classifier. As the study on our mechanistic features (Section 7.3) identified the Ridge classifier (a regression based model), and the MLP as two of the best models to forecast cell drug response, a future work will try to use a multi-layer perceptron to regress the β parameters of the FRETexp at 6h of experiments or Roux et al. model parameters, and then use these parameters as input features in a classifier, as a better proxy of cell death.

In conclusion, this benchmarking chapter demonstrated the difficulties in forecasting drug-response for all the cells before 50 min of experiment. Hopefully, as stated in the introduction of part III, FATE-SEQ pipeline does not require the forecasting of the drug-response of all cells in the population. Hence, in the next chapter, we will combine the features and the best models identified here, with the current methods used in FATE-SEQ pipeline, to up-grade the current cell-selection-for-isolation method, in order to increase the number of cells profiled.

CHAPTER 8

EASIDRUG forecaster: EArly Single-cell Isolation with a Drug Response Up-Graded forecaster for live-cell microscopy assays

Chapter 7 has shown that we can forecast cell fate before one hour of experiment - to preserve the genome integrity of sensitivity cell states - for all cells, but with an accuracy too low for FATE-SEQ pipeline. On the other hand, the number of cells that we can actually sequence in our lab is limited by human and technological constraints. Indeed, even though we could accurately predict drug-response for all cells, we would not be able to profile all of them. Therefore, we first present different methods to identify unpredictable cells before 1h of experiment. These methods combine transformers, models inspired by machine-learning time-series classifiers from Chapter 7 and the current technique used in FATE-SEQ to select cells for isolation (see Chapter 6). The objective is to find the best trade-off between the accuracy (more than 0.9), and the number of cells accurately predicted (more than 1% of the cells), to outperform the results obtained for both CFP/FRET and 1/FRET datasets from Roux et al. study (see the results of the current FATE-SEQ method for 1/FRET and CFP/FRET for Roux et al. datasets in Table 6.1 p.124 and Table D.15 p.214). For CFP/FRET, the challenge is easier as the current FATE-SEQ method did not identify any cell for isolation (Table D.15 p.214)).

Finally, we summarize the final pipeline that will be integrated in the fate-seq workflow to replace the current predictor of the single-cell drug response after one hour of experiment.

How can a cell be unpredictable ?

Several reasons can explain the fact that a cell drug response at 50 min - and even beyond that time - cannot be forecast.

At 50 min, cells may not have had the time to engage their death signaling pathway sufficiently yet and simply need more time, either to "make a decision" by mediating the outcomes of multiple signaling pathways and the integration of external signals, or simply to implement this decision. This hypothesis follows from the conclusions of Section 5.3.2 p.104, which demonstrate that sensitive cells have a slower initiation of the extrinsic pathway by TRAIL but then speed-up during the DISC activation phase. The cell decision might also not be implemented through the caspase 8 pathway and hence would not be observable using our fluorescent probe.

Finally, the last cause is also the absence of relevant tools that could extract finer information from the FRET signal but also from other experimental data.

8.1 Methods

8.1.1 Datasets

In this chapter, we will be using once again the dataset CFP/FRET from Roux et al. However, we will be using only the last two replicates of Roux et al. datasets (TRAIL_Roux_25_2 and TRAIL_Roux_25_3), as discussed in Section 6.2.6 p.125(TRAIL_Roux_25_1 has a really different balance tolerant cells/sensitive cells, but also a much wider range of FRET slope values).

Surprisingly, using only the two comparable replicates leads to poorest performances than using the three replicates combined. This difference of accuracy could be explained by the wider range of dynamics and data brought by TRAIL_Roux_25_1. Indeed, these models "learn" from the data, therefore the larger and more heterogeneous the training data, the more situations the models can fit during testing.

We also notice that if the tree-based methods showed poor results in the last chapter, it is not the case when using only TRAIL_Roux_25_2 and TRAIL_Roux_25_3. Despite these better results, we still choose to use the combination PCA, MaxAbs Scaler, that re-scales each feature by its maximum absolute value, and the Ridge Classifier that led to the best performances in Chapter 7. Therefore, all the features selections and hyper-parameter optimization steps for ML models will be only carried for this combination of models.

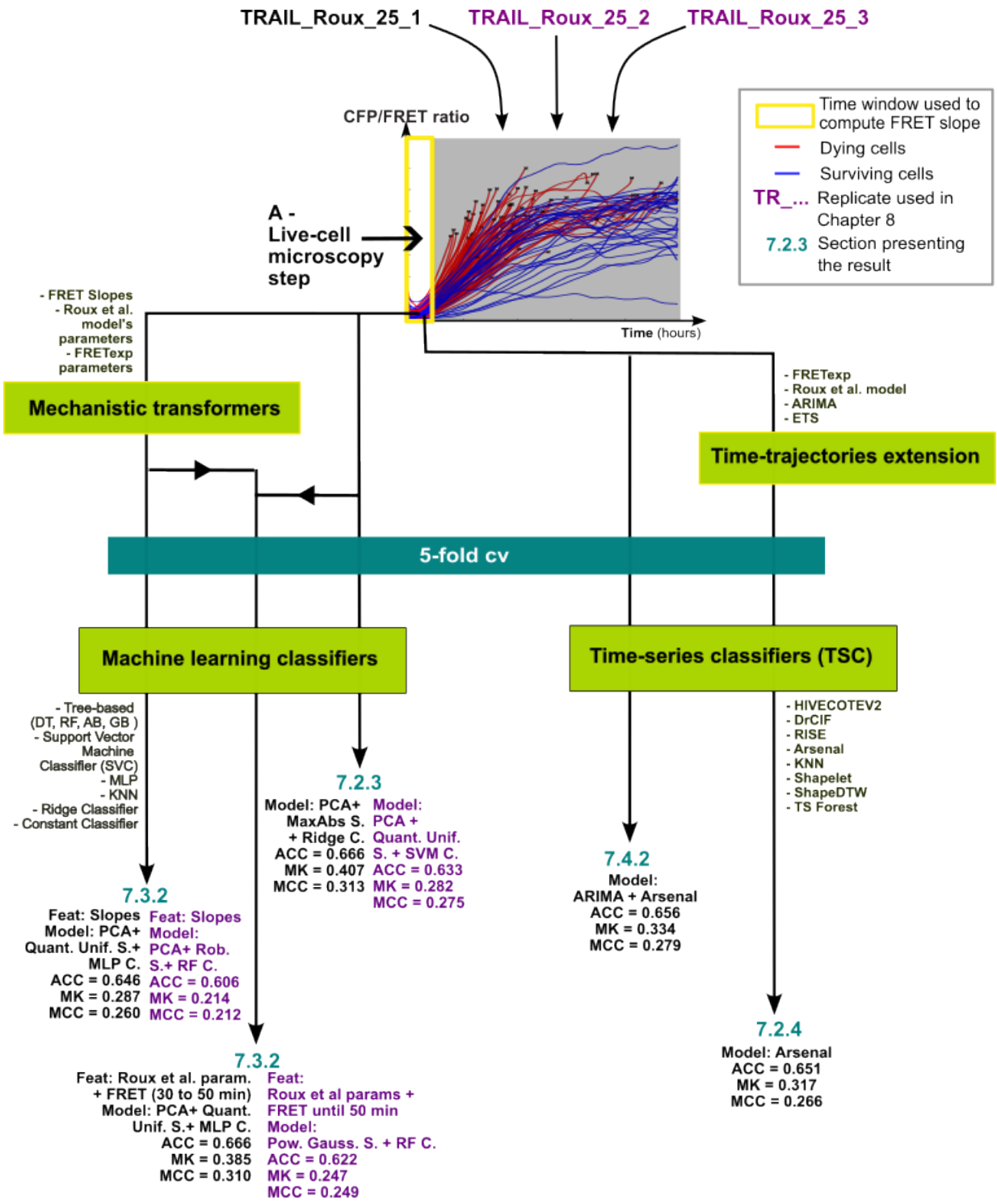

Figure 8.1: **Comparison of the performances obtained in Chapter 7 using the three replicates of CFP/FRET dataset from Roux et al. (in black) and the MCC as selection score with the performances obtained using only TRAIL_Roux_25_2 and TRAIL_Roux_25_3 (in purple)**

8.1.2 Identification methods for cell selection

We evaluate 4 different methods to identify unpredictable cells and forecast drug-response for cells identified as predictable. We define two classes of methods. The first class of methods, named **Unpredictable cells**, follows the opposite idea to FATE-SEQ current selection technique. We first identify unpredictable cells and then try to forecast the cell response for the other cells, instead of identifying the predictable cells for isolation first. The second class of methods, called **Divide and Conquer**, is aligned with the current FATE-SEQ method, but instead of using only one feature and the principle of non-overlapping cells, these methods dedicate a couple model/feature for each drug-response. These methods are composed of a model (a set of features + a method to classify the cells) per drug-response.

8.1.2.1 Unpredictable class

The idea here is that a machine learning classifier uses a different decision criterion than the current FATE-SEQ method, which is based on 1D-linear thresholds. Indeed, in [MP1], unpredictable cells are cells not able to overcome a specific threshold in the derivative value for instance. For a machine learning classifier, unpredictable cells are cells incorrectly predicted during training or testing.

To identify unpredictable cells, we chose the best model from Chapter 7 and carried a 5-fold cross-validation for each replicate. Cells incorrectly predicted in one of the testing phases inside each replicate, are assigned a new label: U for Unpredictable. Then, instead of solving a two-class classification problem, we solve a three-class classification problem: Tolerant (T), Sensitive (S) and Unpredictable (U). For this purpose, we developed two methods:

i) **3rd class:** Using the best method from Chapter 7 on the three-class (T/S/U) problem directly.

ii) **2-step forecasting:**

Step 1 - Classifying cells between unpredictable (U) or predictable (P), P being the combination of T and S classes.

Step 2 - Inside the predicted P, a second model classifies cells between T and S.

Figure 8.2 p.156 illustrates the identification of unpredictable cells during training and the hyperparameters optimization for i) and ii).

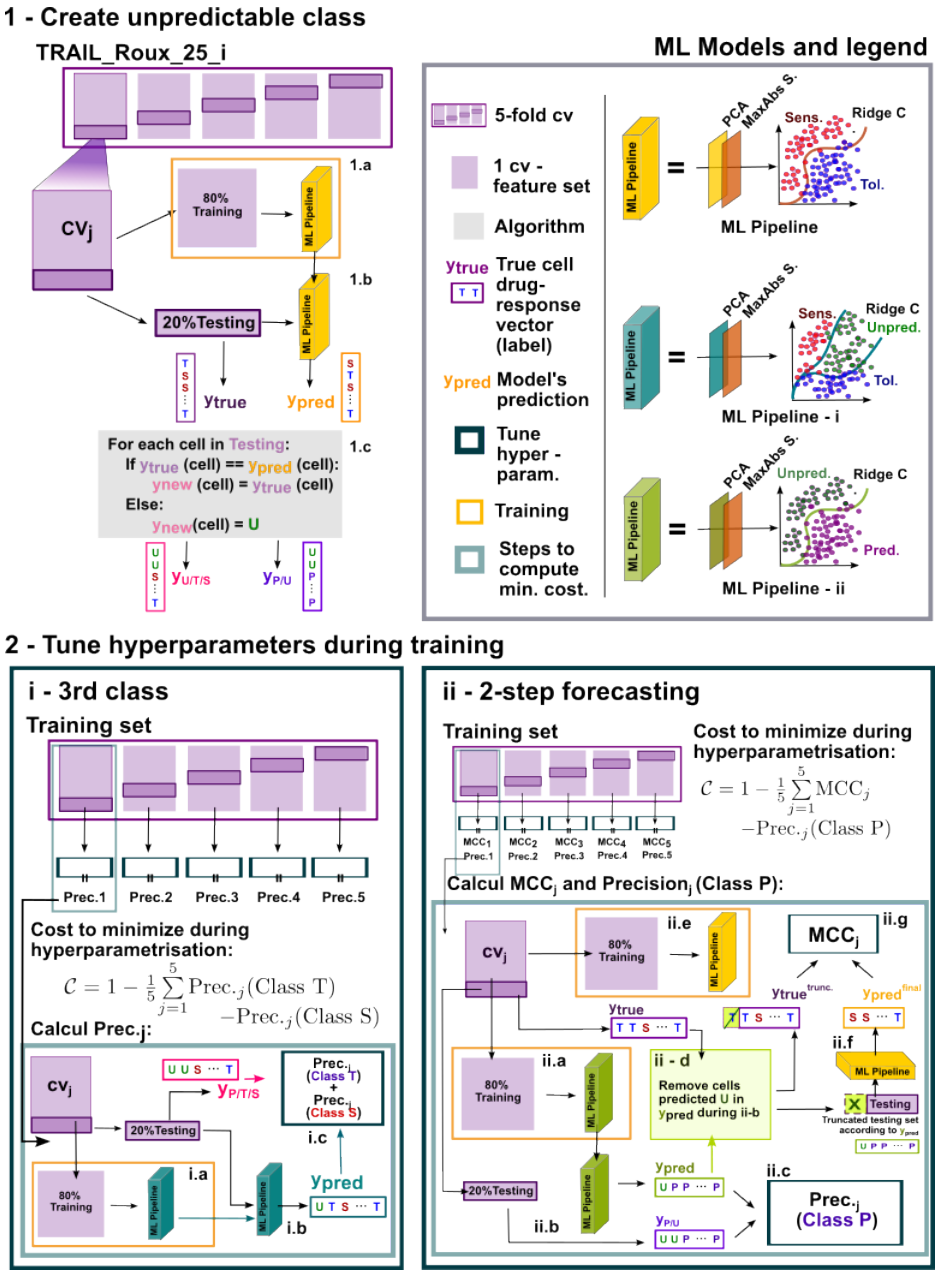

Figure 8.2: **Determining unpredictable cells and tuning ML models' hyperparameters for the methods based on the unpredictable class 1 - Create unpredictable class:** to define new labels for each cell and create the unpredictable class, each replicate dataset is divided 5 times in 80% and 20% such that each cell is once in the testing set. 1.a - Our ML pipeline (PCA + MaxAbs Scaler + Ridge classifier) in yellow is trained on the training set. 1.b - the trained model is applied on the 20% dataset defining the testing set. 1.c - Cells in the testing set not classified accurately get an new label assigned: U, the cells classified accurately keep their original label (T/S) for method i) or get a Predictable label P for method ii). **2 - Tune the hyperparameters during training - i) 3rd class:** On the training replicate set only: for each splitting group cv_j of the 5-cross-validation: i.a - the ML pipeline i (or blue model) is trained on 80% of the replicate dataset, using the labels U/T/S defined during 1 - Create unpredictable class. i.b - the trained blue model is applied on the 20% dataset left. i.c - the Precision score is computed for both Sensitive and Tolerant classes, comparing the true labels U/T/S with the output of the model. **2 - Tune the hyperparameters during training - ii) 2-step forecasting:** For each cv_j: ii.a - the ML Pipeline ii (or green model) is trained on 80% of the replicate dataset using the U/P labels. ii.b - the green model is applied on the 20% of the dataset left. ii.c - the Precision score for the class P (predictable) is computed comparing the true labels (U/P) with the labels predicted by the green model. ii.d - Only cells predicted P in ii-b are conserved in the testing set defining a smaller testing set called truncated testing set. ii.e - the ML Pipeline (yellow model) is trained on the same training set than the green model, using the original labels T/S. ii.f - the yellow model is applied on the truncated testing set. ii.g - the MCC_j is computed comparing the output of the yellow model with the true labels of the cells from the truncated testing set.

8.1.2.2 Divide and conquer

The principle applied in the following is to use different models for each class. The term "model" is employed in the following sense: a model will be a set of features combined with a classifier that could be a machine learning classifier, like in Chapter 7, or another splitting technique like the threshold one [MP1]. Hence, we present two additional methods:

iii) **Separate early responders from the crowd:** This method is an up-grade of the current FATE-SEQ method. We first compute all the features from time-series classification models presented in Chapter 7, but also our mechanistic features (derivative, from mechanistic models, from statistics model or Fourier-type), then two features are selected, one for each drug-response. The tolerant feature will have the highest number of outliers for the tolerant cells (resp. sensitive cells) during the 2-fold cross-validation (cv1: TRAIL_Roux_25_2 is the training set and TRAIL_Roux_25_3 the testing set, cv2: the situation is reversed) according to the threshold criterion (cf Section 6.2). The duo tolerant feature/threshold - sensitive feature/threshold will be our new model.

iv) **One ML-model per class:** Another method that fully relies on machine learning consists in using a model (feature + classifier) per class. We will select the model with the highest true positive rate for tolerant cells (our positive class - resp. the highest true negative rate for sensitive cells), and optimize its hyperparameters to increase its precision for the class of interest. The two models will then forecast drug-response for all cells. Cells classified in opposite classes by the two models will be classified as unpredicted.

8.1.3 Programming

Chapter 7 identified a potential need for a better feature selection before applying any forecasting as using the entire feature set for each Time-Series Classification methods led to an accuracy too low for FATE-SEQ requirements.

8.1.3.1 Features computation

We compute all of our mechanistic features from Chapter 7, along with the Catch22 [Lubba et al., 2019] feature sets because the DrCIF model stood out in the last chapter, and we use this feature set as input. We will also compute the ComprehensiveFCParameters feature set from *tsfresh*.

The Catch22 features were computed with *sktime* library, the ComprehensiveFCParameters features with *tsfresh* library. Machine learning models, performance scores and feature selection were performed with *sklearn*. Mechanistic features (models' parameters and slope) are computed using Chapter 7 methods.

8.1.3.2 Features selection and model hyperparametrization

A first feature selection step is performed before any of the following tests by removing features with Not A Number values (NAN) and features with the same value for all cells. The remaining features define our feature set $\mathcal{F}$.

For ML methods i), ii) and iv) For the three methods including machine learning - i), ii) and iv) - the second step of feature selection consists in selecting 50 features $\mathcal{F}_{50}$ with the function *SelectKBest* from *sklearn* library, using the ANOVA F-value between each feature and the drug-response. Among them, most of the mechanistic features from Chapter 7 can be found: the three slopes , t_0 from Roux et al. model and the parameter β_1 of the FRETexp function. This method selected only one time point (50 min), but none of the features from Catch22, confirming that this set of features is not suitable for our short time-trajectories. The details of the parameter names according to the type of transformer used to extract features could be found in Appendix F.1 p.227. Finally, we still add the time points 30, 35, 40 and 45 min to $\mathcal{F}_{50}$, as they were in the feature set that had given the highest Matthews correlation coefficient (MCC) score previously Chapter 7.

The last selection step uses the *sklearn* function *SequentialFeatureSelector* with a forward direction. This function performs a 5-fold cross validation to select the set of features that leads to the highest mean selection score across the 5-fold cross-validations. It starts by selecting only one feature, testing all of them and keeping the one with the highest selection score. Then, at each step, it adds a new feature to the previous feature set, repeating the same testing operation (increasing the dimension of the feature space), until reaching the desired number of feature n. For each method, we tried different values for n (from 1 to 25) and kept the value with the highest mean selection score of our choice, denoted by N^{best}.

We will be using the MCC as selection score to select the features for the methods from the unpredictable cell class (i and ii). For the last method iv), we will carry two feature selections, one using the sum of MCC and TNR scores to create a model able to accurately identify sensitive cells (in our case the negative class), and the sum of the MCC score plus the Precision score, for the tolerant model. We add the MCC score to prevent the selection of constant classifiers, especially for the tolerant class. Similarly to Chapter 7, we choose to use MCC instead of MK, even though MK evaluates what is important for FATE-SEQ: cells selected for isolation inside - each predicted class - must be accurately classified, in others words we want a high precision for both classes. Once the feature selection is performed for all the methods, we will evaluate the performances of the models. Figure 8.3 p.159 shows the complete feature selection pipeline for the method iv).

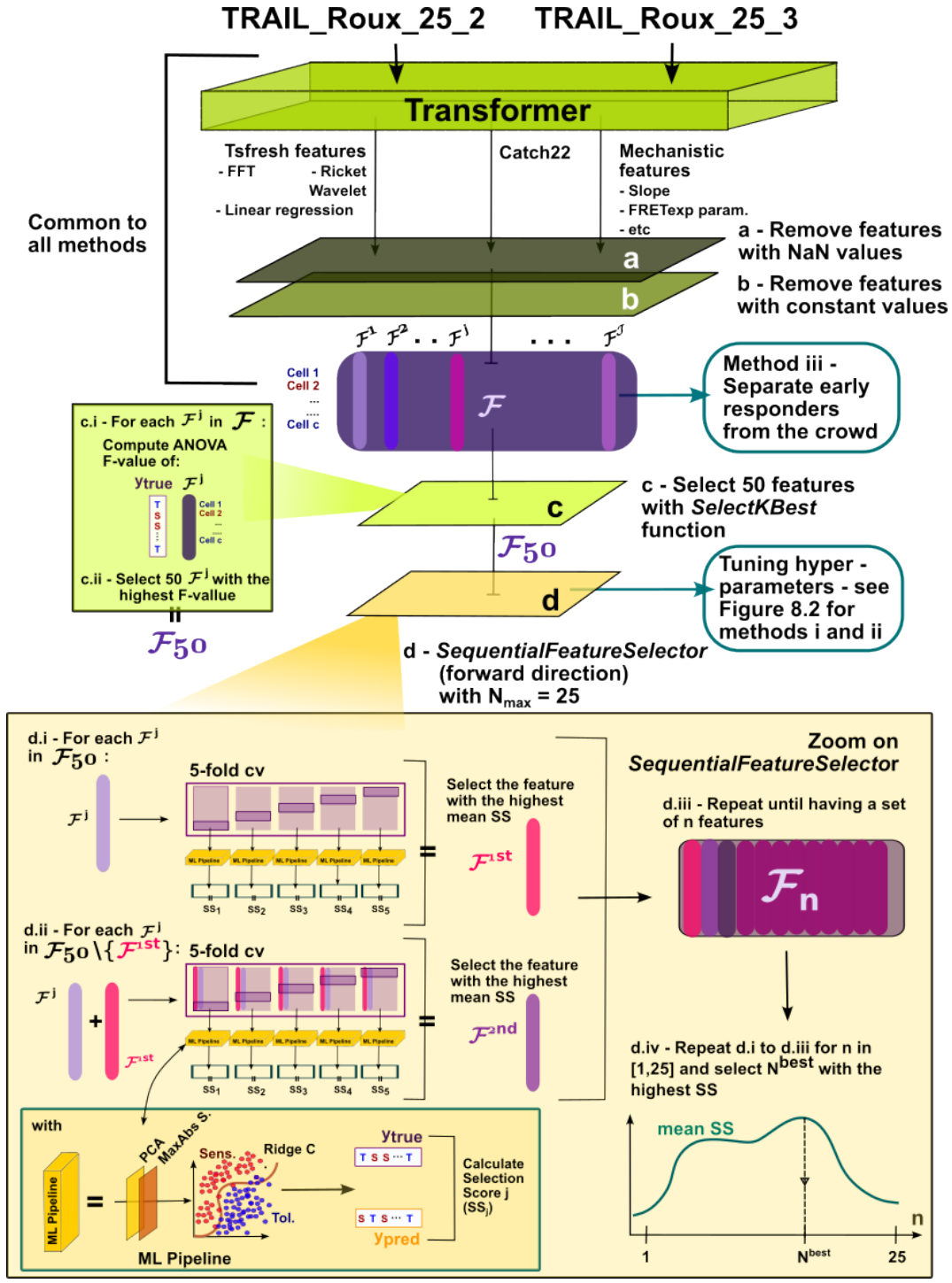

Figure 8.3: **Feature selection pipeline for the method iv):** After extracting the features with a transformer: a - Remove features with Not A Number value. b - Remove features with the same value for all cells. Our commom set of features for all the methods $\mathcal{F}$ is created. c - Apply *SelectKBest* function to create a feature set of 50 features by c.i - computing the ANOVA F-value for each feature in $\mathcal{F}$ with the drug-response vector y_{true} and c.ii - by selecting the 50 features with the highest F-values. These 50 features form $\mathcal{F}_{50}$. d - Apply *SequentialFeatureSelector* to select between 1 and 25 features to create the feature set with the highest mean selection score (SS) during a 5-fold cross-validation: d.i For each feature in $\mathcal{F}_{50}$, carry a 5-fold cross validation (cv) using this feature as input to our ML Pipeline (PCA + MaxAbs Scaler + Ridge Classifier) and computing the selection score. Select the feature $\mathcal{F}^{1st}$ with highest mean selection score. d.ii - For each feature $\mathcal{F}^j$ in $\mathcal{F}_{50} \setminus \{\mathcal{F}^{1st}\}$, compute mean selection score during 5-fold cross validation, using $\left\{\mathcal{F}^{1st}, \mathcal{F}^{|}\right\}$ as input features. d.iii Repeat the process until obtaining a set of n features ($\mathcal{F}^n$). d.iv - Repeat the process by making n varying between 1 and 25. Select the number of feature N^{best} and the corresponding $\mathcal{F}^{N^{best}}$ with the highest mean selection score. Finally, tuning the hyperparameters of the model. Prec. stands for Precision, SS for Selection Score, cv for cross-validation.

Models' hyperparameter tuning is done using bayesian optimization with the library *hyperopt*. We estimate the number of components for the PCA. For the Ridge classifier, we select the solver, the weights associated to each class and the regularization strength. To tune the hyperparameters for each model used in i), ii) and iv), we define a different cost to be minimized for each model.

$$\mathcal{C} = 1 - \frac{1}{5}\sum_{j=5}^{5} \text{Precision}_j \text{ (Tol. class)} - \text{Precision}_j \text{ (Sens. class)} \qquad (\mathcal{C} \text{ - i))}$$

$$\mathcal{C} = 1 - \frac{1}{5}\sum_{j=5}^{5} \text{Precision}_j \text{ (Predicted class)} \qquad (\mathcal{C} \text{ - ii) - Step 1)}$$

$$\mathcal{C} = 1 - \frac{1}{5}\sum_{j=5}^{5} \text{MCC}_j \qquad (\mathcal{C} \text{ - ii) - Step 2)}$$

$$\mathcal{C} = 1 - \frac{1}{5}\sum_{j=5}^{5} \text{Precision}_j \text{ (Tol. class)} - \text{MCC}_j \qquad (\mathcal{C} \text{ - iv) - Tol. Mod)}$$

$$\mathcal{C} = 1 - \frac{1}{5}\sum_{j=5}^{5} \text{Precision}_j \text{ (Sens. class)} - \text{MCC}_j \qquad (\mathcal{C} \text{ - iv) - Sens. Mod)}$$

For ii - step 1, we use the precision score for the predictable class, since cells in the unpredictable class would be discarded and not isolated nor profiled in the FATE-SEQ pipeline. Figure 8.2 (2) p.156 illustrates the hyperparametrization process for the unpredictable class methods i) and ii).

For iii) - Separate early responders from the crowd For this method, we will use the same technique as in FATE-SEQ, computing for each feature the recurrent number of non-overlapping cells for tolerant and sensitive cells. This time, we mean to identify a tolerant feature $\mathcal{F}^T$ with the highest $\mathcal{N}_T$, and a sensitive feature $\mathcal{F}^S$ with the highest $\mathcal{N}_S$ (see Chapter 6). More precisely, for each feature $\mathcal{F}^j$ in our feature set $\mathcal{F}$, we will start by computing our thresholds, for each replicate i. Here, we do not know for each feature if sensitive cell values tend to be greater or smaller than tolerant values. Therefore, we determine 4 thresholds per feature, instead of two (see Equation (6.3) and Equation (6.2) p.120 for the thresholds used in the current FATE-SEQ pipeline):

$$\mathcal{T}^i_{S_{sup}}(\mathcal{F}^j) = \max_{\text{cell in true tol. cells in rep. i}} \underbrace{\left(\mathcal{F}^j_{\text{tol. cells}}\right)}_{\text{Feature j value for each true tolerant cell in replicate i}} \qquad (8.1)$$

$$\mathcal{T}^i_{S_{inf}}(\mathcal{F}^j) = \min_{\text{cell in true tol. cells in rep. i}} \left(\mathcal{F}^j_{\text{tol. cells}}\right) \tag{8.2}$$

and respectively for the tolerant thresholds:

$$\mathcal{T}^i_{T_{sup}}(\mathcal{F}^j) = \max_{\text{cell in true sens. cells in rep. i}} \underbrace{\left(\mathcal{F}^j_{\text{sens. cells}}\right)}_{\text{Feature value for each sensitive cell}} \tag{8.3}$$

$$\mathcal{T}^i_{T_{inf}}(\mathcal{F}^j) = \min_{\text{cell in true sens. cells in rep. i}} \left(\mathcal{F}^j_{\text{sen. cells}}\right) \tag{8.4}$$

We then determine the number of non-overlapping cells $\mathcal{N}^i_{S_{sup}}(\mathcal{F}^j)$ verifying Equation (8.1) for each feature (resp. $\mathcal{N}^i_{S_{inf}}(\mathcal{F}^j)$ for Equation (8.2) and so on). The recurring number of non-overlapping cells per feature is given by:

$$\mathcal{N}_{S_{sup}}(\mathcal{F}^j) = \min_{i \in \text{rep.}} \mathcal{N}^i_{S_{sup}}(\mathcal{F}^j) \tag{8.5}$$

$$\mathcal{N}_{S_{inf}}(\mathcal{F}^j) = \min_{i \in \text{rep.}} \mathcal{N}^i_{S_{inf}}(\mathcal{F}^j) \tag{8.6}$$

$$\mathcal{N}_{T_{inf}}(\mathcal{F}^j) = \min_{i \in \text{rep.}} \mathcal{N}^i_{T_{inf}}(\mathcal{F}^j) \tag{8.7}$$

$$\mathcal{N}_{T_{sup}}(\mathcal{F}^j) = \min_{i \in \text{rep.}} \mathcal{N}^i_{T_{sup}}(\mathcal{F}^j) \tag{8.8}$$

Finally, for each threshold, we select the three features $\mathcal{F}^{1^{st}}$, $\mathcal{F}^{2^{nd}}$, $\mathcal{F}^{3^{rd}}$ with the highest recurring number of non-overlapping cells. For instance,

$$\mathcal{F}^{1^{st}}_{S_{sup}} = \max_{\mathcal{F}^j \in \mathcal{F}} \mathcal{N}_{S_{sup}}(\mathcal{F}^j) \tag{8.9}$$

$$\mathcal{F}^{2^{nd}}_{S_{sup}} = \max_{\mathcal{F}^j \in \mathcal{F} \setminus \{\mathcal{F}^{1^{st}}_{S_{sup}}\}} \mathcal{N}_{S_{sup}}(\mathcal{F}^j) \tag{8.10}$$

$$\mathcal{F}^{3^{rd}}_{S_{sup}} = \max_{\mathcal{F}^j \in \mathcal{F} \setminus \{\mathcal{F}^{1^{st}}_{S_{sup}}, \mathcal{F}^{2^{nd}}_{S_{sup}}\}} \mathcal{N}_{S_{sup}}(\mathcal{F}^j) \tag{8.11}$$

Let us define F^S as the set of features maximizing $\mathcal{N}_S(\mathcal{F})$, that is:

$$F^S = \underset{\mathcal{F}\in\left\{\mathcal{F}^{1st}_{S_{sup}},\mathcal{F}^{2nd}_{S_{sup}},\mathcal{F}^{3rd}_{S_{sup}}\mathcal{F}^{1st}_{S_{inf}},\mathcal{F}^{2nd}_{S_{inf}},\mathcal{F}^{3rd}_{S_{inf}}\right\}}{\text{argmax}} \mathcal{N}_S(\mathcal{F}). \tag{8.12}$$

Finally, we select $\mathcal{F}^S \in F^S$ such that

$$\mathcal{F}^S = \underset{\phi\in F^{S.}}{\text{argmin}} \left|\mathcal{N}_S^{\text{TRAIL\_Roux\_25\_2}}(\phi) - \mathcal{N}_S^{\text{TRAIL\_Roux\_25\_3}}(\phi)\right|. \tag{8.13}$$

The definition of $\mathcal{F}^S$, given by Equation (8.13), ensures similar numbers of non-overlapping cells across replicates and therefore less differences between training and testing in the future. The process is identical for tolerant cells. In the case that a cell is identified as sensitive AND tolerant with this method, it will be not be selected for isolation.

8.2 Performances

For the four methods presented above, we will perform the same evaluation than in Section 6.2 p.118, counting the proportion of cells predicted and the accuracy of the prediction. The objective is to keep the same accuracy (more than 90 %) but predict more cells (more than 1 %).

We first present the results of the feature selection and then analyse the performances of the four methods.

8.2.1 Feature selection for machine learning methods

Surprisingly, using mechanistic features from phenomenological models, which are more realistic, lead to the poorest selection scores for drug-response forecasting and these features were not chosen as relevant by any of the selection methods, similarly to the FRET time-points that were not chosen neither.

Select. Score	MCC	ACC	F1	BACC	Prec.	Rec.	MK	TNR	# feat	Type of feature
MCC	0.276± 0.112	0.635± 0.057	0.639± 0.055	0.636± 0.056	0.616± 0.065	0.673± 0.099	0.281± 0.111	0.664± 0.057	14	Slopes, location of minimum, Auto-correlation coef., t_0 from Roux et al., change in quantiles, linear regression param., Fourier Transform param. and param. of the continuous wavelet transform for the Ricker wavelet
MCC + TNR	0.271± 0.08	0.631± 0.041	0.644± 0.043	0.633± 0.041	0.605± 0.039	0.696± 0.089	0.275± 0.079	0.67 ± 0.049	11	Similar to MCC features
MCC + TPR	0.165± 0.064	0.565± 0.015	0.29 ± 0.05	0.552± 0.014	0.724± 0.165	0.186± 0.042	0.272± 0.166	0.548± 0.01	2	Param. controlling the imaginary part in Fourier Transform spectrum + Change in quantiles

Table 8.1: Performance scores obtained after 5-fold cross-validation on Roux et al. TRAIL_Roux_25_2 and TRAIL_Roux_25_3 replicates combined using CFP/FRET after feature selections. First column gives the score used to select the feature with the function *SequentialFeatureSelector*

8.2.2 Feature selection iii) - separate early responders from the crowd

Figure 8.4(b) shows the results of the feature selection for the iii) method.

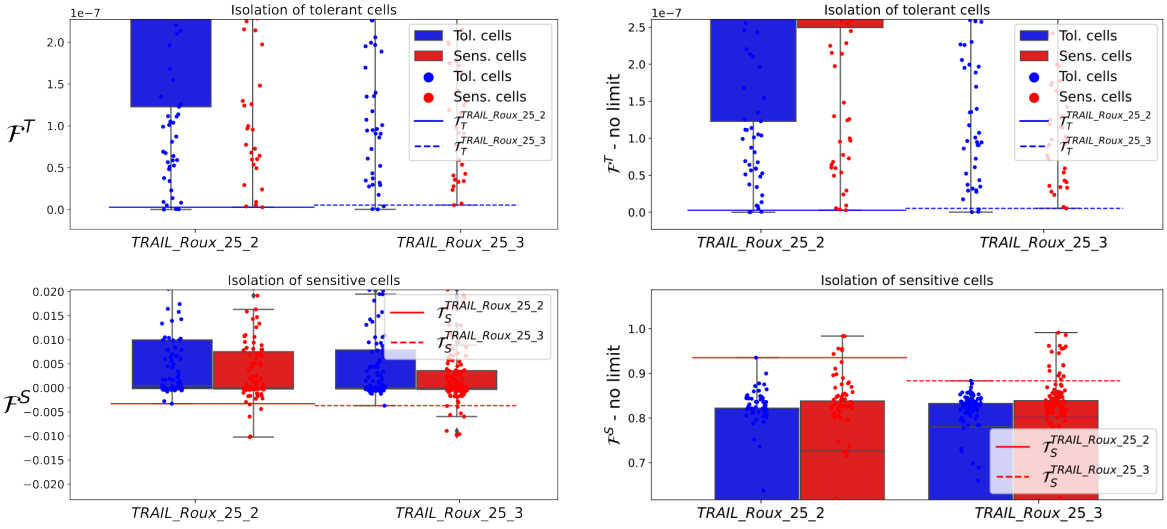

(a) A limit of three cells maximum in the difference between $\mathcal{N}$ and $\mathcal{N}_i$ for each replicate i is fixed

(b) No limit in the difference between $\mathcal{N}$ and $\mathcal{N}_i$ for each replicate i is fixed

Figure 8.4: **Selected portions of boxplots of $\mathcal{F}^T$ (top) and $\mathcal{F}^S$ † (bottom) for TRAIL_Roux_25_2 and TRAIL_Roux_25_3 from CFP/FRET datasets of Roux et al. when and without imposing a maximal difference in the number of outliers cells between the replicates during feature selection.** X-axis represents the true drug-response for each cell (blue: tolerant, red: sensitive) in each replicate, Y-axis shows the cell value for the selected feature.

With some features, like 'value__linear_trend__attr_"rvalue"' [‡] from tsfresh feature set, we can isolate up to 16 sensitive cells in TRAIL_Roux_25_3, but only 6 in TRAIL_Roux_25_2, therefore we decided to discard features with a difference of more than 3 cells isolated per replicate. In other words, (sensitive or tolerant) features $\mathcal{F}^j$ satisfying:

$$\max_{i \in \{TRAIL\_Roux\_25\_2, TRAIL\_Roux\_25\_3\}} |\mathcal{N}_i(\mathcal{F}^j) - \mathcal{N}(\mathcal{F}^j)| \geq 3 \tag{8.14}$$

will not be considered even though they have a higher recurring number of overlapping cells.

Figure 8.4(b) and Section 8.2.2 also highlight the substantial differences between two replicates even though they have a similar balance between tolerant and sensitive cells. These figures also demonstrate the need to have several replicates of the same experiment during feature and model's selection but also for training to avoid selecting features that "over-fit" one replicate.

Eventually, $\mathcal{F}^S$ corresponds to one of the "parameters of the continuous wavelet transform for the Ricker wavelet" from tsfresh feature set (quote from tsfresh documentation) - $\mathcal{F}^S = value\_\_cwt\_coefficients\_\_coeff\_2\_\_w\_2\_\_widths\_(2,5,10,20)$ - and $\mathcal{F}^T = value\_\_change\_quantiles\_\_f\_agg\_"var"\_\_isabs\_True\_\_qh\_0.8\_\_ql\_0.0$, that calculates the variance between 0 and 40 minutes of experiment, from tsfresh feature set too. Once again no mechanistic features were selected which questions the pertinence of using these features as key features to link cell dynamics and cell decision even at 10h of experiment. On the other hand, tsfresh features could be applied to any type of time-trajectories and create the opportunity of applying our pipeline to other signaling pathways or other type of drugs as the features are not obtained from parameters of a phenomenological model therefore do not require prior knowledge of the underlying biology.

8.2.3 Applying the methods

To evaluate the performances of our four methods, we use one replicate as training and one replicate as testing to reproduce the experimental conditions of FATE-SEQ. We then reverse the roles of each dataset to carry a 2-fold cross-validation. The Table 8.2 p.165 presents the results obtained, in a similar way to Chapter 6.

Table 8.2 identifies the method iii) as the best method to forecast accurately cells drug-response for the biggest number of cells with an accuracy greater than 0.9 and very high precision for both classes too. The method represents a significant increase in the number of

[‡] that "calculates a linear least-squares regression for the values of the time series versus the sequence from 0 to length of the time series minus one", with r value representing the proportion of variance of the signal FRET explained by the linear regression model (from tsfresh documentation)

Testing set	TRAIL_Roux_25_2	TRAIL_Roux_25_3	mean	std
Dataset description				
N cells in testing	221	327	297.333	54.42
% tol. cell. in replicate	51.131	45.872	56.559	11.596
i) 3rd class				
i - % of cell pred. for iso. in test	86.88	19.57	53.225	33.655
i - # cell pred. sen. for iso. in test	72	23	47.5	24.5
i - # cell pred. tol. for iso. in test	119	41	80.0	39.0
i - ACC on test	0.557	0.672	0.614	0.057
i - Precision tol. class	0.546	0.585	0.566	0.019
i - Precision sens. class	0.575	0.826	0.7	0.126
ii) 2-step forecasting				
ii - % of cell pred. for iso. in test	17.19	52.91	35.05	17.86
ii - # cell pred. sen. for iso. in test	32	117	74.5	42.5
ii - # cell pred. tol. for iso. in test	6	56	31.0	25.0
ii - ACC on test	0.474	0.566	0.52	0.046
ii - Precision tol. class	0.16	0.446	0.303	0.143
ii - Precision sens. class	0.53	0.624	0.577	0.047
iii) Separate early responders from the crowd				
$\mathcal{N}_T$	3	3	-	-
$\mathcal{N}_S$	5	5	-	-
$\mathcal{N}_T^{\text{train}}$	3	3	-	-
$\mathcal{N}_S^{\text{train}}$	5	8	-	-
$\mathcal{N}_T^{\text{test}}$	3	3	-	-
$\mathcal{N}_S^{\text{test}}$	8	5	-	-
iii - % of cell pred. for iso. in test	4.98%	2.45%	3.715%	1.265%
iii - ACC on test	0.818	1	0.909	0.09
iii - Precision tol. class	1	1	1	0
iii - Precision sens. class	0.75	1	0.875	0.125
iv)1 ML-model per class				
iv - % of cell pred. for iso. in test	29.86	59.63	44.745	14.885
iv - # cell pred. sen. for iso. in test	38	0	19.0	19.0
iv - # cell pred. tol. for iso. in test	28	195	111.5	83.5
iv - ACC on test	0.621	0.559	0.59	0.031
iv - Precision tol. class	0.679	0.559	0.619	0.06
iv - Precision sens. class	0.577	0	0.278	0.278

Table 8.2: Dataset description and performances of the 4 new methods for drug-response forecasting used to identify cells for selection in the FATE-SEQ pipeline during 2-fold cross-validation on CFP/FRET dataset from Roux et al using only the replicates TRAIL_Roux_25_2 and TRAIL_Roux_25_3 - tol. : tolerant, sen.: sensitive, pred. predicted, iso.: isolation, std: standard deviation. In yellow, best mean accuracy in precision for both classes. Results for i) ii) and iv) without tuning the hyperparameters can be found in Table F.25 p.228. For iii) no cells were predicted tolerant and sensitive at the same time. Results for iii) using initial 1/FRET with different SG filters were identical but other features from tsfresh feature set were used.

cells isolated, compared to the current FATE-SEQ method, from 1 to 3 for tolerant cells and 1 to 5 for the sensitive which triples the percentage of the cells isolated, conserving a similar accuracy.

On the other hand, Table 8.2 shows a substantial gap between the precision and accuracy obtained with the method iii) and the scores reached by the other methods. In addition to much higher performance scores, this method benefits also from a bigger explainability as the thresholds

used to identify non-overlapping cells could be drawn on a box-plot.

Finally, even though the two replicates have a similar balance tolerant/sensitive cells, the disparities across the two are significant. A difference of 67 cells isolated between TRAIL_Roux_25_2 and TRAIL_Roux_25_3 for the method i) must be noticed. The method iv) did not isolate a single cell as sensitive for replicate TRAIL_Roux_25_3 whereas it reached a precision of 0.577 for the sensitive class on 28 isolated cells as sensitive in TRAIL_Roux_25_2. Therefore, a small difference in the balance of the dataset could have a real impact on the accuracy of the forecasting in a new dataset. These different balances can also be a sign of bigger differences at the level of the population dynamic between the replicates. These differences prevent us to use hyperparametrization on only one replicate that could result in increasing the effects of over-fitting on the performances. This last remark is confirmed by the better accuracy and precision obtained with the three methods i), ii) and iv), when no hyper-parameter tuning is performed (see Table F.25 p.228).

8.3 EASIDRUG forecaster: Final pipeline in the lab

8.3.1 Benefits of "Separate Early responders from the crowd" and new questions raised

The "Separate early responders from the crowd" method stood out in the last section, with certainly less cells forecast compared to the three other methods implemented, but a significantly higher accuracy and precision, and still a number of isolated cells multiplied by three, compared to the current method used in the lab.

Moreover, this method presents a considerable advantage compared to the current FATE-SEQ method. The features used in "Separate early responders from the crowd" are not extracted from any phenomenological model and therefore do not require any prior knowledge about the biology underlying the molecular process and its dynamics. Therefore, the same methodology (same feature transformers, feature selection steps identical and cell identification based on non-overlapping cells) has a high potential in the application of FATE-SEQ to others systems less known.

On the other side, the performances of this method raise new scientific questions and challenge on our current knowledge about sensitive and tolerant dynamics. Indeed, the feature selection step in this method (see Figure 8.4(b)) has demonstrated that using the r value (obtained after a linear regression of the time-trajectories) to identify sensitive cells, and the variance (of the time-points between the beginning of the experiment and the 40 minutes time-point) for the tolerant ones, could accurately isolate up to 17 cells in the same replicate. These features are classic descriptive features for time-series but they question the biological meaning of their ability to forecast cell

drug-responses and what they tell us about the characterization of sensitive and a tolerant dynamics.

Moreover, having methods and algorithms to compute a large panel of feature sets already implemented will help us to re-assess the questions tackled in this part on new datasets obtained, obtained with the new setup for instance, in the future.

In the following, we will first compare this method with the current FATE-SEQ method for cell selection for isolation, to identify which cells could not be forecast with the previous method. Then we will schematize the full pipeline to be implemented in the lab to create our EArly Single-cell Isolation with a Drug Response Up-Graded forecaster and give a brief overview of the output of the pipeline applied on CFP/FRET dataset from Roux et al.

8.3.2 Link with the previous method

Surprisingly, cells identified with the current FATE-SEQ method - based on the FRET slope feature - were not the ones that were identified using the "Separate early responders from the crowd" technique, and vice-versa.

Figure 8.5 p.168 illustrates the differences, according to the FRET slope feature. Cells predicted by our new method are actually cells in the middle of the overlapping zone for the FRET slope value at 50 min (in grey in Figure 8.5). Indeed, two cells with similar dynamics according to our current criterion based on the FRET slope - meaning with the same FRET slope value at 50 min (or even at 10h of experiment), could be accurately identified as a sensitive cell for one and as tolerant cell for the other with a different criterion - because they have very different values for the $\mathcal{F}^S$ feature for instance. See Figure F.18 p.229 for the boxplot with a slope computed on 10h-experiment data.

Figure 8.6 shows the 10-h time-trajectories of cells isolated with EASIDRUG. Indeed, at 50 minutes this figure confirms what the feature selection for the sensitive cells were assessing, that is, sensitive cells seem to have a clear linear trajectory before 50min of experiment.

Once again these results challenge what we know about the links between cells dynamics and cell responses for TRAIL-inducing apoptosis, even inside the same class, where all cells commit to apoptosis. Further investigations will be needed to understand the causes of the differences between cells that are isolated with the feature r-value from the linear regression (method iii) "Separate early responders from the crowd"), and the cells identified thanks to their high FRET slope value.

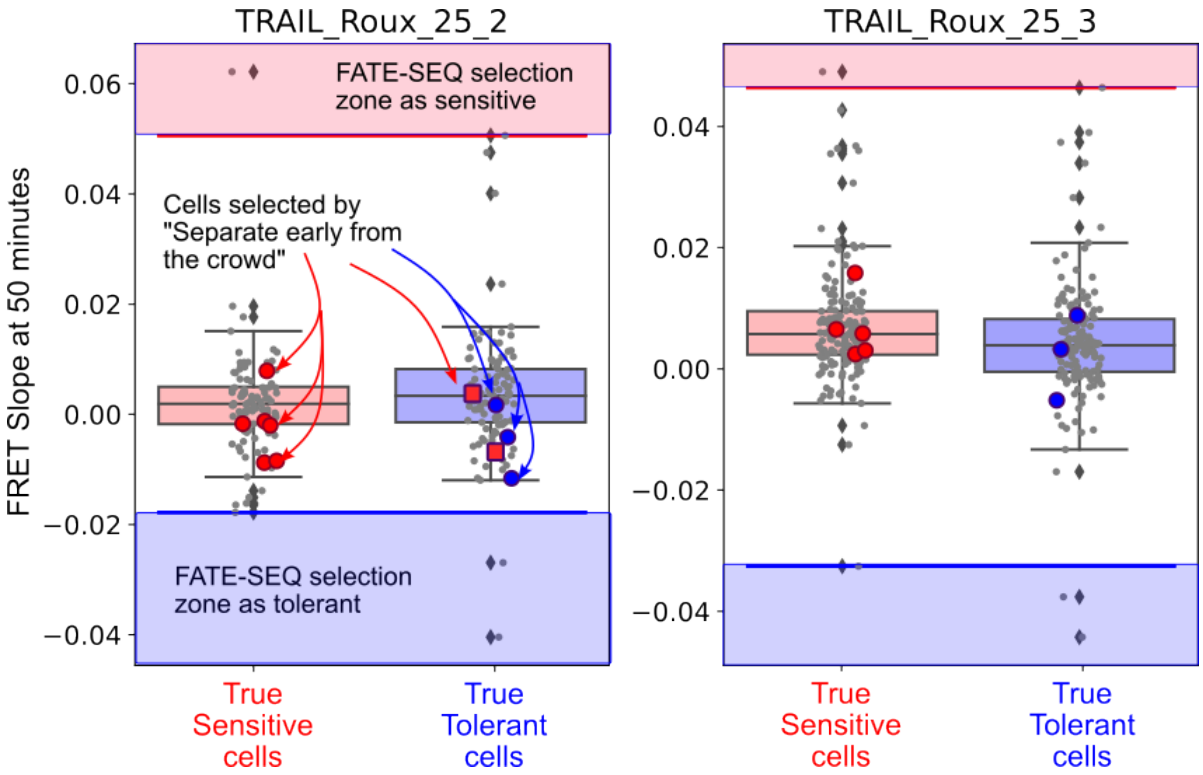

Figure 8.5: **Comparison box-plot of cells identified with the current FATE-SEQ method using the slope feature (boxplots and grey points) and cells identified with the method "Separate early responders from the crowd" (red and blue).** All the features were computed after 50 min of experiment. Each subplot represents the testing replicate set, thresholds and number of non overlapping cells for each method were determined on the other replicate. Each boxplot represents the true cell drug-response (sensitive on the left, tolerant on the right). For instance cells in the left boxplot were identified as sensitive during the 10h experiment. The y-axis represents the value of the FRET slope at 50 min for each cell. Cells above the red threshold, in the light red zone, were isolated as sensitive and cells below the blue threshold, in the light blue zone, were isolated as tolerant with the current FATE-SEQ method based on their FRET slope value. Red dot cells were accurately isolated as sensitive and blue dot cells as tolerant with the method "Separate early responders from the crowd", using a parameter of the continuous Ricker wavelet transform applied on the time-trajectories to identify sensitive cells and the variance of the time-points between the beginning of the experiment and the 40 minutes time-point for tolerant ones. Red squares are cells inaccurately isolated as sensitive with the method "Separate early responders from the crowd" whereas they were actually drug-tolerant during the experiment (in the right boxplot). FRET slope were computed on 1/FRET filtered with a SG filter of window 9 like in Figure 6.1 p.122. See Section 8.2.2 p.163 for the boxplots obtained with "Separate early responders from the crowd" features

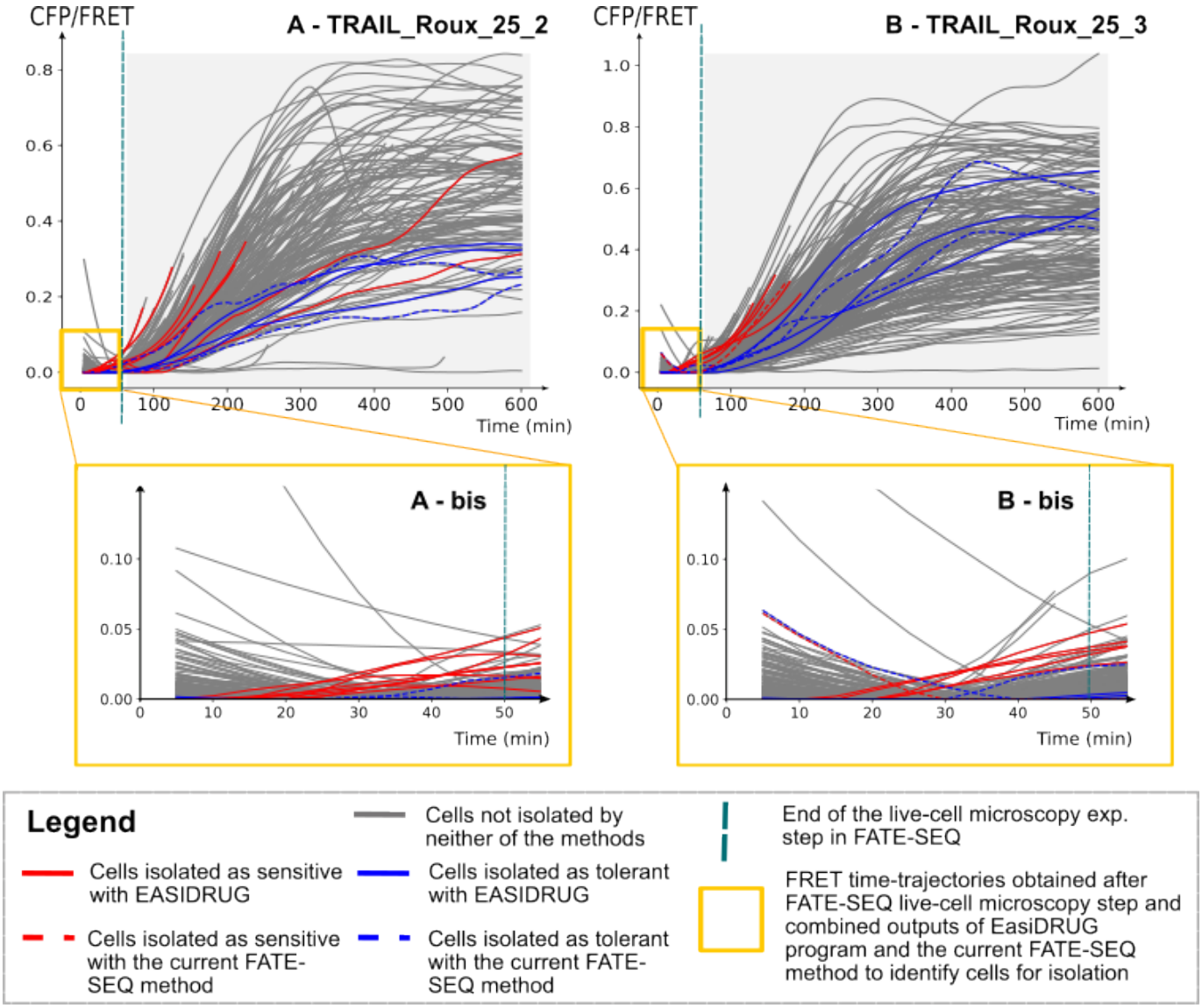

Figure 8.6: **Comparison of the EASIDRUG method with the current FATE-SEQ method to select cells for isolation on Roux et al. CFP/FRET dataset (TRAIL_Roux_25_2 and TRAIL_Roux_25_3):** A - 10h time-trajectories from TRAIL_Roux_25_2 when this replicate is the testing set, A-bis: zoom on the first 50 min of experiment used as input for the selection methods and cells isolated by the two methods. B - 10h time-trajectories from TRAIL_Roux_25_3 when this replicate is the testing set, B-bis: zoom on the first 50 min of experiment used as input for the selection methods and cells isolated by the two methods. Blue: cells isolated as tolerant by EASIDRUG (plain line) or by FATE-SEQ current method (dashed), red: cells isolated as sensitive by EASIDRUG (plain) or by FATE-SEQ current method (dashed), gray: cells non isolated

8.3.3 Integration in the experimental workflow

Figure 8.7 p.171 illustrates how EASIDRUG will be integrated in the FATE-SEQ pipeline. In this figure, we only show when one feature per drug-response is used but we can use several features for each drug-response - for instance the FRET slope and the coefficient of the Ricket Wavelet transform for the sensitive cells - to increase the number of cells isolated for profiling. The training pipeline integrates the necessity to perform several replicates of the same experiment and the adaptation of EASIDRUG to each type of drug, cell line and phenotype as the transformers are not specific to TRAIL-inducing apoptosis and the IC-RP FRET signal.

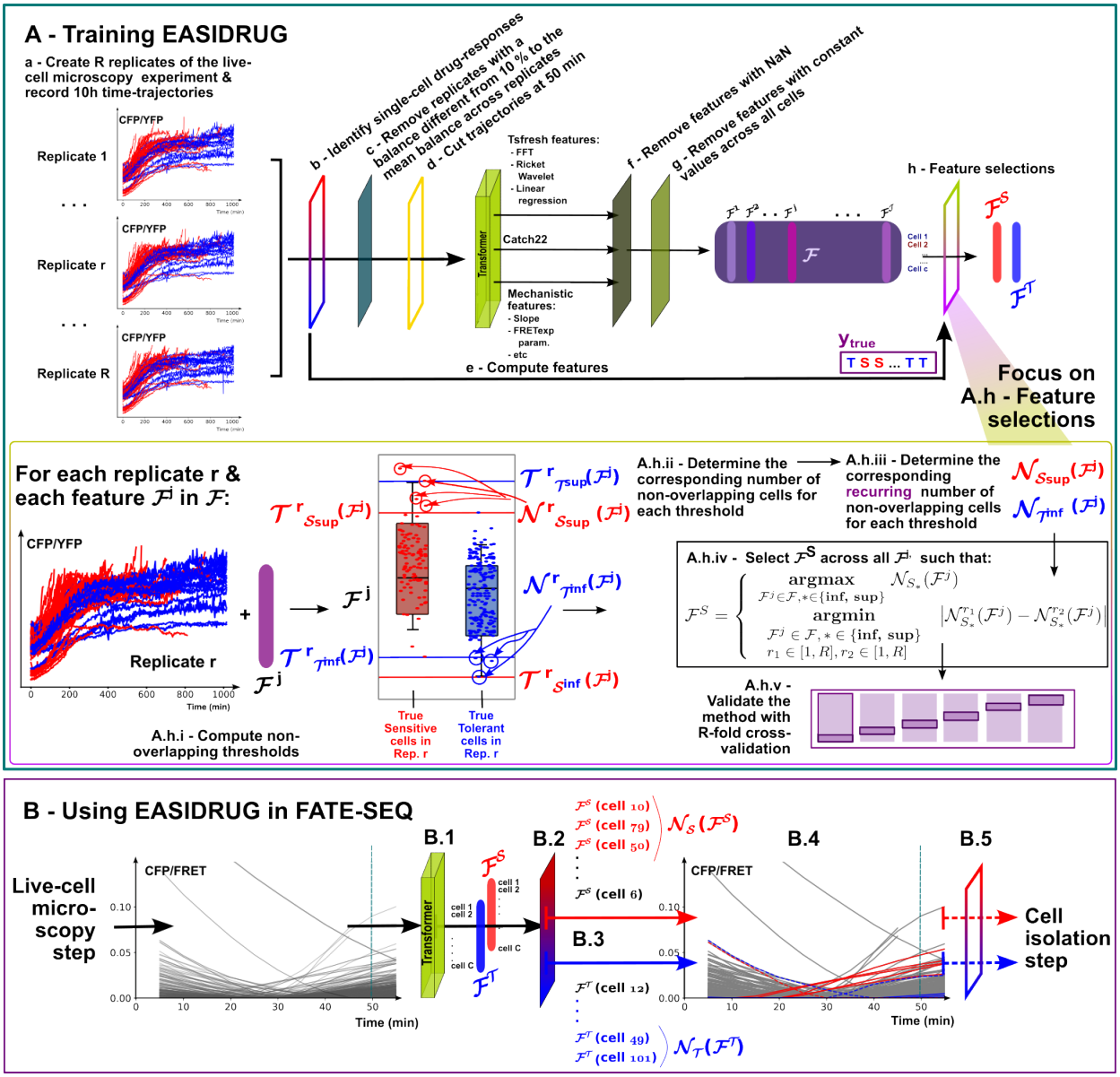

Figure 8.7: **EASIDRUG Pipeline - training and application in FATE-SEQ: A - Training EASIDRUG**: A.a - Create R replicates of the live-cell experiment where clonal cancer cells are treated with a cytotoxic drug at its IC50 at the beginning and then observed for 10 hours. A.b - Identify tolerant and sensitive cells after 10 hours. A.c - Remove replicates with a different balance tolerant/sensitive cells higher than 10 % of the mean balance across the replicates. A.d - Cut the trajectories at 50 min. A.e - Compute the features from the 50-min time-trajectories (preprocess the time-trajectories + apply transformers). A.f - Remove features with Not A Number values (NaN). A.g - Remove features with the same value for all cells. A.h - Apply feature selection from method iii) "Separate early responders from the crowd": A.h.i - Compute the four non-overlapping thresholds for each replicate and each feature. A.h.ii - Compute the number of non-overlapping cells corresponding to each threshold, each replicate and each feature. A.h.iii - Compute the recurring number of non-overlapping cells across the replicates. A.h.iv - Select $\mathcal{F}^S$ and $\mathcal{F}^T$ such that they verify Equation (8.12), Equation (8.13) and Equation (8.14). A.h.v - Validate the features with a R-fold cross-validation. **B - Apply EASIDRUG during FATE-SEQ**: B.1 - Compute the $\mathcal{F}^S$ feature (resp. $\mathcal{F}^T$). B.2 - Cell ranking according to $\mathcal{F}^S$ values (resp. $\mathcal{F}^T$). B.3 - Select $\mathcal{N}^S$ (resp. $\mathcal{N}^T$) + 50% x $\mathcal{N}^S$ more cells B.4 - Plot the selected cell time-trajectories in red (resp. in blue), the rest in gray (for comparison basis) B.5 - Final selection by the biologist among the cells selected by EASIDRUG

8.4 Discussion and link with Chapter 7

This chapter confirms the results of Chapter 7. The machine learning models used to forecast cell drug-response reach an accuracy too low to be included in the FATE-SEQ pipeline, despite a bigger number of cells forecast. Their lack of explainability is also a problem to assess why cells are discarded. However, using the transformers from time-series classification models to extract new features from the time-trajectories brings new benefits. They allow to select more cells for isolation but more importantly, these features are independent from any phenomenological models and do not require prior knowledge about cells dynamics. Therefore, they allow our new method to select cells for isolation, EASIDRUG, to be more flexible and can be adapted to any type of cells or drugs.

But these new selection features lead us to question the links between cell dynamics and cell response. Our results point to relevance of features specifically dedicated to describing the dynamics at the beginning of the experiments. It also emerges that none of the current mechanistic parameters were used as a selected feature. One possible direction for further investigation is thus the finding of new mechanistic parameters for a closer description of the initial trajectory before 50 min of experiment.

In the future, a better identification of the first time TRAIL impacts the cell state will be necessary to exactly know until which time-point we can compute our features. This chapter also highlighted the need to carry several replicates of the same experiment, with an increased number of cells. More than just a larger training set, repeating the experiment could also help us deciphering the causes of such big differences across the replicates, in term of balance sensitive/tolerant cells but also most importantly from the dynamics point of value. We need to better understand the global dynamics of a replicate that could explain the wider range of values for the slope feature observed in replicate but also the different proportions of emerging tolerant cells that *in fine*, has a real impact of the pharmacological profile of the drug under study. Through these repeated experiments, we could also understand the dynamical differences within the sensitive class at 50 min.

PART IV

Conclusions and Perspectives

This thesis explored different mathematical methods and algorithms for single-cell and computational biology analysis, to study the emergence of TRAIL-tolerant persisters. We investigated, implemented and combined different methodologies to obtain a more thorough and complete analysis of the single-cell time-trajectory data from live-cell microscopy experiments available on HeLa cells treated with TRAIL.

This chapter aims at summarizing this thesis' contributions and, in particular, how they answer the questions raised in Chapter 3, thus a parallel structure may be established between Chapter 3 and Part IV. Finally, we will also discuss new perspectives raised by our work and its potential applications.

Our Systems pharmacology approach and the example of TRAIL

In the beginning of this work, we pointed out the importance of creating rational and systematic pipelines to identify potential biomarkers of drug-tolerance, namely for designing combination-therapy from the first step of pre-clinical development. Behind these two statements, lies the urgent need to improve the current treatments available in oncology, and the process of cancer drug-design. As the efficacy of a cancer drug is directly linked to the number of drug-tolerant persisters emerging after a treatment, understanding the mechanistic processes underlying the emergence of these cells is a decisive step towards controlling their numbers, and *in fine* increase the drug efficacy.

Our Systems pharmacology approach, presented in Chapter 1, links cell signaling, cell dynamics and cell decision. This approach, and the methods (programming, single-cell analysis, image processing, etc) employed to build it, take advantage of the systematic emergence of drug-tolerant persisters in tumoral populations, to make a first step toward better cancer treatments. In a previous work [Meyer et al., 2020], we created FATE-SEQ, a rational method to identify biomarkers of drug-tolerance, but also potential therapeutic targets for combination therapy. FATE-SEQ forecasts drug responses of isogenic cancer cells, just after treatment, to profile the innate state of the cells, according to their forescast drug-response. Molecules with striking differences between drug-tolerant and drug sensitive states are identified as biomarkers of drug-tolerance/sensitivity, or as potential targets with the ability to influence drug-response. In Chapter 2, we presented the state-of-the-art of TRAIL *modus operandi* in isogenic cancer cells, that led us to the first proof of concept of FATE-SEQ with TRAIL on clonal Hela cells.

Even though the results of this proof of concept validated the approach, they also showed its limitations: a low number of cells studied. Hence, the project of this thesis was to **propose an improved modeling of TRAIL induced-apoptosis to identify finer predictive features of cell fate decision. These new features are computed from the fluorescent FRET time-trajectories,**

used in the FATE-SEQ pipeline, to observe and forecast cell dynamic after TRAIL binding.

This single objective brought several challenges and constraints. The first challenge was the size of the models to be proposed. The time-trajectories used in the pipeline are relatively short, with only 10 time-points for some of them to preserve the innate state of the cell from the drug effects, constraining us to create models with few parameters to estimate. On the other hand, as the cells studied are isogenic, we assumed from the outset, that most of the cells were following the same signaling pathways with an identical topology. Therefore, the values of the parameters constituted our main leverage to reproduce the cell heterogeneity observed. The second challenge was the new setup for FATE-SEQ: to increase the number of cells profiled, the experimental setup was customized to increase the cell isolation capacity, going from 4 cells to 100. This customization came along with other changes such as the fluorescence technique (using CFP/YFP ratio instead of CFP/FRET), and the choice of Python as the main programming language (instead of Matlab). To develop a suitable analysis algorithm for this new setup, we had to make choices about the datasets used, between a high number of cells from Roux et al. article, and a smaller dataset but closer to the current setup from Meyer et al. Eventually, we decided to use Roux et al. datasets but keeping in mind during the coding part and the results analysis that our programs will be used to other datasets and therefore could be easily adapted.

Modeling apoptosis, precision and analytic constraints

Chapter 4 tackled the first challenge presented above. The goal was to determine a mathematical model of the core reactions involved in TRAIL-inducing apoptosis, upstream of the effector caspases activation, that would be able to reproduce the heterogeneity of cell responses observed in real conditions during a live single-cell imaging experiment. To measure the ability of the models to reproduce certain dynamics, we used 3 features describing FRET signals, inspired by Roux et al. [Roux et al., 2015]. Each of the four models was fitted for each cell and then ranked according to their ability to reproduce the features for all cells. This study identified the cluster C8/C10 and the feedback loop from downstream on caspase 8 as the key reactions in the process but also highlighted the necessity to refine the TRAIL - receptor binding step and include the pro-caspase/caspase 8 relation in our model.

Following Chapter 4 conclusions, Chapter 5 proposed a more complete model of Extrinsic Initiation Core Reactions (EAICR), that was simplified to obtain a piecewise explicit solution: FRETexp. By estimating the parameters of rEAICR on the datasets of Roux et al, we were able to: first locate a first cell decision stage just after TRAIL binding; second, determine that an increase in TRAIL affects the dynamic of isogenic cells and amplifies the gap between drug-tolerant and drug-sensitive cells. More importantly, using the parameters of the FRETexp function, we were

able to predict cell drug-response at 6h for most of the cells treated with the IC50 of TRAIL during Roux et al. experiments, thus outperforming all the methods available. Although the method showed a poor ability to forecast cell TRAIL-response before 6h, it was a first step to improve the cell isolation step for the FATE-SEQ pipeline and showed the benefits of using mechanistic features from fine-tune models to predict cell-drug-response.

Perspective: Considering the specific innate time of each cell

Chapter 5 also brought strong evidence that timing is key in cell decision, confirming the results of [Paek et al., 2016]. More generally, drug-tolerant persisters (and cancer cells in general) have a slower cell cycle [Vallette et al., 2019].

Extrapolating this idea of a different time management for each cell, we could include this differential time processing by choosing a fractional order for the derivative of our EAICR, an order to be estimated for each cell. Indeed, A.A. Stanislavsky [Stanislavsky, 2006] have shown that replacing the classic conception of inner time as linear and continuous in a system, by independent and identically distributed positive random variables following a stable law of order α, the system derivative order 1 turns into a fractional order α. Our assumption would be that the random variables correspond to the different time intervals that cells stay in a given state (for example the cell cycle states). Therefore, by a simple fractional folding, we could integrate in our model the impact of cell inner time heterogeneity.

In addition, this type of fractional model showed a strong ability to reproduce large systems just by changing the derivative order [Riu, 2001, Chen et al., 2021, Mansouri et al., 2010]. Hence, they could be a good option to simulate *in silico* the different pathways involved in cell decision but keeping a reasonable number of variables in the model.

Perspective: Modeling population behaviour to propose better drug metrics

In Part I, we presented the benefits of including cell lineage and population behaviour in the metrics that evaluate drug efficacy in cell-based assays. For now, the first attempt to create new pharmacometrics uses general probabilistic models [Comandante-Lou et al., 2020]. Hence, one possible extension of the work of Part II could be the integration of cell lineage events (division, cell death, quiescence, etc) in our model, but also cell-cell communication and multi-scale modeling [Surdutovich and Solov'yov, 2019, Warner et al., 2019]. The objective would be to integrate different levels of regulation and heterogeneity in our model, and even go to the tumor scale [Rahman et al., 2017], starting by coupling a single-cell model with a population system like [Kallenberger et al., 2014]. This way we could take into account the tumor environment and the

impact of the population on the single-cell behaviour to propose more precise metrics. These metrics could evaluate the impacts of a drug beyond the population final balance sensitive/tolerant and instead integrates the dynamic of each cell all along the experiment or measure the impact of the drug at the tumor scale to have a longer term vision considering not only the in vitro single cell experience but also future tumour scale experiments.

This multi-scale modeling of pharmacodynamic could open the way to design optimal drug-input *in silico*. Our EAICR model already demonstrated its ability to reproduce TRAIL-dose response in single-cell experiments. We can then conceive to use the same model to test the effects of other drugs on TRAIL-induced apoptosis. By applying optimal control theory, we could calculate the best drug dose and the ideal input time in our cells so that a maximum of tolerant cells become sensitive and eliminate drugs with the lowest efficacy (according to our new pharmacological metrics) already *in silico* [Das et al., 2021], as [Mikubo et al., 2021] expressed the necessity in their review.

This better evaluation of drug-efficacy in single-cell experiments goes along with a better modeling of inter-cell communication [AlMusawi et al., 2021, Armingol et al., 2021]. In this thesis, we have deliberately neglected the impact of the population on the cells. Therefore, as a first step to understand how cells communicate when they are reacting to death-ligands and commit to apoptosis, we also plan to couple several EAICR models (cf Chapter 5), with parameter sets corresponding to sensitive and tolerant states, with different coupling methods and topologies. The idea is to represent cell-cell communication whether via gap junction (cellular bridges that connect two cells via their cytoplasm, composed of connexins, which are altered in cancer cells), or by releasing metabolites [Medina et al., 2020] as inter-cellular messengers, but also to take into account the spatial geometry of the cells. Experiments with fluorescent techniques to identify released metabolites [Medina et al., 2020], or the connexins already exist to test such models [Armingol et al., 2021]. Finally, death-ligands are originally produced by immune cells. Therefore, one last lead that could be tested experimentally in our lab (with organ-on-chips [Bretti et al., 2021] or co-culture protocols), is to use multi-culture systems, where the tumoral cells are modeled along with the natural killers cells in addition to TRAIL signaling, to better represent an *in vivo* situation. The mathematical modeling will then help us to understand the cross-talk between the two types of cells by having a insights of their dynamics and how they influence each other.

With more relevant pharmaco-metrics, we will be able to provide a better forecasting of the future tumour response to the drug tested during the single-cell experiment. Part III initiated the first step of the process by proposing a better forecasting of the single-cell drug response.

Early forecasting of cell drug-response

Forecasting a drug-response before the drug starts affecting the innate cell state is a major challenge, like demonstrated in Chapter 6. Using the method developed in Chapter 5, but also cutting-edge machine learning models for classification, the results in Chapter 7 showed an accuracy in forecasting cell drug-response too low to meet the expectations of the FATE-SEQ pipeline. Eventually, Chapter 7 underlined the conclusion that the methods evaluated in this Chapter cannot forecast cell drug-response with a high accuracy for all cells, based exclusively on data from the first hour of experiment and the FRET signal.

Nevertheless, as FATE-SEQ does not require drug-response forecasting for all cells in the experiment, in Chapter 8 we proposed several alternatives to select cells for isolation and profile them. We chose to implement an improved version of the FATE-SEQ current method to select cells for isolation, using a feature for each drug-response instead of a single-one. The two features are from a classic time-series classification feature set, presented in Chapter 7, but this upgraded method still uses the non-overlapping principle. Therefore, coupling our expertise in time-series classification and the conclusions of Chapters 6 to 8, we have finally presented our EArly Single-cell Isolation with a Drug Response Up-Graded forecaster: **EASIDRUG**, our new way to select cells for profiling in the new custom setup of FATE-SEQ. Besides increasing the number of cells profiled in the FATE-SEQ pipeline, EASIDRUG, by using general time-series classification features, allows the adaptation of FATE-SEQ to any type of drugs and cells.

FATE-SEQ 3.0

This idea of FATE-SEQ 3.0 is to keep gaining in adaptability to apply the method to other cell lines, other drugs but also other phenotypes, which implies studying and integrating new signaling pathways and be able to compare them across cell lines and drugs. Hence, in addition to determining new therapeutic targets or bio-markers, we could use FATE-SEQ to gain new insights on the Systems biology by studying the connections between the forecast drug-response, the molecular profile obtained with FATE-SEQ and the dynamics observed during the live-cell microscopy step for other types of drugs and cells.

The direction we choose for now is studying the cross-talk between cancer cells and the immune system by first analyzing molecules released by Natural Killers, such as FAS-L or Granzyme B [Wu et al., 2020]. Then the natural follow-up would be checkpoint inhibitors [de Miguel and Calvo, 2020].

In Chapter 7, we already tested forecasting methods based on signal processing approaches that are independent of any prior-knowledge and are purely data-driven. Following the same idea, we plan to implement in the future two other methods to adapt our pipeline quicker and be more independent on the prior knowledge in Systems biology that FATE-SEQ requires nowadays The hidden objective is also to find common points - across all drugs and cells lines - to better characterize drug-tolerant persisters.

Perspective: Independent gene priorization

The current method used in FATE-SEQ to prioritize the 60 genes from the RNA-seq analysis to highlight around 10 biomarkers of drug-tolerance is called GeNetRank [Sales de Queiroz et al., 2022]. It consists in connecting the 60 genes (sources) from the RNA-seq analysis, with the 120 genes known to be involved in apoptosis (target), with a protein-protein interaction network (PPIN). The PPIN is a weighted and oriented graph. Then random walks are used to travel the graph and find the heaviest paths between a source and a target, representing the fact that the source highly affects the target.

This method has proved effective in the past, as Meyer et al, in [Meyer et al., 2020] were able to validate 6 biomarkers in a cell-based assay. But this approach is highly dependent on the PPIN and the 120 genes already known. However, we want to apply FATE-SEQ to other phenotypes or signaling pathways, where the topology and regulatory genes may be less known.

We therefore propose to use another method to remove the uncertainty from the PPIN network, and the necessary prior knowledge it implies: DeepLIFT (Deep Learning Important FeaTures [Shrikumar et al., 2017]). DeepLIFT is a method to better understand how a neural network predicts a specific outcome. The algorithm assigns a score to each feature used as input to the neural network during the training part. Each score is calculated by back-propagating the contributions of all neurons for each feature. The comparison of scores between features allows to highlight the most important inputs to predict the output of the model.

In our case, a multilayer perceptron will be used to predict the drug response (sensitive/tolerant) of each cell, using RNA-seq gene expression data, from FATE-SEQ, as input to the deep learning model. In a sense, we will replace the PPIN with a neural network, the 120 apoptotic genes with the drug response (sensitive/tolerant) predicted in the live cell microscopy step of FATE-SEQ, and the random walk with DeepLIFT. Therefore, we will be freed from the prior knowledge required by GeNetRank. On the other hand, the neural network/DeepLift combination will only work if we have enough cells as input and very high accuracy in predicting drug response. We could also work on a way to combine the results of GeNetRank and DeepLIFT. Finally, other algorithms to determine bio-markers and therapeutic target by identifying genes with meaningful differential

expression from RNAseq data exist [Labory et al., 2022, Brechtmann et al., 2018, Salkovic et al., 2020], which could also be compared with DeepLift and GeNetRank.

In any case, the performances of the model used to identify new therapeutic target can only be assessed completely, by validating the targets with a cell based-assay showing that targeting these specific genes actually increases the efficacy of the drug used alone.

Perspective: Transpose FATE-SEQ models on different cell lines

In [Brubaker et al., 2019, Brubaker and Lauffenburger, 2020, Carroll et al., 2021, Lee et al., 2021b], Lauffenburger's team investigates the use of machine learning and deep-learning algorithms to generalize results obtained on murine models to humans, always in order to improve pre-clinical research and the translation between animal models and humans.

In [Brubaker et al., 2019], the authors combine a supervised machine learning model that predicts disease state (sick or control) from gene expression data for different datasets (several cell lines and different diseases), with an unsupervised model of human disease-context using human genes expression. We are planning to adapt the pipeline to our fluorescent time-trajectories data, replacing the mice data by HeLa cells data with TRAIL and the human data by the cell lines or other drugs to translate our model. In addition, in order to compare dis-regulated pathways in murine models and human in neuropathologies [Carroll et al., 2021], they rescaled the two gene datasets (one for mice, one for humans) so they have the same mean and variance. After a principal component analysis for the 2 datasets, they project the human dataset into the murine space. Then, they use the combined datasets as input for a machine learning model to classify the phenotype (control/schizophrenia) in the study. Finally, they check the importance of each principal component feature to determine common genes across the two species.

The idea is to apply the same methods to generalize our results on our HeLa cell line to new cells lines (lungs, pancreas, breast, etc). By doing so, we could highlight master regulators of drug-tolerant persisters, common to every cell line, but also understand better the differences too. In the last section, we present three examples of potential applications of the method.

Perspective: Potential application of FATE-SEQ 3.0

FATE-SEQ determines the molecular profile of a drug efficacy. To be used, FATE-SEQ needs a drug of interest, a cell line (or more) to apply the drug on (or simply a cell), a phenotype (sensitive/tolerant in our proof of concept) and finally a sequencing method (RNA, proteomic, etc). Then, we will need a probe to report cell activity in reaction to the drug (probe that could be created by the team if it does not exist yet), but any non-invasive method to forecast the phenotype (other

than a probe), could be used too.

Below are listed three potential new analysis we could perform with FATE-SEQ. To simplify the literature review, for each new analysis, we present a summary table of the elements needed to perform FATE-SEQ (probe, forecasting method, cell lines, drug, etc), oriented on the drug-forecasting step on purpose.

Sensitivity to OXPHOS Inhibitors

Drug	OXPHOS inhibitors
Reference	[Kosaisawe et al., 2021]
Disease	Diabetes and cancer
Cell	MCF10A (non-tumor epithelial cells),184A1 (mammary epithelial), MCF7 (breast cancer), U87 (glioblastoma), and A549 (non-small-cell lung cancer, LKB1-deficient)
Phenotype	Sensitive/Resistant to OXPHOS Inhibitors or OXPHOS-independent/dependant
Sequencing	RNA-seq or proteomic or metabolomic
Probe	Fluorescent protein-based FRET for AMPK (AMPKAR2 FRET ratio) + ATP and ADP/ATP
Forecasting	Baseline-to-peak amplitude of AMPKAR2^{PHOS} after 2h of experiment (see Figure 8.8A. and C. 183)
Signaling pathways	ERK (cell cycle and proliferation) + mTOR (cell metabolism, growth, proliferation and survival.)
Goal	Complete the study about OSPHOS-dep/indp. impact on mTOR/ERK pathway + find new target for combination therapy with OXPHOS inhibitors

Table 8.3: FATE-SEQ for OXPHOS inhibitors

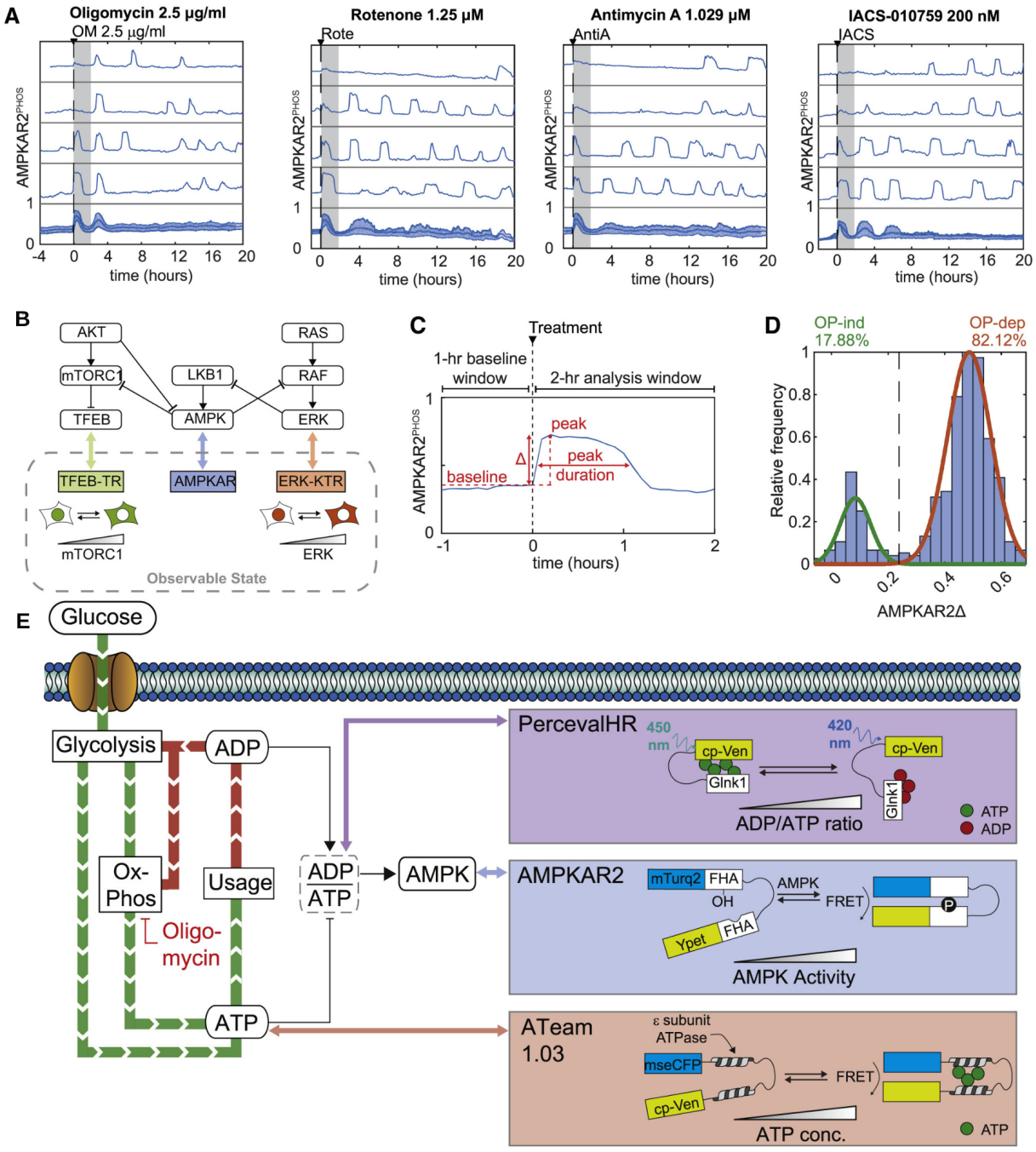

Figure 8.8: **Graphic summary of Kosasaiwe et al. work on Analysing variable AMPK responses to OXPHOS inhibition:** A. Single-cell AMPKAR2$PHOS$ responses for cells grown in 17 mM glucose (Gray shaded area shows the 2 h time window used for analysis of peak height), B. Known connections between AMPK, mTORC1, and ERK, C. Baseline-to-peak amplitude of AMPKAR2^{PHOS}, D.Histogram of AMPKAR2Δ values after treatment with 2.5 μg/mL oligomycin, illustrating 2 distributions according to the dependence to OXPHOS, E. Schematic of ATP metabolism and reporters used. Figure and legend from [Kosaisawe et al., 2021]

Chemotherapy response

Drug	Chemotherapy + ionazing radiation
Reference	[Paek et al., 2016, Hafner et al., 2020]
Disease	Cancer
Cell	Colon cancer (HCT116)
Phenotype	Sensitive/ Tolerant
Sequencing	Proteomic (role of IAP) + RNA-seq
Probe	One allele of TP53 is tagged with a Venus fluorescent protein to record p53 dynamic or we could use p53-CFP trans-gene to monitor p53 levels, and tag one copy of p21 with mCherry at its endogenous locus to monitor its protein levels
Forecasting	Sensitive cells have to overcome a threshold on p53 activity, this threshold is time-depending and gets bigger over time (see Figure 8.9.G p.185), hence p53 onset could be used as a forecaster +regarding the curve early after cisplatin treatment, derivative features could be used too
Signaling pathways	p53 pathway (Int. Apop)
Goal	New target+ quantification of p21 protein level & mRNA level for fix p53+ profiling cell cycle phases

Table 8.4: FATE-SEQ for cisplatin

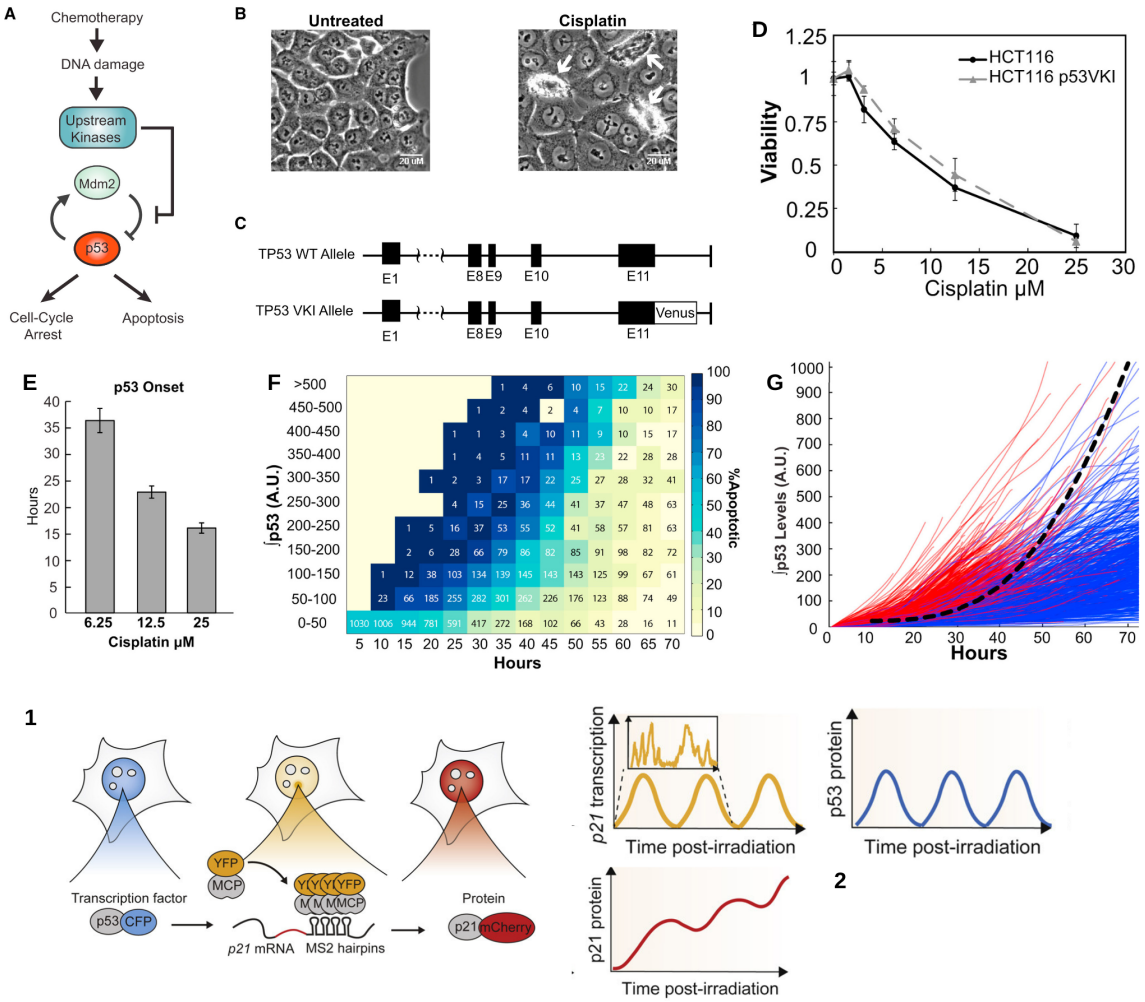

Figure 8.9: **How to Track p53 Levels in Single Cells:** A.Network diagram of the p53 response to chemotherapy treatment, B.Images of unperturbed HCT116 cells (left panel) and in response to cisplatin (right panel), C.Diagram of TP53 alleles in the HCT116 p53-VKI cell line, D.Survival curve of HCT116 cells and p53-VKI cells 72 hr after cisplatin treatment, measured by Cell Titer-Glo. Error bars represent the standard deviation of four replicates, E.Average time of p53 onset for each cisplatin concentration, F. Viability matrix. Traces from all three cisplatin concentrations (N = 1,030) were binned in 5-hr time windows (x axis) and by integrated p53 levels (y axis). The color of each rectangle represents the percentage of apoptotic cells in each bin. Legend is on the right. The number in each rectangle is the number of cells in the bin, G.Single cell traces of integrated p53 levels from all three concentrations of cisplatin (N = 1,030). The dashed line represents the predicted apoptotic threshold and was calculated by performing logistic regression on each time window of the data from (K). Seventy-three percent of cells above the threshold were apoptotic (N = 534), and 34% of cells below the threshold were apoptotic (N = 496). 1.Fluorescent probe to record both p53 ad p21transcription and protein levels. 2. Example of dynamics observed. A to G from [Paek et al., 2016] (A to D fig.1 - E to G fig.2) - 1 to 2 from [Hafner et al., 2020] graphic abstract.

UV response

Drug	UV-C
Reference	[Miura et al., 2018]
Disease	Cancer
Cell	HeLa
Phenotype	Sensitive/Tolerant
Sequencing	RNA-seq
Probe	m JNK KTR+ mCherry
Forecasting	After 2h post-treatment by UV-C, sensitive cells show an activity peak in JNK fluorescent signal that resistant cells do not have, the second pulse in JNK activity could confirm cell decision to commit apoptosis but just before cell death - see Figure 8.10.D p.186. We can also use the mean activity after 4h, that is strongly associated with sensitivity (D - on the article) and B. regarding the curves, the derivative test could work too like with IC-RP
Signaling pathways	Stress Activation Protein Kinase (SAPK) Pathway
Goal	New targets + a better understanding of the pathways (modeling?)

Table 8.5: FATE-SEQ for JNK and UV-C

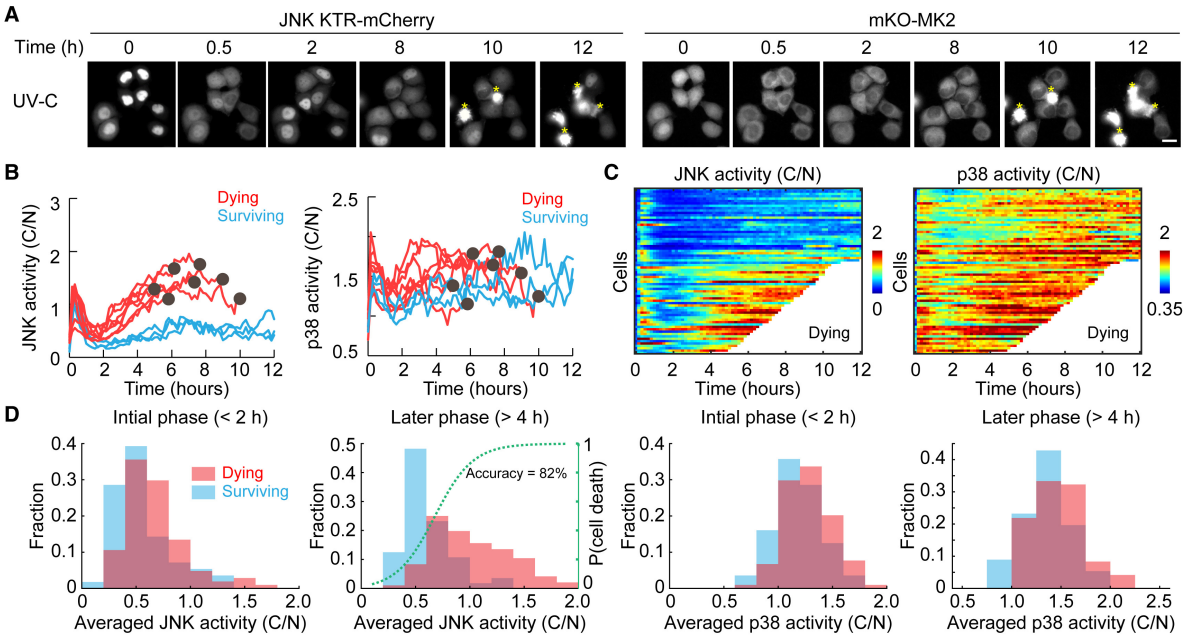

Figure 8.10: **Cell-to-Cell Variation in JNK Activity Leads to Fractional Killing upon UV-C Treatment:** A.Clonal HeLa cells exposed to 100 J/m2 UV-C, B.C:N ratios of JNK KTR-mCherry and mKO-MK2 were quantified for dying (red lines) and surviving (blue lines) cells after 100 J/m2 UV-C stimulation. n = 10 representative cells. Black dots indicate apoptosis, C.JNK KTR-mCherry and mKO-MK2 C:N ratios are displayed as heatmaps, D.Histograms of average JNK and p38 activity in the initial phase (<2 hr) and later phase (>4 hr) of UV-C stimulation are shown in dying (red) and surviving (blue) cells. The green dashed line shows the estimated probability of cell death as a function of JNK activity, which is produced by the logistic regression. Figure and legend 4 from [Miura et al., 2018]

Final note

This work opened a lot of new directions and applications for the future, tackling some of the major limitations of the current FATE-SEQ pipeline. Some of these limitations (noisy and sparse data, un-observability of the phenomenon of interest, size of the model employed), echo in a lot of other domains, in Biology and beyond. Nevertheless, at our scale, the steps we made in this work, by proposing a better modeling of TRAIL-inducing apoptosis to forecast drug-tolerant cells, in the spectrum of our Systems pharmacology approach, will hopefully lead to faster and more accurate pre-clinical steps in drug-development, so patients with cancer can benefit from more personalized and efficient drug-combination in the future.

Appendix

A Chapter 2

A.1 Experiment microscope setup

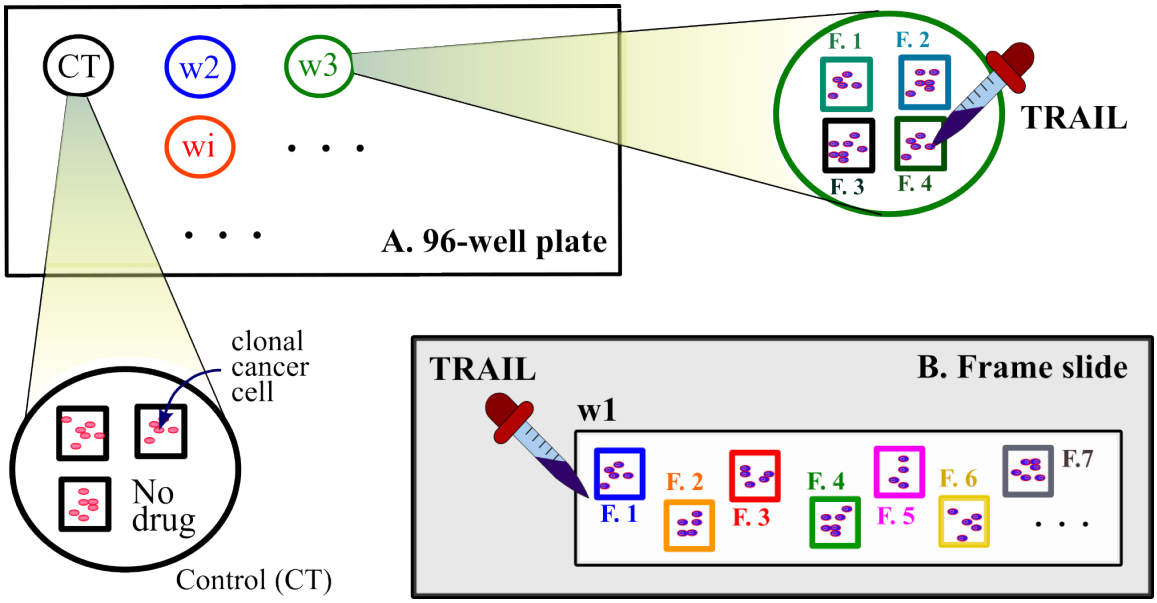

Figure A.11: **Roux lab experiments sets-up**: A. setup used in [Roux et al., 2015, Meyer et al., 2020], B. setup used in [MP1]. **w** stands for well, **F.** for field

A.2 Datasets description per chapter

In the following tables, we describe the datasets used in part Part II and Part III, to estimate the parameters of our models and validate them, but also the experiment set-up and the preprocessing methods. These distributions demonstrate how heterogeneous drug response (and eventually the amount of drug-tolerant persisters) can be across multiple replicates, despite the exact same experimental conditions.

Drug	TRAIL						TRAIL+Bortezomib	TRAIL	
Publication	[Roux et al., 2015]							[Meyer et al., 2020]	
Fluo. signal	CFP/ FRET							CFP/YFP	
Time between two frames	5 min							3 min	
Nb frames before 50 min	10							16	
Drug dose (ng/mL)	5	10	25			50	50 TRAIL./100 B.	20	
Replicate n°	1	1	1	2	3	1	1	1	2
# cells T	308	167	250	113	150	114	0	11	14
# cells S	34	46	94	108	177	300	563	33	63
# cells total	342	213	344	221	327	414	563	44	77
% cells T	90%	78%	73%	51%	46%	28%	0%	25%	18%

Table A.1: Dataset description

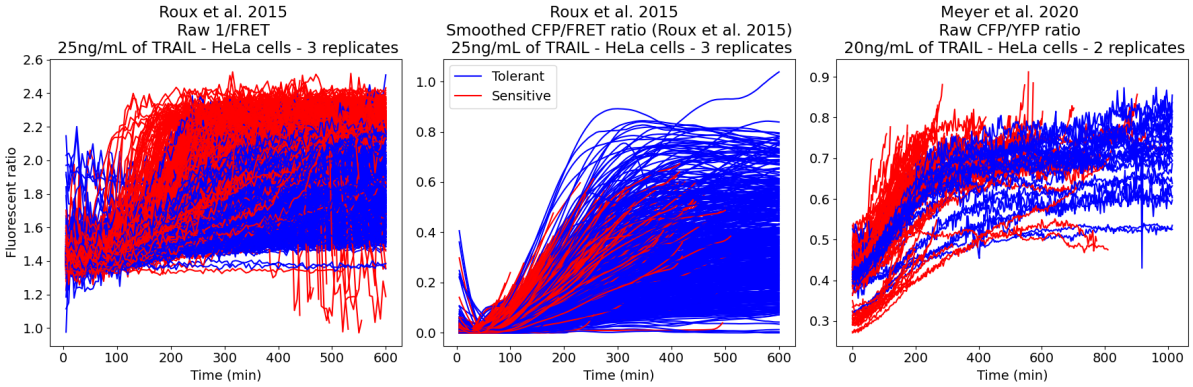

Figure A.12: **Fluorescent time-trajectories** from [Roux et al., 2015, Meyer et al., 2020] used in this work. Subplot 1 - 1/FRET from Roux et al. for HeLa cells treated with 25 ng/mL of TRAIL observed every 5 min during 10 hours, 3 replicates combined. Subplot 2 - CFP/FRET (preprossed using a 0-phase digital filter, a rescaling by the mean untreated cell and a rescaling by the minimum of the FRET time trajectory for each cell) from Roux et al. for HeLa cells treated with 25 ng/mL of TRAIL observed every 5 min during 10 hours, 3 replicates combined. Subplot 2 - CFP/YFP from Meyer et al. for HeLa cells treated with 20 ng/mL of TRAIL observed every 3 min during 10 hours, replicates combined.

We also give a summary table of the datasets used in each chapter of this thesis.

Datasets	Chapter 4	Chapter 5	Chapter 6	Chapter 7	Chapter 8
TRAIL_Roux_5_1		✓			
TRAIL_Roux_10_1		✓			
TRAIL_Roux_25_1		✓	✓	✓	
TRAIL_Roux_25_2		✓	✓	✓	✓
TRAIL_Roux_25_3		✓	✓	✓	✓
TRAIL_Roux_50_1	✓	✓			
TRAIL_Meyer_20_1			✓		
TRAIL_Meyer_20_2			✓		
TRAIL-Bort._Roux_50_1	✓				

Table A.2: Summary of the datasets used in each chapter - the names of the datasets are composed this way: DRUG_Publication_drug dose_replicate number - if the replicate number is not precise, it means that all the replicates have been used and concatenated

In order to have an open-source and open-access method for signal-processing, we chose to translate the MATLAB code used in [Roux et al., 2015] in Python for [MP1] (see our lab github repository).

	Method - Chapters	Chapter 4	Chapter 5	Chapter 6	Chapter 7	Chapter 8
Roux et al. (2015)	Rescale by substracting the average FRET ratio trajectory of all untreated cells (MATLAB)	1	1	1	1	1
	Noise filtration with *filtfilt* function (MATLAB) with 11-frame window	2	2	2	2	2
	Rescale by substracting the minimum value of FRET ratio (MATLAB)	3	3	3	3	3
Bian + Meyer	Filtration with Savitzky-Golay filter from *scipy.signal* of order 3 on 9-frame window once (PYTHON)			1	1	
	Normalize the trajectories by subtracting the FRET minimal value before 50 min (PYTHON)			2	2	
Meyer et al. (2020)	Smoothing with a Moving Average filter from *scipy.signal* of order 3 on 9-frame window once (PYTHON) (with a 11-frame window in the paper)				1	
	Normalize the trajectories by subtracting the FRET minimal value before 50 min (PYTHON)				2	
Bian et al. (2022)	Filtration with Savitzky-Golay filter from *scipy.signal* of order 3 on 5-frame window once (PYTHON)				1	
	Normalize the trajectories by subtracting the FRET value in the first frame (PYTHON)				2	

Table A.3: Summary of the preprocessing techniques applied on the time-trajectories used in each chapter - numbers represent the order of application, the filtration instead of smoothing, and the change of window was done to adapt the different methods to the datasets (only 10 frames before 50 min in Roux et al. (2015), 16 frames for Meyer et al. datasets) and to translate MATLAB function to Python

A.3 Modeling Apoptosis

Reference	Focus	Model	Data used for calibration
[Fussenegger et al., 2000]	Int./Ext. Apop.: effector caspases	ODE (big m.)	Not found
[Bentele et al., 2004]	Int/Ext. Apop.: CD95	ODE (big m.) Input/ Output Black box	TT for concentrations of 15 molecules + human B lymphoblastoid cell line + agonistic anti–APO-1 antibody/LZ-CD95L
[Eissing et al., 2004]	Feedback loop from C3 on C8	ODE (small m.)	HeLa cells + western blot + no treatment
[Hua et al., 2005]	Ext./Int Apop.: Bcl-2 action in Fas-induced apop.	ODE (big m.)	human Jurkat T cell + Fas-L + western blot/FACS
[Stucki and Simon, 2005]	Mitochondria + IAP+ C3	ODE (small m.)	Not found
[Bagci et al., 2006]	Int. Apop.: Mitochondria + C8 + Bax/Bcl-2 in Fas-L induced Apop.	ODE (big m.)	From [Chen et al., 2000] [Riedl et al., 2005] [Deveraux et al., 1997] [Asthagiri and Lauffenburger, 2001]
[Legewie et al., 2006]	Int./Ext. Apop. C3+C9+IAP	ODE (big m.)	TT on the amount of C3 from [Hill et al., 2004] immunopurification + mass spectrometry + Jurkat, BJAB and U937 cells +cytochrome c/dATP
[Rehm et al., 2006]	Int./Ext. Apop. Effector caspases	ODE (big m.)	HeLa cells + FRET + treatment with STS ask JR
[Chen et al., 2007a]	Int. Apop.: Bcl-2 switch	ODE (big m.) + discrete m. + stochastic fluctuations	From [Hua et al., 2005] [Letai et al., 2002] [Kuwana et al., 2002]
[Chen et al., 2007b]	Int. Apop.: MOMP + Bax + Bcl-2	ODE (small m.)	From literature
[Albeck et al., 2008a]	Int./Ext. Apop.	ODE (big m.)	TT. FRET + cycloheximide/TRAIL + HeLa cells

Table A.4: **Summary table of mathematical modeling of TRAIL inducing apoptosis**: Int = intrinsic, Ext. = Extrinsic, Apop. = Apoptosis, ODE = ordinary differential equations, Bool: Boolean, SDE. = stochastic differential equations, DDE = delayed differential equations, Big m. = models with more than 10 variables, data, TT: time-trajectories, DED: death effector domain - Part I

Reference	Focus	Model	Data used for calibration
[Cui et al., 2008]	Int. Apop.: Bcl-2	ODE (small m.)	Not found
[Han et al., 2008]	NF-κB + Ext.Apop.: c-FLIP + Death ligands	ODE (big m.) + black boxes	From [Hua et al., 2005] & [Chang et al., 2002]
[Chaves et al., 2009]	Ext. Apop.B + NF-κB	Bool. (big m.)	Litterature on TNF-α inducing Apop.
[Spencer et al., 2009]	Ext. Apop: Receptor-mediated	ODE (big m.) From [Albeck et al., 2008a]	TT. FRET + cycloheximide/TRAIL + HeLa cells
[Schlatter et al., 2009]	Int./Ext. Apop.	Bool. (big m.)	UV-B dose-effect + mouse hepatocytes + literature
[Zhang et al., 2009]	Int. Apop.: p53	ODE (big m.)	From litterature
[Waldherr et al., 2009]	Ext.Apop. : Parameter estimation	From [Chaves et al., 2009] + Population scale	TRAIL + Flow cytometric fluorescence microscopy
[Ho and Harrington, 2010]	Ext. Apop.: Fas- L	Graph & cluster m.	From literature
[Zhang et al., 2010]	Int. Apop. + Cell cycle + p53 during DNA damage	ODE (big m.)	From [Geva-Zatorsky et al., 2006]: TT: Fluorescently tagged p53 and Mdm2 MCF7 cells (breast cancer) + DNA-damaging γ irradiation
[Calzone et al., 2010]	Apop. + Necrosis + NF-κB	Bool. (big m.)	From literature on cytokines/ death ligands
[Fricker et al., 2010]	Ext.Apop: CD95+ c-FLIP	ODE (big m.)	HeLa cells + LZ-CD95L + western blot
[Neumann et al., 2010]	Ext.Apop: CD95+NF-κB	ODE (big m. + model reduction)	Flow cytometry + anti-CD95 antibodies + HeLa cells

Table A.5: **Summary table of mathematical modeling of TRAIL inducing apoptosis**: Int = intrinsic, Ext. = Extrinsic, Apop. = Apoptosis, ODE = ordinary differential equations, Bool: Boolean, SDE. = stochastic differential equations, DDE = delayed differential equations, Big m. = models with more than 10 variables, data, TT: time-trajectories, DED: death effector domain - Part II

Reference	Focus	Model	Data used for calibration
[Howells et al., 2011]	Int. Apop.: Bcl-2 family, BAD especially	From [Chen et al., 2007a]	Literature on BAD phosphorylation + [Hekman et al., 2006]
[Aldridge et al., 2011]	Int./Ext. Apop.: TRAIL + XIAP + pC3	From [Albeck et al., 2008a]	Multiple tumor cell lines (HCT116 cells + others) + immunoblotting + TRAIL + Fas-L
[Huber et al., 2011]	Int. Apop.: Mitochondria	Review	-
[Hasenauer et al., 2011]	Ext. Apop.	ODE (big m.) from [Albeck et al., 2008a]+ bayesian approach for parameter estimation + Population scale	population snapshot data (flow cytometry, etc)
[Gaudet et al., 2012]	Ext. Apop.: TRAIL + BCL-2	ODE (big m.): Extension of [Albeck et al., 2008a]	HeLa cells + TT: fluorescent live-cell microscopy + TRAIL/cycloheximide + Flow cytometry
[Eydgahi et al., 2013]	Int./Ext. Apop	ODE (big m.) from [Albeck et al., 2008a]	TRAIL/ Fas-L + HeLa cells + live-cell microscopy/ Western blot
[Stoma et al., 2013]	Ext. Apop.: TRAIL	Signal temporal logic m. from [Aldridge et al., 2011]	HCT116, SKW6.4 and T47D cells+ΔXIAP and OE-Bcl2 mutant cell lines + immunoblotting + TRAIL
[Bertaux et al., 2014]	Ext. Apop.: TRAIL	ODE + SDE (big m.) from [Spencer et al., 2009]	From [Thorpe et al., 2008] Prostate cancer cell lines/ primary prostate epithelial cells + TRAIL/Fas-L + Western blot
[Kallenberger et al., 2014]	Ext. Apop.: pC8/C8	ODE (big m.) multiscale m.: Single-cell + Pop.	CD95L + single-cell/ Flow cytometry/ Western blot + HeLa
[Würstle et al., 2014]	Int. Apop.	Review	Chemotherapy

Table A.6: **Summary table of mathematical modeling of TRAIL inducing apoptosis**: Int = intrinsic, Ext. = Extrinsic, Apop. = Apoptosis, ODE = ordinary differential equations, Bool: Boolean, SDE. = stochastic differential equations, DDE = delayed differential equations, Big m. = models with more than 10 variables, data, TT: time-trajectories, DED: death effector domain - Part III

Reference	Focus	Model	Data used for calibration
[Neumann et al., 2014]	Ext. Apop.: Death Receptors	ODE (small m.)	FRET/ Western blot + TRAIL + HeLa/ Mouse embryonic fibroblasts + From literature
[Chong et al., 2015]	Int. Apop.:p53 during DNA damage	DDE (big m.)	from [Loewer et al., 2010] (TT. MCF7) + fluorescent p53 + antibodies against p53
[Roux et al., 2015]	Ext. Apop.: C8 +TRAIL	ODE (small m.)	TT. FRET + TRAIL + HeLa cells
[Ballweg et al., 2017]	p53+Bax	ODE (big m.)	TT from [Paek et al., 2016] (live-cell imaging (through fluorescent p53) on colon cancer cells + chemotherapy)
[Voropaeva et al., 2017]	p53-Mdm2-miRNA	ODE (small m.)	Not found
[Yin et al., 2017]	Int. Apop.:MOMP+ Bcl-2	ODE (small m.)	From [Czabotar et al., 2013]
[Bouhaddou et al., 2018]	Pan-cancer pathways, including Apop. & ERK/AKT	ODE (very big m. around 1200 variables) Combine several m. from literature	MCF10A + From literature
[Buchbinder et al., 2018]	Ext. Apop.: + CD-95 + NF-κB	SDE + ODE	HeLa cell line + CD95L+ flow cytometry [Schleich et al., 2016]
[Márquez-Jurado et al., 2018]	Ext. Apop.: Mitochondria	ODE (big m.) improved from [Albeck et al., 2008a] & [Bertaux et al., 2014]	TRAIL + HeLa + live-cell microscopy (fluo.)/ RNAseq
[Lederman et al., 2018]	Ext. Apop.: TRAIL + circulating tumor cells	ODE (big m.) from [Albeck et al., 2008a]	TRAIL + from [Mitchell et al., 2014]
[Chong et al., 2019]	Int. Apop.: p53	DDE + ODE, extended m. from [Chong et al., 2015]	from [Chong et al., 2015] & [Zhang et al., 2010]
[Matveeva et al., 2019]	Ext. Apop	SDE + ODE	FRET TT. from [Roux et al., 2015]
[Pereira, 2019]	Ext. Apop.	ODE (big m.)	FRET TT. from [Roux et al., 2015]

Table A.7: **Summary table of mathematical modeling of TRAIL inducing apoptosis**: Int = intrinsic, Ext. = Extrinsic, Apop. = Apoptosis, ODE = ordinary differential equations, Bool: Boolean, SDE. = stochastic differential equations, DDE = delayed differential equations, Big m. = models with more than 10 variables, data, TT: time-trajectories, DED: death effector domain - Part IV

Reference	Focus	Model	Data used for calibration
[Hillert et al., 2020a]	Ext. Apopt.: DED+ C8 + c-FLIP	ODE (big m.) + structural m.	HeLa cells + CD95L + flow cytometry/ fluorescent reporter for C3/C7
[Ivanisenko and Lavrik, 2020]	Ext. Apopt.: DED+ C8 + c-FLIP	ODE (big m.) from [Hillert et al., 2020a] + structural m.	From [Hillert et al., 2020a]
[Eduati et al., 2020]	Int./Ext. Apop.	ODE + logic (big m.)	Fluorescent C3 + kinase inhibitors/ cytokines/ chemotherapies + 2 pancreas cancer cell lines
[Chaves et al., 2021]	Ext.Apop.	ODE (big and small m. m. reduction)	FRET TT. from [Roux et al., 2015]
[Lee et al., 2021a]	Apop.: STAT1, STAT3, Bcl-2 and BAX	ODE (small m.)	From literature
[Liu et al., 2021]	Proliferation & Apop.	ODE (small m.): Population scale (not single-cell)	9L and C6 glioma cells + radiotherapy + flowcytometry/ time-resolved microscopy with fluorescence
[Xie et al., 2022]	Int. Apop.: p53	DDE (small m.)	TT from: Chemotherapy + five cancer cell types (A549, U-2 OS, A375, MCF7 and 769-P) + p53-Venue fluorescent reporter
[Plaugher et al., 2022] + [Plaugher and Murrugarra, 2021]	Mutations of KRAS, TP53, SMAD4, & CDKN2A genes + microenvironnement	Stochastic discrete dynamical systems (stochastic + bool. - big m.)	Pancreatic cancer cells + cytokines + parameters from literature
[Amstein et al., 2022]	Survival, Apop., & Necroptosis	Petri net model (discrete m., big m.)	Literature on necrosis factor 1 (TNFR1), on mice and human (*in vivo*)
[Ortega et al., 2022]	Ext. Apop. + JAK2/STAT5	Model from [Albeck et al., 2008a] + (m. reduction)	Data from [Albeck et al., 2008b]

Table A.8: **Summary table of mathematical modeling of TRAIL inducing apoptosis**: Int = intrinsic, Ext. = Extrinsic, Apop. = Apoptosis, ODE = ordinary differential equations, Bool: Boolean, SDE. = stochastic differential equations, DDE = delayed differential equations, Big m. = models with more than 10 variables, data, TT: time-trajectories, DED: death effector domain - Part V

B Chapter 4

B.1 Comparison tables of the EAICM models fitting performances

Fit \ Model	Fate	EAICM-cf	EAICM-c	EAICM-af	EAICM-a	Best model
F1	Sens. cells	177	20	95	8	EAICM-cf
	Tol. cells	51	3	52	8	EAICM-cf/ EAICM-af
F2	Sens. cells	0	20	0	280	EAICM-a
	Tol. cells	0	102	0	12	EAICM-c
F3	Sens. cells	0	63	1	236	EAICM-a
	Tol. cells	2	95	0	17	EAICM-c

Table B.9: Number of cell best approached per EAICM model and type of fits, comparing $\mathcal{C}$ value

Fit \ Model	Fate	EAICM-cf	EAICM-c	EAICM-af	EAICM-a	Best model
F1	Sens. cells	132	98	20	50	EAICM-cf
	Tol. cells	46	43	9	16	EAICM-cf
F2	Sens. cells	130	103	8	59	EAICM-cf
	Tol. cells	55	48	1	10	EAICM-cf
F3	Sens. cells	222	20	17	41	EAICM-cf
	Tol. cells	64	10	33	7	EAICM-cf

Table B.10: Number of cell best approached per EAIC model and type of fits comparing the delay, *ie* $|T_{100000,EAICM,i} - T_{100000,data,i}|$, $i \in \{1, ..., 414\}$

Fit \ Model	Fate	EAICM-cf	EAICM-c	EAICM-af	EAICM-a	Best model
F1	Sens. cells	91	108	46	55	EAICM-c
	Tol. cells	45	16	35	18	EAICM-cf
F2	Sens. cells	68	111	59	62	EAICM-c
	Tol. cells	51	10	44	9	EAICM-cf
F3	Sens. cells	263	0	23	14	EAICM-cf
	Tol. cells	9	26	62	17	EAICM-af

Table B.11: Number of cell best approached per EAIC model and type of fits according to C8 final value, *ie* comparing $|V_{final,EAICM,i} - V_{final,data,i}|$, $i \in \{1, ..., 414\}$

B.2 Feedback loop effects for EAICM-af and EAICM-a

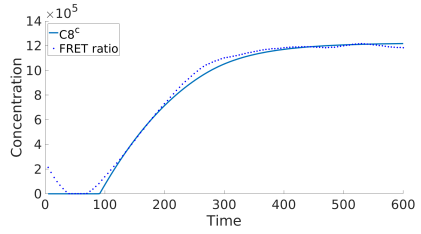

(a) Real FRET ratio and $C8^c$ for EAICM-af

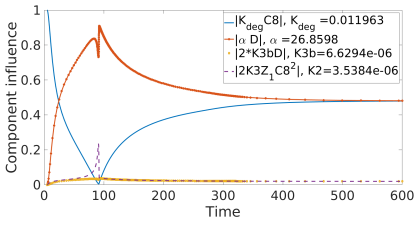

(b) C8 equation component dynamics for EAICM-af

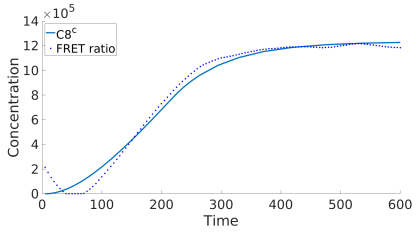

(c) Real FRET ratio and $C8^c$ for EAICM-

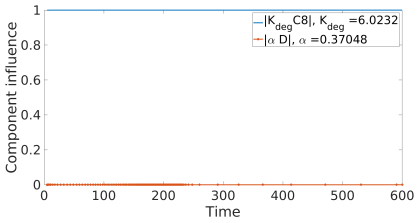

(d) C8 equation component dynamics for EAICM-a

Figure B.13: **Comparison of C8 main features with the dynamic of each C8 equation component** of EAICM-af (a),(b) and EAICM-a (c),(d) for the resistant cell n. 10

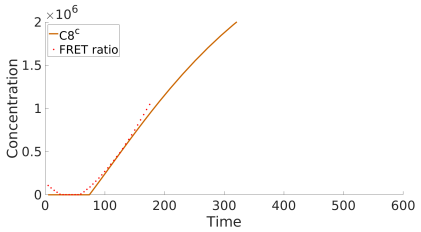

(a) Real FRET ratio and $C8^c$ for EAICM-af

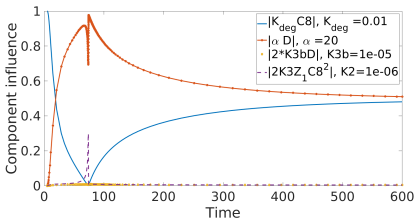

(b) C8 equation component dynamics for EAICM-af

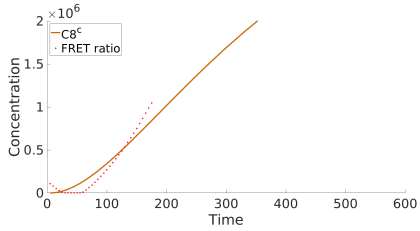

(c) Real FRET ratio and $C8^c$ for EAICM-a

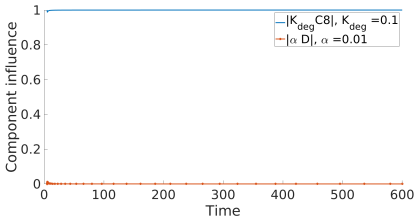

(d) C8 equation component dynamics for EAICM-a

Figure B.14: **Comparison of C8 main features with the dynamic of each C8 equation component** of EAICM-af (a),(b) and EAICM-a (c),(d) for the sensitive cell n. 121 - *simulations were performed for 600 min for comparison needs*

B.3 Median parameter values from the fit on both initial conditions and reaction rates used in Figure 4.7 for the EAIC models

	EAICM-cf		EAICM-c		EAICM-af		EAICM-a	
	Tol. cells	Sens. cells	Tol. cells	Sens. cells	Tol. cells	Sens. cells	Tol. cells	Sens. cells
$\vec{K_1}$	4.3955e-07	2.7388e-07	6.5892e-08	1.2254e-07	1.6320e-07	4.0018e-07	6.5892e-08	1.2254e-07
$\overleftarrow{K_1}$	0.0052	0.01129	1.1176	1.7906	3.4358e-04	0.0011	1.1177	1.7907
$\vec{K_2}$	1.5590e-05	2.4304e-05			0.0525	0.0649	25.5081	14.8725
$\overleftarrow{K_2}$	2.9114e-04	9.6920e-04			3.6929e-06	1.2142e-05	2.3934	2.1489
$\vec{K_3}$	0.0012	0.002792	0.002045	0.002206	4.5915e-05	2.1800e-04		
$\overleftarrow{K_3}$	0.0273	0.1607	20.1550	26.9179	2.0294	9.2971		
$\vec{K_4}$			16.5523	25.6951			16.5524	25.6952
$\overleftarrow{K_4}$			2.6201	2.6749			2.6202	2.6750
K_{deg}	0.0133	0.004012	0.0001165	0.001765	0.0122	0.0108	0.0117	0.0018
α	36.2215	48.8287	1.3188	279.2583	27.3338	76.6511	131.8895	279.2584
R_0	7.6248e+04	6.7850e+04	8.6019e+04	4.0387e+04	4.8968e+04	5.6593e+04	8.6020e+04	4.0388e+04
$C_{8,0}$	288.9734	905.9665	667.2585	337.2630	368.2512	663.5847	667.2585	337.2631
$C_{10,0}$	2.2325e+03	3.1050e+04	761.9486	1.0829e+04				
$F_{D,0}$					2.9291e+03	5.3681e+04	761.9486	1.0830e+04

Table B.12: Median reaction rates and initial conditions for all models determined with the fit on both initial conditions and reactions rates for the EAIC models

C Chapter 5

C.1 Data description and corresponding initial conditions for the EAICR model

TRAIL in ng/mL	T_0 in the model	# Total of cells	# Tol. cells	# Sens. cells
5	115	342	308	34
10	310	213	167	46
25	775	344	250	94
50	1550	414	114	300

Table C.13: Dataset description and corresponding initial conditions for the EAICR model

C.2 An improved fitting method for the rEAICR model

The improved fitting method follows 3 steps:

1. Estimate the FRETexp function (Equation (5.8)) parameters with the *fit* function from the lmfit library (least-square method + Levenberg–Marquardt algorithm for non-linear optimization problems).

2. Compute the corresponding reduced EAICR parameters using (Equation (5.9)).

3. Use the corresponding rEAICR parameters as initial guess for the method described in Chapter 4. In Chapter 4, this method is implemented in Python, using the same least-square-inspired weighted cost and the Nelder-Mead algorithm from the *scipy* package function *optimize.minimize*. The EAIRCM ODE system is solved using the function *solve_ivp* from *scipy.integrate*, using the Radau method.

C.3 Characteristic time computation for the principal process analysis of the EAICR model

For sensitive cells, if τ_i is greater than the death time, τ_i=NaN; same for the resistant cells is $\tau_i > 24h$:

i) $\boldsymbol{\tau_{T.trigger}}$: $\underset{t}{argmax}\, Z0(t)$, $t \in [0, 1]$

ii) $\boldsymbol{\tau_{DISC.ass}}$: $min(t_1, t_2)$ with t_1 first time to satisfy $\dot{R}(t) < 5e{-}2)$ (t_1 is the first time R stabilizes so its derivative gets close to 0), t_2 is the time when $pC8$ becomes linear with its coefficient equals to $-2\alpha_0 T_0$ so t_2 is the first time when $|\dot{pC8} + 2\alpha_0 T_0| < 5e{-}2$, and $5e{-}2$ being our threshold to consider the function closer enough to 0.

iii) $\boldsymbol{\tau_{drug.0}}$: $\underset{t}{argmin}\, T(t)$

iv) $\boldsymbol{\tau_{DISC.end}}$: t first time to satisfies $Z0(t) > pC8(t)$

v) $\boldsymbol{\tau_{C8.final}}$: $\underset{t}{argmin}\, C8(t)$

C.4 Mathematical analysis of EAICR and rEAICR models

EAICRm system is defined by the following system of autonomous ordinary differential equations:

$$EAICRm = \begin{cases} \dot{X} & = f(X,\theta) \\ X(t_0) & = X_0(\theta), \quad (t_0, X_0, \theta) \in \mathbb{R} \times \mathbb{R}_+^{10} \times \mathbb{R}_+^{16}, \end{cases} \tag{C.15}$$

with

$$X = \begin{pmatrix} T \\ R \\ Z0 \\ pC8 \\ Z1 \\ C8 \\ Z2 \\ C10 \\ C^{eff} \\ FRET \end{pmatrix} \tag{C.16}$$

$$\theta = \begin{pmatrix} K_1 \\ \overline{K_1} \\ K_2 \\ \overline{K_2} \\ K_3 \\ \overline{K_3} \\ K_4 \\ \overline{K_4} \\ K_{deg} \\ K_{fret} \\ \alpha_0 \\ \alpha \\ R_0 \\ C8_0 \\ pC8_0 \\ C10_0 \end{pmatrix} \tag{C.17}$$

and

$$f(X,\theta) = \begin{cases} f_1(X,\theta) & = -K_1\,TR^3 + \overline{K_1}\,Z0, \\ f_2(X,\theta) & = -3K_1\,TR^3 + 3\overline{K_1}\,Z0, \\ f_3(X,\theta) & = K_1\,TR^3 - \overline{K_1}\,Z0 - K_2 Z0 pC8^2 + \overline{K_2} Z1 + \alpha_0(Z1+Z2) + \alpha C^{eff}, \\ f_4(X,\theta) & = -2K_2 Z0 pC8^2 + 2\overline{K_2} Z1, \\ f_5(X,\theta) & = K_2 Z0 pC8^2 - \overline{K_2} Z1 - K_3 Z1 C8 + \overline{K_3} Z2 - \alpha_0 Z1, \\ f_6(X,\theta) & = -K_3 Z1 C8 + \overline{K_3} Z2 + \alpha_0 Z1 + 2\alpha_0 Z2 + 2\alpha C^{eff} - (K_{deg} + K_{fret}) C8, \\ f_7(X,\theta) & = K_3 Z1 C8 - \overline{K_3} Z2 - K_4 C10 Z2 + \overline{K_4} C^{eff} - \alpha_0 Z2, \\ f_8(X,\theta) & = -K_4 C10 Z2 + \overline{K_4} C^{eff} + \alpha C^{eff}, \\ f_9(X,\theta) & = K_4 C10 Z2 - \overline{K_4} C^{eff} - \alpha C^{eff}, \\ f_{10}(X,\theta) & = K_{fret} C8. \end{cases} \tag{C.18}$$

We note that f is a polynomial function, hence locally Lipschitz. Thus, we have the following result.

C.4.1 Local uniqueness and existence

Theorem C.1. *The EAICRm System given by Equation* (C.15)*, and the model rEAICRm (Equation* (5.1) *p.100) admit a locally unique solution for* (t_0, X_0) *in* $\mathbb{R} \times \mathbb{R}_+^{10}$ *(resp.* (t_0, X_0) *in* $\mathbb{R} \times \mathbb{R}_+^{7}$*).*

Proof.

f defined by Equation (C.18) (resp. g defined by 5.1 p.100) is polynomial hence $\mathcal{C}^\infty$ and locally Lipchitz on $\mathbb{R} \times \mathbb{R}_+^{10}$, our space of interest. By applying Picard–Lindelöf theorem, the initial value problem defined by Equation (C.15) admits a locally unique solution.
The proof is similar for the rEAICR model.

□

C.4.2 Positivity (Invariance of the system)

An important point in biological models is to check the sign of the solutions.

Theorem C.2. *Let* X_0^* *be the initial condition of Equation* (C.15) *and let* X^* *be the corresponding solution of the system. If* $X_0^* \in [0, +\infty[$ *hence* $X^*(t) \in [0, +\infty[$ *for all* $t \geq 0$ *provided* $X^*(t)$ *exists.*

Proof.

If $X_0^* \in]0, +\infty[$, the continuity of the solutions ensures that $X^* \in]0, +\infty[$.
On the boundary, let us set $X_{0_i} = (x_1, x_2, ..., x_{i-1}, 0, x_{i+1}, ..., x_{10})$. As $\theta \in \mathbb{R}_+^{16}$, we have $f_i(X_{0_i}) \geq 0$, which ensures that X remains nonnegative.

□

Following the same arguments of Theorem C.2 proof, we can prove the following theorem:

Theorem C.3. *Let* Y_0^* *be the initial condition of Equation* (5.1) *p.100 and let* Y^* *be the corresponding solution of the system. If* $Y_0^* \in [0, +\infty[$ *hence* $Y^* \in [0, +\infty[$ $\forall t$*, provided* $X^*(t)$ *exists.*

C.4.3 Equilibrium points

System C.15 admits three types of equilibrium points given by:

$$X_{pC8=0} = \begin{pmatrix} T \\ R \\ \frac{K_1}{\overleftarrow{K_1}} T R^3 \\ 0 \\ 0 \\ 0 \\ 0 \\ C10 \\ 0 \\ FRET \end{pmatrix} \qquad X_{T=0} = \begin{pmatrix} 0 \\ R \\ 0 \\ pC8 \\ 0 \\ 0 \\ 0 \\ C10 \\ 0 \\ FRET \end{pmatrix} \qquad X_{R=0} = \begin{pmatrix} T \\ 0 \\ 0 \\ pC8 \\ 0 \\ 0 \\ 0 \\ C10 \\ 0 \\ FRET \end{pmatrix}$$

obtained by solving $f(X) = 0$, with f given by Equation (C.18) and $X \in \mathbb{R}_+^{10}$, and for which we cannot conclude on the stability.

Indeed, the Jacobian matrix of the system evaluated at the first equilibrium point $X_{T=0}$) is given by:

$$Jac(f)(X_{T=0}) = \begin{pmatrix} -K_1 R^3 & 0 & \overleftarrow{K_1} & 0 & 0 & 0 & 0 & 0 & 0 & 0 \\ -3K_1 R^3 & 0 & \overleftarrow{3K_1} & 0 & 0 & 0 & 0 & 0 & 0 & 0 \\ K_1 R^3 & 0 & -\overleftarrow{K_1} - K_2 pC8^2 & 0 & \overleftarrow{K_2} + \alpha_0 & 0 & \alpha_0 & 0 & \alpha & 0 \\ 0 & 0 & -2K_2 pC8^2 & 0 & \overleftarrow{2K_2} & 0 & 0 & 0 & 0 & 0 \\ 0 & 0 & K_2 pC8^2 & 0 & -\overleftarrow{K_2} - \alpha_0 & 0 & \overleftarrow{K_3} & 0 & 0 & 0 \\ 0 & 0 & 0 & 0 & \alpha_0 & -\left(K_{deg} + K_{fret}\right) & \overleftarrow{K_3} + 2\alpha_0 & 0 & 2\alpha & 0 \\ 0 & 0 & 0 & 0 & 0 & 0 & -\overleftarrow{K_3} - K_4 C10 - \alpha_0 & 0 & \overleftarrow{K_4} & 0 \\ 0 & 0 & 0 & 0 & 0 & 0 & -K_4 C10 & 0 & \overleftarrow{K_4} + \alpha & 0 \\ 0 & 0 & 0 & 0 & 0 & 0 & K_4 C10 & 0 & -\overleftarrow{K_4} - \alpha & 0 \\ 0 & 0 & 0 & 0 & 0 & K_{fret} & 0 & 0 & 0 & 0 \end{pmatrix} \tag{C.19}$$

and admits 10 eigen values:

$$\begin{aligned} val^1_{T=0} &= K_{deg} + K_{fret} \\ val^2_{T=0} &= -5\,K_1\,R^3 - \overleftarrow{K_1}/2 - K_2\,pC8^2/2 - \overleftarrow{K_2}/2 - \alpha_0/2 - \sqrt{\lambda(X)}/2 \\ val^3_{T=0} &= -5\,K_1\,R^3 - \overleftarrow{K_1}/2 - K_2\,pC8^2/2 - \overleftarrow{K_2}/2 - \alpha_0/2 + \sqrt{\lambda(X)}/2 \\ val^4_{T=0} &= -C10\,K_4/2 - \overleftarrow{K_3}/2 - \overleftarrow{K_4}/2 - \alpha/2 - \alpha_0/2 - \sqrt{\gamma(X)}/2 \\ val^5_{T=0} &= -C10\,K_4/2 - \overleftarrow{K_3}/2 - \overleftarrow{K_4}/2 - \alpha/2 - \alpha_0/2 + \sqrt{\gamma(X)}/2 \\ val^{6:10}_{T=0} &= 0 \end{aligned}$$

with:

$$\begin{aligned}\gamma(X) = \;& C10^2\,K_4^2 + 2\,C10\,\overleftarrow{K_3}\,K_4 + 2\,C10\,K_4\,\overleftarrow{K_4} - 2\,C10\,K_4\,\alpha + 2\,C10\,K_4\,\alpha_0 + \overleftarrow{K_3}^{\,2} - 2\,\overleftarrow{K_3}\,\overleftarrow{K_4} \\ & -2\,\overleftarrow{K_3}\,\alpha + 2\,\overleftarrow{K_3}\,\alpha_0 + \overleftarrow{K_4}^{\,2} + 2\,\overleftarrow{K_4}\,\alpha - 2\,\overleftarrow{K_4}\,\alpha_0 + \alpha^2 - 2\,\alpha\,\alpha_0 + \alpha_0^2 \\ = \;& K_4 C10\left(K_4 C10 + 2\left(\overleftarrow{K_3} + \overleftarrow{K_4} - \alpha + \alpha_0\right)\right) + (\overleftarrow{K_3} - \overleftarrow{K_4} - \alpha + \alpha_0)^2\end{aligned}$$

and

$$\begin{aligned}\lambda(X) = \;& 100\,K_1^2\,R^6 + 20\,K_1\,\overleftarrow{K_1}\,R^3 - 20\,K_1\,K_2\,R^3\,pC8^2 - 20\,K_1\,\overleftarrow{K_2}\,R^3 - 20\,K_1\,R^3\,\alpha_0 + \overleftarrow{K_1}^{\,2} \\ & +2\,\overleftarrow{K_1}\,K_2\,pC8^2 - 2\,\overleftarrow{K_1}\,\overleftarrow{K_2} - 2\,\overleftarrow{K_1}\,\alpha_0 + K_2^2\,pC8^4 + 2\,K_2\,\overleftarrow{K_2}\,pC8^2 + 2\,K_2\,\alpha_0\,pC8^2 + \overleftarrow{K_2}^{\,2} \\ & +2\,\overleftarrow{K_2}\,\alpha_0 + \alpha_0^2 \\ = \;& (10K_1R^3 - K_2pC8^2)^2 + (\overleftarrow{K_1} - \overleftarrow{K_2} - \alpha_0)^2 + 2K_2pC8^2(\overleftarrow{K_1} + \overleftarrow{K_2} + \alpha_0) + \\ & 20K_1R^3(\overleftarrow{K_1} - \overleftarrow{K_2} - \alpha_0)\end{aligned}$$

$$Jac(f)(X_{R=0}) = \begin{pmatrix}
0 & 0 & \overleftarrow{K_1} & 0 & 0 & 0 & 0 & 0 & 0 & 0 \\
0 & 0 & 3\overleftarrow{K_1} & 0 & 0 & 0 & 0 & 0 & 0 & 0 \\
0 & 0 & -\overleftarrow{K_1} - K_2pC8^2 & 0 & \overleftarrow{K_2} + \alpha_0 & 0 & \alpha_0 & 0 & \alpha & 0 \\
0 & 0 & -2K_2pC8^2 & 0 & 2\overleftarrow{K_2} & 0 & 0 & 0 & 0 & 0 \\
0 & 0 & K_2pC8^2 & 0 & -\overleftarrow{K_2} - \alpha_0 & 0 & \overleftarrow{K_3} & 0 & 0 & 0 \\
0 & 0 & 0 & 0 & \alpha_0 & -\left(K_{deg} + K_{fret}\right) & \overleftarrow{K_3} + 2\alpha_0 & 0 & 2\alpha & 0 \\
0 & 0 & 0 & 0 & 0 & 0 & -\overleftarrow{K_3} - K_4C10 - \alpha_0 & 0 & \overleftarrow{K_4} & 0 \\
0 & 0 & 0 & 0 & 0 & 0 & -K_4C10 & 0 & \overleftarrow{K_4} + \alpha & 0 \\
0 & 0 & 0 & 0 & 0 & 0 & K_4C10 & 0 & -\overleftarrow{K_4} - \alpha & 0 \\
0 & 0 & 0 & 0 & 0 & K_{fret} & 0 & 0 & 0 & 0
\end{pmatrix} \tag{C.20}$$

and admits 10 eigen values:

$$\begin{aligned}val^1_{R=0} = \;& K_{deg} + K_{fret} \\ val^2_{R=0} = \;& -\overleftarrow{K_1}/2 - K_2\,pC8^2/2 - \overleftarrow{K_2}/2 - \alpha_0/2 - \sqrt{\Lambda(X)}/2 \\ val^3_{R=0} = \;& -\overleftarrow{K_1}/2 - K_2\,pC8^2/2 - \overleftarrow{K_2}/2 - \alpha_0/2 + \sqrt{\Lambda(X)}/2 \\ val^4_{R=0} = \;& -C10\,K_4/2 - \overleftarrow{K_3}/2 - \overleftarrow{K_4}/2 - \alpha/2 - \alpha_0/2 - \sqrt{\gamma(X)}/2 \\ val^5_{R=0} = \;& -C10\,K_4/2 - \overleftarrow{K_3}/2 - \overleftarrow{K_4}/2 - \alpha/2 - \alpha_0/2 + \sqrt{\gamma(X)}/2 \\ val^{6:10}_{R=0} = \;& 0\end{aligned}$$

with:

$$\begin{aligned}\Lambda(X) = \;& \overleftarrow{K_1}^{\,2} + 2\,\overleftarrow{K_1}\,K_2\,pC8^2 - 2\,\overleftarrow{K_1}\,\overleftarrow{K_2} - 2\,\overleftarrow{K_1}\,\alpha_0 + K_2^2\,pC8^4 \\ & +2\,K_2\,\overleftarrow{K_2}\,pC8^2 + 2\,K_2\,\alpha_0\,pC8^2 + \overleftarrow{K_2}^{\,2} + 2\,\overleftarrow{K_2}\,\alpha_0 + \alpha_0^2\end{aligned}$$

$$Jac(f)(X_{pC8=0}) =$$

$$\begin{pmatrix}
-K_1R^3 & -3K_1TR^2 & \overleftarrow{K_1} & 0 & 0 & 0 & 0 & 0 & 0 & 0 \\
-3K_1R^3 & -9K_1TR^2 & 3\overleftarrow{K_1} & 0 & 0 & 0 & 0 & 0 & 0 & 0 \\
K_1R^3 & 3K_1TR^2 & 0 & 0 & \overleftarrow{K_2} + \alpha_0 & 0 & \alpha_0 & 0 & \alpha & 0 \\
0 & 0 & 0 & 0 & 2\overleftarrow{K_2} & 0 & 0 & 0 & 0 & 0 \\
0 & 0 & 0 & 0 & -\overleftarrow{K_2} - \alpha_0 & 0 & \overleftarrow{K_3} & 0 & 0 & 0 \\
0 & 0 & 0 & 0 & +\alpha_0 & -\left(K_{deg} + K_{fret}\right) & \overleftarrow{K_3} + 2\alpha_0 & 0 & 2\alpha & 0 \\
0 & 0 & 0 & 0 & 0 & 0 & -\overleftarrow{K_3} - K_4C10 - \alpha_0 & 0 & \overleftarrow{K_4} & 0 \\
0 & 0 & 0 & 0 & 0 & 0 & -K_4C10 & 0 & \overleftarrow{K_4} + \alpha & 0 \\
0 & 0 & 0 & 0 & 0 & 0 & K_4C10 & 0 & -\overleftarrow{K_4} - \alpha & 0 \\
0 & 0 & 0 & 0 & 0 & K_{fret} & 0 & 0 & 0 & 0
\end{pmatrix} \tag{C.21}$$

and admits 10 eigen values:

$$\begin{aligned}
val^1_{pC8=0} &= K_{deg} + K_{fret} \\
val^2_{pC8=0} &= -5\,K_1\,R^3 - \overleftarrow{K_1}/2 - \overleftarrow{K_2}/2 - \alpha_0/2 - \\
&\quad \sqrt{100\,K_1^2\,R^6 + 20\,K_1\,\overleftarrow{K_1}\,R^3 - 20\,K_1\,\overleftarrow{K_2}\,R^3 - 20\,K_1\,R^3\,\alpha_0 + \overleftarrow{K_1}^{\,2} - 2\,\overleftarrow{K_1}\,\overleftarrow{K_2} - 2\,\overleftarrow{K_1}\,\alpha_0 + \overleftarrow{K_2}^{\,2} + 2\,\overleftarrow{K_2}\,\alpha_0 + \alpha_0^2}/2 \\
val^3_{pC8=0} &= -5\,K_1\,R^3 - \overleftarrow{K_1}/2 - \overleftarrow{K_2}/2 - \alpha_0/2 + \\
&\quad \sqrt{100\,K_1^2\,R^6 + 20\,K_1\,\overleftarrow{K_1}\,R^3 - 20\,K_1\,\overleftarrow{K_2}\,R^3 - 20\,K_1\,R^3\,\alpha_0 + \overleftarrow{K_1}^{\,2} - 2\,\overleftarrow{K_1}\,\overleftarrow{K_2} - 2\,\overleftarrow{K_1}\,\alpha_0 + \overleftarrow{K_2}^{\,2} + 2\,\overleftarrow{K_2}\,\alpha_0 + \alpha_0^2}/2 \\
val^4_{pC8=0} &= -C10\,K_4/2 - \overleftarrow{K_3}/2 - \overleftarrow{K_4}/2 - \alpha/2 - \alpha_0/2 - \sqrt{\gamma(X)}/2 \\
val^5_{pC8=0} &= -C10\,K_4/2 - \overleftarrow{K_3}/2 - \overleftarrow{K_4}/2 - \alpha/2 - \alpha_0/2 + \sqrt{\gamma(X)}/2 \\
val^{6:10}_{pC8=0} &= 0
\end{aligned}$$

Remark: The presence of eigen values equals to zeros also highlights the need to reduce the model size.

Similarly, the rEAICRm system defined by 5.1 admits three types of equilibrium points given by:

$$X_{pC8=0} = \begin{pmatrix} T \\ R \\ \frac{K_1}{\overleftarrow{K_1}} TR^3 \\ 0 \\ 0 \\ 0 \\ FRET \end{pmatrix} \qquad X_{T=0} = \begin{pmatrix} 0 \\ R \\ 0 \\ pC8 \\ 0 \\ 0 \\ FRET \end{pmatrix} \qquad X_{R=0} = \begin{pmatrix} T \\ 0 \\ 0 \\ pC8 \\ 0 \\ 0 \\ FRET \end{pmatrix}$$

for which we can't conclude on their stability.

Therefore, let us use mass conservation law to write an equivalent but smaller model. We have 3 mass conservations:

$$\begin{cases} \dot{T} + \dot{Z0} + \dot{Z1} = 0 & \Rightarrow \quad Z0 = T(t_0) - T - Z1 \\ 3\dot{T} - \dot{R} = 0 & \Rightarrow \quad R = 3T - 3T(t_0) + R(t_0) \\ p\dot{C}8 + 2\dot{Z1} + 2\dot{C}8 + 2\frac{K_{deg}+K_{fret}}{K_{fret}}F\dot{R}ET = 0 & \Rightarrow \quad pC8 = \gamma_{pC8} - 2Z1 - 2C8 - 2\frac{K_{deg}+K_{fret}}{K_{fret}}FRET \end{cases} \tag{C.22}$$

with

$$\gamma_{pC8} = pC8(t_0) + 2C8(t_0) \tag{C.23}$$

as $FRET(t_0) = 0$ and $Z1(t_0) = 0$ for all cells in our case, which leads to:

$$\begin{cases} \dot{T} &= -K_1\, T\left(3T - 3T(t_0) + R(t_0)\right)^3 + \overline{K_1}\,\left(T(t_0) - T - Z1\right), \\ R &= 3T - 3T(t_0) + R(t_0) \\ Z0 &= T(t_0) - T - Z1 \\ pC8 &= \gamma_{pC8} - 2Z1 - 2C8 - 2\frac{K_{deg}+K_{fret}}{K_{fret}}FRET, \\ \dot{Z1} &= K_2\left(T(t_0) - T - Z1\right)pC8^2 - \overline{K_2}Z1 - \alpha_0 Z1, \\ \dot{C}8 &= \alpha_0 Z1 - (K_{deg} + K_{fret})C8, \\ F\dot{R}ET &= K_{fret}C8. \end{cases} \tag{C.24}$$

We note that FRET is increasing and bounded from above (see pC8 equation) therefore it converges to a constant value, denoted $FRET^+$, and its derivative converges to 0. Therefore, in the long term, System C.24 behaves like the following system:

$$\text{rEAICRm}^{\text{red.}} = \begin{cases} \dot{T} &= -K_1\, T\left(3T - 3T(t_0) + R(t_0)\right)^3 + \overline{K_1}\,\left(T(t_0) - T - Z1\right), \\ R &= 3T - 3T(t_0) + R(t_0) \\ Z0 &= T(t_0) - T - Z1 \\ pC8 &= \gamma_{pC8} - 2Z1 - 2\frac{K_{deg}+K_{fret}}{K_{fret}}FRET^+, \\ \dot{Z1} &= K_2\left(T(t_0) - T - Z1\right)pC8^2 - \overline{K_2}Z1 - \alpha_0 Z1, \\ \dot{C}8 &= \alpha_0 Z1. \end{cases} \tag{C.25}$$

Theorem C.4. *Let us assume $R(t_0) >> T(t_0) > 0$. System C.25 admits a unique equilibrium point which is locally asymptotically stable (LAS) and is given by :*

$$X_{pC8=0} = \begin{pmatrix} x_T^+ \\ 3x_T^+ - 3T(t_0) + R(t_0) \\ T(t_0) - x_T^+ \\ 0 \\ 0 \\ 0 \end{pmatrix} \tag{C.26}$$

with x_T^+ the only positive root of the following polynomial:

$$-3K_1T\left(T - T(t_0) + \frac{R(t_0)}{3}\right)^3 - \overline{K_1}\left(T - T(t_0)\right) \tag{C.27}$$

Remark The condition $R(t_0) >> T(t_0) > 0$ is always true in experimental conditions as *in vitro* experiments checked the presence of death receptors at the membrane level and all cells have access to TRAIL.

Proof.

We note that any equilibrium to System C.25 satisfies the following equations:

$$\begin{cases} C8 = 0 \\ Z1 = 0 \\ -3K_1T\left(T - T(t_0) + \frac{R(t_0)}{3}\right)^3 - \overline{K_1}\left(T - T(t_0)\right) = 0 \\ K_2\left(T(t_0) - T\right)\left(\gamma_{pC8} - 2\frac{K_{deg}+K_{fret}}{K_{fret}}FRET\right) = 0 \end{cases} \tag{C.28}$$

To solve C.28 (see fourth equation), we have the two following cases:

Case 1: $T(t_0) - T = 0$.
Following Case 1, from the third equation in C.28, necessarily $T = T(t_0) = 0$ or $R(t_0) = 0$. However, this is impossible in our case as $T(t_0)$ and $R(t_0)$ are always bigger than zero.

Case 2: $\gamma_{pC8} - 2\frac{K_{deg}+K_{fret}}{K_{fret}}FRET = 0$.
Solving equation $\dot{T} = 0$ for Case 2 leads to the following equation for T:

$$P(T) = -3K_1T\left(T - T(t_0) + \frac{R(t_0)}{3}\right)^3 - \overline{K_1}\left(T - T(t_0)\right) = 0. \tag{C.29}$$

We have:

$$P(0) = \overline{K_1}T(t_0) > 0, \tag{C.30}$$

$$P(T(t_0)) = -K_1T(t_0)R(t_0)^3 < 0, \tag{C.31}$$

$$P'(T) = -3K_1\left(T - T(t_0) + \frac{R(t_0)}{3}\right)^3 - 9K_1T\left(T - T(t_0) + \frac{R(t_0)}{3}\right)^2 - \overline{K_1}, \quad \text{(C.32)}$$

Recalling that $R(t_0) >> T(t_0) \geq T > 0$, we obtain:

$$P'(x_T) < 0, \text{ for all } x_T > 0 \quad \text{(C.33)}$$

Hence, P admits one positive root x_T^+ (by Intermediate value theorem).

Stability analysis :

$$Jac_{\text{rEAICRm}^{\text{red.}}}(X) = \begin{pmatrix} P'(T) & -\overline{K_1} & 0 \\ -K2\,pC8_{eq}^2 & -K_2\,pC8_{eq}^2 - 4K_2\,Z0_{eq}\,pC8_{eq} - (\overline{K_2} + \alpha_0) & -4K_2\,Z0_{eq}pC8_{eq} \\ 0 & \alpha 0 & -(K_{deg} + K_{fret}) \end{pmatrix}. \quad \text{(C.34)}$$

Therefore,

$$Jac_{\text{rEAICR}^{ass}}(X_{pC8=0}) = \begin{pmatrix} P'(x_T^+) & -\overline{K_1} & 0 \\ 0 & -(\overline{K_2} + \alpha_0) & 0 \\ 0 & \alpha 0 & -(K_{deg} + K_{fret}) \end{pmatrix} \quad \text{(C.35)}$$

Lets us find the eigen values of $Jac_{\text{rEAICRm}^{\text{red.}}}(X_{pC8=0})$.

$$\begin{aligned} \mid Jac_{\text{rEAICRm}^{\text{red.}}}(X_{pC8=0}) - \lambda \mid &= \begin{vmatrix} P'(x_T^+) - \lambda & -\overline{K_1} & 0 \\ 0 & -(\overline{K_2} + \alpha_0) - \lambda & 0 \\ 0 & \alpha 0 & -(K_{deg} + K_{fret}) - \lambda \end{vmatrix} \\ &= -\left(\overline{K_2} + \alpha_0 + \lambda\right)(P'(x_T^+) - \lambda)(-(K_{deg} + K_{fret}) - \lambda) \end{aligned}$$

The three eigen values ($-(\overline{K_2} + \alpha_0)$, $-(K_{deg} + K_{fret})$ and $P'(x_T^+)$) are all strictly negatives therefore our equilibrium point is LAS.

□

Remarks: In our case, $T(t_0) \leq 1500$ and $R(t_0) \approx 30000$ therefore $P'(T) << 0$ and T goes quickly toward the equilibrium point that is close to 0 and will lead to the approximation done in Chapter 5.

D Chapter 6

D.1 How smoothing, filtering and re-scaling time-trajectories affect the slope values

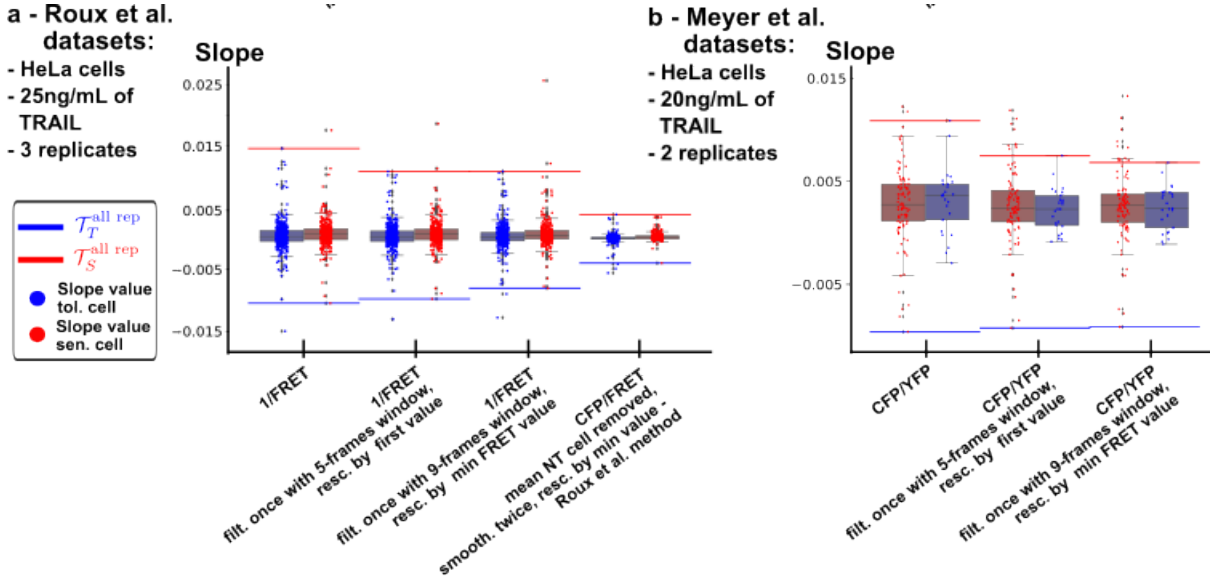

Figure D.15: Comparison of the time-trajectories pre-processing techniques and their effects on the slope value for Roux et al and Meyer et al. datatsets - the Moving Average filter is not represented

In the forecasting step, what is important for the pipeline is the number of recurrent outliers for each drug-response. For the FRET signal from [Roux et al., 2015], the choice between a smoothing step and a filtration, the length of the window for the filter or removing the mean untreated cell affect the derivative but there is still outliers for both drug-response. It is not the case for the ratio CFP/YFP from [Meyer et al., 2020], that requires a big filter window to have outliers for both phenotypes. Obviously, as the derivative of a constant is 0, the re-scaling by any constant number does not affect the derivative value, but it could for other features.

D.2 On the importance of the filter window size for the CFP/YFP dataset of Meyer et al. (2020)

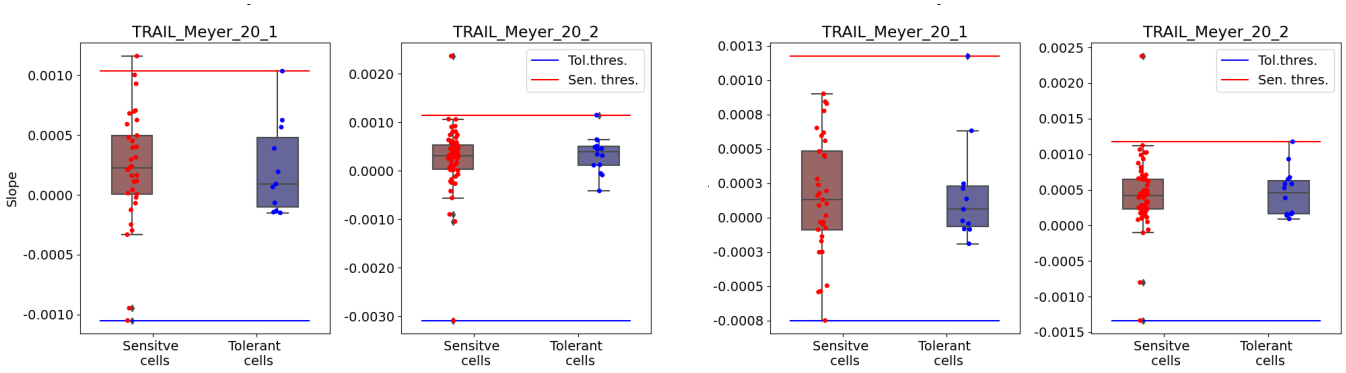

(a) 5-frames window

(b) 9-frames window

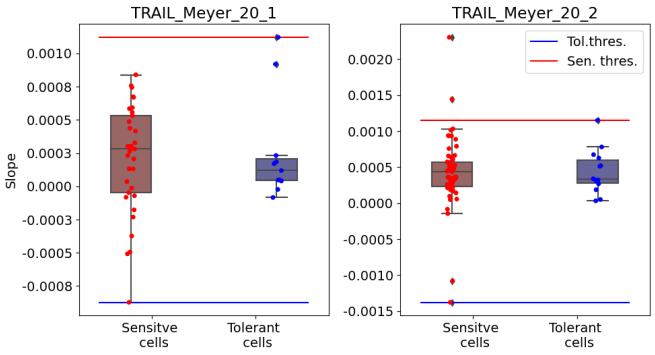

(c) 13-frames window

Figure D.16: Determining threshold study with different filter windows size for Raw CFP/YFP dataset from Meyer et al (2020)

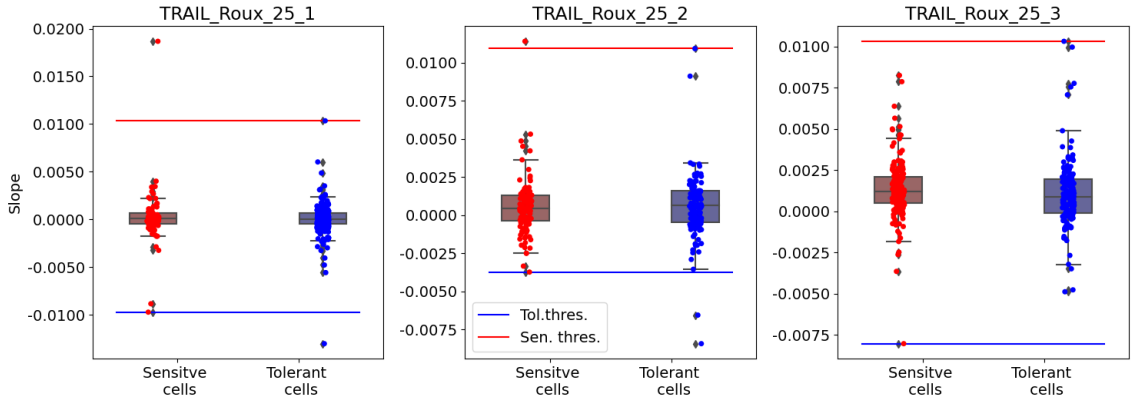

Figure D.17: Determining threshold study with a filter window of 5 frames for the raw 1/FRET ratio datasets from Roux et al. (2015) study

D.3 3-fold (resp. 2) cross validation for the current FATE-SEQ drug-response forecasting method used to select cells for isolation for CFP/FRET and CFP/YFP datasets

Testing set	TRAIL_Meyer_20_1	TRAIL_Meyer_20_2	mean	std
Dataset description				
N cells in testing	44	77	60.5	16.5
% tol. cell. in test	25.0	18.182	21.591	3.409
% tol. cell. in train	18.182	25.0	21.591	3.409
Method application				
$\mathcal{N}_T$	0	0	0.0	0.0
$\mathcal{N}_S$	0	0	0.0	0.0
% of cell represented by $\mathcal{N}_T$ and $\mathcal{N}_S$ in test	0.0	0.0	0.0	0.0
$\mathcal{N}_T^{\text{train}}$	0	0	0.0	0.0
$\mathcal{N}_S^{\text{train}}$	1	0	0.5	0.5
$\mathcal{T}_T^{\text{train}}$	-0.001	-0.001	-0.001	0.0
$\mathcal{T}_S^{\text{train}}$	0.001	0.001	0.001	0.0
$\mathcal{N}_T^{\text{test}}$	0	0	0.0	0.0
$\mathcal{N}_S^{\text{test}}$	0	1	0.5	0.5
i) Overcoming threshold method				
i - ACC on test	1.0	0.0	0.5	0.5
i - % of cell pred. for iso. in test	2.273	3.896	3.084	0.812
i - # cell pred. tol. for iso. in test	0	2	1.0	1.0
i - # cell pred. sen. for iso. in test	1	1	1.0	0.0
ii) Ranking method with 4 cells for each class				
ii - ACC on test	0.375	0.375	0.375	0.0
ii - % of cell pred. for iso. in test	18.182	10.39	14.286	3.896
iii) Ranking with $\mathcal{N}_T^{\text{train}}$ and $\mathcal{N}_S^{\text{train}}$				
iii - ACC on test	0.0	NaN	0	0
iii - % of cell pred. for iso. in test	2.273	0.0	1.136	1.136

Table D.14: Dataset description and performances of the current FATE-SEQ drug-response forecasting method used to select non-overlapping cells for isolation during 3-fold cross-validation on CFP/YFP ratio dataset (Meyer et al.) - tol. : tolerant, sen.: sensitive, pred. predicted, iso.: isolation, std: standard deviation

Testing set	TRAIL_Roux_25_1	TRAIL_Roux_25_2	TRAIL_Roux_25_3	mean	std
Dataset description					
N cells in testing	344	221	327	297.333	54.42
% tol. cell. in test	72.674	51.131	45.872	56.559	11.596
% tol. cell. in train	47.993	59.613	64.248	57.284	6.837
Method application					
$\mathcal{N}_T$	0	0	0	0.0	0.0
$\mathcal{N}_S$	0	0	0	0.0	0.0
% of cell represented by $\mathcal{N}_T$ and $\mathcal{N}_S$ in test	0.0	0.0	0.0	0.0	0.0
$\mathcal{N}_T^{\text{train}}$	0	0	1	0.333	0.471
$\mathcal{N}_S^{\text{train}}$	0	0	1	0.333	0.471
$\mathcal{T}_T^{\text{train}}$	-0.007	-0.01	-0.01	-0.009	0.002
$\mathcal{T}_S^{\text{train}}$	0.013	0.015	0.015	0.014	0.001
$\mathcal{N}_T^{\text{test}}$	1	3	0	1.333	1.247
$\mathcal{N}_S^{\text{test}}$	1	1	0	0.667	0.471
i) Overcoming threshold method					
i - ACC on test	0.4	NaN	NaN	0.4	0
i - % of cell pred. for iso. in test	1.453	0.0	0.0	0.484	0.685
i - # cell pred. tol. for iso. in test	3	0	0	1.0	1.414
i - # cell pred. sen. for iso. in test	2	0	0	0.667	0.943
ii) Ranking method with 4 cells for each class					
ii - ACC on test	0.375	0.625	0.375	0.458	0.118
ii - % of cell pred. for iso. in test	2.326	3.62	2.446	2.797	0.584
iii) Ranking with $\mathcal{N}_T^{\text{train}}$ and $\mathcal{N}_S^{\text{train}}$					
iii - ACC on test	NaN	NaN	0.0	NaN	NaN
iii - % of cell pred. for iso. in test	0.0	0.0	0.612	0.204	0.288

Table D.15: Dataset description and performances of the current FATE-SEQ drug-response forecasting method used to select non-overlapping cells for isolation during 3-fold cross-validation on CFP/FRET ratio dataset (Roux et al.) - tol. : tolerant, sen.: sensitive, pred. predicted, iso.: isolation, std: standard deviation

D.4 5-fold cross validation for the current FATE-SEQ drug-response forecasting method used to select cells for isolation

Testing set	CV 1	CV 2	CV 3	CV 4	CV 5	mean	std
Dataset description							
N cells in testing	179	179	178	178	178	178.4	0.49
% tol. cell. in test	57.542	57.542	57.865	57.303	57.303	57.511	0.207
% tol. cell. in train	57.504	57.504	57.423	57.563	57.563	57.511	0.052
Method application							
$\mathcal{N}_T$	0	0	0	0	0	0.0	0.0
$\mathcal{N}_S$	0	0	0	0	0	0.0	0.0
% of cell represented by $\mathcal{N}_T$ and $\mathcal{N}_S$ in test	0.0	0.0	0.0	0.0	0.0	0.0	0.0
$\mathcal{N}_T^{\text{train}}$	0	1	0	0	0	0.2	0.4
$\mathcal{N}_S^{\text{train}}$	0	0	0	0	0	0.0	0.0
$\mathcal{T}_T^{\text{train}}$	0.011	0.011	0.011	0.011	0.011	0.011	0.0
$\mathcal{T}_S^{\text{train}}$	-0.008	-0.008	-0.008	-0.008	-0.008	-0.008	0.0
$\mathcal{N}_T^{\text{test}}$	3	0	2	1	2	1.6	1.02
$\mathcal{N}_S^{\text{test}}$	1	1	5	0	0	1.4	1.855
i) Overcoming threshold method							
i - ACC on test	1.0	0.0	0.0	1.0	1.0	0.6	0.49
i - % of cell pred. for iso. in test	0.559	1.117	0.562	0.562	0.562	0.672	0.223
i - # cell pred. tol. for iso. in test	1	1	0	1	0	0.6	0.49
i - # cell pred. sen. for iso. in test	0	1	1	0	1	0.6	0.49
ii) Ranking method with 4 cells for each class							
ii - ACC on test	0.625	0.375	0.75	0.375	0.375	0.5	0.158
ii - % of cell pred. for iso. in test	4.469	4.469	4.494	4.494	4.494	4.484	0.012
iii) Ranking with $\mathcal{N}_T^{\text{train}}$ and $\mathcal{N}_S^{\text{train}}$							
iii - ACC on test	NaN	0.0	NaN	NaN	NaN	0	0
iii - % of cell pred. for iso. in test	0.0	0.559	0.0	0.0	0.0	0.112	0.223

Table D.16: Dataset description and performances of the current FATE-SEQ drug-response forecasting method used to select non-overlapping cells for isolation during 5-fold cross-validation on raw 1/ FRET dataset (Roux et al.) - tol. : tolerant, sen.: sensitive, pred. predicted, iso.: isolation, std: standard deviation

Testing set	CV 1	CV 2	CV 3	CV 4	CV 5	mean	std
Dataset description							
N cells in testing	25	24	24	24	24	24.2	0.4
% tol. cell. in test	20.0	20.833	20.833	20.833	20.833	20.667	0.333
% tol. cell. in train	20.833	20.619	20.619	20.619	20.619	20.662	0.086
Method application							
$\mathcal{N}_T$	0	0	0	0	0	0.0	0.0
$\mathcal{N}_S$	0	0	0	0	0	0.0	0.0
% of cell represented by $\mathcal{N}_T$ and $\mathcal{N}_S$ in test	0.0	0.0	0.0	0.0	0.0	0.0	0.0
$\mathcal{N}_T^{\text{train}}$	0	0	0	0	0	0.0	0.0
$\mathcal{N}_S^{\text{train}}$	0	1	0	0	0	0.2	0.4
$\mathcal{T}_T^{\text{train}}$	0.001	0.001	0.001	0.001	0.001	0.001	0.0
$\mathcal{T}_S^{\text{train}}$	-0.001	-0.001	-0.001	-0.001	-0.001	-0.001	0.0
$\mathcal{N}_T^{\text{test}}$	0	0	0	0	0	0.0	0.0
$\mathcal{N}_S^{\text{test}}$	5	0	1	3	4	2.6	1.855
i) Overcoming threshold method							
i - ACC on test	NaN	0.667	0.0	NaN	0.0	0.223	0.314
i - % of cell pred. for iso. in test	0.0	12.5	4.167	0.0	4.167	4.167	4.564
i - # cell pred. tol. for iso. in test	0	0	1	0	0	0.2	0.4
i - # cell pred. sen. for iso. in test	0	3	0	0	1	0.8	1.166
ii) Ranking method with 4 cells for each class							
ii - ACC on test	0.625	0.375	0.5	0.5	0.5	0.5	0.079
ii - % of cell pred. for iso. in test	32.0	33.333	33.333	33.333	33.333	33.067	0.533
iii) Ranking with $\mathcal{N}_T^{\text{train}}$ and $\mathcal{N}_S^{\text{train}}$							
iii - ACC on test	NaN	0.0	NaN	NaN	NaN	0	0
iii - % of cell pred. for iso. in test	0.0	4.167	0.0	0.0	0.0	0.833	1.667

Table D.17: Dataset description and performances of the current FATE-SEQ drug-response forecasting method used to select non-overlapping cells for isolation during 5-fold cross-validation on CFP/YFP ratio dataset (Meyer et al.) - tol. : tolerant, sen.: sensitive, pred. predicted, iso.: isolation, std: standard deviation

Testing set	CV 1	CV 2	CV 3	CV 4	CV 5	mean	std
Dataset description							
N cells in testing	179	179	178	178	178	178.4	0.49
% tol. cell. in test	57.542	57.542	57.865	57.303	57.303	57.511	0.207
% tol. cell. in train	57.504	57.504	57.423	57.563	57.563	57.511	0.052
Method application							
$\mathcal{N}_T$	0	0	0	0	0	0.0	0.0
$\mathcal{N}_S$	0	0	0	0	0	0.0	0.0
% of cell represented by $\mathcal{N}_T$ and $\mathcal{N}_S$ in test	0.0	0.0	0.0	0.0	0.0	0.0	0.0
$\mathcal{N}_T^{\text{train}}$	0	1	0	0	0	0.2	0.4
$\mathcal{N}_S^{\text{train}}$	0	0	0	0	0	0.0	0.0
$\mathcal{T}_T^{\text{train}}$	0.015	0.015	0.015	0.015	0.011	0.014	0.001
$\mathcal{T}_S^{\text{train}}$	-0.01	-0.009	-0.01	-0.01	-0.01	-0.01	0.0
$\mathcal{N}_T^{\text{test}}$	3	0	4	1	1	1.8	1.47
$\mathcal{N}_S^{\text{test}}$	0	1	2	0	0	0.6	0.8
i) Overcoming threshold method							
i - ACC on test	NaN	0.0	NaN	1.0	1.0	0.667	0.471
i - % of cell pred. for iso. in test	0.0	1.117	0.0	0.562	1.685	0.673	0.654
i - # cell pred. tol. for iso. in test	0	1	0	1	0	0.4	0.49
i - # cell pred. sen. for iso. in test	0	1	0	0	3	0.8	1.166
ii) Ranking method with 4 cells for each class							
ii - ACC on test	0.625	0.5	0.875	0.625	0.25	0.575	0.203
ii - % of cell pred. for iso. in test	4.469	4.469	4.494	4.494	4.494	4.484	0.012
iii) Ranking with $\mathcal{N}_T^{\text{train}}$ and $\mathcal{N}_S^{\text{train}}$							
iii - ACC on test	NaN	0.0	NaN	NaN	NaN	0	0
iii - % of cell pred. for iso. in test	0.0	0.559	0.0	0.0	0.0	0.112	0.223

Table D.18: Dataset description and performances of the current FATE-SEQ drug-response forecasting method used to select non-overlapping cells for isolation during 5-fold cross-validation on CFP/FRET ratio dataset (Roux et al.) - tol. : tolerant, sen.: sensitive, pred. predicted, iso.: isolation, std: standard deviation

E Chapter 7

E.1 Metric scores to evaluate performances of a machine learning model for classification

E.1.1 Notations and vocabulary

train: refers to the dataset used to train the model.
test: refers to the dataset used to test the model after training.
all: refers to the whole dataset with train and test datasets combined and mixed.
N: ground truth, negative (=sensitive for us)
P: ground truth, positive (=tolerant for us)
PP: predicted positive
PN: predicted negative
TP: true positive (positive case predicted positive)
TN: true negative
FP: false positive (negative case predicted positive)
FN: false negative
Confusion matrix: $\begin{pmatrix} TP & FN \\ FP & TN \end{pmatrix}$
Decision threshold: between 0 and 1, probability threshold to cross to be predicted positive/resistant. For each cell/observation, if the probability of "being resistant" given by the machine learning model is above the decision threshold then the cell is predicted resistant else it's predicted sensitive.

E.1.2 Evaluation criteria - How to evaluate your model performances

Different scores and methods exist to evaluate the performances of a model (not exhaustive list):
ACC: $ACC = \frac{TP + TN}{P + N}$
False negative rate FNR: $FNR = \frac{FN}{TP + FN}$
False positive rate FPR: $FPR = \frac{FP}{FP + TN}$
False omission rate FOR: $FOR = \frac{FN}{TN + FN}$
False discovery rate FDR: $FDR = \frac{FP}{FP + TP}$
Prec./ Positive predicted value PPV: $PPV = \frac{TP}{TP + FP}$
Negative predicted value NPV: $NPV = \frac{TN}{TN + FN}$
Recall/ True positive rate TPR: $TPR = \frac{TP}{TP + FN}$
True negative rate TNR: $TNR = \frac{TN}{TN + FP}$

Markedness MK: $MK = \frac{TP}{PP} + \frac{TN}{PN} - 1$

Matthews correlation coefficient MCC:
$MCC = \sqrt{TPR \times TNR \times PPV \times NPV} - \sqrt{FNR \times FPR \times FOR \times FDR}$

ROC curve: represents the false positive rate in x and the true positive rate in y when different decision thresholds are applied.

E.1.3 Cross-Validation

A K-fold cross validation consists in running K times your model, each time with a different training set and a testing set to evaluate the model's performances and robustness on different datasets. To do so, the whole dataset is split into a training set and a testing set, K times, with the insurance that each observation (each cell for us) is at least once in the testing set, so never seen by the model.

E.2 Best machine learning models to forecast drug-response from FRET time-trajectories performances

Type of classifier - Time frames used	Best model/ Scores	**Raw 1/FRET**	**1/FRET - 5 fw - SG**	**1/FRET - 9 fw - SG**	**1/FRET - MA**	**CFP/FRET ratio**
ML - 30 min	Model	5NN+ Pow. Gauss.	Constant+ Pow. Gauss.	MLP+ no p.	Constant+ no p.	Ridge+ Quant. Unif.
	MCC	0.128 ± 0.058	0.000 ± 0.000	0.000 ± 0.000	0.000 ± 0.000	0.251 ± 0.039
	ACC	0.577 ± 0.031	0.575 ± 0.002	0.575 ± 0.002	0.575 ± 0.002	0.638 ± 0.012
	F1	0.640 ± 0.040	0.730 ± 0.002	0.730 ± 0.002	0.730 ± 0.002	0.750 ± 0.008
	BACC	0.563 ± 0.028	0.500 ± 0.000	0.500 ± 0.000	0.500 ± 0.000	0.583 ± 0.016
	MK	0.131 ± 0.059	-0.425 ± 0.002	-0.425 ± 0.002	-0.425 ± 0.002	0.381 ± 0.066
	Prec.	0.626 ± 0.022	0.575 ± 0.002	0.575 ± 0.002	0.575 ± 0.002	0.622 ± 0.008
	Rec.	0.659 ± 0.068	1.000 ± 0.000	1.000 ± 0.000	1.000 ± 0.000	0.945 ± 0.025
ML - 50 min	Model	RF+ Pow. Gauss.	Ridge + Min-Max	Ridge+ PCA	Constant+ no p.	AB+ Pow. Gauss.
	MCC	0.095 ± 0.101	0.059 ± 0.053	0.053 ± 0.066	0.000 ± 0.000	0.284 ± 0.063
	ACC	0.577 ± 0.037	0.578 ± 0.009	0.578 ± 0.005	0.575 ± 0.002	0.659 ± 0.028
	F1	0.702 ± 0.048	0.725 ± 0.011	0.730 ± 0.005	0.730 ± 0.002	0.733 ± 0.021
	BACC	0.524 ± 0.025	0.510 ± 0.008	0.506 ± 0.006	0.500 ± 0.000	0.631 ± 0.030
	MK	0.193 ± 0.206	0.191 ± 0.178	0.278 ± 0.401	-0.425 ± 0.002	0.307 ± 0.067
	Prec.	0.588 ± 0.014	0.580 ± 0.003	0.578 ± 0.002	0.575 ± 0.002	0.669 ± 0.022
	Rec.	0.879 ± 0.122	0.967 ± 0.034	0.990 ± 0.015	1.000 ± 0.000	0.813 ± 0.031
ML - 30 to 50 min	Model	MLP+ no p.	MLP + Max-Abs	Ridge+ PCA	MLP+ no p.	MLP+ PCA+ Quant. Unif.
	MCC	0.000 ± 0.000	0.085 ± 0.038	0.046 ± 0.032	0.000 ± 0.000	0.312 ± 0.071
	ACC	0.575 ± 0.002	0.584 ± 0.008	0.577 ± 0.005	0.575 ± 0.002	0.668 ± 0.027
	F1	0.730 ± 0.002	0.719 ± 0.020	0.729 ± 0.005	0.730 ± 0.002	0.744 ± 0.032
	BACC	0.500 ± 0.000	0.522 ± 0.013	0.505 ± 0.003	0.500 ± 0.000	0.636 ± 0.021
	MK	-0.425 ± 0.002	0.182 ± 0.111	0.230 ± 0.198	-0.425 ± 0.002	0.362 ± 0.115
	Prec.	0.575 ± 0.002	0.588 ± 0.009	0.578 ± 0.002	0.575 ± 0.002	0.669 ± 0.014
	Rec.	1.000 ± 0.000	0.932 ± 0.075	0.986 ± 0.013	1.000 ± 0.000	0.844 ± 0.083
ML - 2h	Model	MLP+ no p.	Ridge+ Pow. Gauss.	MLP+ Pow. Gauss.	Constant+ no p.	MLP+ Rob.
	MCC	0.290 ± 0.023	0.347 ± 0.022	0.340 ± 0.070	0.000 ± 0.000	0.367 ± 0.106
	ACC	0.650 ± 0.014	0.681 ± 0.013	0.679 ± 0.035	0.575 ± 0.002	0.695 ± 0.058
	F1	0.749 ± 0.017	0.766 ± 0.007	0.742 ± 0.044	0.730 ± 0.002	0.758 ± 0.073
	BACC	0.604 ± 0.027	0.640 ± 0.022	0.656 ± 0.029	0.500 ± 0.000	0.661 ± 0.045
	MK	0.430 ± 0.107	0.438 ± 0.047	0.373 ± 0.095	-0.425 ± 0.002	0.425 ± 0.145
	Prec.	0.640 ± 0.025	0.663 ± 0.020	0.687 ± 0.019	0.575 ± 0.002	0.712 ± 0.028
	Rec.	0.912 ± 0.086	0.912 ± 0.049	0.813 ± 0.095	1.000 ± 0.000	0.826 ± 0.147
ML - 6h	Model	SVC+ no p.	SVC+ PCA	RF + PCA Standard	Constant + no p.	Ridge + PCA + Quant. Unif.
	MCC	0.719 ± 0.052	0.712 ± 0.049	0.720 ± 0.076	0.000 ± 0.000	0.340 ± 0.068
	ACC	0.862 ± 0.027	0.858 ± 0.026	0.862 ± 0.041	0.575 ± 0.002	0.908 ± 0.013
	F1	0.890 ± 0.020	0.887 ± 0.021	0.883 ± 0.041	0.730 ± 0.002	0.951 ± 0.008
	BACC	0.844 ± 0.035	0.841 ± 0.031	0.854 ± 0.036	0.500 ± 0.000	0.600 ± 0.017
	MK	0.752 ± 0.047	0.745 ± 0.053	0.734 ± 0.084	-0.425 ± 0.002	0.616 ± 0.258
	Prec.	0.848 ± 0.042	0.844 ± 0.035	0.875 ± 0.033	0.575 ± 0.002	0.921 ± 0.003
	Rec.	0.939 ± 0.042	0.937 ± 0.048	0.896 ± 0.082	1.000 ± 0.000	0.982 ± 0.018

Table E.19: Performances of the best machine learning models - according to the ACC score - to forecast drug-response from FRET time-trajectories during 5-fold cross-validation after benchmarking of the state-of-the-art models available

Type of classifier - Time frames used	Best model/ Scores	**Raw 1/FRET**	**1/FRET - 5 fw - SG**	**1/FRET - 9 fw - SG**	**1/FRET - MA**	**CFP/FRET ratio**
TS - 30 min	Model	ShapeDTW	Arsenal	Arsenal	Arsenal	Shapelet
	MCC	0.127 ± 0.062	0.011 ± 0.051	-0.002 ± 0.083	0.011 ± 0.047	0.192 ± 0.071
	ACC	0.574 ± 0.030	0.568 ± 0.012	0.571 ± 0.015	0.554 ± 0.016	0.621 ± 0.028
	F1	0.632 ± 0.028	0.715 ± 0.018	0.712 ± 0.013	0.681 ± 0.015	0.722 ± 0.019
	BACC	0.563 ± 0.031	0.502 ± 0.010	0.508 ± 0.022	0.505 ± 0.019	0.580 ± 0.031
	MK	0.127 ± 0.062	-0.043 ± 0.238	-0.131 ± 0.257	0.012 ± 0.060	0.231 ± 0.083
	Prec.	0.629 ± 0.026	0.576 ± 0.004	0.580 ± 0.011	0.579 ± 0.012	0.625 ± 0.019
	Rec.	0.636 ± 0.040	0.946 ± 0.059	0.926 ± 0.052	0.828 ± 0.046	0.856 ± 0.022
TS - 50 min	Model	DrCIF	TSF	HIVECOTEV2	RISE	Arsenal
	MCC	0.142 ± 0.068	0.055 ± 0.072	0.071 ± 0.068	0.010 ± 0.096	0.266 ± 0.057
	ACC	0.592 ± 0.033	0.555 ± 0.031	0.565 ± 0.032	0.541 ± 0.046	0.651 ± 0.024
	F1	0.673 ± 0.030	0.650 ± 0.021	0.665 ± 0.028	0.656 ± 0.044	0.741 ± 0.022
	BACC	0.567 ± 0.031	0.526 ± 0.035	0.532 ± 0.031	0.502 ± 0.041	0.612 ± 0.022
	MK	0.151 ± 0.074	0.058 ± 0.075	0.079 ± 0.075	0.019 ± 0.114	0.317 ± 0.075
	Prec.	0.623 ± 0.021	0.594 ± 0.027	0.597 ± 0.022	0.575 ± 0.026	0.648 ± 0.013
	Rec.	0.733 ± 0.043	0.717 ± 0.023	0.750 ± 0.039	0.764 ± 0.075	0.868 ± 0.039
TS - 30 to 50 min	Model	Arsenal	HIVECOTEV2	Arsenal	Shapelet	Shapelet
	MCC	-0.058 ± 0.050	0.073 ± 0.065	0.029 ± 0.083	0.076 ± 0.085	0.201 ± 0.044
	ACC	0.55 ± 0.014	0.563 ± 0.025	0.572 ± 0.022	0.577 ± 0.037	0.621 ± 0.022
	F1	0.702 ± 0.012	0.654 ± 0.020	0.713 ± 0.017	0.680 ± 0.03	0.703 ± 0.026
	BACC	0.485 ± 0.013	0.535 ± 0.03	0.509 ± 0.024	0.532 ± 0.037	0.592 ± 0.019
	MK	-0.11 ± 0.098	0.077 ± 0.071	0.044 ± 0.146	0.091 ± 0.099	0.221 ± 0.055
	Prec.	0.567 ± 0.007	0.601 ± 0.023	0.580 ± 0.013	0.596 ± 0.026	0.641 ± 0.012
	Rec.	0.922045 ± 0.025	0.721 ± 0.048	0.924 ± 0.019	0.793 ± 0.050	0.78 ± 0.057
TS - 2h	Model	Shapelet	DrCIF	DrCIF	DrCIF	Shapelet
	MCC	0.321 ± 0.069	0.301 ± 0.056	0.306 ± 0.024	0.218 ± 0.069	0.358 ± 0.048
	ACC	0.675 ± 0.032	0.666 ± 0.024	0.667 ± 0.010	0.627 ± 0.031	0.702 ± 0.021
	F1	0.740 ± 0.022	0.733 ± 0.012	0.733 ± 0.009	0.700 ± 0.026	0.774 ± 0.015
	BACC	0.652 ± 0.035	0.643 ± 0.032	0.644 ± 0.016	0.604 ± 0.033	0.664 ± 0.023
	MK	0.338 ± 0.068	0.318 ± 0.049	0.325 ± 0.023	0.229 ± 0.072	0.391 ± 0.051
	Prec.	0.686 ± 0.029	0.681 ± 0.029	0.681 ± 0.019	0.652 ± 0.025	0.710 ± 0.016
	Rec.	0.805 ± 0.023	0.795 ± 0.025	0.797 ± 0.040	0.756 ± 0.040	0.852 ± 0.016
TS - 6h	Model	DrCIF	DrCIF	DrCIF	Arsenal	DrCIF
	MCC	0.731 ± 0.034	0.728 ± 0.035	0.751 ± 0.041	0.696 ± 0.040	0.176 ± 0.172
	ACC	0.870 ± 0.017	0.869 ± 0.017	0.879 ± 0.020	0.854 ± 0.019	0.907 ± 0.009
	F1	0.895 ± 0.011	0.894 ± 0.013	0.902 ± 0.016	0.881 ± 0.014	0.951 ± 0.005
	BACC	0.854 ± 0.023	0.855 ± 0.021	0.865 ± 0.021	0.839 ± 0.022	0.543 ± 0.041
	MK	0.755 ± 0.021	0.748 ± 0.032	0.772 ± 0.045	0.713 ± 0.036	0.344 ± 0.396
	Prec.	0.856 ± 0.028	0.859 ± 0.025	0.866 ± 0.023	0.848 ± 0.023	0.911 ± 0.007
	Rec.	0.940 ± 0.011	0.932 ± 0.020	0.941 ± 0.030	0.918 ± 0.013	0.994 ± 0.005

Table E.20: Performances of the best machine learning models - according to the ACC score - to forecast drug-response from FRET time-trajectories during 5-fold cross-validation after benchmarking of the state-of-the-art models available - time-series specific models

E.3 Performances of the classic machine learning models using mechanistic features to forecast drug-response

Feat.-Time	Best / Scores	Slope	FRETexp model	Roux et al model	FRET + Slope	FRET + FRET-exp	FRET + Roux et al. param.
50 min	Model	MLP + PCA+ Standard	SVC+ Quant. Unif.	MLP + PCA+ Rob.	RF+ Rob.	Ridge + PCA+ Rob.	Ridge+ Rob.
	MCC	0.257 ± 0.073	0.160 ± 0.066	0.247 ± 0.053	0.280 ± 0.091	0.262 ± 0.089	0.257 ± 0.042
	ACC	0.646 ± 0.034	0.601 ± 0.030	0.640 ± 0.025	0.652 ± 0.047	0.650 ± 0.036	0.647 ± 0.016
	F1	0.731 ± 0.035	0.688 ± 0.038	0.724 ± 0.033	0.718 ± 0.056	0.742 ± 0.024	0.740 ± 0.013
	BACC	0.610 ± 0.033	0.570 ± 0.025	0.607 ± 0.018	0.629 ± 0.038	0.610 ± 0.043	0.605 ± 0.024
	MK	0.300 ± 0.091	0.184 ± 0.089	0.288 ± 0.082	0.304 ± 0.111	0.317 ± 0.102	0.318 ± 0.062
	Prec.	0.650 ± 0.026	0.624 ± 0.016	0.646 ± 0.011	0.670 ± 0.026	0.648 ± 0.031	0.644 ± 0.019
	Rec.	0.838 ± 0.076	0.774 ± 0.093	0.826 ± 0.078	0.777 ± 0.103	0.871 ± 0.052	0.873 ± 0.052
30 to 50 min[§]	Model	SVC + PCA+ Quant. Unif.	MLP+ Quant. Unif.	SVC + PCA+ Quant. Unif.	Ridge+ Rob.	Ridge + PCA+ MinMax	Ridge + PCA+ Rob.
	MCC	0.255 ± 0.096	0.160 ± 0.078	0.245 ± 0.050	0.289 ± 0.067	0.302 ± 0.067	0.310 ± 0.067
	ACC	0.645 ± 0.040	0.601 ± 0.036	0.639 ± 0.025	0.658 ± 0.024	0.663 ± 0.023	0.666 ± 0.023
	F1	0.736 ± 0.035	0.684 ± 0.042	0.717 ± 0.034	0.747 ± 0.025	0.756 ± 0.020	0.751 ± 0.026
	BACC	0.605 ± 0.038	0.573 ± 0.033	0.610 ± 0.020	0.618 ± 0.025	0.618 ± 0.026	0.627 ± 0.021
	MK	0.315 ± 0.131	0.178 ± 0.094	0.275 ± 0.069	0.362 ± 0.114	0.394 ± 0.114	0.385 ± 0.123
	Prec.	0.644 ± 0.028	0.626 ± 0.021	0.651 ± 0.014	0.652 ± 0.019	0.649 ± 0.019	0.659 ± 0.015
	Rec.	0.863 ± 0.074	0.760 ± 0.085	0.803 ± 0.080	0.879 ± 0.068	0.906 ± 0.057	0.877 ± 0.076
2h	Model	Ridge+ Quant. Unif.	MLP+ Quant. Unif.	AB + PCA+ Pow. Gaus.	SVC+ Quant. Unif.	SVC+ Quant. Unif.	SVC+ Quant. Unif.
	MCC	0.371 ± 0.123	0.325 ± 0.070	0.364 ± 0.015	0.380 ± 0.074	0.366 ± 0.084	0.358 ± 0.079
	ACC	0.689 ± 0.068	0.671 ± 0.034	0.693 ± 0.009	0.703 ± 0.040	0.697 ± 0.044	0.694 ± 0.044
	F1	0.740 ± 0.088	0.736 ± 0.042	0.750 ± 0.018	0.769 ± 0.052	0.768 ± 0.052	0.763 ± 0.055
	BACC	0.666 ± 0.048	0.647 ± 0.032	0.673 ± 0.012	0.668 ± 0.031	0.658 ± 0.040	0.656 ± 0.037
	MK	0.420 ± 0.172	0.363 ± 0.094	0.385 ± 0.025	0.436 ± 0.118	0.433 ± 0.124	0.417 ± 0.114
	Prec.	0.726 ± 0.035	0.683 ± 0.029	0.705 ± 0.018	0.716 ± 0.023	0.707 ± 0.029	0.706 ± 0.026
	Rec.	0.775 ± 0.175	0.807 ± 0.105	0.805 ± 0.059	0.842 ± 0.118	0.851 ± 0.118	0.842 ± 0.122
6h	Model	Ridge + PCA+ Rob.	MLP+ Rob.	MLP + PCA+ Quant. Unif.	MLP + PCA+ Standard	MLP+ Pow. Gaus.	MLP + PCA+ MinMax
	MCC	0.310 ± 0.088	0.654 ± 0.045	0.720 ± 0.063	0.339 ± 0.125	0.082 ± 0.164	0.253 ± 0.128
	ACC	0.912 ± 0.008	0.827 ± 0.023	0.860 ± 0.034	0.914 ± 0.012	0.907 ± 0.007	0.907 ± 0.007
	F1	0.953 ± 0.004	0.864 ± 0.016	0.883 ± 0.028	0.954 ± 0.006	0.951 ± 0.004	0.950 ± 0.004
	BACC	0.570 ± 0.022	0.806 ± 0.027	0.849 ± 0.039	0.587 ± 0.041	0.518 ± 0.036	0.575 ± 0.052
	MK	0.716 ± 0.247	0.699 ± 0.034	0.746 ± 0.062	0.705 ± 0.277	0.106 ± 0.407	0.473 ± 0.332
	Prec.	0.916 ± 0.004	0.793 ± 0.027	0.852 ± 0.048	0.919 ± 0.008	0.906 ± 0.007	0.917 ± 0.010
	Rec.	0.994 ± 0.008	0.949 ± 0.011	0.922 ± 0.062	0.992 ± 0.010	1.000 ± 0.000	0.986 ± 0.018

Table E.21: Forecasting single-cell drug-response using mechanistic features in a machine learning classifier - Performances according to ACC. score on CFP/FRET datasets from Roux et al.

E.4 Forecasting single-cell drug-response using mechanistic features in a machine learning classifier for 1/FRET

Feat./ Score	Slope	FRETexp	Roux et al. model	Slope + Time points	FRETexp + Time points	Roux et al. model + Time points
50 min						
Model	Ridge + Rob.	GB + Rob.	GB+ no p.	MLP+PCA+ Quant. Unif.	1NN+ no p.	1NN+PCA+ Pow. Gaus.
MCC	0.037±0.086	0.096±0.056	0.104±0.028	0.064±0.066	0.074±0.072	0.087±0.082
ACC	0.574±0.015	0.576±0.029	0.576±0.019	0.554±0.030	0.546±0.037	0.563±0.035
F1	0.722±0.013	0.677±0.034	0.665±0.036	0.633±0.055	0.600±0.043	0.636±0.047
BACC	0.505±0.014	0.541±0.023	0.547±0.011	0.531±0.033	0.537±0.036	0.543±0.043
MK	0.130±0.281	0.113±0.068	0.116±0.035	0.069±0.067	0.075±0.072	0.091±0.079
Prec.	0.578±0.006	0.601±0.017	0.608±0.007	0.601±0.029	0.607±0.031	0.613±0.039
Rec.	0.961±0.029	0.776±0.066	0.738±0.083	0.686±0.138	0.596±0.067	0.676±0.127
30 to 50 min						
	Ridge + Rob.	GB + Rob.	GB + Rob.	5NN+PCA+ Rob.	MLP+PCA+ Rob.	DT+PCA+ Rob.
MCC	0.037±0.086	0.090±0.067	0.106±0.043	0.094±0.045	0.055±0.059	0.087±0.104
ACC	0.574±0.015	0.573±0.035	0.578±0.018	0.564±0.013	0.535±0.031	0.515±0.078
F1	0.722±0.013	0.673±0.040	0.668±0.028	0.630±0.048	0.580±0.088	0.396±0.259
BACC	0.505±0.014	0.538±0.029	0.549±0.021	0.546±0.025	0.524±0.027	0.538±0.043
MK	0.130±0.281	0.106±0.079	0.116±0.043	0.098±0.041	0.062±0.064	$-0.016\pm$ 0.304
Prec.	0.578±0.006	0.599±0.021	0.611±0.015	0.617±0.025	0.604±0.038	0.500±0.260
Rec.	0.961±0.029	0.770±0.075	0.742±0.070	0.662±0.132	0.590±0.169	0.378±0.310
2h						
Model	MLP + Stand.	MLP + Rob.	Ridge+ Quant. Unif.	Ridge+PCA+ Pow. Gaus.	Ridge + Pow. Gaus.	Ridge+PCA+ Pow. Gaus.
MCC	0.265±0.129	0.278±0.125	0.327±0.101	0.289±0.066	0.286±0.056	0.294±0.062
ACC	0.640±0.066	0.651±0.053	0.673±0.051	0.652±0.036	0.654±0.030	0.656±0.032
F1	0.718±0.083	0.733±0.051	0.724±0.053	0.724±0.055	0.723±0.045	0.726±0.050
BACC	0.607±0.055	0.618±0.048	0.658±0.049	0.624±0.029	0.628±0.023	0.629±0.025
MK	0.336±0.173	0.332±0.169	0.340±0.105	0.346±0.108	0.325±0.091	0.343±0.101
Prec.	0.644±0.040	0.652±0.030	0.701±0.042	0.663±0.023	0.667±0.020	0.667±0.021
Rec.	0.826±0.157	0.842±0.098	0.754±0.094	0.812±0.135	0.799±0.110	0.809±0.125
6h						
Model	AB+PCA+ Pow. Gaus.	5NN+ Quant. Unif.	GB + Stand.	GB+PCA+ Quant. Unif.	GB+PCA+ Stand.	GB+PCA+ Stand.
MCC	0.209±0.117	0.662±0.047	0.680±0.031	0.718±0.052	0.716±0.045	0.715±0.051
ACC	0.627±0.052	0.832±0.026	0.842±0.015	0.862±0.027	0.857±0.028	0.861±0.026
F1	0.718±0.058	0.857±0.028	0.869±0.015	0.886±0.024	0.878±0.032	0.884±0.024
BACC	0.584±0.039	0.822±0.025	0.829±0.016	0.850±0.029	0.850±0.022	0.850±0.026
MK	0.264±0.172	0.680±0.051	0.703±0.045	0.738±0.056	0.732±0.053	0.730±0.056
Prec.	0.644±0.021	0.836±0.037	0.830±0.024	0.864±0.040	0.879±0.050	0.865±0.034
Rec.	0.818±0.120	0.887±0.075	0.914±0.049	0.914±0.060	0.889±0.092	0.908±0.057

Table E.22: Forecasting single-cell drug-response using mechanistic features in a machine learning classifier - Performances according to MCC score - for 1/FRET datasets of Roux et al. with a SG filter with a 5-frames window

Feat./ Score	Slope	FRETexp	Roux et al. model	Slope + Time points	FRETexp + Time points	Roux et al. model + Time points
50 min						
	MLP+ no p.	MLP+PCA+ Quant. Unif.	Ridge+PCA+ Pow. Gaus.	Constant C. + Pow. Gaus.	1NN+PCA+ Pow. Gaus.	Constant C.+PCA+ Quant. Unif.
MCC	0.000±0.000	0.041±0.051	0.059±0.073	0.000±0.000	0.015±0.067	0.000±0.000
ACC	0.575±0.002	0.581±0.006	0.580±0.006	0.575±0.002	0.578±0.011	0.575±0.002
F1	0.730±0.002	0.731±0.003	0.732±0.004	0.730±0.002	0.724±0.009	0.730±0.002
BACC	0.500±0.000	0.509±0.011	0.505±0.006	0.500±0.000	0.511±0.024	0.500±0.000
MK	$-0.425\pm$ 0.002	$-0.147\pm$ 0.342	0.328±0.436	- 0.425±0.002	- 0.308±0.237	- 0.425±0.002
Prec.	0.575±0.002	0.580±0.005	0.578±0.003	0.575±0.002	0.582±0.017	0.575±0.002
Rec.	1.000±0.000	0.988±0.019	0.998±0.004	1.000±0.000	0.963±0.069	1.000±0.000
30 to 50 min						
Model	MLP+ no p.	MLP+ no p.	Ridge+PCA+ Pow. Gaus.	Constant C. + Rob.	1NN+PCA+ Pow. Gaus.	MLP + Pow. Gaus.
MCC	0.000±0.000	0.035±0.099	0.059±0.073	0.000±0.000	0.033±0.072	0.045±0.092
ACC	0.575±0.002	0.577±0.022	0.580±0.006	0.575±0.002	0.580±0.011	0.584±0.019
F1	0.730±0.002	0.722±0.012	0.732±0.004	0.730±0.002	0.724±0.010	0.732±0.006
BACC	0.500±0.000	0.511±0.024	0.505±0.006	0.500±0.000	0.512±0.024	0.513±0.025
MK	- 0.425±0.002	0.057±0.212	0.328±0.436	- 0.425±0.002	- 0.107±0.412	- 0.074±0.439
Prec.	0.575±0.002	0.581±0.014	0.578±0.003	0.575±0.002	0.583±0.017	0.582±0.014
Rec.	1.000±0.000	0.955±0.022	0.998±0.004	1.000±0.000	0.963±0.069	0.988±0.019
2h						
Model	MLP + Stand.	MLP+PCA+ Rob.	AB+ no p.	Ridge + Pow. Gaus.	Ridge + Pow. Gaus.	Ridge + Pow. Gaus.
MCC	0.265±0.129	0.268±0.105	0.325±0.060	0.287±0.057	0.286±0.056	0.291±0.054
ACC	0.640±0.066	0.651±0.048	0.675±0.026	0.655±0.031	0.654±0.030	0.657±0.029
F1	0.718±0.083	0.733±0.040	0.750±0.030	0.724±0.044	0.723±0.045	0.727±0.042
BACC	0.607±0.055	0.619±0.051	0.643±0.021	0.629±0.025	0.628±0.023	0.631±0.023
MK	0.336±0.173	0.305±0.109	0.369±0.085	0.324±0.084	0.325±0.091	0.328±0.082
Prec.	0.644±0.040	0.656±0.038	0.671±0.010	0.668±0.021	0.667±0.020	0.668±0.020
Rec.	0.826±0.157	0.834±0.069	0.852±0.063	0.799±0.106	0.799±0.110	0.805±0.102
6h						
Model	AB+PCA+ Quant. Unif.	5NN+ Quant. Unif.	GB + Stand.	GB+PCA+ Quant. Unif.	SVC + MinMax	GB+PCA+ Stand.
MCC	0.208±0.104	0.662±0.047	0.680±0.031	0.718±0.052	0.712±0.046	0.715±0.051
ACC	0.628±0.044	0.832±0.026	0.842±0.015	0.862±0.027	0.858±0.024	0.861±0.026
F1	0.721±0.049	0.857±0.028	0.869±0.015	0.886±0.024	0.887±0.019	0.884±0.024
BACC	0.583±0.033	0.822±0.025	0.829±0.016	0.850±0.029	0.840±0.029	0.850±0.026
MK	0.266±0.160	0.680±0.051	0.703±0.045	0.738±0.056	0.746±0.050	0.730±0.056
Prec.	0.643±0.017	0.836±0.037	0.830±0.024	0.864±0.040	0.842±0.035	0.865±0.034
Rec.	0.828±0.108	0.887±0.075	0.914±0.049	0.914±0.060	0.939±0.046	0.908±0.057

Table E.23: Forecasting single-cell drug-response using mechanistic features in a machine learning classifier - Performances according to Accuracy score - for 1/FRET datasets of Roux et al. with a SG filter with a 5-frames window

E.5 Time-trajectory extension models

E.5.1 Deterministic models

FRETexp

$$FRETexp(t) = \begin{cases} C8(t) \\ FRET(t) \end{cases} \tag{E.36}$$

with

$$C8(t) = \begin{cases} C8_0 e^{-\beta_0 t} + \dfrac{\alpha_0 T_0 \left(1 - e^{-\beta_0 t)}\right)}{\beta_0}. & \text{if } t < \tau_{DISCend} \\ C8_{\tau_{DISC.end}} e^{-\beta_0 (t - \tau_{DISC.end})} & \text{if } t \geq \tau_{DISCend} \end{cases} \tag{E.37}$$

and

$$FRET(t) = \begin{cases} \beta_1 t + \beta_2 \left(1 - e^{-\beta_0 t}\right) & \text{if } t < \tau_{DISCend} \\ \dfrac{K_{fret} C8_{\tau_{DISC.end}}}{\beta_0} \left(1 - e^{-\beta_0 (t - \tau_{DISC.end})}\right) & \text{if } t \geq \tau_{DISCend} \\ + FRET(\tau_{DISC.end}) \end{cases} \tag{E.38}$$

Phenomenological model of caspase-8 activation and ICRP probe cleavage from [Roux et al., 2015]

$$FRET_{\text{Roux}}(t) = k\,(t - t_0)^2 \tag{E.39}$$

In their study, Roux et al defines a predictive feature of the drug-response τ, $\tau = \theta/(2 * k) + t_0$. θ depends on the drug dose. For 25 ng/mL of TRAIL, $\theta = 2.61 \times 10^{-3}$. Initial guesses for $FRET_{\text{Roux}}$ are also from [Roux et al., 2015], $k = 0.66$ and $t_0 = 20$ min.

Initial guesses for $FRET_{\text{exp}}$ were obtained from a mean treated cell time-trajectory fitted manually on 10 h experiment.

E.5.2 Time-series models

Time-series models assume that the point at time t depends on the n previous measurements, n being the size of the lag function [Hyndman and Athanasopoulos, 2018]. In Chapter 7, 2 time-series models are tested, the autoregressive integrated moving average (ARIMA) and the Error-Trand-Seasonal (ETS) model.

ARIMA model An AutoRegressive Moving Average (ARMA) model of order (p',q) is a statistic model assuming that your observation at time t_i is linearly dependant of the $p + d$ previous observation with a additional noise represented by random variables independent and identically

distributed (i.d.d). Hence, we have:

$$\left(1-\sum_{i=1}^{p'}\alpha_i L_i\right)X_t=\left(1+\sum_{i=1}^{q}\beta_i L_i\right)\epsilon_t \text{ with } \epsilon\sim\mathcal{N}(0,r)\ \ i.d.d. \tag{E.40}$$

with the lag operator L. And if L can be factorised, we obtain an AutoRegressive Integrated Moving Average (ARIMA) of order (p,d,q) with p+d=p' and:

$$\left(1-\sum_{i=1}^{p}\gamma_i L_i\right)(1-L)^d X_t=\left(1+\sum_{i=1}^{q}\beta_i L_i\right)\epsilon_t \text{ with } \epsilon\sim\mathcal{N}(0,r)\ \ i.d.d. \tag{E.41}$$

ETS model An Error (E), Trend (T) and Seasonal (S) model (ETS), also known as simple exponential smoothing (SES), is composed of 4 components as defined in the model's name: a damping term (l), a trend component (b - none, additive or damped), a seasonal part (s - none, additive or multiplicative), and an error term (e - could be additive or multiplicative) and we have :

$$X_t = D *^s S *^t T *^e E \tag{E.42}$$

with$*$can be a multiplication or an addition according to the type of component you choose. For instance, an exponential smoothing method that incorporate an additive trend and an additive seasonal component is given by:

$$\begin{aligned} X_t &= l_{t-1}+b_{t-1}+s_{t-m}+e_t \\ l_t &= l_{t-1}+b_{t-1}+\alpha e_t \\ b_t &= b_{t-1}+\beta e_t \\ s_t &= {}_{t-m}+\gamma e_t \end{aligned} \tag{E.43}$$

Model's selection The Augmented Dickey-Fuller (ADF) Test carried with 6h-data showed that the time-serie was not stationnary, confirming the choice of an ARIMA. The results of the ADF test on the differenciated time-trajectories suggested to use an (1,1,4) ARIMA to extend our time-trajectories. For the ETS model, the S component is set to None, as there is not seasonal trend in our data. For E and T, 6h-fit suggested E and T must be additive as we do not have strictly positive data. The rest of the parameters estimation for the time-series models are defaults values from *statmodels* library.

F Chapter 8

F.1 List of features selected *SelectKBest* function

List of features obtained after ramoving features with a low variance (below 0.5) and features with NaN values. We refer to tsfresh and Catch22 documentation for the exact computation of the associated features :

Transformer	Features
Time points	50 min
Slope	Slope by mean value over the last 5 frames before 50 min Slope by maximum value of derivative before 50 min Slope by last deriv. value before 50 min
Roux et al	t_0
FRETexp	β_1
ETS	smoothing trend parameters
TSFRESH	mean_change,last_location_of_minimum and first_location_of_minimum , autocorrelation__lag_9, agg_autocorrelation__f_agg_"mean"__maxlag_40 index_mass_quantile__q, with q from 0.7 to 0.9 change_quantiles__f_agg_"mean"__isabs_False__qh__ql qh = [0.8,1.0,0.6], ql = [0.0,0.2,0.4,0.6,0.8] linear_trend__attr : rvalue and slope cwt_coefficients__coeff_i__w_2__widths_(2, 5, 10, 20), i =[4,7,8,9] number_cwt_peaks__n_5 fft_coefficient__attr_"real"__coeff_i', i = [3,4,5] fft_coefficient__attr_imag"__coeff_i', i =[1,2,3,4] fft_coefficient__attr_"angle"__coeff_i', i =[1,2,3,4,5] fft_aggregated__aggtype_"variance" agg_linear_trend__attr_"rvalue"__chunk_len_5__f_agg_"mean", agg_linear_trend__attr_"slope"__chunk_len_5__f_agg_"max", agg_linear_trend__attr_"slope"__chunk_len_5__f_agg_"mean", energy_ratio_by_chunks__num_segments_10__segment_focus_i, i = [1,2,3,9]

Table F.24: Features conserved after first selection step. From tsfresh documentation: index_mass_quantile: "Calculates the relative index i of time series x where q% of the mass of x lies left of i. For example for q = 50% this feature calculator will return the mass center of the time series". change_quantiles: "First fixes a corridor given by the quantiles ql and qh of the distribution of x. Then calculates the average, absolute value of consecutive changes of the series x inside this corridor". linear_trend: "Calculate a linear least-squares regression for the values of the time series versus the sequence from 0 to length of the time series minus one. This feature assumes the signal to be uniformly sampled. It will not use the time stamps to fit the model. The parameters control which of the characteristics are returned". agg_linear_trend: "Calculates a linear least-squares regression for values of the time series that were aggregated over chunks versus the sequence from 0 up to the number of chunks minus one." .energy_ratio_by_chunks: "Calculates the sum of squares of chunk i out of N chunks expressed as a ratio with the sum of squares over the whole series.", cwt:"Calculates a Continuous wavelet transform for the Ricker wavelet", fft_coefficient: "Returns the spectral centroid (mean), variance, skew, and kurtosis of the absolute Fourier transform spectrum".

F.2 Results of the three methods using ML models to isolate cells according to their forecast drug-response without hyperparameters tuning

Testing set	TRAIL_Roux_25_2	TRAIL_Roux_25_3	mean	std
Dataset description				
N cells in testing	221	327	297.333	54.42
% tol. cell. in replicate	51.131	45.872	56.559	11.596
i) 3rd class				
i - % of cell pred. for iso. in test	43.12	19.57	31.345	11.775
i - # cell pred. sen. for iso. in test	67	69	68	1
i - # cell pred. tol. for iso. in test	38	72	55	17
i - ACC on test	0.6	0.631	0.615	0.016
i - Precision tol. class	0.605	0.569	0.587	0.018
i - Precision sens. class	0.597	0.696	0.646	0.049
ii) 2-step forecasting				
ii - % of cell pred. for iso. in test	88.69	52.91	70.8	17.89
ii - # cell pred. sen. for iso. in test	91	131	111.0	20.0
ii - # cell pred. tol. for iso. in test	105	140	122.5	17.5
ii - ACC on test	0.571	0.635	0.603	0.032
ii - Precision tol. class	0.571	0.607	0.589	0.018
ii - Precision sens. class	0.571	0.664	0.617	0.047
iv)1 ML-model per class				
iv - % of cell pred. for iso. in test	61.54	74.62	68.08	6.54
iv - # cell pred. sen. for iso. in test	109	45	77.0	32.0
iv - # cell pred. tol. for iso. in test	27	179	103.0	76.0
iv - ACC on test	0.574	0.598	0.586	0.012
iv - Precision tol. class	0.667	0.581	0.624	0.043
iv - Precision sens. class	0.55	0.667	0.608	0.058

Table F.25: Dataset description and performances of the 3 methods using ML models for drug-response forecasting to identify cells for selection in the FATE-SEQ pipeline during 2-fold cross-validation on CFP/FRET dataset from Roux et al using only the replicates TRAIL_Roux_25_2 and TRAIL_Roux_25_3 - tol. : tolerant, sen.: sensitive, pred. predicted, iso.: isolation, std: standard deviation.

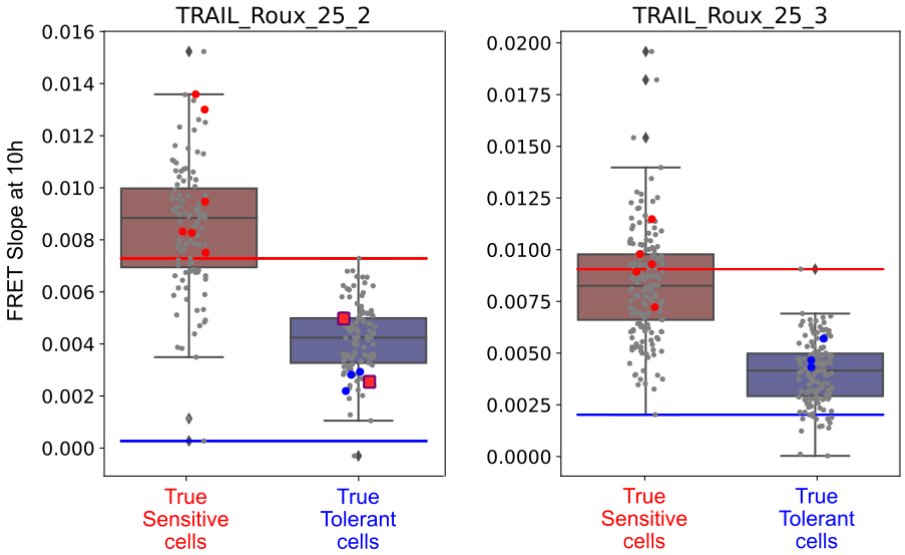

Figure F.18: Comparison boxplot of cells identified with the current FATE-SEQ method using the slope feature computed after 10 hours of experiment and cells identified with the method Separate early responders from the crowd at 50 min. Each subplot represents the testing replicate set, thresholds and number of non overlapping cells for each method were determined on the other replicate. Cells above the red threshold were isolated as sensitive and cells below the blue threshold were isolated as tolerant with the current FATE-SEQ method based on their FRET slope value. Red dot cells were isolated as sensitive and blue cells as tolerant with the method Separate early responders from the crowd. Red squares are cells inaccurately isolated as sensitive with the method Separate early responders from the crowd whereas they were actually drug-tolerant during the experiment.

G Posters

Lot of this work has already been presented during conferences and seminars over the past 3 years. Here are the posters we created to illustrate 4 chapters of this thesis.

Core models of receptor reactions evaluate basic pathway designs enabling heterogeneous commitments to apoptosis

Marielle Péré[1,2], Madalena Chaves[1], Jérémie Roux[1,2]
[1] *Université Côte d'Azur, Inria, INRA, CNRS, Sorbonne Université, Biocore team, Sophia Antipolis, France*
[2] *Institute for Research on Cancer and Aging, Nice (CNRS UMR7284, Inserm U1081)*

Introduction

- Isogenic cells can respond differently to cytotoxic treatments, such as the tumor necrosis factor-related apoptosis inducing ligand (TRAIL), with only a fraction committing to apoptosis. This non-genetic **transient resistance to TRAIL** has been shown to **dependent on caspase-8** dynamics at the receptor level *in vitro*.
- Here we investigate the **core reactions leading to caspase-8 activation**, to evaluate the **basic mechanisms giving rise to the observed heterogeneous response**.
- We fit our models to single-cell trajectories of time-resolved caspase-8 activation measured in clonal cells after treatment with TRAIL.
- We analyse our results to assess the relevance of each model and evaluate how well it captures the extent of biological heterogeneity observed *in vitro* with a focus on a **positive feedback loop on caspase-8, the impacts of initial condition variations and the relevance of the caspase-10 and the FADD actions**.

Extrinsic apoptosis initiation core models (EAICM)

The models studied :

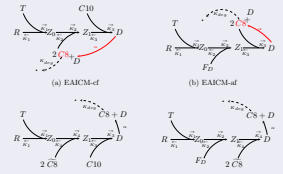

(a) EAICM-cf (b) EAICM-af (c) EAICM-c (d) EAICM-a

Figure 1: Extrinsic apoptosis initiation core models (EAICM) schemes

Using mass-action kinetics, we obtain four seven-equations models with the following C8 equations :

EAICM-cf :

$$\dot{C8} = -2\overrightarrow{K_2}\, Z_0 C8^2 + 2\overleftarrow{K_2}\, Z_1 + \alpha\, D - K_{deg}\, C8, \quad (1)$$

EAICM-af :

$$\dot{C8} = -2\overrightarrow{K_3}\, Z_1 C8^2 + 2\overleftarrow{K_3}\, D + \alpha\, D - K_{deg}\, C8, \quad (2)$$

EAICM-c :

$$\dot{C8} = \alpha\, D - K_{deg}\, C8, \quad (3)$$

EAICM-a :

$$\dot{C8} = \alpha\, D - K_{deg}\, C8, \quad (4)$$

Reference values for model comparison

Figure 2: Reference values and fundamental C8 features scheme to compare the models

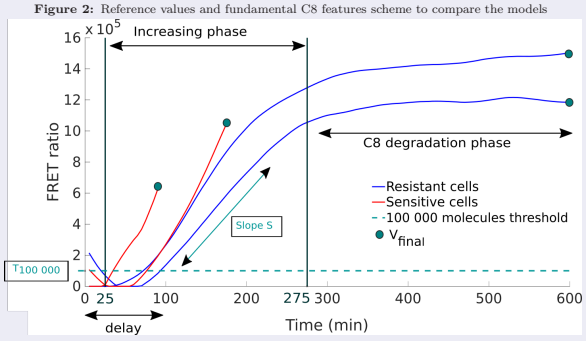

	EAICM-cf	EAICM-c	EAICM-af	EAICM-a	Best model
S. cells	269	8	20	3	EAICM-cf
R. cells	51	23	31	9	EAICM-cf

Table 1: Number of cells best approached per model according to S

Analysing mechanisms for generating heterogeneity

The feedback loop mechanism :

We applied a method developed in [1]. It consists in representing the absolute values curve of each term that composes the C8 equation, normalized by the sum of all absolute values. For EAICM-c, considering the C8 equation, the plotted curves are:

$$\left\{ \frac{|K_{deg}\, C8|}{|K_{deg}\, C8| + |\alpha\, D|}\,,\ \frac{|\alpha\, D|}{|K_{deg}\, C8| + |\alpha\, D|} \right. \quad (5)$$

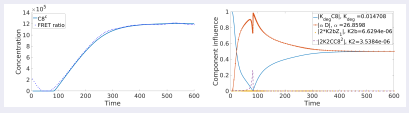

(a) Real FRET ratio and $C8^c$ for EAICM-cf (b) C8 equation component dynamics for EAICM-cf

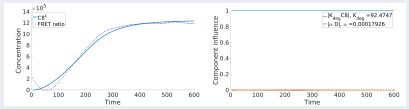

(c) Real FRET ratio and $C8^c$ for EAICM-c (d) C8 equation component dynamics for EAICM-c

Figure 3: Feedback loop mechanism analysis for resistant cell n. 10

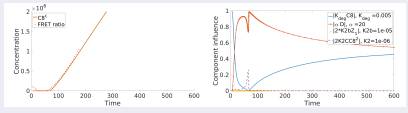

(a) Real FRET ratio and $C8^c$ for EAICM-cf (b) C8 equation component dynamics for EAICM-cf

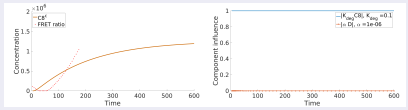

(c) Real FRET ratio and $C8^c$ for EAICM-c (d) C8 equation component dynamics for EAICM-c

Figure 4: Feedback loop mechanism analysis for sensitive cell n. 121

Comparison of C8 dynamics and main properties for models EAICM-cf (a),(b) and EAICM-c (c),(d), for the resistant cell n. 10 (**Figure 3**) and the sensitive one n. 121 (**Figure 4**)- (a) and (c) compare the FRET ratio and the $C8^c$ curve, (b) and (d) compare the relative weights of the different terms that contribute to C8 activation.

Initial conditions impacts on slope values :

Figure 5: Initial condition variation effects on C8 dynamic. The estimated parameters P_i are indicated at the top left corners and used as reference values to vary the initial condition, in the range $[0, 10X_0]$, where $X_0 = R_0$ in (a)-(d); $X_0 = C10_0$ in (e)-(f); and $X_0 = F_{D,0}$ in (g)-(h).

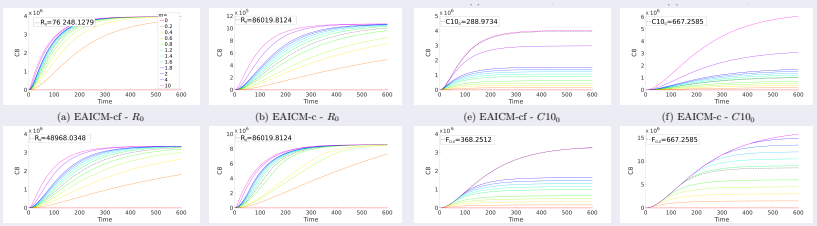

(a) EAICM-cf - R_0 (b) EAICM-c - R_0 (e) EAICM-cf - $C10_0$ (f) EAICM-c - $C10_0$

(c) EAICM-af - R_0 (d) EAICM-a - R_0 (g) EAICM-af - $F_{D,0}$ (h) EAICM-a - $F_{D,0}$

References
[1] S. Casagranda, S. Touzeau, D. Ropers, and J.-L. Gouzé. Principal process analysis of biological models. *BMC systems biology*, 2018.
[2] J. Roux, M. Hafner, S. Bandara, J. J. Sims, H. Hudson, and P. K Chai, D.and Sorger. Fractional killing arises from cell-to-cell variability in overcoming a caspase activity threshold. *Molecular systems biology*, 2015.

Conclusions :

- The formation of **C8/C10 clusters accelerates C8 activation** by increasing C8 production as well as the slope.
- **Caspase clusterization** has a greater capacity to **generate variability in cell response** as F_D reaction does not greatly affect the slope but only delays the stabilization time.
- **Balance between feedback loop and C8 degradation plays a major role in cell fate**.
- The **positive feedback** is important in the timing of C8 dynamics, particularly in **reproducing the initial delay** observed in C8 activation.
- The feedback loop introduces a **saturation on the maximum level of C8 induced by variability in initial conditions**.
- A **large robustness of the feedback models** with respect to variations in initial amounts of molecules is observed.

Figure G.19: **Poster: "Core models of receptor reactions evaluate basic pathway designs enabling heterogeneous commitments to apoptosis"**, presenting at CMSB 2020, Online - cf Chapter 4

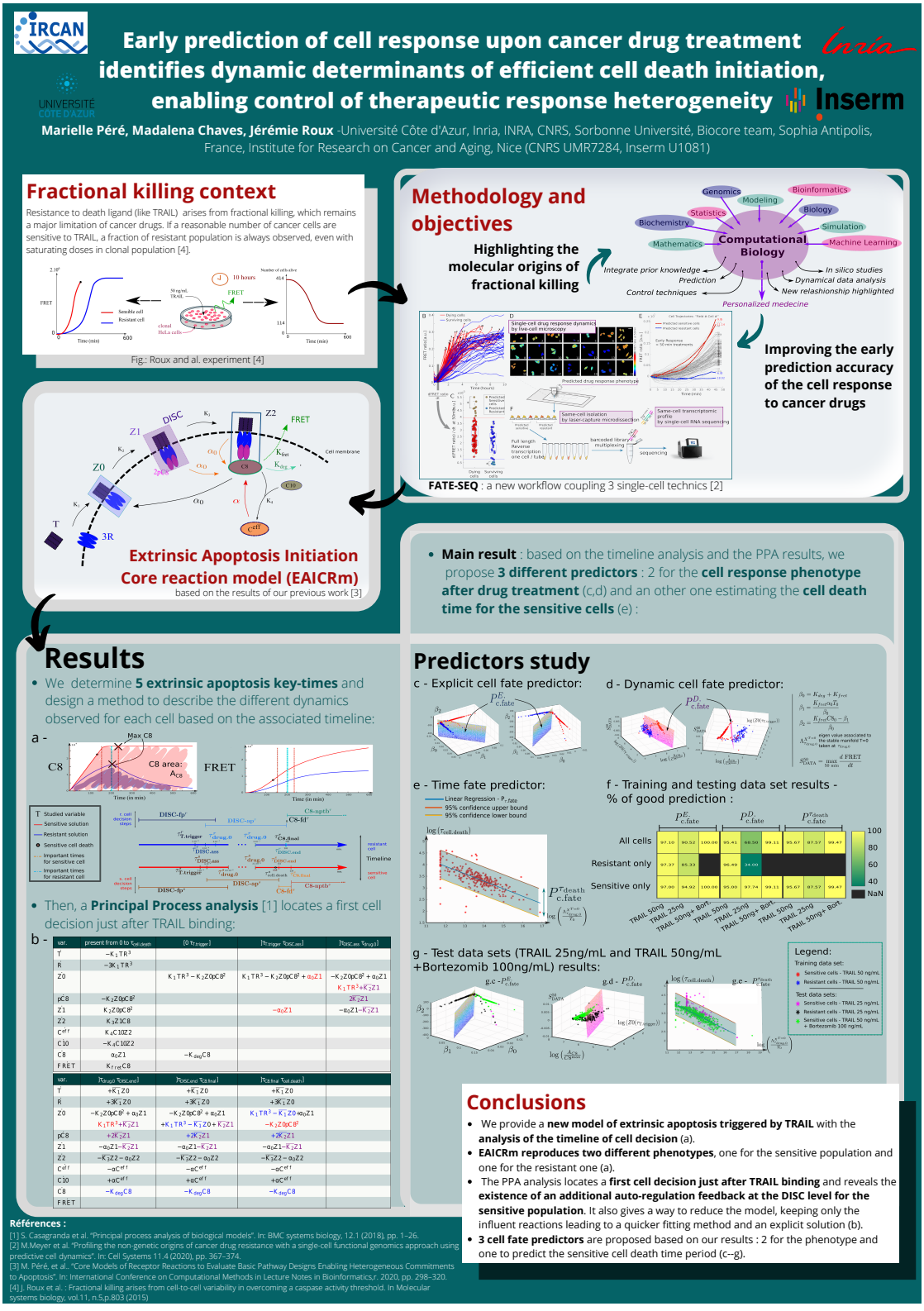

Figure G.20: **Poster: "Early prediction of cell response upon cancer drug treatment identifies dynamic determinants of efficient cell death initiation, enabling control of therapeutic response heterogeneity"**, presenting at CMSB, 2021 and for the Canceropole PACA annual meeting, 2021 - cf Chapter 5

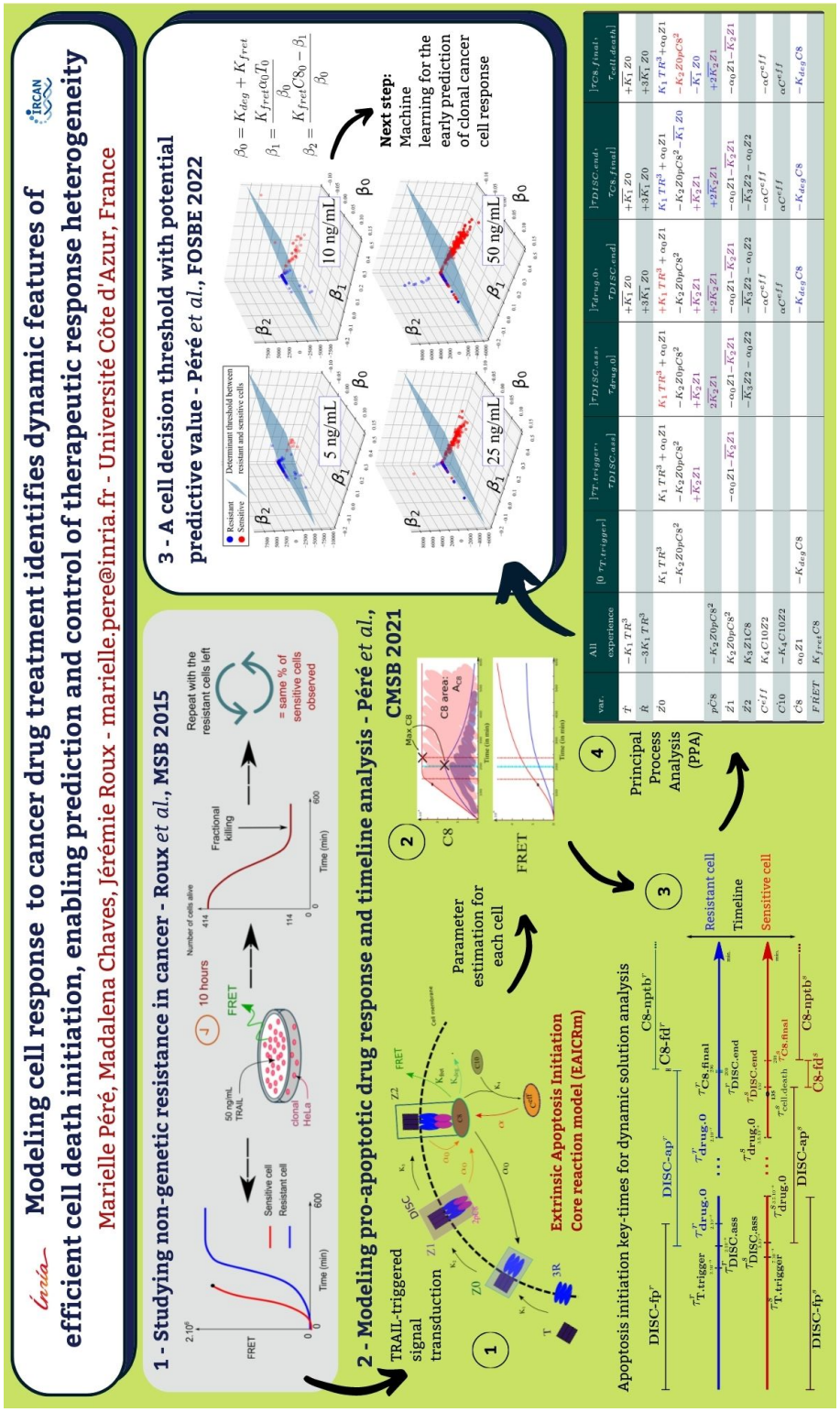

Figure G.21: **Poster: "Modeling cell response to cancer drug treatment identifies dynamic features of efficient cell death initiation, enabling prediction and control of therapeutic response heterogeneity"**, presenting on the INside Seminars, Online, 2022 - cf Chapter 5

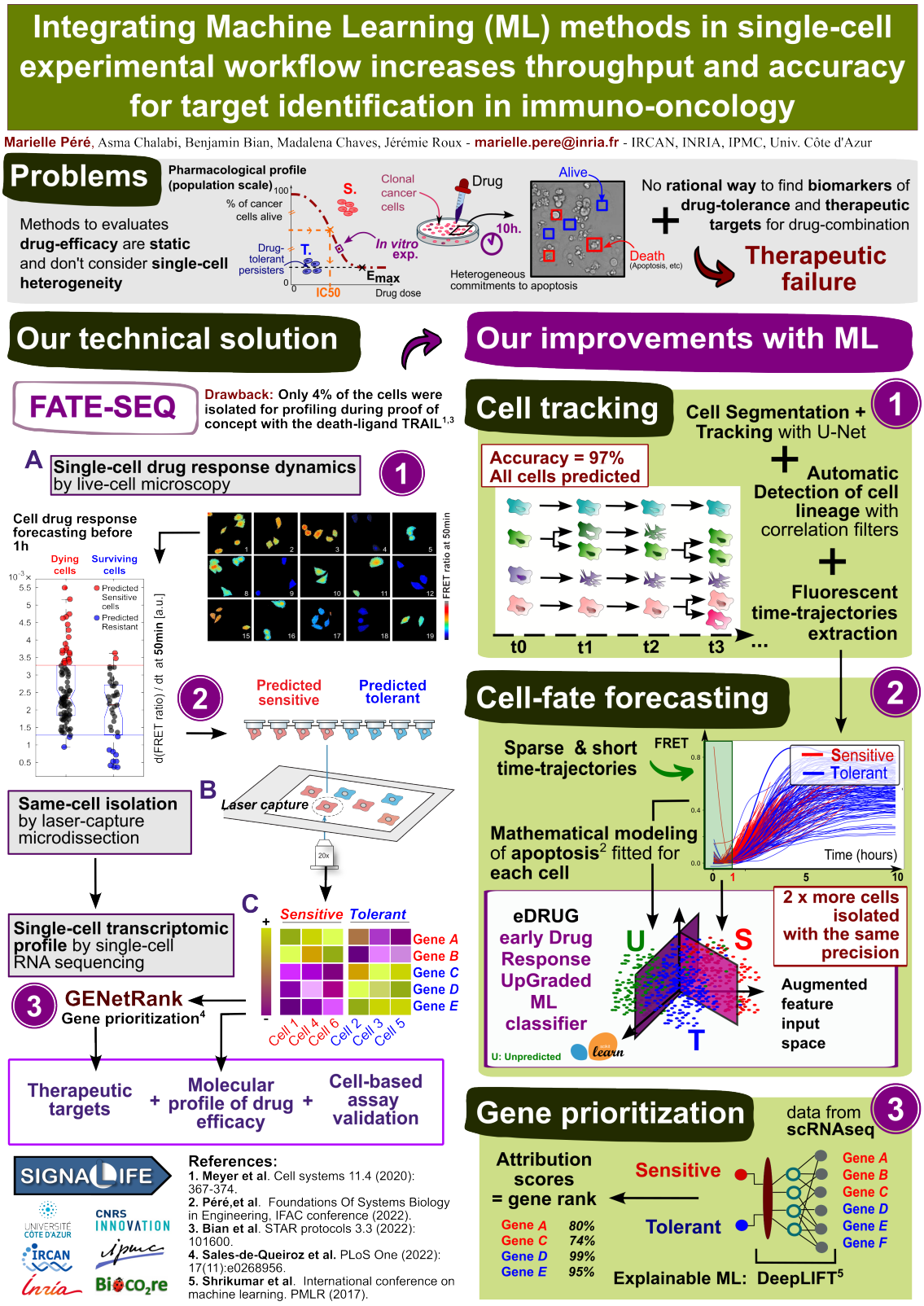

Figure G.22: **Poster: "Integrating machine learning methods to single cell signaling analyses increases throughput and accuracy for target identification in immuno-oncology":** presenting on the Signalife Annual Meeting, Nice, 2022 and at the Sophia Summit AI, Sophia-Antipolis, 2022 - The poster has been rewarded with two best poster prizes- cf Chapter 8 and part IV

References

[Adossa et al., 2021] Adossa, N., Khan, S., Rytkönen, K. T., and Elo, L. L. (2021). Computational strategies for single-cell multi-omics integration. *Computational and Structural Biotechnology Journal*, 19:2588–2596.

[Albeck et al., 2008a] Albeck, J. G., Burke, J. M., Aldridge, B. B., Zhang, M., Lauffenburger, D. A., and Sorger, P. K. (2008a). Quantitative analysis of pathways controlling extrinsic apoptosis in single cells. *Molecular cell*, 30(1):11–25.

[Albeck et al., 2008b] Albeck, J. G., Burke, J. M., Spencer, S. L., Lauffenburger, D. A., and Sorger, P. K. (2008b). Modeling a snap-action, variable-delay switch controlling extrinsic cell death. *PLoS biology*, 6(12):e299.

[Aldridge et al., 2011] Aldridge, B. B., Gaudet, S., Lauffenburger, D. A., and Sorger, P. K. (2011). Lyapunov exponents and phase diagrams reveal multi-factorial control over trail-induced apoptosis. *Molecular systems biology*, 7(1):553.

[Ali et al., 2021] Ali, S., Alam, M., Hasan, G. M., and Hassan, M. I. (2021). Potential therapeutic targets of Klebsiella pneumoniae: a multi-omics review perspective. *Briefings in Functional Genomics*, 21(2):63–77.

[AlMusawi et al., 2021] AlMusawi, S., Ahmed, M., and Nateri, A. S. (2021). Understanding cell-cell communication and signaling in the colorectal cancer microenvironment. *Clinical and Translational Medicine*, 11(2):e308.

[Amstein et al., 2022] Amstein, L. K., Ackermann, J., Hannig, J., Đikić, I., Fulda, S., and Koch, I. (2022). Mathematical modeling of the molecular switch of tnfr1-mediated signaling pathways applying petri net formalism and in silico knockout analysis. *PLoS computational biology*, 18(8):e1010383.

[Anchang et al., 2018] Anchang, B., Davis, K. L., Fienberg, H. G., Williamson, B. D., Bendall, S. C., Karacosta, L. G., Tibshirani, R., Nolan, G. P., and Plevritis, S. K. (2018). Drug-nem: Optimizing drug combinations using single-cell perturbation response to account for intratumoral heterogeneity. *Proceedings of the National Academy of Sciences*, 115(18):E4294–E4303.

[Anderson and Maini, 2018] Anderson, A. R. and Maini, P. K. (2018). Mathematical oncology. *Bulletin of mathematical biology*, 80(5):945–953.

[Ansari et al., 2022] Ansari, M. J., Bokov, D., Markov, A., Jalil, A. T., Shalaby, M. N., Suksatan, W., Chupradit, S., Al-Ghamdi, H. S., Shomali, N., Zamani, A., et al. (2022). Cancer combination therapies by angiogenesis inhibitors; a comprehensive review. *Cell Communication and Signaling*, 20(1):1–23.

[Armingol et al., 2021] Armingol, E., Officer, A., Harismendy, O., and Lewis, N. E. (2021). Deciphering cell–cell interactions and communication from gene expression. *Nature Reviews Genetics*, 22(2):71–88.

[Asthagiri and Lauffenburger, 2001] Asthagiri, A. R. and Lauffenburger, D. A. (2001). A computational study of feedback effects on signal dynamics in a mitogen-activated protein kinase (mapk) pathway model. *Biotechnology progress*, 17(2):227–239.

[Bagci et al., 2006] Bagci, E., Vodovotz, Y., Billiar, T., Ermentrout, G., and Bahar, I. (2006). Bistability in apoptosis: roles of bax, bcl-2, and mitochondrial permeability transition pores. *Biophysical journal*, 90(5):1546–1559.

[Bagnall et al., 2017] Bagnall, A., Lines, J., Bostrom, A., Large, J., and Keogh, E. (2017). The great time series classification bake off: a review and experimental evaluation of recent algorithmic advances. *Data Mining and Knowledge Discovery*, 31:606–660.

[Bai et al., 2021] Bai, D., Peng, J., and Yi, C. (2021). Advances in single-cell multi-omics profiling. *RSC Chemical Biology*, 2(2):441–449.

[Ballester et al., 2021] Ballester, P. J., Stevens, R., Haibe-Kains, B., Huang, R. S., and Aittokallio, T. (2021). Artificial intelligence for drug response prediction in disease models. *Briefings in Bioinformatics*, 23(1). bbab450.

[Ballweg et al., 2017] Ballweg, R., Paek, A. L., and Zhang, T. (2017). A dynamical framework for complex fractional killing. *Scientific reports*, 7(1):1–12.

[Baslan et al., 2022] Baslan, T., Morris, J. P., Zhao, Z., Reyes, J., Ho, Y.-J., Tsanov, K. M., Bermeo, J., Tian, S., Zhang, S., Askan, G., et al. (2022). Ordered and deterministic cancer genome evolution after p53 loss. *Nature*, 608(7924):795–802.

[Bell and Gilan, 2020] Bell, C. C. and Gilan, O. (2020). Principles and mechanisms of non-genetic resistance in cancer. *British journal of cancer*, 122(4):465–472.

[Benguigui et al., 2018] Benguigui, M., Alishekevitz, D., Timaner, M., Shechter, D., Raviv, Z., Benzekry, S., and Shaked, Y. (2018). Dose-and time-dependence of the host-mediated response to paclitaxel therapy: a mathematical modeling approach. *Oncotarget*, 9(2):2574.

[Bentele et al., 2004] Bentele, M., Lavrik, I., Ulrich, M., Stosser, S., Heermann, D., Kalthoff, H., Krammer, P., and Eils, R. (2004). Mathematical modeling reveals threshold mechanism in cd95-induced apoptosis. *The Journal of cell biology*, 166(6):839–851.

[Benzekry, 2020] Benzekry, S. (2020). Artificial intelligence and mechanistic modeling for clinical decision making in oncology. *Clinical Pharmacology & Therapeutics*, 108(3):471–486.

[Benzekry et al., 2021] Benzekry, S., Grangeon, M., Karlsen, M., Alexa, M., Bicalho-Frazeto, I., Chaleat, S., Tomasini, P., Barbolosi, D., Barlesi, F., and Greillier, L. (2021). Machine learning for prediction of immunotherapy efficacy in non-small cell lung cancer from simple clinical and biological data. *Cancers*, 13(24):6210.

[Benzekry et al., 2014] Benzekry, S., Lamont, C., Beheshti, A., Tracz, A., Ebos, J. M., Hlatky, L., and Hahnfeldt, P. (2014). Classical mathematical models for description and prediction of experimental tumor growth. *PLoS computational biology*, 10(8):e1003800.

[Bera et al., 2022] Bera, K., Braman, N., Gupta, A., Velcheti, V., and Madabhushi, A. (2022). Predicting cancer outcomes with radiomics and artificial intelligence in radiology. *Nature Reviews Clinical Oncology*, 19(2):132–146.

[Berraondo et al., 2019] Berraondo, P., Sanmamed, M. F., Ochoa, M. C., Etxeberria, I., Aznar, M. A., Pérez-Gracia, J. L., Rodríguez-Ruiz, M. E., Ponz-Sarvise, M., Castañón, E., and Melero, I. (2019). Cytokines in clinical cancer immunotherapy. *British journal of cancer*, 120(1):6–15.

[Bertaux et al., 2014] Bertaux, F., Stoma, S., Drasdo, D., and Batt, G. (2014). Modeling dynamics of cell-to-cell variability in trail-induced apoptosis explains fractional killing and predicts reversible resistance. *PLoS computational biology*, 10(10):e1003893.

[Berthoumieux et al., 2011] Berthoumieux, S., Brilli, M., de Jong, H., Kahn, D., and Cinquemani, E. (2011). Identification of metabolic network models from incomplete high-throughput datasets. *Bioinformatics*, 27(13):i186–i195.

[Berthoumieux et al., 2013] Berthoumieux, S., Brilli, M., Kahn, D., De Jong, H., and Cinquemani, E. (2013). On the identifiability of metabolic network models. *Journal of mathematical biology*, 67(6):1795–1832.

[Bijman et al., 2021] Bijman, E. Y., Kaltenbach, H.-M., and Stelling, J. (2021). Experimental analysis and modeling of single-cell time-course data. *Current Opinion in Systems Biology*, 28:100359.

[Birtwistle et al., 2011] Birtwistle, M. R., von Kriegsheim, A., Kida, K., Schwarz, J. P., Anderson, K. I., and Kolch, W. (2011). Linear approaches to intramolecular förster resonance energy transfer probe measurements for quantitative modeling. *PloS one*, 6(11):e27823.

[Boice and Bouchier-Hayes, 2020] Boice, A. and Bouchier-Hayes, L. (2020). Targeting apoptotic caspases in cancer. *Biochimica et Biophysica Acta (BBA)-Molecular Cell Research*, page 118688.

[Bouhaddou et al., 2018] Bouhaddou, M., Barrette, A. M., Stern, A. D., Koch, R. J., DiStefano, M. S., Riesel, E. A., Santos, L. C., Tan, A. L., Mertz, A. E., and Birtwistle, M. R. (2018). A mechanistic pan-cancer pathway model informed by multi-omics data interprets stochastic cell fate responses to drugs and mitogens. *PLoS computational biology*, 14(3):e1005985.

[Bouralexis et al., 2005] Bouralexis, S., Findlay, D., and Evdokiou, A. (2005). Death to the bad guys: targeting cancer via apo2l/trail. *Apoptosis*, 10(1):35–51.

[Bowes et al., 2022] Bowes, A. L., Tarabichi, M., Pillay, N., and Van Loo, P. (2022). Leveraging single-cell sequencing to unravel intratumour heterogeneity and tumour evolution in human cancers. *The Journal of Pathology*.

[Bradshaw et al., 2019] Bradshaw, E. L., Spilker, M. E., Zang, R., Bansal, L., He, H., Jones, R. D., Le, K., Penney, M., Schuck, E., Topp, B., et al. (2019). Applications of quantitative systems pharmacology in model-informed drug discovery: perspective on impact and opportunities. *CPT: pharmacometrics & systems pharmacology*, 8(11):777–791.

[Brand and Morrissey, 2020] Brand, M. and Morrissey, E. (2020). Single cell fate decisions of bipotential hematopoietic progenitors. *Current opinion in hematology*, 27(4):232.

[Brechtmann et al., 2018] Brechtmann, F., Mertes, C., Matusevičiūtė, A., Yépez, V. A., Avsec, Ž., Herzog, M., Bader, D. M., Prokisch, H., and Gagneur, J. (2018). Outrider: a statistical method for detecting aberrantly expressed genes in rna sequencing data. *The American Journal of Human Genetics*, 103(6):907–917.

[Bretti et al., 2021] Bretti, G., De Ninno, A., Natalini, R., Peri, D., and Roselli, N. (2021). Estimation algorithm for a hybrid pde–ode model inspired by immunocompetent cancer-on-chip experiment. *Axioms*, 10(4):243.

[Brubaker and Lauffenburger, 2020] Brubaker, D. K. and Lauffenburger, D. A. (2020). Translating preclinical models to humans. *Science*, 367(6479):742–743.

[Brubaker et al., 2019] Brubaker, D. K., Proctor, E. A., Haigis, K. M., and Lauffenburger, D. A. (2019). Computational translation of genomic responses from experimental model systems to humans. *PLoS computational biology*, 15(1):e1006286.

[Buchbinder et al., 2018] Buchbinder, J. H., Pischel, D., Sundmacher, K., Flassig, R. J., and Lavrik, I. N. (2018). Quantitative single cell analysis uncovers the life/death decision in cd95 network. *PLoS computational biology*, 14(9):e1006368.

[Cabanos and Hata, 2021] Cabanos, H. F. and Hata, A. N. (2021). Emerging insights into targeted therapy-tolerant persister cells in cancer. *Cancers*, 13(11):2666.

[Cai et al., 2022a] Cai, S., Mao, Z., Wang, Z., Yin, M., and Karniadakis, G. E. (2022a). Physics-informed neural networks (pinns) for fluid mechanics: A review. *Acta Mechanica Sinica*, pages 1–12.

[Cai et al., 2022b] Cai, Z., Poulos, R. C., Liu, J., and Zhong, Q. (2022b). Machine learning for multi-omics data integration in cancer. *Iscience*, page 103798.

[Calzone et al., 2010] Calzone, L., Tournier, L., Fourquet, S., Thieffry, D., Zhivotovsky, B., Barillot, E., and Zinovyev, A. (2010). Mathematical modelling of cell-fate decision in response to death receptor engagement. *PLoS computational biology*, 6(3):e1000702.

[Camp and Lukonin, 2022] Camp, J. G. and Lukonin, I. (2022). Single-cell, single-organoid phenotypic landscapes. *Nature Methods*, 19(3):280–281.

[Carlsen et al., 2022] Carlsen, L., Huntington, K. E., and El-Deiry, W. S. (2022). Immunotherapy for colorectal cancer: Mechanisms and predictive biomarkers. *Cancers*, 14(4).

[Carroll et al., 2021] Carroll, M. J., Garcia-Reyero, N., Perkins, E. J., and Lauffenburger, D. A. (2021). Translatable pathways classification (transpath-c) for inferring processes germane to human biology from animal studies data: example application in neurobiology. *Integrative Biology*, 13(10):237–245.

[Casado-Pelaez et al., 2022] Casado-Pelaez, M., Bueno-Costa, A., and Esteller, M. (2022). Single cell cancer epigenetics. *Trends in Cancer*.

[Casagranda et al., 2018] Casagranda, S., Touzeau, S., Ropers, D., and Gouzé, J.-L. (2018). Principal process analysis of biological models. *BMC systems biology*, 12(1):1–26.

[Chang et al., 2003] Chang, D. W., Xing, Z., Capacio, V. L., Peter, M. E., and Yang, X. (2003). Interdimer processing mechanism of procaspase-8 activation. *The EMBO journal*, 22(16):4132–4142.

[Chang et al., 2002] Chang, D. W., Xing, Z., Pan, Y., Algeciras-Schimnich, A., Barnhart, B. C., Yaish-Ohad, S., Peter, M. E., and Yang, X. (2002). c-flipl is a dual function regulator for caspase-8 activation and cd95-mediated apoptosis. *The EMBO journal*, 21(14):3704–3714.

[Chatterjee and Bivona, 2019] Chatterjee, N. and Bivona, T. G. (2019). Polytherapy and targeted cancer drug resistance. *Trends in cancer*, 5(3):170–182.

[Chaves et al., 2009] Chaves, M., Eissing, T., and Allgöwer, F. (2009). Regulation of apoptosis via the nfκb pathway: modeling and analysis. In *Dynamics on and of Complex Networks*, pages 19–33. Springer.

[Chen et al., 2007a] Chen, C., Cui, J., Lu, H., Wang, R., Zhang, S., and Shen, P. (2007a). Modeling of the role of a bax-activation switch in the mitochondrial apoptosis decision. *Biophysical Journal*, 92(12):4304–4315.

[Chen et al., 2007b] Chen, C., Cui, J., Zhang, W., and Shen, P. (2007b). Robustness analysis identifies the plausible model of the bcl-2 apoptotic switch. *FEBS letters*, 581(26):5143–5150.

[Chen et al., 2019] Chen, G., Ning, B., and Shi, T. (2019). Single-cell rna-seq technologies and related computational data analysis. *Frontiers in genetics*, page 317.

[Chen et al., 2000] Chen, K. C., Csikasz-Nagy, A., Gyorffy, B., Val, J., Novak, B., and Tyson, J. J. (2000). Kinetic analysis of a molecular model of the budding yeast cell cycle. *Molecular biology of the cell*, 11(1):369–391.

[Chen et al., 2015] Chen, Y., Keogh, E., Hu, B., Begum, N., Bagnall, A., Mueen, A., and Batista, G. (2015). The ucr time series classification archive. www.cs.ucr.edu/~eamonn/time_series_data/.

[Chen et al., 2021] Chen, Y., Liu, F., Yu, Q., and Li, T. (2021). Review of fractional epidemic models. *Applied mathematical modelling*, 97:281–307.

[Chicco et al., 2021] Chicco, D., Tötsch, N., and Jurman, G. (2021). The matthews correlation coefficient (mcc) is more reliable than balanced accuracy, bookmaker informedness, and markedness in two-class confusion matrix evaluation. *BioData mining*, 14(1):1–22.

[Chong et al., 2015] Chong, K. H., Samarasinghe, S., and Kulasiri, D. (2015). Mathematical modelling of p53 basal dynamics and dna damage response. *Mathematical Biosciences*, 259:27–42.

[Chong et al., 2019] Chong, K. H., Samarasinghe, S., Kulasiri, D., and Zheng, J. (2019). Mathematical modelling of core regulatory mechanism in p53 protein that activates apoptotic switch. *Journal of theoretical biology*, 462:134–147.

[Chung et al., 0] Chung, C., Yeung, V. T., and Wong, K. C. (0). Prognostic and predictive biomarkers with therapeutic targets in breast cancer: A 2022 update on current developments, evidence, and recommendations. *Journal of Oncology Pharmacy Practice*, 0(0):10781552221119797. PMID: 35971313.

[Ciccolini et al., 2020] Ciccolini, J., Barbolosi, D., André, N., Barlesi, F., and Benzekry, S. (2020). Mechanistic learning for combinatorial strategies with immuno-oncology drugs: Can model-informed designs help investigators? *JCO precision oncology*, 108(4):486–491.

[Cinquemani et al., 2019] Cinquemani, E., Mairet, F., Yegorov, I., de Jong, H., and Gouzé, J.-L. (2019). Optimal control of bacterial growth for metabolite production: The role of timing and costs of control. In *2019 18th European Control Conference (ECC)*, pages 2657–2662. IEEE.

[Comandante-Lou et al., 2020] Comandante-Lou, N., Khaliq, M., Venkat, D., Manikkam, M., and Fallahi-Sichani, M. (2020). Phenotype-based probabilistic analysis of heterogeneous responses to cancer drugs and their combination efficacy. *PLoS computational biology*, 16(2):e1007688.

[Coskun et al., 2016] Coskun, A. F., Eser, U., and Islam, S. (2016). Cellular identity at the single-cell level. *Molecular BioSystems*, 12(10):2965–2979.

[Cristini et al., 2017] Cristini, V., Koay, E., and Wang, Z. (2017). *An introduction to physical oncology: How mechanistic mathematical modeling can improve cancer therapy outcomes*. CRC Press.

[Cui et al., 2008] Cui, J., Chen, C., Lu, H., Sun, T., and Shen, P. (2008). Two independent positive feedbacks and bistability in the bcl-2 apoptotic switch. *PLoS One*, 3(1):e1469.

[Czabotar et al., 2013] Czabotar, P. E., Westphal, D., Dewson, G., Ma, S., Hockings, C., Fairlie, W. D., Lee, E. F., Yao, S., Robin, A. Y., Smith, B. J., et al. (2013). Bax crystal structures reveal how bh3 domains activate bax and nucleate its oligomerization to induce apoptosis. *Cell*, 152(3):519–531.

[Das et al., 2021] Das, P., Das, S., Das, P., Rihan, F. A., Uzuntarla, M., and Ghosh, D. (2021). Optimal control strategy for cancer remission using combinatorial therapy: a mathematical model-based approach. *Chaos, Solitons & Fractals*, 145:110789.

[De Conti et al., 2021] De Conti, G., Dias, M. H., and Bernards, R. (2021). Fighting drug resistance through the targeting of drug-tolerant persister cells. *Cancers*, 13(5):1118.

[De Jong et al., 2017] De Jong, H., Casagranda, S., Giordano, N., Cinquemani, E., Ropers, D., Geiselmann, J., and Gouzé, J.-L. (2017). Mathematical modelling of microbes: metabolism, gene expression and growth. *Journal of The Royal Society Interface*, 14(136):20170502.

[de Miguel and Calvo, 2020] de Miguel, M. and Calvo, E. (2020). Clinical challenges of immune checkpoint inhibitors. *Cancer Cell*, 38(3):326–333.

[Demaree et al., 2021] Demaree, B., Delley, C. L., Vasudevan, H. N., Peretz, C. A., Ruff, D., Smith, C. C., and Abate, A. R. (2021). Joint profiling of dna and proteins in single cells to dissect genotype-phenotype associations in leukemia. *Nature communications*, 12(1):1–10.

[Dempster et al., 2020] Dempster, A., Petitjean, F., and Webb, G. I. (2020). Rocket: exceptionally fast and accurate time series classification using random convolutional kernels. *Data Mining and Knowledge Discovery*, 34(5):1454–1495.

[Deng et al., 2013] Deng, H., Runger, G., Tuv, E., and Vladimir, M. (2013). A time series forest for classification and feature extraction. *Information Sciences*, 239:142–153.

[Deveraux et al., 1997] Deveraux, Q. L., Takahashi, R., Salvesen, G. S., and Reed, J. C. (1997). X-linked iap is a direct inhibitor of cell-death proteases. *Nature*, 388(6639):300–304.

[Dickens et al., 2012] Dickens, L. S., Boyd, R. S., Jukes-Jones, R., Hughes, M. A., Robinson, G. L., Fairall, L., Schwabe, J. W., Cain, K., and MacFarlane, M. (2012). A death effector domain chain disc model reveals a crucial role for caspase-8 chain assembly in mediating apoptotic cell death. *Molecular cell*, 47(2):291–305.

[Dudal et al., 2022] Dudal, S., Bissantz, C., Caruso, A., David-Pierson, P., Driessen, W., Koller, E., Krippendorff, B.-F., Lechmann, M., Olivares-Morales, A., Paehler, A., et al. (2022). Translating pharmacology models effectively to predict therapeutic benefit. *Drug Discovery Today*.

[Ebert et al., 2022] Ebert, K., Haffner, I., Zwingenberger, G., Keller, S., Raimúndez, E., Geffers, R., Wirtz, R., Barbaria, E., Hollerieth, V., Arnold, R., et al. (2022). Combining gene expression analysis of gastric cancer cell lines and tumor specimens to identify biomarkers for anti-her therapies—the role of has2, shb and hbegf. *BMC cancer*, 22(1):1–17.

[Echeverria et al., 2019] Echeverria, G. V., Ge, Z., Seth, S., Zhang, X., Jeter-Jones, S., Zhou, X., Cai, S., Tu, Y., McCoy, A., Peoples, M., et al. (2019). Resistance to neoadjuvant chemotherapy in triple-negative breast cancer mediated by a reversible drug-tolerant state. *Science translational medicine*, 11(488):eaav0936.

[Eduati et al., 2020] Eduati, F., Jaaks, P., Wappler, J., Cramer, T., Merten, C. A., Garnett, M. J., and Saez-Rodriguez, J. (2020). Patient-specific logic models of signaling pathways from screenings on cancer biopsies to prioritize personalized combination therapies. *Molecular systems biology*, 16(2):e8664.

[Eissing et al., 2004] Eissing, T., Conzelmann, H., Gilles, E. D., Allgower, F., Bullinger, E., and Scheurich, P. (2004). Bistability analyses of a caspase activation model for receptor-induced apoptosis. *Journal of Biological Chemistry*, 279(35):36892–36897.

[El Zarif et al., 2022] El Zarif, T., Yibirin, M., De Oliveira-Gomes, D., Machaalani, M., Nawfal, R., Bittar, G., Bahmad, H. F., and Bitar, N. (2022). Overcoming therapy resistance in colon cancer by drug repurposing. *Cancers*, 14(9):2105.

[Elmore, 2007] Elmore, S. (2007). Apoptosis: a review of programmed cell death. *Toxicologic pathology*, 35(4):495–516.

[Esfahani et al., 2020] Esfahani, K., Roudaia, L., Buhlaiga, N. a., Del Rincon, S., Papneja, N., and Miller, W. (2020). A review of cancer immunotherapy: from the past, to the present, to the future. *Current Oncology*, 27(s2):87–97.

[Eskes et al., 2000] Eskes, R., Desagher, S., Antonsson, B., and Martinou, J.-C. (2000). Bid induces the oligomerization and insertion of bax into the outer mitochondrial membrane. *Molecular and cellular biology*, 20(3):929–935.

[Eydgahi et al., 2013] Eydgahi, H., Chen, W. W., Muhlich, J. L., Vitkup, D., Tsitsiklis, J. N., and Sorger, P. K. (2013). Properties of cell death models calibrated and compared using bayesian approaches. *Molecular systems biology*, 9(1):644.

[Eyler et al., 2020] Eyler, C. E., Matsunaga, H., Hovestadt, V., Vantine, S. J., van Galen, P., and Bernstein, B. E. (2020). Single-cell lineage analysis reveals genetic and epigenetic interplay in glioblastoma drug resistance. *Genome biology*, 21(1):1–21.

[Fallahi-Sichani et al., 2013] Fallahi-Sichani, M., Honarnejad, S., Heiser, L. M., Gray, J. W., and Sorger, P. K. (2013). Metrics other than potency reveal systematic variation in responses to cancer drugs. *Nature chemical biology*, 9(11):708–714.

[Falschlehner et al., 2009] Falschlehner, C., Schaefer, U., and Walczak, H. (2009). Following trail's path in the immune system. *Immunology*, 127(2):145–154.

[Faouzi, 2022] Faouzi, J. (2022). Time series classification: A review of algorithms and implementations. *Machine Learning (Emerging Trends and Applications)*.

[Ferreira et al., 2020] Ferreira, S., Fisher, C., Furlong, L. I., Laplanche, L., Park, B. K., Pin, C., Saez-Rodriguez, J., and Trairatphisan, P. (2020). Quantitative systems toxicology modeling to address key safety questions in drug development: a focus of the transqst consortium.

[Fischer et al., 2019] Fischer, D. S., Fiedler, A. K., Kernfeld, E. M., Genga, R. M., Bastidas-Ponce, A., Bakhti, M., Lickert, H., Hasenauer, J., Maehr, R., and Theis, F. J. (2019). Inferring population dynamics from single-cell rna-sequencing time series data. *Nature biotechnology*, 37(4):461–468.

[Fleisher et al., 2017] Fleisher, B., Brown, A. N., and Ait-Oudhia, S. (2017). Application of pharmacometrics and quantitative systems pharmacology to cancer therapy: The example of luminal a breast cancer. *Pharmacological Research*, 124:20–33.

[Flusberg et al., 2013] Flusberg, D. A., Roux, J., Spencer, S. L., and Sorger, P. K. (2013). Cells surviving fractional killing by trail exhibit transient but sustainable resistance and inflammatory phenotypes. *Molecular biology of the cell*, 24(14):2186–2200.

[Flynn et al., 2019] Flynn, M., Large, J., and Bagnall, T. (2019). The contract random interval spectral ensemble (c-rise): the effect of contracting a classifier on accuracy. In *International Conference on Hybrid Artificial Intelligence Systems*, pages 381–392. Springer.

[Forcina et al., 2017] Forcina, G. C., Conlon, M., Wells, A., Cao, J. Y., and Dixon, S. J. (2017). Systematic quantification of population cell death kinetics in mammalian cells. *Cell systems*, 4(6):600–610.

[Fox et al., 2021] Fox, J. L., Hughes, M. A., Meng, X., Sarnowska, N. A., Powley, I. R., Jukes-Jones, R., Dinsdale, D., Ragan, T. J., Fairall, L., Schwabe, J. W., et al. (2021). Cryo-em structural analysis of fadd: Caspase-8 complexes defines the catalytic dimer architecture for co-ordinated control of cell fate. *Nature communications*, 12(1):1–17.

[Fricker et al., 2010] Fricker, N., Beaudouin, J., Richter, P., Eils, R., Krammer, P. H., and Lavrik, I. N. (2010). Model-based dissection of cd95 signaling dynamics reveals both a pro-and antiapoptotic role of c-flipl. *Journal of cell biology*, 190(3):377–389.

[Friedel and Loewer, 2022] Friedel, L. and Loewer, A. (2022). The guardian's choice: how p53 enables context-specific decision-making in individual cells. *The FEBS Journal*, 289(1):40–52.

[Fröhlich et al., 2018] Fröhlich, F., Kessler, T., Weindl, D., Shadrin, A., Schmiester, L., Hache, H., Muradyan, A., Schütte, M., Lim, J.-H., Heinig, M., et al. (2018). Efficient parameter estimation enables the prediction of drug response using a mechanistic pan-cancer pathway model. *Cell systems*, 7(6):567–579.

[Fulcher et al., 2013] Fulcher, B. D., Little, M. A., and Jones, N. S. (2013). Highly comparative time-series analysis: the empirical structure of time series and their methods. *Journal of the Royal Society Interface*, 10(83):20130048.

[Fulda et al., 2010] Fulda, S., Gorman, A. M., Hori, O., and Samali, A. (2010). Cellular stress responses: cell survival and cell death. *International journal of cell biology*, 2010.

[Fussenegger et al., 2000] Fussenegger, M., Bailey, J. E., and Varner, J. (2000). A mathematical model of caspase function in apoptosis. *Nature biotechnology*, 18(7):768–774.

[Gabor et al., 2021] Gabor, A., Tognetti, M., Driessen, A., Tanevski, J., Guo, B., Cao, W., Shen, H., Yu, T., Chung, V., Bodenmiller, B., et al. (2021). Cell-to-cell and type-to-type heterogeneity of signaling networks: Insights from the crowd. *bioRxiv*.

[Gaudet et al., 2012] Gaudet, S., Spencer, S. L., Chen, W. W., and Sorger, P. K. (2012). Exploring the contextual sensitivity of factors that determine cell-to-cell variability in receptor-mediated apoptosis. *PLoS computational biology*, 8(4):e1002482.

[Geva-Zatorsky et al., 2006] Geva-Zatorsky, N., Rosenfeld, N., Itzkovitz, S., Milo, R., Sigal, A., Dekel, E., Yarnitzky, T., Liron, Y., Polak, P., Lahav, G., et al. (2006). Oscillations and variability in the p53 system. *Molecular systems biology*, 2(1):2006–0033.

[Gonzalez et al., 2013] Gonzalez, A. M., Uhlendorf, J., Schaul, J., Cinquemani, E., Batt, G., and Ferrari-Trecate, G. (2013). Identification of biological models from single-cell data: a comparison between mixed-effects and moment-based inference. In *2013 European Control Conference (ECC)*, pages 3652–3657. IEEE.

[Gottesman et al., 2002] Gottesman, M. M. et al. (2002). Mechanisms of cancer drug resistance. *Annual review of medicine*, 53(1):615–627.

[Gottipati et al., 2020] Gottipati, S. K., Sattarov, B., Niu, S., Pathak, Y., Wei, H., Liu, S., Blackburn, S., Thomas, K., Coley, C., Tang, J., et al. (2020). Learning to navigate the synthetically accessible chemical space using reinforcement learning. In *International Conference on Machine Learning*, pages 3668–3679. PMLR.

[Götz et al., 2022] Götz, M., Barth, A., Bohr, S. S.-R., Börner, R., Chen, J., Cordes, T., Erie, D. A., Gebhardt, C., Hadzic, M. C., Hamilton, G. L., et al. (2022). A blind benchmark of analysis tools to infer kinetic rate constants from single-molecule fret trajectories. *Nature Communications*, 13(1):1–12.

[Greener et al., 2022] Greener, J. G., Kandathil, S. M., Moffat, L., and Jones, D. T. (2022). A guide to machine learning for biologists. *Nature Reviews Molecular Cell Biology*, 23(1):40–55.

[Guilbaud and Galluzzi, 2022] Guilbaud, E. and Galluzzi, L. (2022). Adaptation to momp drives cancer persistence. *Cell Research*, pages 1–2.

[Hafner et al., 2020] Hafner, A., Reyes, J., Stewart-Ornstein, J., Tsabar, M., Jambhekar, A., and Lahav, G. (2020). Quantifying the central dogma in the p53 pathway in live single cells. *Cell systems*, 10(6):495–505.

[Han et al., 2008] Han, L., Zhao, Y., and Jia, X. (2008). Mathematical modeling identified c-flip as an apoptotic switch in death receptor induced apoptosis. *Apoptosis*, 13(10):1198–1204.

[Hasanovic et al., 2020] Hasanovic, A., Simsir, M., Choveau, F. S., Lalli, E., and Mus-Veteau, I. (2020). Astemizole sensitizes adrenocortical carcinoma cells to doxorubicin by inhibiting patched drug efflux activity. *Biomedicines*, 8(8):251.

[Hasenauer et al., 2011] Hasenauer, J., Waldherr, S., Doszczak, M., Radde, N., Scheurich, P., and Allgöwer, F. (2011). Identification of models of heterogeneous cell populations from population snapshot data. *BMC bioinformatics*, 12(1):1–15.

[Hastie et al., 2009] Hastie, T., Tibshirani, R., Friedman, J. H., and Friedman, J. H. (2009). *The elements of statistical learning: data mining, inference, and prediction*, volume 2. Springer.

[Hatron, 2021] Hatron, J. (2021). La recherche clinique en immuno-oncologie et ses phases précoces: état des lieux et perspectives.

[Hekman et al., 2006] Hekman, M., Albert, S., Galmiche, A., Rennefahrt, U. E., Fueller, J., Fischer, A., Puehringer, D., Wiese, S., and Rapp, U. R. (2006). Reversible membrane interaction of bad requires two c-terminal lipid binding domains in conjunction with 14-3-3 protein binding. *Journal of Biological Chemistry*, 281(25):17321–17336.

[Hill et al., 2004] Hill, M. M., Adrain, C., Duriez, P. J., Creagh, E. M., and Martin, S. J. (2004). Analysis of the composition, assembly kinetics and activity of native apaf-1 apoptosomes. *The EMBO journal*, 23(10):2134–2145.

[Hillert et al., 2020a] Hillert, L. K., Ivanisenko, N. V., Busse, D., Espe, J., König, C., Peltek, S. E., Kolchanov, N. A., Ivanisenko, V. A., and Lavrik, I. N. (2020a). Dissecting disc regulation via pharmacological targeting of caspase-8/c-flipl heterodimer. *Cell Death & Differentiation*, 27(7):2117–2130.

[Hillert et al., 2020b] Hillert, L. K., Ivanisenko, N. V., Espe, J., König, C., Ivanisenko, V. A., Kähne, T., and Lavrik, I. N. (2020b). Long and short isoforms of c-flip act as control checkpoints of ded filament assembly. *Oncogene*, 39(8):1756–1772.

[Hills et al., 2014] Hills, J., Lines, J., Baranauskas, E., Mapp, J., and Bagnall, A. (2014). Classification of time series by shapelet transformation. *Data mining and knowledge discovery*, 28(4):851–881.

[Ho and Harrington, 2010] Ho, K. L. and Harrington, H. A. (2010). Bistability in apoptosis by receptor clustering. *PLoS computational biology*, 6(10):e1000956.

[Holland, 2014] Holland, P. M. (2014). Death receptor agonist therapies for cancer, which is the right trail? *Cytokine & growth factor reviews*, 25(2):185–193.

[Honkala et al., 2022] Honkala, A., Malhotra, S. V., Kummar, S., and Junttila, M. R. (2022). Harnessing the predictive power of preclinical models for oncology drug development. *Nature Reviews Drug Discovery*, 21(2):99–114.

[Horn et al., 2017] Horn, S., Hughes, M. A., Schilling, R., Sticht, C., Tenev, T., Ploesser, M., Meier, P., Sprick, M. R., MacFarlane, M., and Leverkus, M. (2017). Caspase-10 negatively regulates caspase-8-mediated cell death, switching the response to cd95l in favor of nf-κb activation and cell survival. *Cell reports*, 19(4):785–797.

[Howells et al., 2011] Howells, C. C., Baumann, W. T., Samuels, D. C., and Finkielstein, C. V. (2011). The bcl-2-associated death promoter (bad) lowers the threshold at which the bcl-2-interacting domain death agonist (bid) triggers mitochondria disintegration. *Journal of theoretical biology*, 271(1):114–123.

[Hu et al., 2022] Hu, J., Serra-Picamal, X., Bakker, G.-J., Van Troys, M., Winograd-katz, S., Ege, N., Gong, X., Didan, Y., Grosheva, I., Polansky, O., et al. (2022). Multi-site assessment of reproducibility in high-content live cell imaging data. *bioRxiv*.

[Hu and Zhang, 2016] Hu, X. and Zhang, Z. (2016). Understanding the genetic mechanisms of cancer drug resistance using genomic approaches. *Trends in Genetics*, 32(2):127–137.

[Hu et al., 2018] Hu, Y., An, Q., Sheu, K., Trejo, B., Fan, S., and Guo, Y. (2018). Single cell multi-omics technology: methodology and application. *Frontiers in cell and developmental biology*, 6:28.

[Hua et al., 2005] Hua, F., Cornejo, M. G., Cardone, M. H., Stokes, C. L., and Lauffenburger, D. A. (2005). Effects of bcl-2 levels on fas signaling-induced caspase-3 activation: molecular genetic tests of computational model predictions. *The Journal of Immunology*, 175(2):985–995.

[Huber et al., 2011] Huber, H. J., Duessmann, H., Wenus, J., Kilbride, S. M., and Prehn, J. H. (2011). Mathematical modelling of the mitochondrial apoptosis pathway. *Biochimica et biophysica acta (BBA)-molecular cell research*, 1813(4):608–615.

[Hughes et al., 2016] Hughes, M. A., Powley, I. R., Jukes-Jones, R., Horn, S., Feoktistova, M., Fairall, L., Schwabe, J. W., Leverkus, M., Cain, K., and MacFarlane, M. (2016). Co-operative and hierarchical binding of c-flip and caspase-8: a unified model defines how c-flip isoforms differentially control cell fate. *Molecular cell*, 61(6):834–849.

[Hyndman and Athanasopoulos, 2018] Hyndman, R. J. and Athanasopoulos, G. (2018). *Forecasting: principles and practice*. OTexts.

[Ildefonso et al., 2022] Ildefonso, G. V., Oliver-Metzig, M., Hoffmann, A., Harris, L. A., and Lopez, C. F. (2022). Distinct execution modes of a biochemical necroptosis model explain cell type-specific responses and variability to cell-death cues. *bioRxiv*.

[Inde and Dixon, 2018] Inde, Z. and Dixon, S. J. (2018). The impact of non-genetic heterogeneity on cancer cell death. *Critical reviews in biochemistry and molecular biology*, 53(1):99–114.

[Inde et al., 2020] Inde, Z., Forcina, G. C., Denton, K., and Dixon, S. J. (2020). Kinetic heterogeneity of cancer cell fractional killing. *Cell reports*, 32(1):107845.

[Ivanisenko and Lavrik, 2020] Ivanisenko, N. and Lavrik, I. (2020). Mathematical modeling reveals the importance of the ded filament composition in the effects of small molecules targeting caspase-8/c-flipl heterodimer. *Biochemistry (Moscow)*, 85(10):1134–1144.

[Jaaks et al., 2022] Jaaks, P., Coker, E. A., Vis, D. J., Edwards, O., Carpenter, E. F., Leto, S. M., Dwane, L., Sassi, F., Lightfoot, H., Barthorpe, S., et al. (2022). Effective drug combinations in breast, colon and pancreatic cancer cells. *Nature*, 603(7899):166–173.

[Jenkins et al., 2018] Jenkins, R. W., Barbie, D. A., and Flaherty, K. T. (2018). Mechanisms of resistance to immune checkpoint inhibitors. *British journal of cancer*, 118(1):9–16.

[Jiao et al., 2022] Jiao, Y., Gao, L., Ji, Y., and Liu, W. (2022). Recent advances in microfluidic single-cell analysis and its applications in drug development. *TrAC Trends in Analytical Chemistry*, page 116796.

[Jones et al., 2022] Jones, I., Dent, L. G., Higo, T., Roumeliotis, T. I., Arias-Garcia, M., Shree, H., Pedersen, M., Chaudhary, J. S., and Bakal, C. (2022). Characterization of proteome-size scaling by integrative omics reveals mechanisms of proliferation control in cancer. *bioRxiv*.

[Jong et al., 2022] Jong, K. X. J., Mohamed, E. H. M., and Ibrahim, Z. A. (2022). Escaping cell death via trail decoy receptors: a systematic review of their roles and expressions in colorectal cancer. *Apoptosis*, pages 1–13.

[Kalkavan et al., 2022] Kalkavan, H., Chen, M. J., Crawford, J. C., Quarato, G., Fitzgerald, P., Tait, S. W., Goding, C. R., and Green, D. R. (2022). Sublethal cytochrome c release generates drug-tolerant persister cells. *Cell*, 185(18):3356–3374.

[Kallenberger et al., 2014] Kallenberger, S. M., Beaudouin, J., Claus, J., Fischer, C., Sorger, P. K., Legewie, S., and Eils, R. (2014). Intra-and interdimeric caspase-8 self-cleavage controls strength and timing of cd95-induced apoptosis. *Science signaling*, 7(316):ra23–ra23.

[Kashima et al., 2020] Kashima, Y., Sakamoto, Y., Kaneko, K., Seki, M., Suzuki, Y., and Suzuki, A. (2020). Single-cell sequencing techniques from individual to multiomics analyses. *Experimental & Molecular Medicine*, 52(9):1419–1427.

[Kazerouni et al., 2020] Kazerouni, A. S., Gadde, M., Gardner, A., Hormuth II, D. A., Jarrett, A. M., Johnson, K. E., Lima, E. A., Lorenzo, G., Phillips, C., Brock, A., et al. (2020). Integrating quantitative assays with biologically based mathematical modeling for predictive oncology. *Iscience*, 23(12):101807.

[Kelly, 2020] Kelly, R. T. (2020). Single-cell proteomics: progress and prospects. *Molecular & Cellular Proteomics*, 19(11):1739–1748.

[Kischkel et al., 2001] Kischkel, F. C., Lawrence, D. A., Tinel, A., LeBlanc, H., Virmani, A., Schow, P., Gazdar, A., Blenis, J., Arnott, D., and Ashkenazi, A. (2001). Death receptor recruitment of endogenous caspase-10 and apoptosis initiation in the absence of caspase-8. *Journal of Biological Chemistry*, 276(49):46639–46646.

[Kochanowski et al., 2018] Kochanowski, K., Morinishi, L., Altschuler, S. J., and Wu, L. F. (2018). Drug persistence–from antibiotics to cancer therapies. *Current opinion in systems biology*, 10:1–8.

[Kong et al., 2022] Kong, W., Midena, G., Chen, Y., Athanasiadis, P., Wang, T., Rousu, J., He, L., and Aittokallio, T. (2022). Systematic review of computational methods for drug combination prediction. *Computational and Structural Biotechnology Journal*, 20:2807–2814.

[Kosaisawe et al., 2021] Kosaisawe, N., Sparta, B., Pargett, M., Teragawa, C. K., and Albeck, J. G. (2021). Transient phases of oxphos inhibitor resistance reveal underlying metabolic heterogeneity in single cells. *Cell metabolism*, 33(3):649–665.

[Kovachka et al., 2021] Kovachka, S., Malloci, G., Vargiu, A. V., Azoulay, S., Mus-Veteau, I., and Ruggerone, P. (2021). Molecular insights into the patched1 drug efflux inhibitory activity of panicein a hydroquinone: a computational study. *Physical Chemistry Chemical Physics*, 23(13):8013–8022.

[Kramer et al., 2022] Kramer, B. A., Sarabia del Castillo, J., and Pelkmans, L. (2022). Multimodal perception links cellular state to decision-making in single cells. *Science*, 377(6606):642–648.

[Kuang et al., 2000] Kuang, A. A., Diehl, G. E., Zhang, J., and Winoto, A. (2000). Fadd is required for dr4-and dr5-mediated apoptosis: lack of trail-induced apoptosis in fadd-deficient mouse embryonic fibroblasts. *Journal of Biological Chemistry*, 275(33):25065–25068.

[Kumari et al., 2019] Kumari, R., Deshmukh, R. S., and Das, S. (2019). Caspase-10 inhibits atp-citrate lyase-mediated metabolic and epigenetic reprogramming to suppress tumorigenesis. *Nature communications*, 10(1):1–15.

[Kuwana et al., 2002] Kuwana, T., Mackey, M. R., Perkins, G., Ellisman, M. H., Latterich, M., Schneiter, R., Green, D. R., and Newmeyer, D. D. (2002). Bid, bax, and lipids cooperate to form supramolecular openings in the outer mitochondrial membrane. *Cell*, 111(3):331–342.

[Kyrochristos et al., 2019] Kyrochristos, I. D., Ziogas, D. E., and Roukos, D. H. (2019). Drug resistance: origins, evolution and characterization of genomic clones and the tumor ecosystem to optimize precise individualized therapy. *Drug discovery today*, 24(6):1281–1294.

[Labory et al., 2022] Labory, J., Le Bideau, G., Pratella, D., Yao, J.-E., Ait-El-Mkadem Saadi, S., Bannwarth, S., El-Hami, L., Paquis-Fluckinger, V., and Bottini, S. (2022). Abeille: a novel method for aberrant expression identification employing machine learning from rna-sequencing data. *Bioinformatics*, 38(20):4754–4761.

[Labrie et al., 2022] Labrie, M., Brugge, J. S., Mills, G. B., and Zervantonakis, I. K. (2022). Therapy resistance: opportunities created by adaptive responses to targeted therapies in cancer. *Nature Reviews Cancer*, 22(6):323–339.

[Lam et al., 2022] Lam, I., Pilla Reddy, V., Ball, K., Arends, R. H., and Mac Gabhann, F. (2022). Development of and insights from systems pharmacology models of antibody-drug conjugates. *CPT: Pharmacometrics & Systems Pharmacology*, 11(8):967–990.

[Lavrik et al., 2009] Lavrik, I. N., Eils, R., Fricker, N., Pforr, C., and Krammer, P. H. (2009). Understanding apoptosis by systems biology approaches. *Molecular bioSystems*, 5(10):1105–1111.

[Lawen, 2003] Lawen, A. (2003). Apoptosis—an introduction. *Bioessays*, 25(9):888–896.

[Lederman et al., 2018] Lederman, E. E., Hope, J. M., and King, M. R. (2018). Mass action kinetic model of apoptosis by trail-functionalized leukocytes. *Frontiers in Oncology*, 8:410.

[Lee et al., 2020] Lee, J., Hyeon, D. Y., and Hwang, D. (2020). Single-cell multiomics: technologies and data analysis methods. *Experimental & Molecular Medicine*, 52(9):1428–1442.

[Lee et al., 2021a] Lee, J., Lee, D., and Kim, Y. (2021a). Mathematical model of stat signalling pathways in cancer development and optimal control approaches. *Royal Society open science*, 8(9):210594.

[Lee et al., 2021b] Lee, M. J., Wang, C., Carroll, M. J., Brubaker, D. K., Hyman, B. T., and Lauffenburger, D. A. (2021b). Computational interspecies translation between alzheimer's disease mouse models and human subjects identifies innate immune complement, tyrobp, and tam receptor agonist signatures, distinct from influences of aging. *Frontiers in neuroscience*, 15.

[Legewie et al., 2006] Legewie, S., Blüthgen, N., and Herzel, H. (2006). Mathematical modeling identifies inhibitors of apoptosis as mediators of positive feedback and bistability. *PLoS computational biology*, 2(9):e120.

[Leonavicius et al., 2019] Leonavicius, K., Nainys, J., Kuciauskas, D., and Mazutis, L. (2019). Multi-omics at single-cell resolution: comparison of experimental and data fusion approaches. *Current opinion in biotechnology*, 55:159–166.

[Leonce et al., 2022] Leonce, C., Saintigny, P., and Ortiz-Cuaran, S. (2022). Cell-intrinsic mechanisms of drug tolerance to systemic therapies in cancerdefining and targeting drug-tolerant persister cells in cancer. *Molecular Cancer Research*, 20(1):11–29.

[Letai et al., 2002] Letai, A., Bassik, M. C., Walensky, L. D., Sorcinelli, M. D., Weiler, S., and Korsmeyer, S. J. (2002). Distinct bh3 domains either sensitize or activate mitochondrial apoptosis, serving as prototype cancer therapeutics. *Cancer cell*, 2(3):183–192.

[Li and You, 2013] Li, B. and You, L. (2013). Predictive power of cell-to-cell variability. *Quantitative Biology*, 1(2):131–139.

[Li et al., 2021] Li, X., Zhong, C.-Q., Wu, R., Xu, X., Yang, Z.-H., Cai, S., Wu, X., Chen, X., Yin, Z., He, Q., et al. (2021). Rip1-dependent linear and nonlinear recruitments of caspase-8 and rip3 respectively to necrosome specify distinct cell death outcomes. *Protein & Cell*, pages 1–19.

[Liao et al., 2022] Liao, J., Wang, Q., Wu, F., and Huang, Z. (2022). In silico methods for identification of potential active sites of therapeutic targets. *Molecules*, 27(20):7103.

[Liu et al., 2021] Liu, J., Hormuth, D. A., Davis, T., Yang, J., McKenna, M. T., Jarrett, A. M., Enderling, H., Brock, A., and Yankeelov, T. E. (2021). A time-resolved experimental–mathematical model for predicting the response of glioma cells to single-dose radiation therapy. *Integrative Biology*, 13(7):167–183.

[Liu et al., 2022] Liu, Y., Fan, Z., Qiao, L., and Liu, B. (2022). Advances in microfluidic strategies for single-cell research. *TrAC Trends in Analytical Chemistry*, page 116822.

[Llamosi et al., 2016] Llamosi, A., Gonzalez-Vargas, A. M., Versari, C., Cinquemani, E., Ferrari-Trecate, G., Hersen, P., and Batt, G. (2016). What population reveals about individual cell identity: single-cell parameter estimation of models of gene expression in yeast. *PLoS computational biology*, 12(2):e1004706.

[Loewer et al., 2010] Loewer, A., Batchelor, E., Gaglia, G., and Lahav, G. (2010). Basal dynamics of p53 reveal transcriptionally attenuated pulses in cycling cells. *Cell*, 142(1):89–100.

[Long et al., 2020] Long, L., Assaraf, Y. G., Lei, Z.-N., Peng, H., Yang, L., Chen, Z.-S., and Ren, S. (2020). Genetic biomarkers of drug resistance: A compass of prognosis and targeted therapy in acute myeloid leukemia. *Drug Resistance Updates*, 52:100703.

[Löning and Király, 2020] Löning, M. and Király, F. J. (2020). Forecasting with sktime: Designing sktime's new forecasting API and applying it to replicate and extend the M4 study. *CoRR*, abs/2005.08067.

[Loo et al., 2017] Loo, L.-H., Bougen-Zhukov, N. M., and Tan, W.-L. C. (2017). Early spatiotemporal-specific changes in intermediate signals are predictive of cytotoxic sensitivity to tnfα and co-treatments. *Scientific reports*, 7(1):1–15.

[Loos and Hasenauer, 2019] Loos, C. and Hasenauer, J. (2019). Mathematical modeling of variability in intracellular signaling. *Current Opinion in Systems Biology*, 16:17–24.

[Lubba et al., 2019] Lubba, C. H., Sethi, S. S., Knaute, P., Schultz, S. R., Fulcher, B. D., and Jones, N. S. (2019). catch22: Canonical time-series characteristics. *Data Mining and Knowledge Discovery*, 33(6):1821–1852.

[Ma et al., 2020] Ma, A., McDermaid, A., Xu, J., Chang, Y., and Ma, Q. (2020). Integrative methods and practical challenges for single-cell multi-omics. *Trends in Biotechnology*.

[Ma et al., 2022] Ma, A., Xin, G., and Ma, Q. (2022). The use of single-cell multi-omics in immuno-oncology. *Nature Communications*, 13(1):1–5.

[Macaulay et al., 2017] Macaulay, I. C., Ponting, C. P., and Voet, T. (2017). Single-cell multiomics: multiple measurements from single cells. *Trends in genetics*, 33(2):155–168.

[Mansouri et al., 2010] Mansouri, R., Bettayeb, M., and Djennoune, S. (2010). Approximation of high order integer systems by fractional order reduced-parameters models. *Mathematical and Computer Modelling*, 51(1-2):53–62.

[Márquez-Jurado et al., 2018] Márquez-Jurado, S., Díaz-Colunga, J., das Neves, R. P., Martinez-Lorente, A., Almazán, F., Guantes, R., and Iborra, F. J. (2018). Mitochondrial levels determine variability in cell death by modulating apoptotic gene expression. *Nature communications*, 9(1):1–11.

[Martinez et al., 2022] Martinez, C., Cinquemani, E., de Jong, H., and Gouzé, J.-L. (2022). Optimal protein production by a synthetic microbial consortium: Coexistence, distribution of labor, and syntrophy. *bioRxiv*.

[Matson and Cook, 2017] Matson, J. P. and Cook, J. G. (2017). Cell cycle proliferation decisions: the impact of single cell analyses. *The FEBS journal*, 284(3):362–375.

[Matveeva et al., 2019] Matveeva, A., Fichtner, M., McAllister, K., McCann, C., Sturrock, M., Longley, D. B., and Prehn, J. H. (2019). Heterogeneous responses to low level death receptor activation are explained by random molecular assembly of the caspase-8 activation platform. *PLoS computational biology*, 15(9):e1007374.

[Medina et al., 2020] Medina, C. B., Mehrotra, P., Arandjelovic, S., Perry, J. S., Guo, Y., Morioka, S., Barron, B., Walk, S. F., Ghesquière, B., Krupnick, A. S., et al. (2020). Metabolites released from apoptotic cells act as tissue messengers. *Nature*, 580(7801):130–135.

[Micheau et al., 2013] Micheau, O., Shirley, S., and Dufour, F. (2013). Death receptors as targets in cancer. *British journal of pharmacology*, 169(8):1723–1744.

[Middlehurst et al., 2020] Middlehurst, M., Large, J., and Bagnall, A. (2020). The canonical interval forest (cif) classifier for time series classification. In *2020 IEEE international conference on big data (big data)*, pages 188–195. IEEE.

[Middlehurst et al., 2021] Middlehurst, M., Large, J., Flynn, M., Lines, J., Bostrom, A., and Bagnall, A. (2021). Hive-cote 2.0: a new meta ensemble for time series classification. *Machine Learning*, 110(11):3211–3243.

[Mikubo et al., 2021] Mikubo, M., Inoue, Y., Liu, G., and Tsao, M.-S. (2021). Mechanism of drug tolerant persister cancer cells: the landscape and clinical implication for therapy. *Journal of Thoracic Oncology*, 16(11):1798–1809.

[Mitchell et al., 2014] Mitchell, M. J., Wayne, E., Rana, K., Schaffer, C. B., and King, M. R. (2014). Trail-coated leukocytes that kill cancer cells in the circulation. *Proceedings of the National Academy of Sciences*, 111(3):930–935.

[Miura et al., 2018] Miura, H., Kondo, Y., Matsuda, M., and Aoki, K. (2018). Cell-to-cell heterogeneity in p38-mediated cross-inhibition of jnk causes stochastic cell death. *Cell reports*, 24(10):2658–2668.

[Mokhtari et al., 2017] Mokhtari, R. B., Homayouni, T. S., Baluch, N., Morgatskaya, E., Kumar, S., Das, B., and Yeger, H. (2017). Combination therapy in combating cancer. *Oncotarget*, 8(23):38022.

[Montinaro and Walczak, 2022] Montinaro, A. and Walczak, H. (2022). Harnessing trail-induced cell death for cancer therapy: a long walk with thrilling discoveries. *Cell Death & Differentiation*, pages 1–13.

[Mund et al., 2022] Mund, A., Coscia, F., Kriston, A., Hollandi, R., Kovács, F., Brunner, A.-D., Migh, E., Schweizer, L., Santos, A., Bzorek, M., et al. (2022). Deep visual proteomics defines single-cell identity and heterogeneity. *Nature Biotechnology*, pages 1–10.

[Najafi et al., 2022] Najafi, M., Jahanbakhshi, A., Gomar, M., Iotti, C., Giaccherini, L., Rezaie, O., Cavallieri, F., Deantonio, L., Bardoscia, L., Botti, A., et al. (2022). State of the art in combination immuno/radiotherapy for brain metastases: Systematic review and meta-analysis. *Current Oncology*, 29(5):2995–3012.

[Nam et al., 2021] Nam, A. S., Chaligne, R., and Landau, D. A. (2021). Integrating genetic and non-genetic determinants of cancer evolution by single-cell multi-omics. *Nature Reviews Genetics*, 22(1):3–18.

[Nath and Bild, 2021] Nath, A. and Bild, A. H. (2021). Leveraging single-cell approaches in cancer precision medicine. *Trends in Cancer*, 7(4):359–372.

[Neumann et al., 2010] Neumann, L., Pforr, C., Beaudouin, J., Pappa, A., Fricker, N., Krammer, P. H., Lavrik, I. N., and Eils, R. (2010). Dynamics within the cd95 death-inducing signaling complex decide life and death of cells. *Molecular systems biology*, 6(1):352.

[Neumann et al., 2014] Neumann, S., Hasenauer, J., Pollak, N., and Scheurich, P. (2014). Dominant negative effects of tumor necrosis factor (tnf)-related apoptosis-inducing ligand (trail) receptor 4 on trail receptor 1 signaling by formation of heteromeric complexes. *Journal of Biological Chemistry*, 289(23):16576–16587.

[Nicolò et al., 2020] Nicolò, C., Périer, C., Prague, M., Bellera, C., Macgrogan, G., Saut, O., and Benzekry, S. (2020). Machine learning and mechanistic modeling for prediction of metastatic relapse in early-stage breast cancer. *JCO clinical cancer informatics*, 4:259–274.

[Niepel et al., 2013] Niepel, M., Hafner, M., Pace, E. A., Chung, M., Chai, D. H., Zhou, L., Schoeberl, B., and Sorger, P. K. (2013). Profiles of basal and stimulated receptor signaling networks predict drug response in breast cancer lines. *Science signaling*, 6(294):ra84–ra84.

[Okada et al., 2022] Okada, D., Zheng, C., and Cheng, J. H. (2022). Mathematical model for the relationship between single-cell and bulk gene expression to clarify the interpretation of bulk gene expression data. *Computational and Structural Biotechnology Journal*, 20:4850–4859.

[Olsson et al., 2016] Olsson, A., Venkatasubramanian, M., Chaudhri, V. K., Aronow, B. J., Salomonis, N., Singh, H., and Grimes, H. L. (2016). Single-cell analysis of mixed-lineage states leading to a binary cell fate choice. *Nature*, 537(7622):698–702.

[Ooi and Ma, 2013] Ooi, H. K. and Ma, L. (2013). Modeling heterogeneous responsiveness of intrinsic apoptosis pathway. *BMC systems biology*, 7(1):65.

[Ortega et al., 2022] Ortega, O. O., Ozen, M., Wilson, B. A., Pino, J. C., Irvin, M. W., Ildefonso, G. V., Garbett, S. P., and Lopez, C. F. (2022). Probability-based mechanisms in biological networks with parameter uncertainty. *bioRxiv*, pages 2021–01.

[Oxnard, 2016] Oxnard, G. R. (2016). The cellular origins of drug resistance in cancer. *Nature medicine*, 22(3):232–234.

[Paek et al., 2016] Paek, A. L., Liu, J. C., Loewer, A., Forrester, W. C., and Lahav, G. (2016). Cell-to-cell variation in p53 dynamics leads to fractional killing. *Cell*, 165(3):631–642.

[Partin et al., 2022] Partin, A., Brettin, T. S., Zhu, Y., Narykov, O., Clyde, A., Overbeek, J., and Stevens, R. L. (2022). Deep learning methods for drug response prediction in cancer: predominant and emerging trends. *arXiv preprint arXiv:2211.10442*.

[Pedregosa et al., 2011] Pedregosa, F., Varoquaux, G., Gramfort, A., Michel, V., Thirion, B., Grisel, O., Blondel, M., Prettenhofer, P., Weiss, R., Dubourg, V., Vanderplas, J., Passos, A., Cournapeau, D., Brucher, M., Perrot, M., and Duchesnay, E. (2011). Scikit-learn: Machine learning in Python. *Journal of Machine Learning Research*, 12:2825–2830.

[Peng et al., 2020] Peng, A., Mao, X., Zhong, J., Fan, S., and Hu, Y. (2020). Single-cell multi-omics and its prospective application in cancer biology. *Proteomics*, 20(13):1900271.

[Pham et al., 2021] Pham, T., Tyagi, A., Wang, Y.-S., and Guo, J. (2021). Single-cell proteomic analysis. *WIREs Mechanisms of Disease*, 13(1):e1503.

[Plaugher et al., 2022] Plaugher, D., Aguilar, B., and Murrugarra, D. (2022). Uncovering potential interventions for pancreatic cancer patients via mathematical modeling. *Journal of theoretical biology*, 548:111197.

[Plaugher and Murrugarra, 2021] Plaugher, D. and Murrugarra, D. (2021). Modeling the pancreatic cancer microenvironment in search of control targets. *Bulletin of Mathematical Biology*, 83(11):1–26.

[Pomeroy et al., 2022] Pomeroy, A. E., Schmidt, E. V., Sorger, P. K., and Palmer, A. C. (2022). Drug independence and the curability of cancer by combination chemotherapy. *Trends in Cancer*, 8(11):915–929.

[Portt et al., 2011] Portt, L., Norman, G., Clapp, C., Greenwood, M., and Greenwood, M. T. (2011). Anti-apoptosis and cell survival: a review. *Biochimica et Biophysica Acta (BBA)-Molecular Cell Research*, 1813(1):238–259.

[Powers, 2020] Powers, D. M. (2020). Evaluation: from precision, recall and f-measure to roc, informedness, markedness and correlation. *arXiv preprint arXiv:2010.16061*.

[Purvis et al., 2012] Purvis, J. E., Karhohs, K. W., Mock, C., Batchelor, E., Loewer, A., and Lahav, G. (2012). p53 dynamics control cell fate. *Science*, 336(6087):1440–1444.

[Rahman et al., 2017] Rahman, M. M., Feng, Y., Yankeelov, T. E., and Oden, J. T. (2017). A fully coupled space–time multiscale modeling framework for predicting tumor growth. *Computer methods in applied mechanics and engineering*, 320:261–286.

[Ramanujan et al., 2016] Ramanujan, S., Gadkar, K., and Kadambi, A. (2016). Quantitative systems pharmacology: applications and adoption in drug development. In *Systems pharmacology and pharmacodynamics*, pages 27–52. Springer.

[Raue et al., 2015] Raue, A., Steiert, B., Schelker, M., Kreutz, C., Maiwald, T., Hass, H., Vanlier, J., Tönsing, C., Adlung, L., Engesser, R., et al. (2015). Data2dynamics: a modeling environment tailored to parameter estimation in dynamical systems. *Bioinformatics*, 31(21):3558–3560.

[Raulf et al., 2014] Raulf, N., El-Attar, R., Kulms, D., Lecis, D., Delia, D., Walczak, H., Papenfuss, K., Odell, E., and Tavassoli, M. (2014). Differential response of head and neck cancer cell lines to trail or smac mimetics is associated with the cellular levels and activity of caspase-8 and caspase-10. *British journal of cancer*, 111(10):1955–1964.

[Rees et al., 2022] Rees, M. G., Brenan, L., do Carmo, M., Duggan, P., Bajrami, B., Arciprete, M., Boghossian, A., Vaimberg, E., Ferrara, S. J., Lewis, T. A., et al. (2022). Systematic identification of biomarker-driven drug combinations to overcome resistance. *Nature Chemical Biology*, 18(6):615–624.

[Rehm et al., 2006] Rehm, M., Huber, H. J., Dussmann, H., and Prehn, J. H. (2006). Systems analysis of effector caspase activation and its control by x-linked inhibitor of apoptosis protein. *The EMBO journal*, 25(18):4338–4349.

[Rehman et al., 2021] Rehman, S. K., Haynes, J., Collignon, E., Brown, K. R., Wang, Y., Nixon, A. M., Bruce, J. P., Wintersinger, J. A., Mer, A. S., Lo, E. B., et al. (2021). Colorectal cancer cells enter a diapause-like dtp state to survive chemotherapy. *Cell*, 184(1):226–242.

[Ren et al., 2022] Ren, T., Zhu, X., Jusko, N. M., Krzyzanski, W., and Jusko, W. J. (2022). Pharmacodynamic model of slow reversible binding and its applications in pharmacokinetic/pharmacodynamic modeling: review and tutorial. *Journal of Pharmacokinetics and Pharmacodynamics*, pages 1–18.

[Riedl et al., 2005] Riedl, S. J., Li, W., Chao, Y., Schwarzenbacher, R., and Shi, Y. (2005). Structure of the apoptotic protease-activating factor 1 bound to adp. *Nature*, 434(7035):926–933.

[Riu, 2001] Riu, D. (2001). *Modélisation des courants induits dans les machines électriques par des systèmes d'ordre un demi*. PhD thesis, Institut National Polytechnique de Grenoble-INPG.

[Rockne and Scott, 2019] Rockne, R. C. and Scott, J. G. (2019). Introduction to mathematical oncology. *JCO clinical cancer informatics*, 3.

[Rodriguez-Meira et al., 2019] Rodriguez-Meira, A., Buck, G., Clark, S.-A., Povinelli, B. J., Alcolea, V., Louka, E., McGowan, S., Hamblin, A., Sousos, N., Barkas, N., et al. (2019). Unravelling intratumoral heterogeneity through high-sensitivity single-cell mutational analysis and parallel rna sequencing. *Molecular cell*, 73(6):1292–1305.

[Rueff and Rodrigues, 2016] Rueff, J. and Rodrigues, A. S. (2016). Cancer drug resistance: a brief overview from a genetic viewpoint. *Cancer Drug Resistance*, pages 1–18.

[Sagar and Grün, 2020] Sagar and Grün, D. (2020). Deciphering cell fate decision by integrated single-cell sequencing analysis. *Annual review of biomedical data science*, 3:1–22.

[Saint-Antoine et al., 2022] Saint-Antoine, M. M., Grima, R., and Singh, A. (2022). A fluctuation-based approach to infer kinetics and topology of cell-state switching. *bioRxiv*.

[Salgia and Kulkarni, 2018] Salgia, R. and Kulkarni, P. (2018). The genetic/non-genetic duality of drug 'resistance'in cancer. *Trends in cancer*, 4(2):110–118.

[Salkovic et al., 2020] Salkovic, E., Abbas, M. M., Belhaouari, S. B., Errafii, K., and Bensmail, H. (2020). Outpyr: Bayesian inference for rna-seq outlier detection. *Journal of Computational Science*, 47:101245.

[Sammut et al., 2022] Sammut, S.-J., Crispin-Ortuzar, M., Chin, S.-F., Provenzano, E., Bardwell, H. A., Ma, W., Cope, W., Dariush, A., Dawson, S.-J., Abraham, J. E., et al. (2022). Multi-omic machine learning predictor of breast cancer therapy response. *Nature*, 601(7894):623–629.

[Sancho-Araiz et al., 2021] Sancho-Araiz, A., Mangas-Sanjuan, V., and Trocóniz, I. F. (2021). The role of mathematical models in immuno-oncology: Challenges and future perspectives. *Pharmaceutics*, 13(7):1016.

[Schäfer, 2015] Schäfer, P. (2015). The boss is concerned with time series classification in the presence of noise. *Data Mining and Knowledge Discovery*, 29(6):1505–1530.

[Schipper et al., 2022] Schipper, L. J., Zeverijn, L. J., Garnett, M. J., and Voest, E. E. (2022). Can drug repurposing accelerate precision oncology? *Cancer Discovery*, pages OF1–OF8.

[Schlatter et al., 2009] Schlatter, R., Schmich, K., Avalos Vizcarra, I., Scheurich, P., Sauter, T., Borner, C., Ederer, M., Merfort, I., and Sawodny, O. (2009). On/off and beyond-a boolean model of apoptosis. *PLoS computational biology*, 5(12):e1000595.

[Schleich et al., 2016] Schleich, K., Buchbinder, J., Pietkiewicz, S., Kähne, T., Warnken, U., Öztürk, S., Schnölzer, M., Naumann, M., Krammer, P., and Lavrik, I. (2016). Molecular architecture of the ded chains at the disc: regulation of procaspase-8 activation by short ded proteins c-flip and procaspase-8 prodomain. *Cell Death & Differentiation*, 23(4):681–694.

[Schmiester et al., 2021] Schmiester, L., Schälte, Y., Bergmann, F. T., Camba, T., Dudkin, E., Egert, J., Fröhlich, F., Fuhrmann, L., Hauber, A. L., Kemmer, S., et al. (2021). Petab—interoperable specification of parameter estimation problems in systems biology. *PLoS computational biology*, 17(1):e1008646.

[Schmiester et al., 2020] Schmiester, L., Weindl, D., and Hasenauer, J. (2020). Parameterization of mechanistic models from qualitative data using an efficient optimal scaling approach. *Journal of Mathematical Biology*, 81(2):603–623.

[Schneider et al., 2012] Schneider, A., Klingmüller, U., and Schilling, M. (2012). Short-term information processing, long-term responses: Insights by mathematical modeling of signal transduction: early activation dynamics of key signaling mediators can be predictive for cell fate decisions. *Bioessays*, 34(7):542–550.

[Schneider et al., 2019] Schneider, B. K., Boyer, A., Ciccolini, J., Barlesi, F., Wang, K., Benzekry, S., and Mochel, J. P. (2019). Optimal scheduling of bevacizumab and pemetrexed/cisplatin dosing in non-small cell lung cancer. *CPT: pharmacometrics & systems pharmacology*, 8(8):577–586.

[Schwarzer et al., 2020] Schwarzer, R., Jiao, H., Wachsmuth, L., Tresch, A., and Pasparakis, M. (2020). Fadd and caspase-8 regulate gut homeostasis and inflammation by controlling mlkl-and gsdmd-mediated death of intestinal epithelial cells. *Immunity*, 52(6):978–993.

[Seabold and Perktold, 2010] Seabold, S. and Perktold, J. (2010). statsmodels: Econometric and statistical modeling with python. In *9th Python in Science Conference*.

[Seidel and von Karstedt, 2022] Seidel, E. and von Karstedt, S. (2022). Extrinsic cell death pathway plasticity: a driver of clonal evolution in cancer? *Cell Death Discovery*, 8(1):1–6.

[Seyrek et al., 2020] Seyrek, K., Ivanisenko, N. V., Richter, M., Hillert, L. K., König, C., and Lavrik, I. N. (2020). Controlling cell death through post-translational modifications of ded proteins. *Trends in Cell Biology*.

[Sharma et al., 2010] Sharma, S. V., Lee, D. Y., Li, B., Quinlan, M. P., Takahashi, F., Maheswaran, S., McDermott, U., Azizian, N., Zou, L., Fischbach, M. A., et al. (2010). A chromatin-mediated reversible drug-tolerant state in cancer cell subpopulations. *Cell*, 141(1):69–80.

[Shehab et al., 2022] Shehab, M., Abualigah, L., Shambour, Q., Abu-Hashem, M. A., Shambour, M. K. Y., Alsalibi, A. I., and Gandomi, A. H. (2022). Machine learning in medical applications: A review of state-of-the-art methods. *Computers in Biology and Medicine*, 145:105458.

[Shen et al., 2019] Shen, S., Faouzi, S., Bastide, A., Martineau, S., Malka-Mahieu, H., Fu, Y., Sun, X., Mateus, C., Routier, E., Roy, S., et al. (2019). An epitranscriptomic mechanism underlies selective mrna translation remodelling in melanoma persister cells. *Nature communications*, 10(1):1–14.

[Shen et al., 2020] Shen, S., Faouzi, S., Souquere, S., Roy, S., Routier, E., Libenciuc, C., André, F., Pierron, G., Scoazec, J.-Y., and Robert, C. (2020). Melanoma persister cells are tolerant to braf/mek inhibitors via acox1-mediated fatty acid oxidation. *Cell reports*, 33(8):108421.

[Shi et al., 2021] Shi, Y., Dolan, M., Mastri, M., Hill, J. W., Dommer, A., Benzekry, S., Eng, K., and Ebos, J. M. (2021). Acquired resistance to pd-l1 inhibition is associated with an enhanced type i ifn-stimulated secretory program in tumor cells. *bioRxiv*.

[Shin, 2021] Shin, E.-C. (2021). Cancer immunotherapy: Special issue of bmb reports in 2021. *BMB reports*, 54(1):1.

[Shlyakhtina et al., 2017] Shlyakhtina, Y., Pavet, V., and Gronemeyer, H. (2017). Dual role of dr5 in death and survival signaling leads to trail resistance in cancer cells. *Cell death & disease*, 8(8):e3025–e3025.

[Shrikumar et al., 2017] Shrikumar, A., Greenside, P., and Kundaje, A. (2017). Learning important features through propagating activation differences. In *International conference on machine learning*, pages 3145–3153. PMLR.

[Simsir and Mus-Veteau, 2020] Simsir, M. and Mus-Veteau, I. (2020). Rnd family efflux pumps: from antibioresistance to chemotherapy resistance. *Swedish J. Biosci. Res.*, 1:51–61.

[Singh and Kaushik, 2022] Singh, D. P. and Kaushik, B. (2022). A systematic literature review for the prediction of anticancer drug response using various machine learning and deep learning techniques. *Chemical Biology & Drug Design*.

[Sontag, 2020] Sontag, E. D. (2020). Some control theory ideas in systems and synthetic biology. In *2020 European Control Conference (ECC)*, pages 1–1. IEEE.

[Sorger et al., 2011] Sorger, P. K., Allerheiligen, S. R., Abernethy, D. R., Altman, R. B., Brouwer, K. L., Califano, A., D'Argenio, D. Z., Iyengar, R., Jusko, W. J., Lalonde, R., et al. (2011). Quantitative and systems pharmacology in the post-genomic era: new approaches to discovering drugs and understanding therapeutic mechanisms. In *An NIH white paper by the QSP workshop group*, volume 48, pages 1–47. NIH Bethesda Bethesda, MD.

[Soto-Gamez et al., 2022] Soto-Gamez, A., Wang, Y., Zhou, X., Seras, L., Quax, W., and Demaria, M. (2022). Enhanced extrinsic apoptosis of therapy-induced senescent cancer cells using a death receptor 5 (dr5) selective agonist. *Cancer letters*, 525:67–75.

[Spencer et al., 2009] Spencer, S. L., Gaudet, S., Albeck, J. G., Burke, J. M., and Sorger, P. K. (2009). Non-genetic origins of cell-to-cell variability in trail-induced apoptosis. *Nature*, 459(7245):428–432.

[Spiller et al., 2010] Spiller, D. G., Wood, C. D., Rand, D. A., and White, M. R. (2010). Measurement of single-cell dynamics. *Nature*, 465(7299):736–745.

[Srinivasan et al., 2022] Srinivasan, M., Clarke, R., and Kraikivski, P. (2022). Mathematical models of death signaling networks. *Entropy*, 24(10):1402.

[Stanislavsky, 2006] Stanislavsky, A. A. (2006). Hamiltonian formalism of fractional systems. *The European Physical Journal B-Condensed Matter and Complex Systems*, 49(1):93–101.

[Stapor et al., 2022] Stapor, P., Schmiester, L., Wierling, C., Merkt, S., Pathirana, D., Lange, B. M., Weindl, D., and Hasenauer, J. (2022). Mini-batch optimization enables training of ode models on large-scale datasets. *Nature communications*, 13(1):1–17.

[Stapor et al., 2018] Stapor, P., Weindl, D., Ballnus, B., Hug, S., Loos, C., Fiedler, A., Krause, S., Hroß, S., Fröhlich, F., and Hasenauer, J. (2018). Pesto: parameter estimation toolbox. *Bioinformatics*, 34(4):705–707.

[Stefan et al., 2015] Stefan, D., Pinel, C., Pinhal, S., Cinquemani, E., Geiselmann, J., and de Jong, H. (2015). Inference of quantitative models of bacterial promoters from time-series reporter gene data. *PLoS computational biology*, 11(1):e1004028.

[Stewart and Watson, 1983] Stewart, M. and Watson, I. (1983). Standard units for expressing drug concentrations in biological fluids. *British journal of clinical pharmacology*, 16(1):3.

[Stoma et al., 2013] Stoma, S., Donzé, A., Bertaux, F., Maler, O., and Batt, G. (2013). Stl-based analysis of trail-induced apoptosis challenges the notion of type i/type ii cell line classification. *PLoS computational biology*, 9(5):e1003056.

[Strasser and Vaux, 2020] Strasser, A. and Vaux, D. L. (2020). Cell death in the origin and treatment of cancer. *Molecular Cell*.

[Stucki and Simon, 2005] Stucki, J. W. and Simon, H.-U. (2005). Mathematical modeling of the regulation of caspase-3 activation and degradation. *Journal of theoretical biology*, 234(1):123–131.

[Sun et al., 2022] Sun, Q., Wei, X., Wang, Z., Zhu, Y., Zhao, W., and Dong, Y. (2022). Primary and acquired resistance against immune check inhibitors in non-small cell lung cancer. *Cancers*, 14(14):3294.

[Sun et al., 2016] Sun, W., Sanderson, P. E., and Zheng, W. (2016). Drug combination therapy increases successful drug repositioning. *Drug discovery today*, 21(7):1189–1195.

[Suo et al., 2022] Suo, F., Zhou, X., Setroikromo, R., and Quax, W. J. (2022). Receptor specificity engineering of tnf superfamily ligands. *Pharmaceutics*, 14(1):181.

[Surdutovich and Solov'yov, 2019] Surdutovich, E. and Solov'yov, A. V. (2019). Multiscale modeling for cancer radiotherapies. *Cancer Nanotechnology*, 10(1):1–22.

[Swayden et al., 2020] Swayden, M., Chhouri, H., Anouar, Y., and Grumolato, L. (2020). Tolerant/persister cancer cells and the path to resistance to targeted therapy. *Cells*, 9(12):2601.

[Szalai et al., 2021] Szalai, A. M., Zaza, C., and Stefani, F. D. (2021). Super-resolution fret measurements. *Nanoscale*, 13(44):18421–18433.

[Tagliaferri et al., 2022] Tagliaferri, L., Lancellotta, V., Fionda, B., Mangoni, M., Casà, C., Di Stefani, A., Pagliara, M. M., D'Aviero, A., Schinzari, G., Chiesa, S., et al. (2022). Immunotherapy and radiotherapy in melanoma: a multidisciplinary comprehensive review. *Human Vaccines & Immunotherapeutics*, 18(3):1903827.

[Tang et al., 2018] Tang, J., Shalabi, A., and Hubbard-Lucey, V. M. (2018). Comprehensive analysis of the clinical immuno-oncology landscape. *Annals of Oncology*, 29(1):84–91.

[Team, 2020] Team, J. D. (2020). Joblib: running python functions as pipeline jobs.

[Tellez-Gabriel et al., 2016] Tellez-Gabriel, M., Ory, B., Lamoureux, F., Heymann, M.-F., and Heymann, D. (2016). Tumour heterogeneity: the key advantages of single-cell analysis. *International journal of molecular sciences*, 17(12):2142.

[Terai et al., 2018] Terai, H., Kitajima, S., Potter, D. S., Matsui, Y., Quiceno, L. G., Chen, T., Kim, T.-j., Rusan, M., Thai, T. C., Piccioni, F., et al. (2018). Er stress signaling promotes the survival of cancer "persister cells" tolerant to egfr tyrosine kinase inhibitorsufmylation-regulated er stress and egfr tki cell persistence. *Cancer research*, 78(4):1044–1057.

[Thorpe et al., 2008] Thorpe, J. A., Christian, P. A., and Schwarze, S. R. (2008). Proteasome inhibition blocks caspase-8 degradation and sensitizes prostate cancer cells to death receptor-mediated apoptosis. *The Prostate*, 68(2):200–209.

[Torkamannia et al., 2022a] Torkamannia, A., Omidi, Y., and Ferdousi, R. (2022a). A review of machine learning approaches for drug synergy prediction in cancer. *Briefings in Bioinformatics*, 23(3). bbac075.

[Torkamannia et al., 2022b] Torkamannia, A., Omidi, Y., and Ferdousi, R. (2022b). A review of machine learning approaches for drug synergy prediction in cancer. *Briefings in Bioinformatics*, 23(3):bbac075.

[Trilla-Fuertes et al., 2020] Trilla-Fuertes, L., Gámez-Pozo, A., López-Camacho, E., Prado-Vázquez, G., Zapater-Moros, A., López-Vacas, R., Arevalillo, J. M., Díaz-Almirón, M., Navarro, H., Maín, P., et al. (2020). Computational models applied to metabolomics data hints at the relevance of glutamine metabolism in breast cancer. *BMC cancer*, 20(1):1–11.

[Tsuchiya et al., 2015] Tsuchiya, Y., Nakabayashi, O., and Nakano, H. (2015). Flip the switch: Regulation of apoptosis and necroptosis by cflip. *International journal of molecular sciences*, 16(12):30321–30341.

[Tummers et al., 2020] Tummers, B., Mari, L., Guy, C. S., Heckmann, B. L., Rodriguez, D. A., Rühl, S., Moretti, J., Crawford, J. C., Fitzgerald, P., Kanneganti, T.-D., et al. (2020). Caspase-8-dependent inflammatory responses are controlled by its adaptor, fadd, and necroptosis. *Immunity*, 52(6):994–1006.

[Vallette et al., 2019] Vallette, F. M., Olivier, C., Lezot, F., Oliver, L., Cochonneau, D., Lalier, L., Cartron, P.-F., and Heymann, D. (2019). Dormant, quiescent, tolerant and persister cells: Four synonyms for the same target in cancer. *Biochemical pharmacology*, 162:169–176.

[Villaverde et al., 2019] Villaverde, A. F., Fröhlich, F., Weindl, D., Hasenauer, J., and Banga, J. R. (2019). Benchmarking optimization methods for parameter estimation in large kinetic models. *Bioinformatics*, 35(5):830–838.

[Vistain and Tay, 2021] Vistain, L. F. and Tay, S. (2021). Single-cell proteomics. *Trends in biochemical sciences*, 46(8):661–672.

[Vittadello and Stumpf, 2022] Vittadello, S. T. and Stumpf, M. P. (2022). Open problems in mathematical biology. *arXiv preprint arXiv:2206.09516*.

[Voropaeva et al., 2017] Voropaeva, O. F., Shokin, Y. I., et al. (2017). Deregulation of p53-dependent micrornas: the results of mathematical modeling. *Mathematical Biology and Bioinformatics*, 12(1):151–175.

[Wachmann et al., 2010] Wachmann, K., Pop, C., van Raam, B. J., Drag, M., Mace, P. D., Snipas, S. J., Zmasek, C., Schwarzenbacher, R., Salvesen, G. S., and Riedl, S. J. (2010). Activation and specificity of human caspase-10. *Biochemistry*, 49(38):8307–8315.

[Waldherr et al., 2009] Waldherr, S., Hasenauer, J., and Allgöwer, F. (2009). Estimation of biochemical network parameter distributions in cell populations. *IFAC Proceedings Volumes*, 42(10):1265–1270.

[Wang et al., 2001] Wang, J., Chun, H. J., Wong, W., Spencer, D. M., and Lenardo, M. J. (2001). Caspase-10 is an initiator caspase in death receptor signaling. *Proceedings of the National Academy of Sciences*, 98(24):13884–13888.

[Wang et al., 2019] Wang, X., Zhang, H., and Chen, X. (2019). Drug resistance and combating drug resistance in cancer. *Cancer Drug Resistance*, 2(2):141.

[Ward et al., 2020] Ward, R. A., Fawell, S., Floc'h, N., Flemington, V., McKerrecher, D., and Smith, P. D. (2020). Challenges and opportunities in cancer drug resistance. *Chemical Reviews*, 121(6):3297–3351.

[Warner et al., 2019] Warner, H. V., Sivakumar, N., Peirce, S. M., and Lazzara, M. J. (2019). Multiscale computational models of cancer. *Current Opinion in Biomedical Engineering*, 11:137–144.

[Watson et al., 2021] Watson, E. R., Fard, A. T., and Mar, J. C. (2021). Computational methods for single-cell imaging and omics data integration. *Frontiers in molecular biosciences*, 8.

[Weiss et al., 2022] Weiss, F., Lauffenburger, D., and Friedl, P. (2022). Towards targeting of shared mechanisms of cancer metastasis and therapy resistance. *Nature Reviews Cancer*, 22(3):157–173.

[Wen and Tang, 2022] Wen, L. and Tang, F. (2022). Recent advances in single-cell sequencing technologies. *Precision Clinical Medicine*, 5(1):pbac002.

[Wong et al., 2019] Wong, C. H., Siah, K. W., and Lo, A. W. (2019). Estimation of clinical trial success rates and related parameters. *Biostatistics*, 20(2):273–286.

[Wouters et al., 2020] Wouters, O. J., McKee, M., and Luyten, J. (2020). Estimated research and development investment needed to bring a new medicine to market, 2009-2018. *Jama*, 323(9):844–853.

[Wu et al., 2020] Wu, Y., Li, J., Kaboli, P. J., Shen, J., Wu, X., Zhao, Y., Ji, H., Du, F., Zhou, Y., Wang, Y., et al. (2020). Natural killer cells as a double-edged sword in cancer immunotherapy: A comprehensive review from cytokine therapy to adoptive cell immunotherapy. *Pharmacological research*, 155:104691.

[Wuerth et al., 2016] Wuerth, R., Thellung, S., Bajetto, A., Mazzanti, M., Florio, T., and Barbieri, F. (2016). Drug-repositioning opportunities for cancer therapy: novel molecular targets for known compounds. *Drug discovery today*, 21(1):190–199.

[Würstle et al., 2014] Würstle, M., Zink, E., Prehn, J., and Rehm, M. (2014). From computational modelling of the intrinsic apoptosis pathway to a systems-based analysis of chemotherapy resistance: achievements, perspectives and challenges in systems medicine. *Cell Death & Disease*, 5(5):e1258–e1258.

[Xia et al., 2022] Xia, F., Allen, J., Balaprakash, P., Brettin, T., Garcia-Cardona, C., Clyde, A., Cohn, J., Doroshow, J., Duan, X., Dubinkina, V., et al. (2022). A cross-study analysis of drug response prediction in cancer cell lines. *Briefings in bioinformatics*, 23(1):bbab356.

[Xie et al., 2022] Xie, J., Zhang, L., Liu, B., Liang, X., and Shi, J. (2022). Single-cell analysis of p53 transitional dynamics unravels stimulus-and cell type-dependent signaling output motifs. *BMC biology*, 20(1):1–14.

[Yang et al., 2020a] Yang, L., George, J., and Wang, J. (2020a). Deep profiling of cellular heterogeneity by emerging single-cell proteomic technologies. *Proteomics*, 20(13):1900226.

[Yang et al., 2020b] Yang, N., Sun, T., and Shen, P. (2020b). Deciphering p53 dynamics and cell fate in dna damage response using mathematical modeling. *Genome Instability & Disease*, 1(5):265–277.

[Yin et al., 2017] Yin, Z., Qi, H., Liu, L., and Jin, Z. (2017). The optimal regulation mode of bcl-2 apoptotic switch revealed by bistability analysis. *Biosystems*, 162:44–52.

[Yuan et al., 2018] Yuan, X., Gajan, A., Chu, Q., Xiong, H., Wu, K., and Wu, G. S. (2018). Developing trail/trail death receptor-based cancer therapies. *Cancer and Metastasis Reviews*, 37(4):733–748.

[Yurkovsky and Nachman, 2013] Yurkovsky, E. and Nachman, I. (2013). Event timing at the single-cell level. *Briefings in functional genomics*, 12(2):90–98.

[Zhang et al., 2022a] Zhang, T., Androulakis, I. P., Bonate, P., Cheng, L., Helikar, T., Parikh, J., Rackauckas, C., Subramanian, K., and Cho, C. R. (2022a). Two heads are better than one: current landscape of integrating qsp and machine learning. *Journal of Pharmacokinetics and Pharmacodynamics*, pages 1–14.

[Zhang et al., 2009] Zhang, T., Brazhnik, P., and Tyson, J. J. (2009). Computational analysis of dynamical responses to the intrinsic pathway of programmed cell death. *Biophysical journal*, 97(2):415–434.

[Zhang et al., 2010] Zhang, X.-P., Liu, F., and Wang, W. (2010). Coordination between cell cycle progression and cell fate decision by the p53 and e2f1 pathways in response to dna damage. *Journal of Biological Chemistry*, 285(41):31571–31580.

[Zhang et al., 2022b] Zhang, Z., Qin, S., Chen, Y., Zhou, L., Yang, M., Tang, Y., Zuo, J., Zhang, J., Mizokami, A., Nice, E. C., et al. (2022b). Inhibition of npc1l1 disrupts adaptive responses of drug-tolerant persister cells to chemotherapy. *EMBO molecular medicine*, 14(2):e14903.

[Zhao and Itti, 2018] Zhao, J. and Itti, L. (2018). shapedtw: Shape dynamic time warping. *Pattern Recognition*, 74:171–184.

[Zhu et al., 2020] Zhu, C., Preissl, S., and Ren, B. (2020). Single-cell multimodal omics: the power of many. *Nature methods*, 17(1):11–14.

Modélisation des dynamiques de réponse de cellules uniques aux anticancéreux pour prédire l'émergence des cellules tolérantes

Marielle Péré

Résumé

La **résistance des cellules** aux traitements **anticancéreux** est la première cause d'**échec thérapeutique** en oncologie et sert de **base** pour **évaluer l'efficacité des médicaments**. Malgré des avancées considérables dans l'amélioration des traitements disponibles, et leur personnalisation, l'**émergence de cellules tolérantes** aux médicaments, et plus globalement leur dynamique, sont encore mal comprises.

Cette thèse explore l'**initiation de l'apoptose** déclenchée par les ligands agonistes des récepteurs de mort, dans des **populations tumorales isogéniques**, afin d'étudier l'**émergence de cellules tolérantes** aux médicaments. Dans ce but, nous couplons des **données de fluorescence sur cellule unique**, provenant d'expériences de **microscopie sur cellules vivantes**, avec la **modélisation mathématique de la voie transcriptomique** de l'apoptose extrinsèque et des techniques d'**apprentissage automatique** pour atteindre deux objectifs. Le premier est de **mieux comprendre la dynamique des cellules tolérantes** aux médicaments et les différences par rapport aux cellules sœurs sensibles, qui pourraient expliquer l'apparition d'un phénotype tolérant. Le second objectif est d'**identifier les signes précoces de résistance dans ces cellules clonales** afin de prédire le plus tôt possible le premier événement menant à la tolérance. L'inclusion de cette prédiction dans notre **protocole expérimental FATE-SEQ** contribuera à obtenir les **facteurs moléculaires des états cellulaires transitoires de résistance et de sensibilité**, tout en préservant l'intégrité des cellules de l'impact du médicament. À long terme, ce protocole permettra d'**identifier de nouvelles cibles thérapeutiques** (gènes, protéines, etc.) pour la création de **co-traitements**, dès les **premiers stades pré-cliniques** du développement des médicaments.

Afin de développer un **modèle dynamique pour la voie de l'apoptose**, nous **comparons d'abord le rôle de plusieurs composants** de cette forme de mort cellulaire programmée, afin d'**identifier les contributions dominantes**. Nous utilisons ensuite des données expérimentales de cellules uniques pour **estimer les paramètres de différents modèles mathématiques** d'initiation de l'apoptose extrinsèque par ligands de mort, afin d'**étudier les engagements hétérogènes vers la mort** et de mettre en évidence les d**éterminants cinétiques** (réaction chimique, protéines ou une chronologie spécifique) **de la décision cellulaire**. Enfin, en utilisant ces signes de mort comme seuil prédictif, et en les couplant avec des **classificateurs d'apprentissage automatique**, nous construisons un **prédicteur du destin cellulaire en réponse à un ligand de mort** pour les expériences de microscopie sur cellules uniques vivantes.

Mots-clés : Dynamiques des cellules uniques, Cellules tolérantes, Modèles EDO, Apprentissage automatique, Estimation de paramètres, Prédiction du devenir cellulaire, Anticancéreux, Microscopie sur cellules vivantes.